Springer Earth System Sciences

Gerrit Lohmann · Helge Meggers
Vikram Unnithan · Dieter Wolf-Gladrow
Justus Notholt · Astrid Bracher *Editors*

Towards an Interdisciplinary Approach in Earth System Science

Advances of a Helmholtz Graduate Research School

Springer

Towards an Interdisciplinary Approach in Earth System Science

Springer Earth System Sciences

More information about this series at http://www.springer.com/series/10178

Gerrit Lohmann · Helge Meggers
Vikram Unnithan · Dieter Wolf-Gladrow
Justus Notholt · Astrid Bracher
Editors

Towards an Interdisciplinary Approach in Earth System Science

Advances of a Helmholtz Graduate Research School

Springer

Editors

Gerrit Lohmann
Alfred Wegener Institute
Helmholtz Centre for Polar and Marine Research
Bremerhaven
Germany

Helge Meggers
Alfred Wegener Institute
Helmholtz Centre for Polar and Marine Research
Bremerhaven
Germany

Vikram Unnithan
School of Engineering and Science
Jacobs University
Bremen
Germany

Dieter Wolf-Gladrow
Alfred Wegener Institute
Helmholtz Centre for Polar and Marine Research
Bremerhaven
Germany

Justus Notholt
Institute of Environmental Physics
University of Bremen
Bremen
Germany

Astrid Bracher
Alfred Wegener Institute
Helmholtz Centre for Polar and Marine Research
Bremerhaven
Germany

Springer Earth System Sciences
ISBN 978-3-319-13864-0 ISBN 978-3-319-13865-7 (eBook)
DOI 10.1007/978-3-319-13865-7

Library of Congress Control Number: 2014957302

Springer Cham Heidelberg New York Dordrecht London

Printed on acid-free paper

Springer International Publishing AG Switzerland is part of Springer Science+Business Media (www.springer.com)

Acknowledgments

The editors gratefully acknowledge funding of the Earth System Science Research School (ESSReS) by the Helmholtz Association and the support by the Alfred Wegener Institute, Helmholtz Centre for Polar and Marine Research, the University of Bremen and the Jacobs University.

The editors would like to thank the internal reviewers from the AWI, the University of Bremen and the Jacobs University: Werner Armonies, Jelle Bijma, Astrid Bracher, Michael Buchwitz, Martin Butzin, Sergey Danilov, Wolfgang Dierking, Klaus Grosfeld, Claudia Hanfland, Oliver Huhn, Johannes Kaiser, Gregor Knorr, Peter Lemke, Stefanie Linow, Helge Meggers, Christian Melsheimer, Stefan Noel, Justus Notholt, Christian Schäfer-Neth, Reiner Schlitzer, Claudia Sprengel, Malte Thoma, Christoph Waldmann, Mark Weber and Martin Werner.

We also express our gratitude to the external reviewers: Karen Assmann, Per Arne Björkum, Erik Bonsdorff, Paul Butler, Patricia Castellanos, Jonathan Franklin, Peter Gege, Thomas Gölles, Corinna Harms, Christian Hensen, Heike Leitte, Mauricio Mata, Leif Toudal Petersen, Monica Pondrelli, Simone Sabbatini, Christian von Savigny, Julienne Stroeve, Sonja Sucro, Matthew Toohey, Bo Vinther, Jinsongdi Yu and three anonymous reviewers.

We would like to thank the Advisory Board of ESSReS, namely the Director of the AWI (Prof. Dr. K. Lochte), the President of the Bremen University (Prof. Dr. B. Scholz-Reiter) and the President of the Jacobs University (Prof. Dr.-Ing. Katja Windt). The editors finally wish to thank Ludvig Löwemark for his coordination work and Stefanie Klebe and Klaus Grosfeld for their kind support during the editing processes of this second ESSReS Springer Briefs book.

Contents

Part I Introduction

Part II Remote Sensing and Modelling of Atmospheric Chemistry and Sea Ice Parameters

Part III Physical Oceanography

Part IV Sea-ice Physics

Part V Earth System Modelling and Data Analysis

Part VI Climate Archives and Geotectonics

Part VII Geoinformatics

Part I
Introduction

Earth System Science—Past Experiences and Future Trends

Vikram Unnithan, Astrid Bracher, Klaus Grosfeld, Annette Ladstätter-Weißenmayer, Gerrit Lohmann, Helge Meggers, Justus Notholt and Dieter Wolf-Gladrow

Abstract Earth System Science has developed over the last two decades from an interesting concept in Earth sciences education to a fully integrative science focussed on understanding the complex system Earth. This evolution is partially due to the radical and far reaching anthropogenic changes and the general feeling of helplessness with regards to the possible consequences and future impacts on the Earth System. This paper proposes that a paradigm shift in undergraduate and graduate education is needed to further develop Earth System Science. Graduate programs such as the Earth System Science Research School (ESSReS), which are intrinsically trans- and interdisciplinary will help to change rigid subject specific mind-set among faculty and students. The health and sustainability of our planet is at stake.

1 Introduction

Astronomers have been looking for habitable planets for many decades (Fritz et al. 2014). It could be argued that the primary motivation was not to find other life forms but to find a suitable alternative for Earth. If some of the doom and gloom scenarios (Elliott and Hanson 2003) are to be believed, we would need this alternative soon, perhaps even within this century. What is clear and a fact is that the future of Earth is in our hands and it is in our interest as a species to keep it going/habitable.

V. Unnithan (✉)
Jacobs University, Bremen, Germany
e-mail: v.unnithan@jacobs-university.de

A. Bracher · K. Grosfeld · G. Lohmann · H. Meggers · D. Wolf-Gladrow
Alfred Wegener Institute Helmholtz Centre for Polar and Marine Research, Bremerhaven, Germany

A. Bracher · A. Ladstätter-Weißenmayer · J. Notholt
Institute of Environmental Physics, University of Bremen, Bremen, Germany

G. Lohmann et al. (eds.), *Towards an Interdisciplinary Approach in Earth System Science*, Springer Earth System Sciences,
DOI 10.1007/978-3-319-13865-7_1

The understanding that the Earth is a complex system with many interwoven feedback mechanisms is not new—Jacques-Joseph Ébelmen who in 1845 correctly identified fundamental process and factors affecting global biogeochemical cycles (Berner 2012), Vladimir Vernadsky's noosphere or the science of science (Winkler 2014), GAIA theory (Lovelock 1972), or 'Goldilocks' planet[1] to name a few. At any time, natural processes have determined the Earth's climatic history. For example various processes that have historically altered the Earth's view, such as the Milankovitch cycles in the Earth's movements around the sun, various shifts in Earth tectonic plates occurring over thousands of years, asteroid impacts on Earth or volcanic eruptions have had strong natural effects on different time-scales on Earth. Until the middle or later part of the 20th century scientists (natural/social) were getting to grips with the details and methods in their own specialized fields. However, in the past decades, with increasing anthropogenic impact, there has been a growing need to understand the interconnections and tele-connections between the various parts of the Earth system. This is even more urgent since we are slowly but steadily changing/influencing aspects of this system without fully understanding the impacts and consequences. Dramatic increase in CO_2 and methane emissions, excessive bio-geo resource exploitation, manifold increase in population, decreasing biodiversity, changing land-use practices to name just a few changes.

Earth System Science (ESS) has been varying described as the "the whole in the sum of its parts" (Victor Smetacek, per. comms) or "an integrative super-discipline that accepts that biophysical sciences and social sciences are equally important in any attempts to understand the state, and future of the Earth System" (Pitman 2005) or "seeks to integrate various fields of academic study to understand the Earth as a system and considers interaction between the various elements of the Earth System".[2] The aim is to take a step back, not to focus on the details of the particular part or subject or nuance but to understand the workings of the system as a whole. For most scientists this is difficult since this implies an intrinsic degree of uncertainty or not understanding a particular aspect or part of the system. For educators, this is complicated since it is impossible to provide comprehensive ESS education when there are large uncertainties in our understanding. Nevertheless, ESS programs at undergraduate levels were designed and started in the 90s (Love et al. 1993; Miall 1995; Ireton et al. 1996). Good examples of visionary programs are those of Stanford or ETH, Zurich. In the early to mid 2000, graduate (MSc) and PhD programs we being offered under the umbrella of ESS. ESSReS (Grosfeld et al. 2013) was one of the few PhD schools, funded by the Helmholtz Association, to embark on this holistic journey.

---

[1] Goldilocks planet may be just right for life—space—25 April 2007—New Scientist. http://www.newscientist.com/article/dn11710#.U-sd04CSwRo.

[2] Earth System Science. http://en.wikipedia.org/wiki/Earth_system_science.

2 Review

The last 15 years have seen a significant increase in awareness of global climate change and sustainability issues. Slowly but steadily scientists, engineers, economists, politicians are all beginning to accept that there is a problem which transcends political boundaries. The 2001 Amsterdam Global Change Conference (Canadell and Noble 2001) highlighted this acceptance and put forward a plea to governments, public-private institutions and people of the world to agree on ethical framework for global stewardship and strategies for Earth system management, and importantly for the development of a new international system for global environmental science that draws from existing expertise, integrates natural and social sciences, and creates bridges between environmental and developmental issues. These sentiments have been reiterated over the years by the IGBP program (William et al. 2010), various IPCC reports[3] and countless global forums and scientific conferences such as the ESS 2010 (Downy and Cornell 2011) or Bonn Climate Change Conference 2014.[4]

What has changed significantly in the last decade (Ignaciuk et al. 2012) is the advancement in terms of sensors and observational systems, especially satellite remote sensing-based. Enhanced tools to store and digest this data coupled by significant advances in computation have led to the development of more sophisticated models which can describe biophysical processes in greater details. This in turn provides a better handle on model uncertainties and predictions for future Earth scenarios. In addition, the plea to setup educational programs that focus more on the integrative aspects has not fallen on deaf ears. Earth and Environmental Sciences or Earth System Sciences are currently the most important keywords used in most biogeoscience undergraduate and graduate programs.[5] Neither is ESS a concept of the western world (Walker 1999), it has established itself as an important educational concept which is accepted globally (Dong et al. 2009).

The ESSReS PhD program (Grosfeld et al. 2013; Meggers et al. 2014) was designed to address this aspect of collaborative science across the bio, geo-physics to computing sciences. In its second term, ESSReS brought together 23 outstanding PhD students from 12 countries to conduct their research in various disciplines, ranging from climate sciences, bio-geosciences, geo-information sciences to computer modelling and remote sensing of the atmosphere (Meggers et al. this volume). From these numbers it is clear that the program has been successful in its primary aim of educating the next batch of academics. The ESSReS program also highlighted aspects that could be improved. For example, it is not sufficient to broaden the horizon for the students. Faculty, and especially supervising faculty need to

---

[3] IPCC—Intergovernmental Panel on Climate Change. http://www.ipcc.ch/.

[4] Bonn climate change conference—June (2014). http://unfccc.int/meetings/bonn_jun_2014/meeting/8031.php.

[5] Earth System Science Courses. http://serc.carleton.edu/introgeo/earthsystem/nutshell/courses.html.

understand the benefits of such trans-disciplinary education as opposed to the more traditional roles in graduate, highly specialised education. Additional opportunities and incentives are needed to help faculty in this aspect. Perhaps, it would be beneficial if funding agencies and educational institutions are not stuck in their traditional roles to support individual sciences but open and expand their support to inter- and trans-disciplinary sciences.

3 Future Trends

Optimisms is one of the human traits that according to Walker (1999) might be the key factor determining the future of mankind. The optimistic bias inclines us to believe that natural disasters will not happen to us and that human advancement and ingenuity would release mankind from a dependence on nature. Social scientists might argue what “us” means in this context. It is clear that our capacity to understand the environment and the complex feedback mechanisms at variable spatial and temporal scales has dramatically improved. However, our capacity to predict and control the environment is still in its infancy. The link between science, technology on the one hand and human behavioural evolution on the other will determine the future of the Earth system.

Elliott and Hanson (2003) argues that the future of the geosciences is going to look very different to that of today. The revolution in education will see the bringing down of the wall between the natural and social sciences. This shift will be accompanied by process-driven, technology biased and (energy) resource focussed earth system science. The danger of such a process is the possibility of syndication (Elliott and Hanson 2003), in which resources form the basis for economic and social divides. A holistic education, at graduate and undergraduate levels, is probably the only way to continue the change in mind-set from the grassroots upwards. Other challenges for the future are institutional (Lawton 2001) and rely on international bodies and governments accepting joint responsibility and stewardship of our planet.

4 Conclusion

Earth System Science remains in a state of infancy albeit a distinct growth spurt in the last decades. Encouragement comes from various fields of social, natural and engineering sciences where the realisation starts to form that the future of the planet is in our own hands.

For higher education, especially graduate and PhD studies, there is a clear need to further foster inter- and trans-disciplinary and holistic sciences by including students and faculty from a variety of fields and different institutions. The ESSReS PhD program has been exceptionally successful in this aspect. In addition, there is an urgent need to change the mind-set within faculty, science administrators and students to accept and promote such system science approaches. ESSReS has only been partially successful in breaking these barriers and mind-set between scientific fields. For example the computer scientist needs to understand that not only computer algorithms are of interest but also processes, processes interactions and relationships between parameters are critical for climate science.

It is clear that ESS is the way forward and ESSReS was one of the first steps, especially in higher education landscape in Germany. It is necessary to continue this initiative, as it is the way forward towards a sustainable and health planet.

References

Berner RA (2012) Jacques-Joseph Ébelmen, the founder of Earth System Science. CR Geosci 344:544–548

Canadell J, Noble I (2001) Challenges of a changing Earth. Trends Ecol Evol 16:664–666

Dong S, Xu S, Lu X (2009) Development of online instructional resources for Earth system science education: an example of current practice from China. Comput Geosci 35:1271–1279

Downy C, Cornell S (2011) Editorial: key themes and messages from the Earth System Science 2010 conference. Procedia Environ Sci 6:3–14

Elliott SM, Hanson HP (2003) Syndication of the Earth system: the future of geoscience? Environ Sci Policy 6:457–463

Fritz J, Bitsch B, Kührt E et al (2014) Earth-like habitats in planetary systems. Planet Space Sci 98:254–267

Grosfeld K, Lohmann G, Wolf-Gladrow D et al (2013) The structural and educational concept in an interdisciplinary research school for Earth System Science

Ignaciuk A, Rice M, Bogardi J et al (2012) Responding to complex societal challenges: a decade of Earth System Science partnership (ESSP) interdisciplinary research. Curr Opin Environ Sustain 4:147–158

Ireton MFW, Manduca CA, Mogk DW (1996) Shaping the future of undergraduate Earth science education: Innovation and change using an Earth system approach. American Geophysical Union, Washington DC

Lawton J (2001) Earth System Science. Science 292:1965

Love DJ, Wilson FK, Murty KS et al (1993) An interdisciplinary Earth System Science (ESS) curriculum, community outreach, and research program. Comput Environ Urban Syst 17:73–82

Lovelock JE (1972) GAIA as seen through the atmosphere. Atmos Environ (1967) 6:579–580

Meggers H, Hanfland C, Sprengel C et al (2014) ESSReS-PeP-POLMAR, an international and interdisciplinary postgraduate education concept on earth and environmental sciences. European Geoscience Union, General Assembly, Vienna

Miall AD (1995) The blue planet: an introduction to Earth System Science. Earth Sci Rev 39:269–271

Pitman AJ (2005) On the role of geography in Earth System Science. Geoforum 36:137–148

Walker JC (1999) Earth System Science and the western worldview. Chem Geol 161:365–371

William MA, Helen J, Gaffney O (eds) (2010) Developing an integrated history and future of people on Earth (IHOPE): Research plan. IGBP Report No. 59. IGBP Secretariat, Stockholm. p 40

Winkler R-L (2014) Vladimir Ivanovich Vernadsky—an outstanding historian of science and a pioneer of the science of science. J Geochem Explor 147:65–68

The Educational Program of the Earth System Science Research School (ESSReS)

Helge Meggers, Matthias Buschmann, Klaus Grosfeld and Stefanie Klebe

Abstract The Earth System Science Research School (ESSReS) is an international and interdisciplinary research school for 23 PhD students at the Alfred Wegener Institute Helmholtz Centre for Polar and Marine Research (AWI) and their partner universities: University of Bremen and Jacobs University Bremen. ESSReS combines observations, modelling, and data analysis in order to decipher the Earth's complex climate system. Structured training, international exchange and supervision support interdisciplinary research at an early stage of the scientific career.

Keywords Post-graduate education · Earth System Science · Research school · Progress assessment

1 Introduction

Post-graduate education in Germany has changed a lot over the past decades. Formerly, PhD students generally did not have the option to attend formal classes and lectures and were expected to conduct their independent research, including occasionally teaching courses for students. Since the introduction of bachelor and masters studies with the Bologna Process in the late 90th, the higher education in Europe has been harmonized, leading to more structured and focused studies at the expense of a broad and universal disciplinary education. At this same time, special fields such as Earth System Science became more interdisciplinary. In consequence, universities and research institutes have established so-called research schools and/or graduate schools, offering specific courses and training alongside the doctorate.

H. Meggers (✉) · K. Grosfeld · S. Klebe
Alfred Wegener Institute Helmholtz Centre for Polar and Marine Research,
Bremerhaven, Germany
e-mail: helge.meggers@awi.de

M. Buschmann
Institute of Environmental Physics, University of Bremen, Bremen, Germany

G. Lohmann et al. (eds.), *Towards an Interdisciplinary Approach in Earth System Science*, Springer Earth System Sciences,
DOI 10.1007/978-3-319-13865-7_2

The Helmholtz "*Earth System Science Research School*" (ESSReS) is a small unit of PhD students co-organized by three educational and research institutions in the city state Bremen: University of Bremen (Institute for Environmental Physics, IUP), Jacobs University (School of Engineering and Science, JU), and Alfred Wegener Institute, Helmholtz Centre for Polar and Marine Research in Bremerhaven (AWI).

The principal concept of ESSReS and its management structure has already been introduced by Grosfeld et al. (2013). For the educational program the existing research infrastructure at the host institutes offered a unique research environment to study past, present and future changes of the Earth System (compare to Meggers et al. 2014). In its second term ESSReS brought together 23 PhD students from 12 countries to conduct their research in various disciplines, ranging from climate sciences, bio-geosciences, geo-information sciences to computer modeling and remote sensing of the atmosphere. After successful completion of the first ESSReS group (Grosfeld et al. 2013), the second generation of PhD students within ESSReS have been trained and prepared in this interdisciplinary environment since October 2011. This book in the Springer Briefs on Climate Change series provides an overview of the various PhD students' research projects. We present the structure of the accompanying academic program of ESSReS including seminars and courses, and illustrate how the courses were conceived and carried out.

2 The Educational Program

ESSReS aims to exchange and cooperate with other graduate programs that have related topics, since this cooperation produces synergy and added value. The associated Helmholtz Graduate School for Polar and Marine Research (POLMAR) at the AWI offers an educational training program, which is also open for interested ESSReS PhD students. Thus, the PhD students have access to a huge range of research facilities, course offers, and to a larger scientific community. This helps building their individual scientific network. Larger events like self-organized PhD conferences, career symposia or cost-intensive training courses were more easily tackled by joining resources of different research schools. In the following, we present a number of selected activities.

2.1 Introductory Courses

Throughout the duration of the ESSReS program a series of courses were conducted, covering most of the scientific fields within the research school participating institutes. In the first year, a set of lectures was organized to address the basics of the respective fields in order to provide an overview of the various methodologies. The aim was to create a common scientific language by bridging the various field-specific approaches to a common understanding of how to address

Fig. 1 One of the ESSReS excursions included a trip on-board RV Heincke (*left*) to get hand-on experience in sea floor mapping in the German Bight near Helgoland, another excursion was carried out with the RC Uthörn (*right*) to the Weser Mouth *photos* Dimitar Misev (ESSReS PhD student) [The RV Heincke cruise 2012 has been effective and interesting for both, the ESSReS PhD students and the shipboard system operator. An ESSReS computer scientist, who had never been on-board of a research vessel before, worked within the bathymetry group to learn the mapping of the North Sea seafloor nearby Helgoland. The ESSReS PhD student learned a lot about the multi-beam echo-sounder system, but recognized that the data processing on-board was inefficient. He wrote a few scripts to automate the manual work and to enhance the shipboard workflow, which is now helpful for all shipboard scientists in the future]

scientific questions in Earth System Science. Introductory lectures were given by senior scientists from the participating institutes, covering topics such as remote sensing of the atmosphere, the climate system and its components, and an overview of the complex system within the living ocean. Two cruises with research vessels (RC Uthörn, RV Heincke) were offered with practical courses, providing an introduction to ship-borne marine bio-geoscience research methods and to gain first-hand experience in applied oceanography, biology, geology and geophysics (Fig. 1). Next to these scientific topics, marine navigation and positioning systems were introduced to the PhD students. After participating in these short trips to Helgoland (RV Heincke) or to the Weser Mouth (RC Uthörn) some PhD students were highly motivated to join longer research trips to the northern and southern polar region (e.g. on board RV Polarstern).

2.2 *Expert Courses*

The expert courses from the second academic year onwards were designed to give a more detailed insight into the research fields of the participating institutes. The content is focused on their respective expertise in Climate Sciences, Physics, Geology, Geophysics and Biology.

In addition to a series of lectures, the physics/geophysics course “*Remote Sensing of the Atmosphere and Cryosphere*” offered visits to Bremen companies to illustrate current alternatives to a scientific career. The geology course "*Paleoclimate: From proxies to climate data*" introduced the PhD students geological records like sediment cores and the age determination of sediments. Paleoceanographic changes were explained on different time scales. The biology course "*Bioarchives, a source of climate reconstructions*" was held by biologists from AWI to illustrate work on carbonate bio-archives (mainly bivalves) for the reconstruction of past climate and environmental variability. Both courses had an efficient practical part, working with sediment cores (Geology) and molluscs (Biology).

2.3 Seminar Series

The ESSReS student group gathered for monthly seminars, which alternately took place at one of the participating institutes. Main goal of these student/coordinator-organized meetings was a regular informal exchange of the PhD students, providing a familiar atmosphere and an open working environment. This set-up not only strengthened the social network of the group, but also enabled scientific exchange and student-to-student learning. Usually, up to three presentations per event were given by the students, fostering motivation and the bottom-up approach, team building effects and conflict management.

In the beginning, the student talks covered the personal background, i.e. master thesis or earlier work, which later evolved into regular updates on their current research work. Some students also used the familiar and interdisciplinary audience to practice talks later to be held at a conference or summer school. The informal atmosphere was a perfect setting to get comfortable presenting to a bigger, more specialized audience. It was of great benefit that most of the audience were not from the same scientific field, which fostered a clear presentation and bottom-up explanation of background processes and pre-requisites. Consequently, some specific experiences of PhD students were used to tutor the group in special skills like, e.g., "*Python*" or "*Rasdaman*" (see Sect. 2.5).

2.4 Computational Skills Courses

In the first and second year of the program, a series of courses were offered to teach several computational skills needed for a productive work flow. These courses included an introduction to Unix/Linux operating systems, to scripting languages (*Bash*, *Python*) and to a series of specialized tools for plotting and data analysis (*GMT*, *GIS*). In addition to the three main courses, a workshop in Earth System Modeling (organized together with POLMAR) provided practical hands-on learning in Earth System Modeling, giving the chance to explore the dynamics of the Earth's climate system as well as of global carbon cycling and the biogeochemical impacts of fossil fuel CO_2 emissions. The ESSReS students were trained in advanced computer skills and gained experience with high-level data visualisation packages.

2.5 Transferable Skill Courses

Beyond an excellent scientific education, social skills are of great importance in today's professional business. Therefore, additionally to the scientific work a set of mandatory transferable skills courses were developed and offered in cooperation with the Imperial College London. The courses were designed to prepare PhD students for their future career and reflect on personal characteristics like presentation and communication skills, personal development, leadership and time management.

The first course for PhD students in their first academic year entitled "*Research skills development*" focused on personal and research effectiveness including team working, networking and communication skills. The second course "*Presentation and communication skills*" concentrated on the presentation of own results in front of a group including feedback. It included learning to prepare a presentation, to eliminate excitement, to prepare a structured scientific text or talk and to understand the review process. In the third academic year, the last course "*Career and leadership*" aimed at career planning (in and outside of science) and the development of an understanding of leadership. Further topics were team working in a heterogeneous group, planning the own career and "*real life*" training exercises.

The feedback on these courses from ESSReS participants was very positive and the course contents were regarded as helpful for their daily work. The mixed group, including PhD students from different Helmholtz research schools in each of the courses was considered an asset. Additionally, it was appreciated that the venue was far away from daily life, enabling a focused and effective course environment.

2.6 Academic Writing Courses

A cooperation with the Centre for Foreign Languages at the University of Bremen was established for individual English language training sessions. Besides workshops and individual coaching sessions, a seminar on "*How to manage writing processes efficiently*" was held and the students' feedback was very positive. During individual coaching sessions, students were asked to bring own manuscripts or research papers soon to be published. Individual challenges were discussed and strategies for a better-written language developed. This approach to work with current texts was perceived as very effective and useful.

2.7 Excursions

Various excursions within ESSReS were offered to the PhD students as on-site training, practical application and social event. While the visit of RV Polarstern and the participation on cruises with RV Heincke and RC Uthörn also focused on scientific topics (see Sect. 2.1) and the preparation for the participation of a longer expedition, additional social gatherings were organized to foster networking opportunities. An excursion to the Harz mountain range and the meteorological observatory on the "Brocken" peak gave the opportunity to become acquainted with the history and the geology of the northern part of Germany. After visiting northern Germany's highest elevation, another excursion went to the national park Waddensea near Cuxhaven including a hike through the tidal flats from the mainland to the island of Neuwerk.

2.8 Annual Retreat

An annual retreat in autumn of each year was held to ensure a regular exchange between the PhD students and the supervisors/senior scientists of the three institutions (Fig. 2). The supervisors and other scientists from the working fields of each PhD student were invited to participate in the retreat, where oral and poster

Fig. 2 ESSReS students and supervisors at the second ESSReS retreat at the Botanika Conference Centre in Bremen (November 2013)

presentations of all PhD students as well as invited talks were given. All PhD students had to give at least one talk and present two posters in total during the three retreats. An evaluation sheet for both, talk- and poster presentation was prepared and all supervisors and guest scientists of the retreat were asked to evaluate the student contributions. The best poster and the best talk were awarded with a present and an ESSReS certificate.

3 International Exchange

ESSReS maintains cooperation with foreign institutions and offered an international exchange for all PhD students. ESSReS recruited PhD students originating from 12 countries (Austria, Brazil, China, Ecuador, Germany, Iran, Italy, Japan, Macedonia, The Netherlands, Poland and Russia). Thus, a high level of intercultural exchange was guaranteed.

A dedicated ESSReS website (http://earth-system-science.org/) was created to inform the PhD students and the international public about the scientific work and the students' personal developments (see Grosfeld et al. 2013).

3.1 International and National Meetings

The students within ESSReS had the possibility to apply for travel grants for workshops, meetings, conferences and stays at external institutes (see Sect. 3.2). In order to receive a grant, a proposal had to be submitted to the Academic Council. All PhD students used this possibility and students travelled to meetings all over the globe (see map in Fig. 3). Additionally, the students had the possibility to participate in semi-annual AWI/IUP seminars with special topics like "*Advances in Earth System Modeling*" or "*Climate Variability*".

3.2 Visit in a Foreign Lab

Apart from various visits of conferences or seminars ESSReS offered its students support for a three-month stay abroad to enhance collaboration with specialists of the respective research field. Within their first two years, three PhD students of group II took advantage of this possibility and visited Copenhagen (Denmark), Paris (France) and Toronto (Canada). All these visits to foreign labs had specific outcomes and contributed to papers of the PhD students.

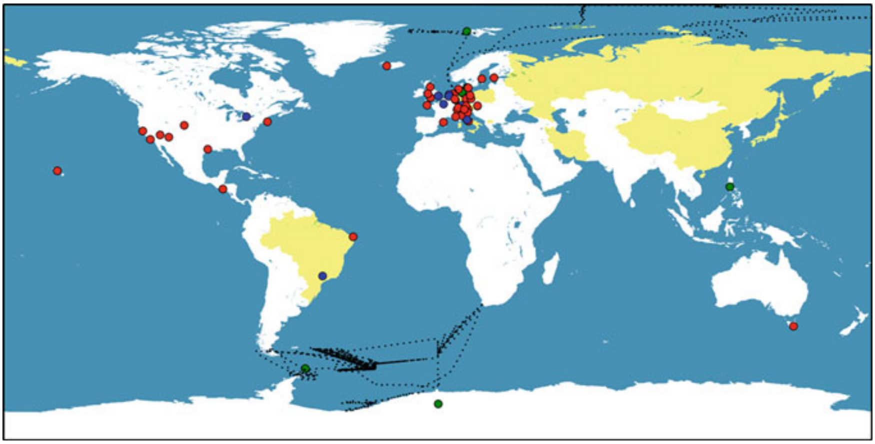

Fig. 3 Overview of the travel destinations (both ESSReS and third party funded) of ESSReS group II students including conferences, meetings or summer schools (*red*), fieldwork (*green*), RV Polarstern tracks/Polar aircraft routes (*black*) or research visits to a foreign lab (*blue*). The home countries of the students were marked in *yellow*

3.3 Invited Guest Scientists

Both ESSReS PhD students and supervisors had the opportunity to invite external experts from academia or industry to the research school. One of the guests was an expert in risk management modeling who gave a valuable insight into the field of "*Catastrophe Modeling*" and the students got insights into how their work may be implemented outside academia. Another guest of ESSReS gave a series of scientific lectures on "*Spectral methods for time series analysis*" and was available for consultation by the PhD students, which was used frequently. Finally, ESSReS has invited a senior editor of the scientific journal *Nature* to inform the PhD students about the internal and external challenges in science publishing. Exclusively for the PhD students the every-day work of an editor and possible future career options at a scientific publisher were presented.

4 Progress Assessments

ESSReS developed and established a Progress Assessment Form for both, PhD students and supervisors. This was done to evaluate the individual progress of the PhD students' projects. The form was filled-out independently by PhD students and supervisors in order to identify different perceptions of progress and the PhD timeline. Apart from this intermediate assessment, the PhD students were asked to set up bi-annual PhD committee meetings on a regular basis, during which the PhD students were asked to present a progress report of the last months and the goals for the upcoming months, discuss problems and planned publications, conference attendance or expeditions. An assessment of potential risks within the work plan, methodological approaches or external factors was required to anticipate delays in the completion of the PhD.

Anonymous feedback was given to the PhD students during the monthly seminar and a discussion was encouraged where the students reflected on their individual progress compared to the overall results of the assessment survey.

5 Conclusions

Climate change and its regional to global impact on the Earth system is one of the crucial questions in Earth and Climate System Sciences. Hence, PhD education in Earth System Science in present times is focusing on a highly interdisciplinary and herewith also on inter-institutional education programs. With this approach we prepare young experts for scientific or industrial/economy careers or work in the public sector. The integration of both, climate observation and climate modeling in a research school entailed collaboration and networks of PhD students and experts (supervisors) in a spectrum of subjects and timescales. Earth System Science includes various disciplines and methods. The education program at the three institutes/universities, cooperating within ESSReS is built on the connection of scientists from the field of Climate System Science.

ESSReS aims at the integration of research at the interface of Geology, Biology, Physics, Geophysics, Mathematics and Informatics. It is therefore multi- and interdisciplinary in every aspect. The training, curriculum, and PhD research subjects are closely located at the interfaces between the participating disciplines. This is guaranteed by interdisciplinary supervision of the PhD project, documented by the members of the so-called "*PhD committee*" (advisory team; Grosfeld et al. 2013). The long-term goal is not only to enhance exchange and interaction between these disciplines, but to enforce a newly integrated concept, where separation between disciplines becomes more and more obsolete. Consequently, ESSReS provide a solid base for a new generation of excellent scientists in Earth and Environmental Sciences.

References

Grosfeld K, Lohmann G, Wolf-Gladrow D, Ladstätter-Weißenmayer A, Notholt J, Unnithan V, Wegener A (2013) The structural and educational concept in an Interdisciplinary Research School for Earth System Sciences. In: Lohmann G, Grosfeld K, Wolf-Gladrow D, Unnithan V, Notholt J, Wegener A (eds.) Earth System Science: bridging the gaps between disciplines. Perspectives from a multi-disciplinary Helmholtz Research School. Springer Briefs in Earth System Sciences. Springer, Germany, pp 3–8. doi: 10.1007/978-3-642-32235-8

Meggers H, Hanfland C, Sprengel C, Grosfeld K, Lohmann G, Bijma J, Unnithan V, Ladstätter-Weißenmayer A, Burrows JP (2014) ESSReS-PeP-POLMAR, an international and interdisciplinary postgraduate education concept on Earth and Environmental Sciences, European Geoscience Union, General Assembly, Vienna, 28 Apr–2 May 2014, hdl:10013/epic.4350

Time Evolution of a PhD Student's Mood—A Review of My Time as PhD Student of the Research School ESSReS

Christoph Gregor Hoffmann

Keywords Post-graduate education · Earth System Science · Research school

1 Introduction

I had quite a few doubts whether my PhD project will have a happy ending for about two years. I think that this perception is common to many PhD students: the enthusiasm drops steadily in the beginning, when all the individual smaller and bigger problems appear and hinder apparently any progress. But sooner or later most of the PhD students get the project going and even start to enjoy their work again!

This is a short reflection on how my PhD project evolved and how ESSReS influenced it. It is not a scientific analysis, but the story of my personal perception during the project. I would be happy if one or the other present PhD student could recognize himself in some situations and maybe learn something from my experience. Please note that many people supported me during the project and I apologize for not mentioning all of them appropriately, particularly my working group at the University of Bremen. The reason is my aim to focus this story on the PhD student's own scope for action based on my individual experience.

2 Time Evolution of a PhD Students's Mood

To guide through this personal side of my project without going too much into the scientific aspects, I recapitulated my mood with respect to the PhD project during the major phases. Figure 1 shows this mood development—with a touch of humor normalized to a scale between zero and one.

C.G. Hoffmann (✉)
Institute of Environmental Physics, University of Bremen, Bremen, Germany
e-mail: christoph.hoffmann@multiteq.de; christoph.hoffmann@iup.physik.uni-bremen.de

G. Lohmann et al. (eds.), *Towards an Interdisciplinary Approach in Earth System Science*, Springer Earth System Sciences,
DOI 10.1007/978-3-319-13865-7_3

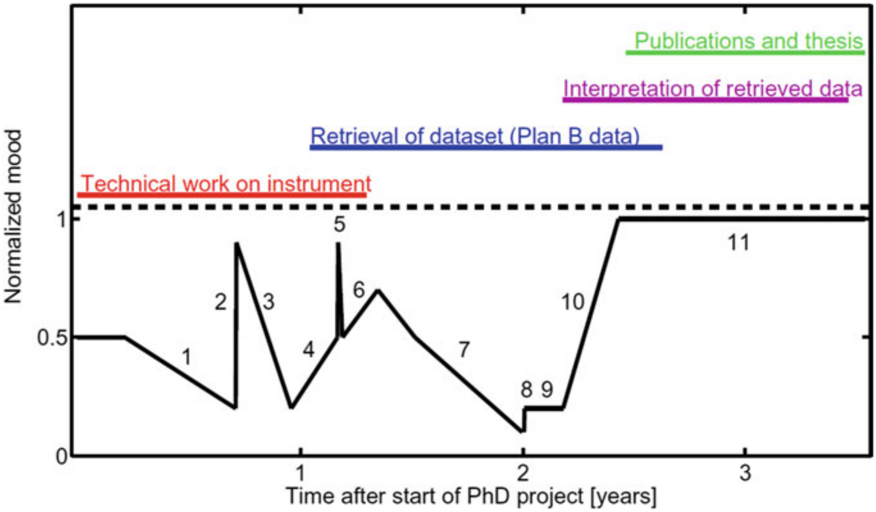

Fig. 1 The development of my mood with respect to my PhD project—with a touch of humor normalized to a scale between zero (should I quit this job?) and one (the job of my dreams?). The numbers correspond to the same numbers in the text (in brackets), and mark the individual phases that are described

Just a few words about the scientific background of my project. I worked on the application of Carbon Monoxide (CO) as a tracer for mesospheric dynamics (Hoffmann et al. 2013). Abstractly speaking, the project included three major parts. First, a technical part, during which a measurement device should be constructed for observations of CO radiation in the atmosphere. Second, the observed data should be analyzed numerically to gain the quantities of interest. This “retrieval” of the data is particularly important and complex for atmospheric observations. And third, the retrieved data should of course be used to contribute to the work on current scientific questions in the field.

This project structure including technical work, data processing and validation, and the scientific interpretation is roughly common to many projects in Earth System Science. Also common to many PhD projects is the fact that major steps depend on each other and have to be performed consecutively. This poses immediately problems if the first part takes longer than expected or even does not work at all. And this is where my story begins.

The technical phase started with waiting for commercially produced parts of the measurement device. One of these components had to be designed specially for my project and it turned out that this was more difficult than expected. Several months, which were not included in the original schedule, elapsed without major progress in the lab and my project seemed to be already stuck (1).

In the meantime, we had the first ESSReS research skills development course, which included project management and time planning. With a grown awareness for these topics, I made a timeline showing the milestones of my project. It became obvious that reaching the final goals in the three years period was already improbable. So I started to underline the importance of an alternative "Plan B" already during the first ESSReS PhD committee meeting. After an intense discussion, all committee members shared the opinion that Plan B has to be set up while I still try to push the initial "Plan A".

Luckily, Plan B was established quite quickly. Our partners from the Swedish Institute of Space Physics gave us willingly access to their set of already measured CO radiation data. This dataset was obtained with the same observation technique, but scientifically complementary to the one I was going to measure. This allowed me to breakup the consecutive order of the first two steps of my original plan: I could gain experience with the retrieval before having finished the work on my own instrument. In the best case, I could combine both datasets in the analysis, otherwise I would completely rely on the Plan B data.

But firstly, I kept on pursuing Plan A for a while. After some more time, the missing component was finally delivered (2). However, the following tests indicated that it did not work stable and it might take again several months for the supplier to solve the problems. Of course, this kind of trouble has to be expected if one tries to go beyond the limitations of state-of-the-art technique. But for me it was very disappointing and I seriously felt the tension between the uncertainties of scientific work and the need to fulfill formal requirements like the 3-year project timeframe in this case. So, my optimism was damped again (3) until I really started to work on Plan B, simultaneously (4).

Some months later, we had one more try with the re-engineered component (5), but it became clear very quickly that the problem remained and that any solution will come too late for my project. So, during the second committee meeting, we decided that I will switch entirely to Plan B and thus skip the technical part completely. While this was of course disappointing at that moment, I was lucky, since the work on Plan B was already in progress and allowed for a seamless transition into the next part of my project.

To keep it short, I started with refreshed motivation into the second phase (6), but had to face new disappointments after a few months. I made progress in the numerical data retrieval and got first results. But these results were not only inconsistent with previous observations, moreover there were also inconsistencies within my dataset itself. At this point it became highly questionable if the dataset is applicable at all. So I spent several months (7) on finding possible explanations in every direction: deficiencies of the retrieval technique, calibration problems of the instrument, eventually a new atmospheric feature, or simply my own inability? So, I had created dozens of pieces of a puzzle, but no idea how to put them together—if they fit together at all. After about two years of my PhD, apparently nothing was achieved and I felt that it might be better to give up.

Luckily, I had another iron in the fire. During my research in the months before, I came across an interesting atmospheric model and I had the idea to replace the missing technical part of my work with some modeling experiments. With the help of my PhD committee members, I came into touch with the model developers at the National Center for Atmospheric Research (NCAR) in Boulder, USA, and we considered a research stay of several months. Although not directly part of the ESSReS program, the prospects of such a research stay were underlined in ESSReS from the very first, so that I was directly prepared to apply for a stipend at the German Academic Exchange Service (DAAD).

And exactly when my mood reached its minimum (8), I received the acceptance of my DAAD proposal and I decided to use this opportunity as final attempt. Just a few weeks (9) were left before my departure. During this time I prepared the stay by restructuring all the open questions, approaches, preliminary findings and opinions; I grouped all the pieces of the puzzle and tried to estimate their rough position in the overall picture. This helped me to clarify the aspects about which I wanted to learn something during my stay at NCAR.

And indeed, I achieved the breakthrough of my project during this research visit (10). Looking back, there were several factors contributing to this breakthrough: First, the preparation, which helped me to carve out the missing links. Second, the intense discussions with my hosts, of course. They are experts in this field and had an unbiased, still optimistic view on my project. They confirmed from the beginning my thoughts about the missing links and supported me steadily with their experience. Third, the change of the typical workdays, which allowed for more and longer phases of continuous concentration at NCAR where I was unknown and did not have any other duties than my own research. And forth, the excitement, which comes with a new, inspiring environment.

However, the major precondition for this success was my work during the two years before! Although my efforts appeared to be wasted at that time, I have to admit in retrospect that it was only possible to piece this puzzle together in Boulder using the experience that I had gained during all the attempts before. This surprising turn of my perception became one of the major eye-openers for me with respect to scientific work.

When I came back home, I had prototypes for each of the parts of my work: the retrieval, a validation of my dataset, a comparison to the NCAR model and some more ideas on top of that. In the meantime, we had applied for a prolongation of my project and also the DAAD stipend had shifted the end of my funding a bit. Altogether about one year (11) was left for me to refine all the prototypes, to write the publications (Hoffmann et al. 2011, 2012) and finally to write up my thesis. This was only little time for all these tasks, but I was again enthusiastic enough to contrive a sophisticated final timeline and to finish more or less everything in time: the happy ending of my PhD story!

I think, that the development of my PhD project was not extraordinary negative or positive. Contrarily, I think that all these phases of different moods can be found in many scientific projects, also after the PhD phase. Scientific work is always connected to uncertainties. But tight deadlines of the projects and particularly of the funding put pressure on the scientist, so that these uncertainties might finally be perceived as stress or frustration. And this transformation from uncertainty to frustration works probably particularly well at the beginning of a PhD project, when positive scientific experiences, which strengthen the optimism, are still missing. So, I suspect that it is easier for experienced scientists to overlook failures and disappointments and to keep on working towards the next successful phase with optimism. Of course, this experience has to be build up first. And from this point of view, it might be helpful to face the complete spectrum of moods during the PhD project (see Grosfeld et al. 2013).

3 Conclusion

In conclusion, a research school like ESSReS should not (and cannot) prevent each failure and disappointment in the individual PhD projects, although me and other ESSReS students wished for this from time to time. But a research school can help to deal with the negative phases constructively. This means that a middle way has to be found between supporting the students as much as possible, but without confining their personal responsibility for the development of the project. Hence, the research school should act as a multiplicator for the student's own initiative. This was from my perspective very well realized in ESSReS. Beyond the given organizational structure of courses and seminars, there were lots of elements, which had to be adjusted by each student according to his special needs. For me personally, the most powerful support came from the committee meetings, from the research skills development courses, and from the possibility to present and discuss the own project with broader and more diverse audiences in addition to the own working group (see Grosfeld et al. 2013). Motivating for me were also the excursions, laboratory visits, and some inspiring talks, which reminded me particularly during the unsuccessful phases of the nice side of scientific work.

References

Grosfeld K, Lohmann G, Wolf-Gladrow D, Ladstätter-Weißenmayer A, Notholt J, Unnithan V, Wegener A (2013) The structural and educational concept in an interdisciplinary research school for Earth System Sciences. In: Lohmann G, Grosfeld K, Wolf-Gladrow D, Unnithan V, Notholt J, Wegener A (eds), Earth System Science: Bridging the gaps between disciplines. Perspectives from a multi-disciplinary Helmholtz Research School, Springer Briefs in Earth System Sciences

Hoffmann CG, Raffalski U, Palm M, Funke B, Golchert SHW, Hochschild G, Notholt J (2011) Observation of strato-mesospheric CO above Kiruna with ground-based microwave radiometry —retrieval and satellite comparison. Atmos Meas Tech 4:2389–2408

Hoffmann CG, Kinnison DE, Garcia RR, Palm M, Notholt J, Raffalski U, Hochschild G (2012) CO at 40–80 km above Kiruna observed by the ground-based microwave radiometer KIMRA and simulated by the whole atmosphere community climate model. Atmos Chem Phys 12:3261–3271

Hoffmann CG, Palm M, Notholt J, Raffalski U, Hochschild G (2013) A brief example of the application of remotely sensed tracer observations in atmospheric science—studying the impact of stratosphere-mesosphere coupling on polar ozone variability. In: Lohmann G, Grosfeld K, Wolf-Gladrow D, Unnithan V, Notholt J, Wegner A (eds) Earth System Science: bridging the gaps between disciplines—perspectives from a multi-disciplinary Helmholtz Research School, Springer, Berlin

Progress in Earth System Science: What Does It Take to Make Our Ideas Clear?

Gerrit Lohmann

Abstract To describe the progress in Earth System Science, a conceptual framework is proposed which includes hypothesis testing, the formulation of models with different complexity as well as expressing discoveries in terms of metaphors. The later approach is demonstrated by the conveyor belt concept in oceanography which influenced the discussion about abrupt climate changes where the ocean circulation may be involved. It is argued that the combination of different methodologies/complexities and independent results is necessary to prevent over-simplistic views in each discipline of Earth System Science. Emphasis is given on typical steps to obtain new ideas for a new discovery. Examples for over-simplistic views are mentioned for past climate information from proxy data. The recorder system of the proxy has to be taken into account, otherwise the climate information can be misinterpreted. It is concluded that in the field of Earth System Science, basic knowledge and true collaborative problem solving is necessary to make scientists aware of the underlying principles, the limitations and open questions. This is furthermore necessary to develop and sharpen our ideas about the complex Earth System.

1 Self-critical Approach

In Earth System Science, there is a diversity of methods, and the modeling, observational and reconstructing communities are still rather distinct. As we mentioned in our first book (Lohmann et al. 2013a), the linking of 'data and modeling', as is the special emphasis of our graduate school, enables graduate students from a variety of disciplines to cooperate and exchange views on the common theme of Earth System Science, which leads to a better understanding of

---

G. Lohmann (✉)
Alfred Wegener Institute Helmholtz Centre for Polar and Marine Research,
Bussestr. 24, 27570 Bremerhaven, Germany
e-mail: Gerrit.Lohmann@awi.de

G. Lohmann et al. (eds.), *Towards an Interdisciplinary Approach in Earth System Science*, Springer Earth System Sciences,
DOI 10.1007/978-3-319-13865-7_4

processes in a global context. Interdisciplinary collaboration does not happen naturally and it can be (basically it needs to be) purposefully fostered by an educational program (see Grosfeld et al. 2013; Meggers et al. 2015, article in this book). One challenge for interdisciplinarity is that the set of perspectives, approaches, and values that characterize one field do not align exactly with those of another field. To the extent that these are implicit and unarticulated, as well as unaligned, they can lead to misunderstandings, also differing on standards of evidence, acceptable forms of reasoning, appropriate means of conveying findings, and even on what vocabulary to use (Manduca and Kastens 2012). A scientist in Earth System Science, has to overcome these distinctions for any true collaboration and collaborative problem solving. Developing such is the central goal of our PhD graduate program.

Basic knowledge in the other disciplines in Earth System Science enables graduate students from a variety of disciplines to cooperate and to overcome too simplistic (and narrow) approaches. To give an example for the complexity of climate variability and change: A general difficulty in climate research is the estimate of natural variations since historical records of direct temperature measurements are too short and fall already within the period of strong human impact on natural conditions. For the period beyond the instrumental record, one has to reconstruct climate information from proxy data. These proxy data provide indirect information about past environmental conditions for which explicit knowledge of the recorder system is required. Examples for models of the recorder systems are for instance the seasonality of snowfall for ice core and in marine sediment records (Laepple et al. 2011), the lagging and smoothing of the climate signature in speleothems (Lohmann et al. 2013b), or the biogeochemistry of carbon isotopes in foraminifera (Hesse et al. 2014) which can change the interpretation of the proxy records in terms of a climate signal.[1]

Past, present and future scenarios rely furthermore on models of the climate system under appropriate external forcing (e.g., Lorenz and Lohmann 2004;

---

[1] These 3 examples shall be explored in more detail here. Laepple et al. (2011) investigate the phase relation of air temperatures in Antarctica with insolation. Ignoring the seasonal bias of the recorder system (more local precipitation in winter than in summer) one might conclude that the record is nearly in phase with Northern Hemisphere summer insolation. Taking into account the seasonal bias, one finds however that the local insolation in the Southern Hemisphere may be a more suitable explanation of these records on orbital timescales, basically the opposite than the original interpretation of the records. Lohmann et al. (2013b) investigate the link between the large-scale climate with a simulated speleothem climate archive. Mixing processes in the soil and karst above the cave represent a natural low-pass filter of the speleothem climate archive. Stalagmite stable oxygen isotope values can furthermore lag the regional surface climate by several years, indicating that the proxy system provides a lagged and smoothed recorder which is difficult to reconcile with a direct climate-proxy relationship. Hesse et al. (2014) use a reaction-diffusion model for calcification in order to quantify the effects of different physical, chemical and biological processes on stable isotope carbon isotopes of benthic foraminiferal shells. It is shown that stable isotope carbon isotopes of the shells are not only strongly affected by changes in the stable isotope carbon isotope composition in the water, but also on temperature, respiration rate and pH. The later effects can be even larger than the first one for glacial-interglacial changes which has huge consequences for the interpretation of paleoceanographic records.

IPCC 2007, 2013). Future scenarios on the other hand will largely depend on future societies and their decisions about energy consumption and greenhouse gas emissions. The Report of the Intergovernmental Panel on Climate Change (IPCC 2007, 2013) can be viewed as a (still incomplete) compilation of what is known about climate change, whereas several uncertainties are spelled out. The reliability of the representation of climate processes such as clouds, the cryosphere and biogeochemical cycles has strongly increased, but many details still need to be fully elaborated. Non-specialists may be not aware of the limitations and assumptions of Earth System Science. In contrast to many areas in pure physics, there is no laboratory to test scenarios (other than numerical models of the Earth) since we have just the one real live experiment, the Earth.

Let us think about the typical steps to produce an idea for a new discovery which is usually the basis for a publication or a PhD thesis (as for our graduate research school (Lohmann et al. 2013a)). As Peirce (1878) pointed out that when Descartes (1644) set about the reconstruction of philosophy, his first step was to theoretically permit scepticism and to discard the practice of regarding authority as the ultimate source of truth.[2] That done, he sought a more natural fountain of true principles, and thought to have found it in the human mind; thus passing, in the most direct way, from the method of authority to that of apriority. Self-consciousness was to furnish us with our fundamental truths, and to decide what was agreeable to reason. During our scientific career the step from a school-like, more dependent situation to an independent, self-critical approach is not trivial, and in some cases the transition never takes place. One goal of modern PhD education shall be to make scientists aware of the underlying principles, the limitations and open questions in the field. Holding opposite opinions upon fundamental principles, Descartes was further led to say that clearness of ideas was not sufficient, but that they needed also to be distinct. Kuhn (1962) argues in terms of evolution of scientific theories where different phases do not emerge from the straightforward accumulation of facts, but rather from a set of changing intellectual circumstances and possibilities.

Climate science went already through a pre-paradigm phase in the sense of Kuhn (1962), in which there is no consensus on any particular approach. Somehow, climate and Earth System Science in general are partly already in a second phase, in which the open questions are solved within the context of the established methods and these are documented in review articles, books and reports (e.g., Berger 1988;

---

[2] Interestingly, there are people in and around Earth System Science assuming a more ‘sceptical’ point of view. Those are convinced that the rapid climate change theory is only a myth, a way of turning attention of media and society to scientific research (e.g., Singer 2007). Global climate models often appear as a cornerstone of this disagreement. However, the majority of these scepticists do not have a background in climate science and have not published papers in the peer-review process (e.g., Lee and Bero 2006). This process is important to overcome a subjective view and a way to distinguish between an idea *seemingly* clear and really being so. There are indications for parallels between the climate change debate and earlier controversies over tobacco smoking, acid rain and the hole in the ozone layer (Oreskes and Conway 2010) where spreading doubt and confusion was the basic strategy of those opposing action in each case. The typical structure of arguments is easily identified in this debate (McCright and Dunlap 2000).

Peixoto and Oort 1992; Marshall and Plumb 2007; Holton and Hakim 2012; McGuffie and Henderson-Sellers 2014).

However, more scientific effort in the field of Earth System Science yields more complex views, which can be sometimes even contradictory. For instance, for some past warm climate states climate models show a mismatch with the data or these proxy data have to be interpreted in a different way, e.g. for the Holocene (e.g., Lohmann et al. 2013c; Liu et al. 2014) or the Eocene and Pliocene (e.g., Valdes 2011; Salzmann et al. 2013). This indicates that at least some underlying assumptions might need to be revisited, reflecting phase three of Kuhn's (1962) theory of scientific development.

2 Hypothesis Testing and Models

Let us consider what steps are usually taken to clarify our ideas. Earth System Scientists test their hypotheses against observations or reconstructions of the system using multiple lines of evidence. The first step is quite often an empirical evidence or an established and to be revised model. Data (they can be old, new, or just preliminary) provide a basis for the analysis. Such analysis can be supplemented by analytical or numerical models (e.g., Gershenfeld 2003). Models provide the perspective beyond the local information from observations/reconstructions and show that spatial and temporal patterns are fundamental to understanding Earth systems and processes (Manduca and Kastens 2012; Tewksbury et al. 2013). Their interpretations yield results (preliminary, critical view) and provide a new idea. This new idea serves then as the basis for a question, which has to be again tested using the (now refined) model and the quality controlled data. This in turn is analyzed again using analysis methods: numerical, statistical or conceptual models, other self-consistent methods to obtain more evidence, see e.g. Gershenfeld (2003). This evolves over time to get a clear idea about the result and the underlying interpretation.

Following this idea (Fig. 1), it is clear that the reliability of models in general cannot be shown in an all-encompassing statement. A model is a tool to test a hypothesis, it does a priori not stand for its own. The degree of model complexity is defined by the question asked. The reliability of the model output therefore depends on the question asked and model used. Individual studies should detail the limitations and assumptions of the respective methods. Or to put it more specifically, Earth system models are computer programs in which physical, chemical and biological processes are quantitatively described by mathematical equations. Models are used to study the past and present dynamics of the Earth's climate system, and project future climate conditions. To test hypotheses about how the Earth system works requires information, not just about the current and past state of the three-dimensional globe, but also its processes, feedbacks, and changes through time. The information that results from a climate model is called a "climate simulation". A model is like a laboratory where one can change parameters (such as

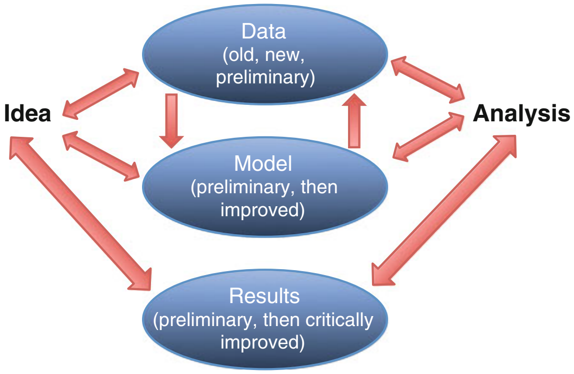

Fig. 1 Schematic view of evidences, data, modelling, interpretation. The progress is usually an iterative loop with hypotheses testing and developing ideas

CO_2 levels) and study the direction and magnitude of response (such as an increase in sea level or ocean acidification), which is constrained by physical laws, observations or other models. Based on the state of our current knowledge, climate simulations give the most probable outcome under different scenarios.

Important to note, the type of model used depends on the nature of, and the timescales relevant to, the question asked. On the one extreme are the relatively simple Conceptual Models that contain a very limited number of processes, but which clarify the key features of a system (Fig. 2). On the other extreme, Comprehensive Models require super computers and large research teams for maintenance (such as General Circulation Models, so called GCMs) operating at a high spatial and temporal resolution (e.g., Peixoto and Oort 1992; McGuffie and Henderson-Sellers 2014). Between these two extremes are the Models of Intermediate Complexity (Claussen et al. 2002). The transition from highly complex dynamical equations to a low-order description of climate is an important step since it gives more credibility to the approach and its results. Low-order systems can clarify the main effects in the system, neglecting all the second order processes and selecting the specific temporal and spatial scales, or can be used as a data-interpretation tool using statistical-conceptual models analyzing the complex observational system (e.g., Stommel 1961; Hasselmann 1976; Lemke 1997; Rooth 1982; Lohmann and Schneider 1999; Stocker and Johnsen 2003; Laepple et al. 2011).

Our concepts become clear if we describe the phenomena on different levels of model hierarchies as sketched in Fig. 2. In his book, Saltzman (2002) formulated a dynamical system approach in order to differentiate between fast-response and slow-response variables for long-term climate variability and change. One straightforward approach is coarse graining where the underlying dynamics are projected onto the macroscopic dynamics, which are used in statistical physics theory of non-equilibrium statistical mechanics (e.g., Zwanzig 1960; Mori et al. 1974). A similar concept in climate sciences had already been proposed by Hasselmann (1976), in which the climate system is described by climate variables (in statistical physics they are called “macroscopic”) and weather (“microscopic”)

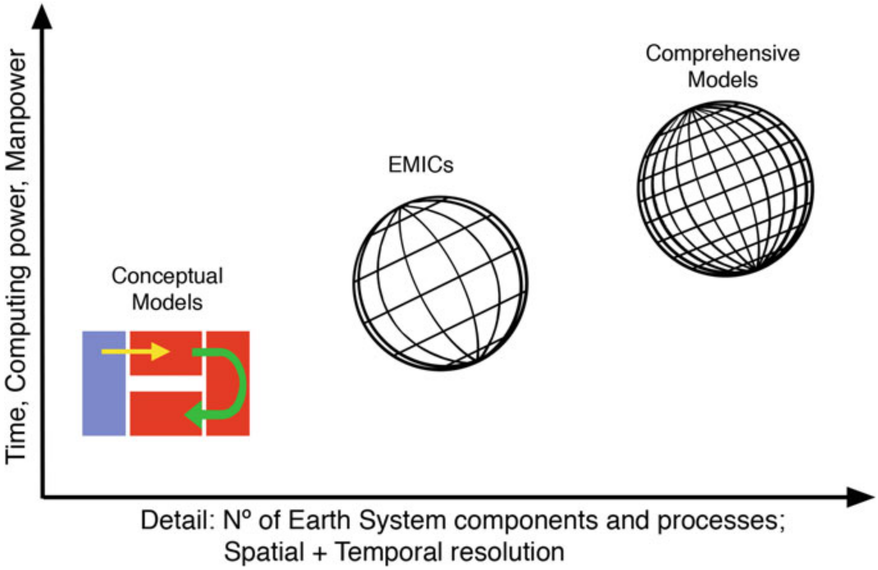

Fig. 2 Different categories of earth system models: when the spatial and temporal resolution or the number of earth system components increases, the required time and computing power also increase. Earth system models of intermediate complexity (EMICs) could be low-order model versions of a comprehensive model, or models with simplified physics parameterizing unresolved spatial and temporal scales (Claussen et al. 2002). Conceptual models can be very low-dimensional systems like the one displayed (Stommel 1961; Rooth 1982) and where sometimes even the analytical solution is known (Lohmann and Schneider 1999), or statistical-conceptual approaches

variables. The original idea stems from statistical physics for the description of Brownian motion (Einstein 1905).

The effect of the weather on climate is seen by red-noise spectra in the climate system, showing one of the most fundamental aspects of climate, and serving also as a null hypothesis for climate variability studies (Frankignoul and Hasselmann 1977; Timmermann et al. 1998). Such hypothesis is required for our iterative process in Fig. 1. It can be of great utility to reduce the complexity of the system being studied by using low-order, box, and conceptual models. This approach has been successfully applied to a number of questions regarding feedback mechanisms and the basic dynamical behavior of the Earth system. In some cases, such models can provide a hypothesis for the dynamics of a complex system and make our ideas clear. Such different hierarchies of models and independent results provide a distinction between an idea seeming clear and really being so (Peirce 1878, 1974).

3 Building of Models and Expressing the Scientific Discoveries

Another type of model can be even as short as a metaphor. Metaphors can pre-structure and prepare the building of a model in science: the diagram of the parallelism predicate is less complicated than its subject. Its simpler composition helps to structure the subject by emphasizing special features of the complicated structure (Brüning and Lohmann 1999).

One prominent example is to be found in oceanography (Fig. 3): The ocean conveyor is driven by deepwater formation in the northern North Atlantic, making it the engine of conveyor belt circulation (Broecker 1991). The conveyor belt metaphor necessarily simplifies the ocean system, it is of course not a full description of the deep ocean circulation, but contains different aspects of it (Brüning and Lohmann 1999). Broecker's (1991) concept provides a successful approach for global ocean circulation, although several features are strongly simplified like the missing Antarctic bottom water, the upwelling areas etc. One is tempted to say: The ocean is of course not a conveyor belt! However, the global conveyor belt metaphor inspired principally new ideas of halting or reversing the ocean circulation and put it into a global climate context (e.g., Bryan 1986). The halting ocean circulation was helpful for the interpretation of Greenland ice core

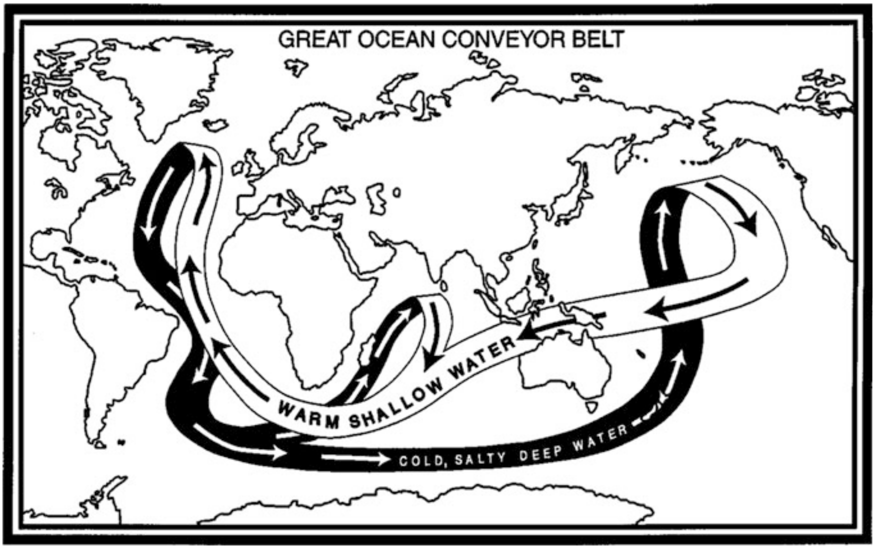

Fig. 3 Broecker (1991)'s great ocean conveyor. Warm and salty water entering the North Atlantic region is cooled. The dense water formed at the surface is conveyed to the deep ocean and is part of the southward return flow. For Broecker's findings, it was necessary to **a** identify the relevance of North Atlantic deep water production, and **b** realize the possibility of multiple equilibriums of ocean circulation states and their association with two different climatic states

records (Dansgaard et al. 1984; Oeschger et al. 1984) indicating different climate states with different ocean modes of operation (like on and off states of a mechanical machine). This idea has been indeed followed by numerical and analytical models using EMICs (Ganopolski and Rahmstorf 2001), low-dimensional systems (Stocker and Johnsen 2003; Kwasniok and Lohmann 2009), and full GCMs (Zhang et al. 2014).

Another example in the Earth system is the term "tipping points" (Russil and Nyssa 2009). Common of all these metaphors is that they link to already established ideas and pictures across different cultural and scientific traditions (Peirce 1878; Brüning and Lohmann 1999). As described above, these ideas can be used to build and test hypotheses against observations and comparing observations to theory-based prediction (Weyl 1927; Manduca and Kastens 2012; Tewksbury et al. 2013). One has to be aware that in most of our approaches, we use implicit models (quite often not well articulated models) where a clarification through a metaphor or a conceptual model would help and such simplification is of great value for interdisciplinary research. The language expressing the scientific discoveries could be seen as important as the knowledge about the discovery itself (Weyl 1927). Emergence and decline of scientific paradigms can be even described by mathematical models of consensus and opinion formation using agents and multiple states (Bornholdt et al. 2011).

While it is certainly important to know how to make our ideas clear, they may be ever so clear without being completely true. One prominent example of disagreement between different schools is in the foundation of quantum mechanics.[3] On the other hand, we expect that the processes of investigation, if only pushed far enough, will give a solution to the question to which they are applied due to a steady increase in the number of competing ideas and hypotheses. A theory is a self-consistent description and general thinking with some predictive power. In this sense, the statistical quantum theory was favored because of its power of explaining experiments. Nevertheless, it can be only preliminary until a better, simpler, more consistent theory appears which can explain more experiments and phenomena. The process described in Fig. 1 seems to be a proper description of testing again and again the hypotheses in the field of Earth System Science and beyond.

---

[3] Born, Pauli, Heisenberg and others claimed the double nature of all corpuscles (corpuscular and wave character), giving the final solution in the statistical quantum theory (e.g., Bohr 1928). The strength of this theory is that it provides a theoretically complete description of a system involving only statistical quantities like probabilities concerning the measurable quantities of this system. Einstein argued that this did not satisfy a theory, because the complete description of any individual real situation existed irrespective of any act of observation or substantiation (Einstein 1949) and favored a non-statistical interpretation.

References

Berger A (1988) Milankovitch theory and climate. Rev Geophys 26(4):624–657

Bohr N (1928) The quantum postulate and the recent development of atomic theory. Nature 121:580–590

Bornholdt S, Jensen MH, Sneppen K (2011) Emergence and decline of scientific paradigms. Phys Rev Lett 106:058701

Broecker WS (1991) The great ocean conveyor. Oceanography 4(2):79–89

Brüning R, Lohmann G (1999) Charles S. Peirce on creative metaphor: a case study of the conveyor belt metaphor in oceanography. Found Sci 4(4):389–403 (Special issue for scientific discovery and creativity)

Bryan F (1986) High latitude salinity effects and inter-hemispheric thermohaline circulations. Nature 323:301–304

Claussen M, Mysak LA, Weaver AJ, Crucifix M, Fichefet T, Loutre M-F, Weber SL, Alcamo J, Alexeev VA, Berger A, Calov R, Ganopolski A, Goosse H, Lohmann G, Lunkeit F, Mokhov II, Petoukhov V, Stone P, Wang Z (2002) Earth system models of intermediate complexity: closing the gap in the spectrum of climate system models. Clim Dyn 18:579–586

Dansgaard W, Johnsen SJ, Clausen HB, Dahl-Jensen D, Gundestrup N, Hammer CU, Oeschger H (1984) North Atlantic climatic oscillations revealed by deep Greenland ice cores. In: Hansen JE, Takahashi T (eds) Climate processes and climate sensitivity. Geophysical monograph series, vol 29. AGU, Washington, DC, pp 288–298

Descartes R (1644) Principia philosophiae. English edition: Principles of Philosophy (trans: Rodger V, Miller RP (Reprint ed)). Reidel, Dordrecht. ISBN 90-277-1451-7

Einstein A (1905) Über die von der molekularkinetischen Theorie der Wärme geforderte Bewegung von in ruhenden Flüssigkeiten suspendierten Teilchen. Ann Phys 322(8):549–560

Einstein A (1949) Philosopher-scientist. The library of living philosophers series. Cambridge University Press, Cambridge

Frankignoul C, Hasselmann K (1977) Stochastic climate models, part II. Application to sea-surface temperature anomalies and thermocline variability. Tellus 29(289):1977

Ganopolski A, Rahmstorf S (2001) Rapid changes of glacial climate simulated in a coupled climate model. Nature 409:153–158

Gershenfeld N (2003) The nature of mathematical modeling. Cambridge University Press, Cambridge 344 pp

Grosfeld K, Lohmann G, Wolf-Gladrow D, Ladstätter-Weißenmayer A, Notholt J, Unnithan V, Wegner A (2013) The structural and educational concept in an interdisciplinary research school for earth system science. In: Lohmann G, Grosfeld K, Wolf-Gladrow D, Unnithan V, Notholt J, Wegner A (eds) Earth system science: bridging the gaps between disciplines perspectives from a multi-disciplinary Helmholtz Research School. Springer briefs in earth system sciences, pp 3–8. Springer, Heidelberg, vol 138. p 61 illus., 52 in color. doi:10.1007/978-3-642-32235-8. ISBN 978-3-642-32234-1

Hasselmann K (1976) Stochastic climate models. Part I: theory. Tellus 28:473–485

Hesse T, Wolf-Gladrow D, Lohmann G, Bijmaa J, Mackensen A, Zeebe RE (2014) Modelling d13C in benthic foraminifera: insights from model sensitivity experiments. Mar Micropaleontol 112:50–61. doi: 10.1016/j.marmicro.2014.08.001

Holton JR, Hakim GJ (2012) An introduction to dynamic meteorology, 5th edn. Academic Press, Waltham. ISBN-13: 978-0123848666; ISBN-10: 0123848660

IPCC (2007) Report of the intergovernmental panel on climate change. 2007. In: Solomon S, Qin D, Manning M, Chen Z, Marquis M, Averyt KB, Tignor M, Miller HL (eds) Contribution of working group I to the 4th assessment report of the intergovernmental panel on climate change. Cambridge University Press, Cambridge, p 996

IPCC (2013) Climate change 2013: the physical science basis. In: Stocker TF, Qin D, Plattner GK, Tignor M, Allen SK, Boschung J, Nauels A, Xia Y, Bex V, Midgley PM (eds) Contribution of working group I to the 5th assessment report of the intergovernmental panel on climate change. Cambridge University Press, Cambridge, p 1535. doi:10.1017/CBO9781107415324

Kuhn TS (1962) The Structure of scientific revolutions, 1st edn, 4th edn 2012. University of Chicago Press, Chicago. ISBN 9780226458113

Kwasniok F, Lohmann G (2009) Deriving dynamical models from paleoclimatic records: application to glacial millennial-scale climate variability. Phys Rev E 80(6):066104. doi:10.1103/PhysRevE.80.066104

Laepple T, Werner M, Lohmann G (2011) Synchronicity of Antarctic temperatures and local solar insolation on orbital time-scales. Nature 471:91–94. doi:10.1038/nature09825

Lee K, Bero L (2006) Ethics: increasing accountability. What authors, editors and reviewers should do to improve peer review. Nature. doi:10.1038/nature05007

Lemke P (1977) Stochastic climate models, part 3, application to zonally averaged energy balance models. Tellus 29:385–392

Liu Z, Zhua J, Rosenthal Y, Zhang X, Otto-Bliesner B, Timmermann A, Smith RS, Lohmann G, Zheng W, Timm OE (2014) The holocene temperature conundrum. PNAS 111(34): E3501–E3505. doi:10.1073/pnas.1407229111

Lohmann G, Schneider J (1999) Dynamics and predictability of Stommel's box model: a phase space perspective with implications for decadal climate. Tellus A 51(2):326–336

Lohmann G, Grosfeld K, Wolf-Gladrow D, Unnithan V, Notholt J, Wegner A (2013a) General aspects of earth system science. In: Lohmann G, Grosfeld K, Wolf-Gladrow D, Unnithan V, Notholt J, Wegner A (eds) Earth system science: bridging the gaps between disciplines perspectives from a multi-disciplinary Helmholtz Research School. Springer Briefs in earth system sciences, p 61 illus., 52 in color, vol 138. Springer, Heidelberg, pp 1–3. doi:10.1007/978-3-642-32235-8. ISBN 978-3-642-32234-1

Lohmann G, Wackerbarth A, Langebroek P, Werner M, Fohlmeister J, Scholz D, Mangini A (2013b) Simulated European stalagmite record and its relation to a quasi-decadal climate mode. Clim Past 9:89–98. doi:10.5194/cp-9-89-2013

Lohmann G, Pfeiffer M, Laepple T, Leduc G, Kim J-H (2013c) A model-data comparison of the Holocene global sea surface temperature evolution. Clim Past 9:1807–1839. doi:10.5194/cp-9-1807-2013

Lorenz S, Lohmann G (2004) Acceleration technique for Milankovitch typeforcing in a coupled atmosphere-ocean circulation model: method and application for the Holocene. Clim Dyn 23 (7–8):727–743. doi:10.1007/s00382-004-0469-y

Manduca CA, Kastens KA (2012) Fostering knowledge integration in geoscience education. Geoscience and geoscientists: uniquely equipped to study earth. Geol Soc Am Spec Pap 486:1–12. doi:10.1130/2012.2486(01

Marshall J, Plumb RA (2007) Atmosphere, ocean and climate dynamics: an introductory text. Int Geophys 93:345 (ISBN 0125586914)

McGuffie K, Henderson-Sellers A (2014) The climate modelling primer, 4 rev edn, p 480. ISBN 111994337X

McCright AM, Dunlap RE (2000) Challenging global warming as a social problem: an analysis of the conservative movement's counter-claims. Soc Probl 47(4):499–522. doi:10.2307/3097132

Meggers H, Buschmann M, Grosfeld K, Klebe S (2015) The educational program of the Earth System Science Research School (ESSReS), In: Lohmann G, Meggers H, Unnithan V, Wolf-Gladrow D, Notholt J, Bracher A (eds) Towards an interdisciplinary approach in Earth System Science, Springer, Heidelberg, Germany, pp 9–17. doi: 10.1007/978-3-319-13865-7_2

Mori H, Fujisaka H, Shigematsu H (1974) A new expansion of the master equation. Prog Theoret Phys 51(1):109–122

Oreskes N, Conway E (2010) Merchants of doubt: how a handful of scientists obscured the truth on issues from tobacco smoke to global warming, 1st edn. Bloomsbury Press, London. ISBN 978-1-59691-610-4

Oeschger H, Beer J, Siegenthaler U, Stauffer B, Dansgaard W, Langway CC (1984) Late glacial climate history from ice cores. In: JE Hansen, T Takahashi (eds) Climate processes and climate sensitivity. Geophysical monograph series, vol 29. AGU, Washington, DC, pp 299–306

Peirce CS (1878) How to make our ideas clear. Popul Sci Mon 12:286–302

Peirce CS (1974) Collected papers of Charles Sanders Pierce. In: Hartshorne C, Weiss P (eds), vol I–VI. Belknap Press of Harvard University Press, Cambridge

Peixoto JP, Oort AH (1992) Physics of climate. American Institute of Physics, New York

Rooth C (1982) Hydrology and ocean circulation. Prog Oceanog 11:131–149

Russill C, Nyssa Z (2009) The tipping point trend in climate change communication. Glob Environ Change 19(3):336–344

Saltzman B (2002) Dynamical paleoclimatology—a generalized theory of global climate change. Academic Press, San Diego p 354

Salzmann U, Dolan AM, Haywood AM, Chan W-L, Hill DJ, Abe-Ouchi A, Otto-Bliesner B, Bragg F, Chandler MA, Contoux C, Jost A, Kamae Y, Lohmann G, Lunt DJ, Pickering SJ, Pound MJ, Ramstein G, Rosenbloom NA, Sohl L, Stepanek C, Ueda H, Zhang Z (2013) How well do models reproduce warm terrestrial climates of the Pliocene? Nat Clim Change. doi:10.1038/nclimate2008

Singer SF (2007) Climate policy from Rio to Kyoto: a political issue for 2000- and beyond. Essays in public policy, no. 102. Stanford University: Hoover Institution, Stanford, p 49. ISBN 978-0-8179-4372-1

Stocker TF, Johnsen SJ (2003) A minimum thermodynamic model for the bipolar seesaw. Paleoceanography 18:1087. doi:10.1029/2003PA000920,4

Stommel H (1961) Thermohaline convection with two stable regimes of flow. Tellus 13:224–230

Tewksbury BJ, Manduca CA, Mogk DW, Macdonald RH (2013) Geoscience education for the Anthropocene. Geol Soc Am Spec Pap 501:189–201. doi:10.1130/2013.2501(08)

Timmermann A, Latif M, Voss R, Grötzner A (1998) Northern hemispheric interdecadal variability: a coupled air-sea mode. J Clim 11:1906–1931

Valdes P (2011) Built for stability. Nat Geosci 4:414–416. doi:10.1038/ngeo1200

Weyl H (1927) Philosophie der Mathematik und Naturwissenschaft. Oldenbourg Verlag, München

Zwanzig R (1960) Ensemble method in the theory of irreversibility. J Chem Phys 33:1338

Zhang X, Lohmann G, Knorr G, Purcell C (2014) Control of rapid glacial climate shifts by variations in intermediate ice-sheet volume. Nature 512:290–294. doi:10.1038/nature13592

Part II
Remote Sensing and Modelling of Atmospheric Chemistry and Sea Ice Parameters

Towards a Better Tropospheric Ozone Data Product from SCIAMACHY: Improvements in High Latitude Stratospheric Ozone

Jia Jia, Annette Ladstätter-Weißenmayer, Alexei Rozanov and John P. Burrows

Abstract Tropospheric ozone is a photochemically produced secondary pollutant and a main component of summer smog. Measurements from the space borne spectrometer SCIAMACHY are well suited to investigate sources and transport mechanisms of tropospheric ozone in a global view. Exploiting alternating observations in limb and nadir modes, the Limb-Nadir Matching technique (LNM) is used to retrieve global distributions of tropospheric ozone for the entire duration of the SCIAMACHY mission (Aug. 2002–Apr. 2012). The LNM technique is rather unique since SCIAMACHY observes the same air mass within 7 min first in the limb and then in the nadir viewing modes. As 90 % of atmospheric ozone is located in the stratosphere, the LNM technique applied to satellite measurements requires very high accuracy of the input limb and nadir data. Accurate ozone data bases are not only benefitting LNM tropospheric ozone retrieval, but also requirements for ozone trends study as well as the establishment of a long-term essential climate variable (ecv) data record. This study contributes to the improvement of the quality of SCIAMACHY limb stratospheric ozone profiles retrieved over the high latitudes of the Northern Hemisphere, hence improving the accuracy of the tropospheric ozone retrieval. Furthermore we provide comparisons of partial stratospheric ozone columns (from 15 to 30 km, referred to as SPO) resulting from SCIAMACHY limb measurements with ozone sonde data.

Keywords Remote sensing · Tropospheric ozone · Stratospheric ozone · Limb-nadir matching · SCIAMACHY · Satellite instruments

---

J. Jia (✉) · A. Ladstätter-Weißenmayer · A. Rozanov · J.P. Burrows
Institute of Environmental Physics, University of Bremen,
Otto-Hahn-Allee 1, 28359 Bremen, Germany
e-mail: jia@iup.physik.uni-bremen.de

G. Lohmann et al. (eds.), *Towards an Interdisciplinary Approach in Earth System Science*, Springer Earth System Sciences,
DOI 10.1007/978-3-319-13865-7_5

1 Introduction

Tropospheric ozone is a main component of the summer smog. The investigation of tropospheric ozone based on satellite measurements has been performed for a long time to improve the understanding of its sources, sinks and transport processes (Thompson 2001). The Limb-Nadir matching (LNM) technique is one of the residual methods to retrieve tropospheric ozone by subtracting the stratospheric ozone column (usually retrieved from limb or occultation measurements) from the total ozone column (obtained from nadir observations). This technique has previously been used for over 20 years by combining measurements from two different instruments (e.g., Fishman et al. 1990, 1999; Thompson and Hudson 1999; Ziemke et al. 1998, 2006, 2011; Schoeberl et al. 2007). Altering limb and nadir viewing geometries within 7 min, the passive imaging spectrometer SCIAMACHY (Burrows et al. 1995; Bovensmann et al. 1999) provides an opportunity to apply the LNM technique to collect information about both total and stratospheric ozone for the same volume of air from the same instrument. A SCIAMACHY tropospheric ozone database covering about 10 years (August 2002–April 2012) has been generated by Ebojie et al. (2014).

As 90 % of ozone is located in the stratosphere, the usage of the LNM technique requires very high accuracy of the input limb, nadir, and tropopause height data. Our previous studies revealed that the current SCIAMACHY LNM retrieval overestimates tropospheric ozone in northern high latitudes by 12–28 DU. In addition to the need of LNM tropospheric ozone retrieval, an accurate stratospheric ozone data base is also a requirement for stratospheric ozone trends study as well as the establishment of a long-term essential climate variable (ecv) data record.

This work suggests a method to improve the results of SCIAMACHY limb ozone retrieval in the lower stratosphere at high northern latitudes and provides a first verification of the obtained results. The verification results are presented in terms of stratospheric ozone columns (integrated limb profiles) as they are the direct input to the LNM technique. Section 2 introduces the limb measurements and methodology of the limb partial column comparisons. Algorithm basics and limitations of the current limb retrieval are described in Sect. 3. Algorithm improvements and first verification results for the upcoming SCIAMACHY limb retrieval (V3.0) follow in Sect. 4. Section 5 summarizes our principal results and conclusions.

2 Limb Measurements and Comparison Methodology

The SCIAMACHY instrument operated from August 2002 to April 2012 on board the European satellite Envisat (Bovensmann et al. 1999). SCIAMACHY was designed to measure radiances in 8 channels covering a wide spectral range from 214 to 2,384 nm with a moderate spectral resolution of 0.21–1.56 nm depending on the channel. The UV radiation was directed to channel 1 (214–314 nm) and channel 2 (309–404 nm). The visible light passed to channel 3 (392–605 nm) and channel 4 (598–790 nm). These measured radiances contain 'fingerprint' information caused by the absorption of atmospheric species which is used to retrieve their concentrations. SCIAMACHY operated in three observation modes: nadir, limb and solar/lunar occultation. In limb viewing geometry, the line of sight was pointed tangentially to the Earth's surface, with a field of view of 110 km horizontally and 2.6 km vertically at the tangent point. Limb measurement sequence started from 3 km below the horizon (0 km after October 2010) and continued with a vertical scan up to around 93 km. At each tangent height, SCIAMACHY performed a horizontal scan with a total swath of about 960 km. The tangent height (TH) step between subsequent horizontal scans is around 3.3 km. During the vertical scan, SCIAMACHY keeps the same signal integration time for all THs while the scattered limb radiance decreases exponentially. This results in a strong decrease of S/N ratio in the measured spectra with increasing TH.

To evaluate ozone profiles retrieved from SCIAMACHY limb measurements, ozone sonde data from stations which belong to the World Ozone and Ultraviolet Radiation Data Centre (WOUDC) are used. This study is focused on the results obtained at high latitudes of the Northern Hemisphere. Only stations which provide more than 30 measurements from January 2003 to December 2012 are selected for comparisons. These are Alert, Eureka, Ny-Alesund, Sodankyla, Lerwick and Resolute. The locations of the stations are shown in Fig. 1. Coincident SCIAMACHY limb profiles are selected for each ozone sonde profile. The geographic distance between the ozone sonde station and the footprint centre of the co-located SCIAMACHY measurement is required to be within 5° in latitude and 10° in longitude. A maximum time difference of 24 h is allowed. Since a larger attenuation in a longer optical pathway results in a lower signal, the coincident limb profiles with a solar zenith angle larger than 80° are rejected. In general, an altitude range between 15 and 30 km is selected for the comparisons. This choice is justified by larger uncertainties of the current limb retrieval below 15 km and increasing uncertainty in the ozone sonde data above 30 km. The latter is mostly caused by the decaying pump efficiency at lower pressures (Johnson et al. 2002). For each particular profile pair, the integration was done either from the first cloud-free level of SCIAMACHY limb data or from 15 km whichever is higher and ended at either the ozone sonde burst height or at 30 km whichever is lower.

For the partial column comparison, both SCIAMACHY limb ozone data and raw ozone sonde measurements are integrated to calculate the stratospheric partial ozone column (SPO) C_{strato}:

$$C_{strato} = \sum_{i_{tph}}^{i=TH_{max}} \left(\frac{N(z_{i-1}) + N(z_i)}{2} \right) (z_i - z_{i-1});$$

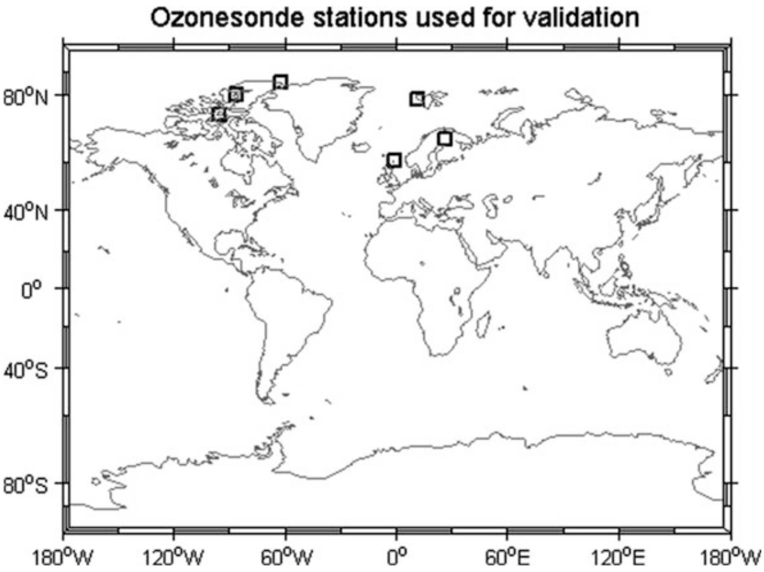

Fig. 1 Ozone sonde stations from WOUDC used for the comparisons. They are: Alert (82.5°N, 62.3°W), Eureka (80.1°N, 85.9°W), Ny-Alesund (78.9°N, 11.9°W), Sodankyla (67.4°N, 26.6°E), Lerwick (60.1°N, 1.2°W) and Resolute (74.7°N, 94.9°W)

where $N(z)$ is the stratospheric ozone profile in number density units (molecules per cm^2 per km), z_i represents the altitude in km and i is the layer index. SPO time series are analyzed for the period from January 2003 to December 2012.

3 SCIAMACHY Limb Retrieval of Version 2.9

The current SCIAMACHY limb retrieval (V2.9) uses combined spectral information from the UV and visible spectral ranges to obtain vertical profiles of ozone. The limb radiances measured in the visible spectral range are processed as suggested by Flittner et al. (2000). At the first step, the entire limb radiance profile is normalized with a limb measurement at an upper TH (often referred to as the reference TH): $I_n(\lambda, TH_i) = I(\lambda, TH_i)/I(\lambda, TH_{ref})$, with λ denoting wavelength and TH_i the tangent height at elevation step i. The normalization removes the solar Fraunhofer structures and reduces the influence of the lower atmosphere, e.g. due to multiple scattering and reflection from the surface. Furthermore, it provides a kind of self-calibration of the instrument since the instrument calibration parameters do not differ much for different THs. Subsequently, to minimize the influence of the broad-band spectral features, e.g. Rayleigh and aerosol scattering, the so called triplet method is used. Thereby the measurement vector, y, is obtained from the normalized radiances at 525, 589 and 675 nm as follows:

$$y(TH_i) = \frac{I_n(589.0\ \text{nm}, TH_i)}{\exp[\frac{1}{2}(\ln I_n(525\ \text{nm}, TH_i) + \ln I_n(675\ \text{nm}, TH_i))]}$$

In the UV spectral range the method described by Rohen et al. (2006) is used. The measurement vector, y, was originally obtained from the normalized limb radiance profiles at eight single wavelengths (264, 267.5, 273, 283, 286, 288, 290.5, and 305 nm) (Sonkaew et al. 2009). These wavelengths are chosen to avoid strong Fraunhofer lines and terrestrial airglow emissions. The SCIAMACHY limb ozone profiles are then retrieved by using a non-linear inversion scheme with the first order Tikhonov regularization (Rozanov et al. 2007, 2011). The forward modelling is done with the radiative transfer model SCIATRAN (Rozanov et al. 2014).

A comparison of SCIAMACHY SPO V2.9 with ozone sonde data from Eureka (80.1°N, 85.9°W) is shown in Fig. 2. Similar seasonal variations are observed in the time series from both SCIAMACHY and sonde data (upper panel). This annual variation is the result of chemical and dynamical processes (Chipperfield et al. 1999). The Brewer-Dobson circulation causing the diabatic descent of ozone rich air in the high latitudes is most efficient in winter. As a result, the lower stratospheric ozone steadily increases over winter and reaches its maximum in March

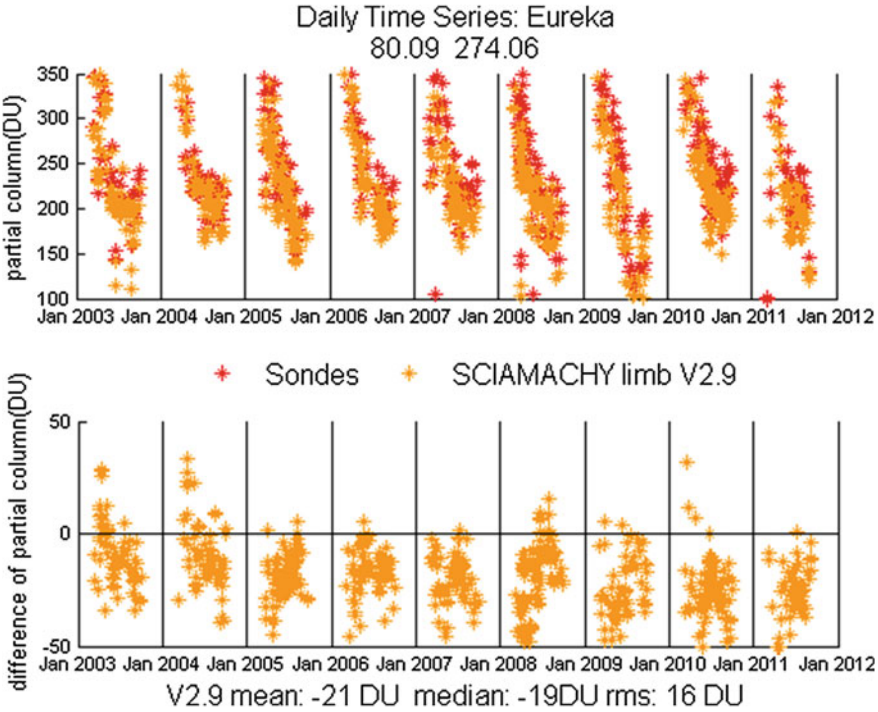

Fig. 2 SPO time series from SCIAMACHY V2.9 limb data and ozone sonde data (*upper panel*) and the absolute difference in SPO (*lower panel*) for Eureka (80.1°N, 85.9°W)

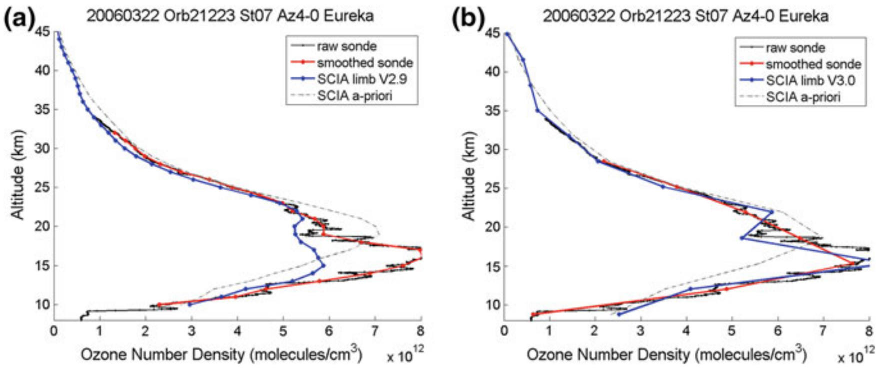

Fig. 3 Comparison of ozone vertical profiles from SCIAMACHY and from ozone sonde at station Eureka. **a** SCIAMACHY limb retrieval version 2.9. **b** SCIAMACHY limb retrieval version 3.0

(e.g. Weber et al. 2011). After that the Brewer-Dobson circulation gets weaker, leading to colder polar stratospheric temperatures, thus causes polar ozone loss. Combining with the weaker Brewer-Dobson circulation and the increasing solar shortwave radiation, stratospheric ozone concentration decreases after spring and reaches its minimum in fall. The lower panel of Fig. 2 depicts the difference between SPOs from SCIAMACHY and ozone sonde at Eureka. A severe underestimation by SCIAMACHY with a median difference of 19 DU is clearly seen. The reasons for that can be identified by analysing the left panel of Fig. 3. The left panel of this figure shows a comparison of a single V2.9 SCIAMACHY ozone limb profile (blue solid line) with a collocated ozone sonde profile (black solid line indicates the original data and red solid line sonde data smoothed to the vertical resolution of SCIAMACHY) at Eureka for 22 March, 2006. The ozone concentration peak near 17 km is not captured by data version 2.9. This is a typical behaviour that explains the underestimation seen in Fig. 2. This behaviour is probably attributed to the instrumental influence to the SCIAMACHY V2.9 retrieval.

4 SCIAMACHY Limb Retrieval of Version 3.0 and Comparison Results

In the new SCIAMACHY limb retrieval (V3.0), extra-terrestrial solar spectrum is used instead of the reference TH to normalize the measured limb radiance. A drawback of this method is that the instrument calibration features are not fully cancelled out any more since the optical paths for limb and solar measurements are not identical anymore. This might have serious consequences for the ozone retrieval quality because the short and long wavelength wings of the Chappuis absorption band of ozone are measured in different spectral channels of the SCIAMACHY instrument (see Sect. 2). Thus, usage of the whole Chappuis band in combination with the solar spectrum normalization requires a very high quality of the inter-channel calibration. One possible solution is to use only one wing of the Chappuis absorption band recorded within one channel. In this case, the highly efficient triplet method cannot be employed anymore. Instead, we exploit the differential structure of the ozone absorption signature in the short wavelength wing of the Chappuis absorption band and employ the DOAS technique (Platt 1994) to retrieve the vertical ozone profiles. Differential limb spectra are obtained then as

$$y = \ln(\mathrm{I}(\lambda_\mathrm{L}, \mathrm{TH_i})) - \mathrm{P_n}$$

where I is the sun-normalized radiance and $\mathrm{P_n}$ is a polynomial of order n in λ whose coefficients are obtained by fitting the logarithms of the normalized limb radiance in the wavelength domain for each TH independently. Since the ozone absorption signature is smaller compared to the whole Chappuis band, the influence of weaker absorbers, namely, NO_2 and O_4 needs to be taken into account. The inversion problem is solved then in a similar way as before (Rozanov et al. 2007). The using of DOAS-type retrieval may reduce the instrumental influences by performing polynomial calculation. This retrieval scheme is used to produce V3.0 limb ozone profiles.

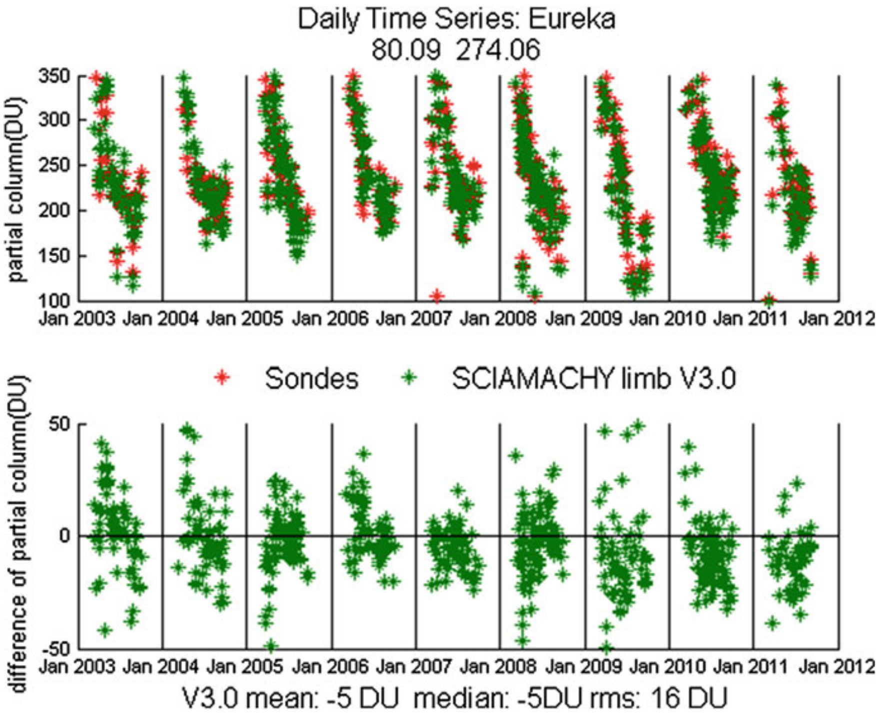

Fig. 4 Same as Fig. 2 but for SCIAMACHY V3.0 data

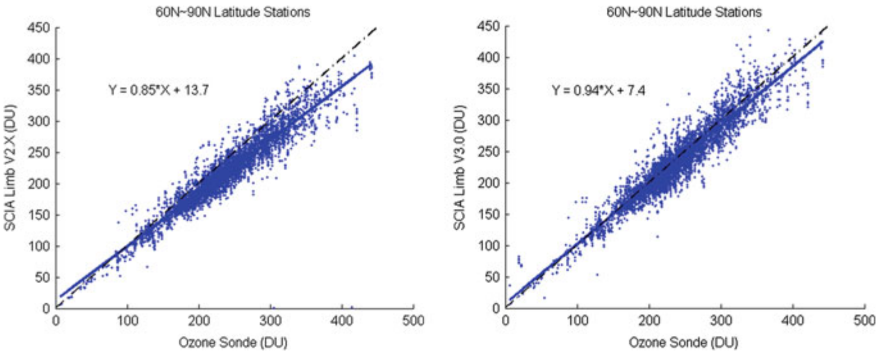

Fig. 5 Scatter plots for the six northern high latitude stations. *Left panel* SCIAMACHY current V2.9 limb ozone results versus ozone sonde data. *Right panel* same as the left panel but for the upcoming SCIAMACHY V3.0 results

The right panel of Fig. 3 shows the comparison of ozone vertical profiles from SCIAMACHY limb V3.0 data with ozone sonde data at Eureka station for 22 March, 2006. The results are presented in the same way as it was done for the SCIAMACHY V2.9 results in the left panel of the figure. One sees clearly that the ozone maximum at 17 km observed by the sonde is now captured properly by SCIAMACHY. Similarly to Figs. 2 and 4 shows the time series of SPO and the difference between SPOs from SCIAMACHY limb retrieval V3.0 and ozone sonde data at Eureka station. In comparison to SCIAMACHY V2.9 data, the median difference is reduced to 5 DU in V3.0. The statistical results for all six northern high latitude stations for both current and upcoming SCIAMACHY limb retrieval versions are shown as scatter plots in the left and right panels of Fig. 5, respectively. With a higher correlation coefficient of R = 0.94 and smaller deviation of σ = 7.4 DU, the SCIAMACHY V3.0 dataset exhibits much better agreement with ozone sonde data at high latitudes (60°N–90°N).

5 Conclusions

Underestimations of ozone concentrations in the high latitudes lower stratosphere has been identified in the current limb ozone retrieval leading to a significant underestimation of the stratospheric column, and in turn, to overestimation of tropospheric ozone from the limb-nadir technique at these latitudes. The issue has been resolved by optimizing the SCIAMACHY limb ozone retrieval algorithm. The solar spectrum is used for the normalization of the limb radiances instead of the reference TH limb radiance. Due to instrumental issues the used wavelength region had to be narrowed to the short wavelength wing of the Chappuis absorption band. As a consequence the triplet method was replaced by the DOAS technique, which may reduce the unclear instrumental influences to the limb retrieval. Six northern high latitude ozone sonde stations are used to evaluate the limb ozone products before (V2.9) and after (V3.0) this optimization. While the verification of V2.9 limb data reveals systematic underestimation of SPO, the V3.0 limb data shows significantly better agreement with ozone sonde data, e.g. the relative difference at Eureka (80.09°N, 85.94°W) improved from −19 DU for SCIAMACHY V2.9 to −5 DU for V3.0. The comparisons for all six northern high latitude locations indicate good agreement between SCIAMACHY limb ozone V3.0 and ozone sonde data with a high correlation coefficient R = 0.94. The global validation of SCIAMACHY stratospheric ozone columns of V3.0 is ongoing.

Acknowledgments We thank WOUDC (http://woudc.org) for providing ozone sonde station data. JJ also wants to thank CSC (China Scholarship Council) and ESSReS (Earth System Science Research School) for supporting during the project study. This work has been funded in parts by the German Aerospace DLR project SADOS (FKZ 50EE1105) and by the University and State of Bremen.

References

Burrows JP, Hölzle E et al (1995) SCIAMACHY—scanning imaging absorption spectrometer for atmospheric chartography. Acta Astron 35:445–451

Bovensmann H, Burrows JP et al (1999) SCIAMACHY: mission objectives and measurement modes. J Atmos Sci 56:127–150

Chipperfield MP, Jones RL (1999) Relative influences of atmospheric chemistry and transport on Arctic ozone trends. Nature 400:551–554

Ebojie F, von Savigny C et al (2014) Tropospheric column amount of ozone retrieved from SCIAMACHY limb-nadir-matching observations. Atmos Meas Tech 7:2073–2096

Fishman J, Balok AE (1999) Calculation of daily tropospheric ozone residuals using TOMS and empirically improved SBUV measurements: application to an ozone pollution episode over the eastern United States. J Geophys Res 104:30319–30340

Fishman J, Watson C et al (1990) Distribution of tropospheric ozone determined from satellite data. J Geophys Res 95:3599–3617

Flittner DE, Bhartia PK et al (2000) O_3 profiles retrieved from limb scatter measurements: theory. Geophys Res Lett 27:2601–2604

Johnson BJ, Oltmans SJ et al (2002) Electrochemical concentration cell (ECC) ozonesonde pump efficiency measurements and tests on the sensitivity to ozone of buffered and unbuffered ECC sensor cathode solutions. J Geophys Res 107:4393

Platt U (1994) Differential optical absorption spectroscopy (DOAS). Chem Anal Ser 127:27–83

Rohen GJ, von Savigny C et al (2006) First results of ozone profiles between 35 and 65 km retrieved from SCIAMACHY limb spectra and observations of ozone depletion during the solar proton events in October/November 2003. Adv Space Res 37:2263–2268

Rozanov A, Eichmann K-U et al (2007) Comparison of the inversion algorithms applied to the ozone vertical profile retrieval from SCIAMACHY limb measurements. Atmos Chem Phys 7:4763–4779

Rozanov A, Kühl S et al (2011) BrO vertical distributions from SCIAMACHY limb measurements: comparison of algorithms and retrieval results. Atmos Meas Tech 4:1319–1359

Rozanov VV, Rozanov AV et al (2014) Radiative transfer through terrestrial atmosphere and ocean: software package SCIATRAN. J Quant Spectrosc Radiat Transfer 133:13–71

Schoeberl MR, Ziemke JR et al (2007) A trajectory-based estimate of the tropospheric ozone column using the residual method. J Geophys Res 112:D24S49

Sonkaew T, Rozanov VV et al (2009) Cloud sensitivity studies for stratospheric and lower mesospheric ozone profile retrievals from measurements of limb-scattered solar radiation. Atmos Meas Tech 2:653–678

Thompson AM (2001) Tropical tropospheric ozone and biomass burning. Science 291:2128–2132

Thompson AM, Hudson RD (1999) Tropical tropospheric ozone (TTO) maps from Nimbus 7 and Earth Probe TOMS by the modified-residual method: evaluation with sondes, ENSO signals, and trends from Atlantic regional time series. J Geophys Res 104:26961–26975

Weber M, Dikty S et al (2011) The Brewer-Dobson circulation and total ozone from seasonal to decadal time scales. Atmos Chem Phys 11:11221–11235

Ziemke JR, Chandra S et al (1998) Two new methods for deriving tropospheric column ozone from TOMS measurements: assimilated UARS MLS/HALOE and convective-cloud differential techniques. J Geophys Res 103:22115–22128

Ziemke JR, Chandra S et al (2006) Tropospheric ozone determined from Aura OMI and MLS: evaluation of measurements and comparison with the global modelling initiative's chemical transport model. J Geophys Res 111:D19303

Ziemke JR, Chandra S et al (2011) A global climatology of tropospheric and stratospheric ozone derived from Aura OMI and MLS measurements. Atmos Chem Phys 11:9237–9251

Ten-Year SCIAMACHY Stratospheric Aerosol Data Record: Signature of the Secondary Meridional Circulation Associated with the Quasi-Biennial Oscillation

Lena A. Brinkhoff, Alexei Rozanov, René Hommel,
Christian von Savigny, Florian Ernst, Heinrich Bovensmann
and John P. Burrows

Abstract The ten-year long stratospheric aerosol data record, retrieved from SCIAMACHY limb scattered sunlight measurements, is a continuous data set during the period from 2002 to 2012. As a result of the relatively high vertical resolution (3–4 km) and near global coverage on the sun-facing side of the Earth, the retrieved data set (V1.1) provides global information about the variability of stratospheric aerosol extinction between the tropopause and about 33 km altitude. Stratospheric aerosols are near-spherical droplets mainly comprised of sulfuric acid and water. The background aerosol load in the stratosphere results from the tropical injection of tropospheric air containing precursors of stratospheric aerosols. A sporadic but important source is the injection of gases from volcanic eruptions. These release the precursor gas SO_2 into the troposphere or even directly into the stratosphere due to convection induced by volcanic heat. Stratospheric aerosols belong to the essential climate variables, as they influence the Earth's radiation budget and are involved in the depletion of ozone. In this study, we analyse the time series of SCIAMACHY observed tropical aerosol extinction coefficients at 30 km altitude. A distinct biennial variation has been found. Based on ECMWF ERA-Interim reanalysis data, this variation is explained by the secondary meridional circulation that is induced by the quasi-biennial oscillation of the tropical zonal wind in the stratosphere.

Keywords Stratospheric aerosols · Tropical stratosphere · QBO · Secondary meridional circulation · SCIAMACHY

L.A. Brinkhoff (✉) · A. Rozanov · R. Hommel · F. Ernst · H. Bovensmann · J.P. Burrows
Institute of Environmental Physics and Remote Sensing, University of Bremen, Bremen, Germany
e-mail: brinkhoff@uni-bremen.de; brinkhoff@iup.physik.uni-bremen.de

C. von Savigny
Institute of Physics, Ernst-Moritz-Arndt-University of Greifswald, Greifswald, Germany

G. Lohmann et al. (eds.), *Towards an Interdisciplinary Approach in Earth System Science*, Springer Earth System Sciences,
DOI 10.1007/978-3-319-13865-7_6

1 Introduction

Stratospheric aerosols (SAs) are spherical droplets comprised of about 75 % sulfuric acid (H_2SO_4) and about 25 % water (H_2O) (e.g., Rosen 1971). Precursors of SAs are sulfur dioxide (SO_2) and carbonyl sulfide (COS). One key source are volcanic eruptions, which release SO_2 and may cause a pyrocumulus cloud transporting the SO_2 from the troposphere into the stratosphere. A weaker but permanent source is the tropical injection of tropospheric air containing SO_2 and COS, and to a lesser extent sulfate aerosols, which have been formed in the troposphere. The actual composition and the constituents of SAs depend on several parameters such as, e.g., temperature and altitude. Stratospheric aerosols can also partly comprise meteoric dust, especially in the middle and upper stratosphere (Thomason and Peter 2006).

Stratospheric aerosols play an important role in the Earth's radiative balance and climate, as they increase the Earth's planetary albedo by scattering solar radiation (e.g., Valero and Pilewskie 1992; Deshler 2008). Especially after strong volcanic eruptions, the effect of stratospheric aerosols on the Earth's radiation budget is stratospheric warming and tropospheric cooling (e.g., Lacis et al. 1992; Deshler 2008). Furthermore, SAs influence stratospheric chemistry. They are precursors for polar stratospheric clouds and thus support the destruction of ozone inside the polar vortex (e.g., Hofmann and Solomon 1989). They may even lead to a halogen-driven ozone destruction outside polar vortices (Erle et al. 1998). Based on these properties, the Global Climate Observing System (GCOS) defined stratospheric aerosols as an Essential Climate Variable (ECV). Aerosol size plays an important role for the climate response of stratospheric sulfate aerosols (e.g., Timmreck et al. 2010), however, the exact aerosol size distribution is often not known. In addition, the indirect radiation impact, like the aerosol cirrus cloud formation potential, is poorly quantified (e.g., Thomason and Peter 2006; Deshler 2008).

A distinction is drawn between volcanic and non-volcanic aerosols, as they differ in size and concentration. The radii of non-volcanic SAs, also referred to as background SAs, are 0.1–0.5 μm and the corresponding concentrations are 0.5–0.005 cm^{-3}. After large volcanic eruptions, the concentrations increase by a factor of 10–1,000 and the radii by a factor of 2–4 (Deshler 2008). The concentration maximum of background SAs in the low and mid-latitudes is at about 20 km altitude (e.g., Junge et al. 1961). The background SA concentration typically varies with time and space (Solomon et al. 2011), nevertheless, there appears to be no long-term trend between 1970 and 2005 (Deshler 2008). Variability of the SA load in the lower stratosphere (from the tropopause to about 24 km altitude in the low latitudes) is mainly driven by volcanic eruptions (Vernier et al. 2011) and to a lesser extent by atmospheric dynamics. However, as shown in this work, the primary reason for the variability of the SA load in the middle stratosphere is atmospheric dynamics.

As stratospheric aerosols have typical lifetimes of several years (Hamill et al. 1997), they are well suited tracers for dynamical processes in the stratosphere with shorter periods (e.g., Trepte and Hitchman 1992). One dominant dynamic feature of the atmosphere (below around 50 km) is the residual mean meridional circulation (reviewed in Butchart 2014), also known as Brewer-Dobson circulation, which is primarily driven by planetary wave breaking in the stratosphere. The main properties of this atmospheric circulation are tropical upwelling combined with air mass transport from the tropics to the extratropics and to the poles (shallow branches) in the lower and middle stratosphere and from the tropics to the winter pole (deep branch) in the middle and upper stratosphere.

Another relevant dynamical process in the stratosphere is the quasi-biennial oscillation (QBO) of the equatorial zonal wind. The QBO is caused by the interaction of the zonal wind with tropical gravity, inertia-gravity, Kelvin, and Rossby-gravity waves and appears as easterly and westerly wind regimes propagating downward from the stratopause (around 50 km) to the tropopause (around 16 km) while at a fixed altitude the wind changes from east to west and back to east within 28 months (≈2 years) on average. The period and the amplitude of the zonal wind QBO are, for instance, influenced by the residual mean meridional circulation (Kawatani and Hamilton 2013; Butchart 2014).

The QBO has a significant impact on the global chemistry and climate, as it affects the distribution of trace species and aerosols in the stratosphere (reviewed in Baldwin et al. 2001). Furthermore, it causes the secondary meridional circulation in the tropical and subtropical stratosphere (Baldwin et al. 2001; Ribera et al. 2004). Aerosol effects associated with the secondary meridional circulation of the QBO have been first described by Trepte and Hitchman (1992) for the stratospheric background aerosol, based on SAGE II aerosol extinction ratios. Bingen et al. (2004) showed that the QBO has a clear influence on the aerosol size distribution derived from SAGE II data over the period 1984–2000.

One satellite observation method for SAs, which began with the SAM II mission in the late 1970s followed by SAGE I–III, exploits the solar occultation geometry (e.g., McCormick et al. 1979). The use of limb scattered solar radiation measurements, e.g., by OSIRIS/Odin (Llewellyn et al. 2004) and SCIAMACHY/ENVISAT (see Sect. 2) is a new approach to quantify stratospheric aerosols during the day. We employ the SCIAMACHY limb stratospheric aerosol record from August 2002 to April 2012 (Ernst et al. 2012; Ernst 2013) in order to focus on the tropical aerosol distribution in the upper part of the aerosol layer at an altitude of about 30 km.

2 Instrument and Data

This study makes use of aerosol extinction coefficients derived from limb scattered sunlight measurements of the SCIAMACHY (SCanning Imaging Absorption spectroMeter for Atmospheric CartograHY) satellite instrument (Burrows et al. 1995; Bovensmann et al. 1999) aboard the ENVISAT (ENVIronmental SATellite) of the European Space Agency (ESA). The satellite was launched on 1st March 2002 into a polar, sun-synchronous orbit of about 800 km altitude. It ceased operation on 8th April 2012. During this time of almost ten years, it orbited the Earth every 100.6 min in a repeat interval of 35 days (corresponding to 501 orbits) with a descending node at 10:00 a.m. local time.

In the limb geometry, the SCIAMACHY instrument scanned the atmosphere from 0 km to about 93 km altitude with tangent height steps of 3.3 km, whereby vertical profiles of the scattered solar radiation between 214 and 2,386 nm (spectral sampling between 0.11 and 0.74 nm) were measured (e.g., Gottwald and Bovensmann 2011). The advantage of this geometry is a high vertical resolution compared to the nadir geometry and a near-global coverage within a few days that cannot be achieved by the occultation geometry.

In order to retrieve the aerosol extinction coefficients, the vertical radiation profiles at 470 and 750 nm (SCIAMACHY Level 1 data version 7.04) were used. Each measurement vector is generated in a two-step approach. The first step is a tangent height normalisation (reference tangent height is 35 km), and the second step is the so-called wavelength pairing, where the normalised limb radiance profile of the longer wavelength, i.e. 750 nm, is divided by the one of the shorter wavelength, i.e. 470 nm, yielding the measurement vector (Bourassa et al. 2007). The first step reduces the influence of the ground albedo and the second step amplifies the Mie scattering signal compared to the Rayleigh scattering signal, which is useful, as aerosols are Mie scatterers. Subsequently, the underlying inverse problem is solved employing the optimal estimation method (Rodgers 2000).

For the aerosol parametrisation, extinction coefficient profiles of a climatological model (ECSTRA, Fussen and Bingen 1999) were used and the phase function was calculated with a standard Mie code. To perform forward simulations, i.e., to calculate the scattered solar radiation and weighting functions of various atmospheric parameters in the spectral range of the measurements, the radiative transfer model SCIATRAN developed at the University of Bremen (Rozanov et al. 2014) was used.

This work is based on aerosol extinction coefficient profiles in units of 1/km at 750 nm of the retrieval version V1.1 (Ernst et al. 2012; Ernst 2013). The data is on a monthly-mean, 1-km-altitude, 5°-latitude, and 5°-longitude grid with a vertical resolution of about 4 km, and horizontal resolution of about 240 km across the flight direction, and about 400 km along flight direction.

3 Results and Discussion

Figure 1 shows a latitude-time cross section of the zonal and monthly mean aerosol extinction coefficients for 750 nm at about 30 km altitude. The enhanced aerosol extinction coefficients in the tropics and subtropics compared to the mid and high-latitudes result from tropical upwelling of the residual mean meridional circulation. In addition, Fig. 1 indicates that the tropical aerosol extinction varies with an almost two-year period. Maximum extinction coefficients are found around January 2003, 2005, 2007, 2009, and with a slight delay and a weaker extent in 2011. This

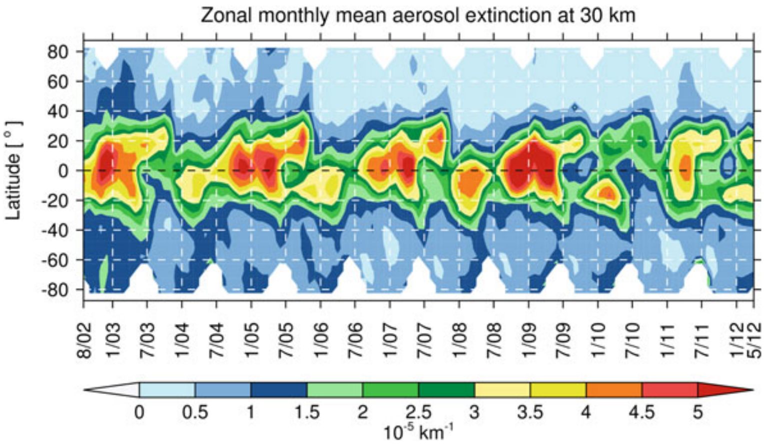

Fig. 1 Latitude-time cross section of the zonal and monthly mean aerosol extinction for the wavelength 750 nm at 30 km altitude from August 2002 to April 2012

sequence of enhanced extinctions is also very pronounced in Fig. 2 representing an altitude-time section, which shows the zonal and monthly average for latitudes between 5°N and 5°S. The contour lines of the aerosol extinction indicate a near biennial variation in the vertical extension of the aerosol layer. As this variation is fairly regular and does not coincide with volcanic eruption events, it is most likely explained by atmospheric dynamics. Due to the biennial pattern, it is obvious to presume the quasi-biennial oscillation (QBO) of the zonal wind in the tropical stratosphere to be the cause of the aerosol distribution at this altitude. The described

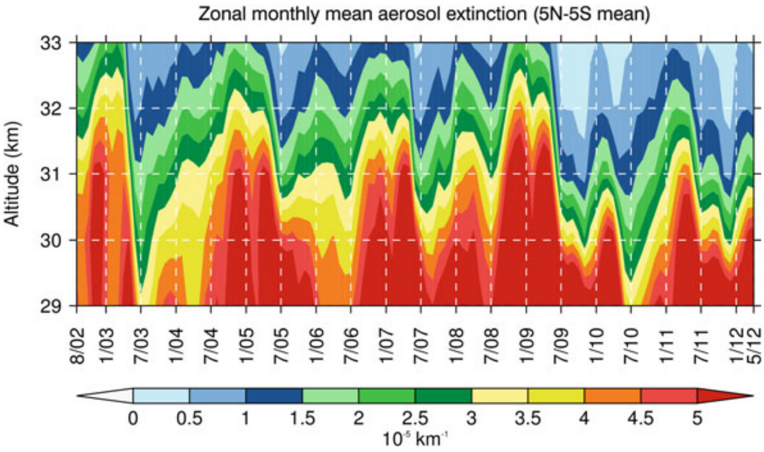

Fig. 2 Altitude-time cross section of the zonal and monthly mean aerosol extinction for the wavelength 750 nm averaged between 5°N and 5°S from August 2002 to April 2012 showing the variation in the vertical extension of the aerosol layer

signature found in the SCIAMACHY aerosol extinction coefficients around 30 km altitude is consistent with the known QBO periods (22–34 months). Following this idea, Fig. 3a shows an altitude-time cross section of the ERA-Interim equatorial zonal-mean zonal wind averaged between 3°N and 3°S. About every two years, the zonal-mean zonal wind changes its direction from eastwards (westerly winds) to westwards (easterly winds) and from westwards to eastwards, respectively. The wind transition line is also called the shear line, as the strongest vertical wind shear generally occurs at the time of the wind transition (Baldwin et al. 2001). In the following, the time period when a wind transition occurs at pressure levels between 7 and 50 hPa (21–35 km) is referred to as wind shear period. Furthermore, we define the wind phase by the zonal wind at 50 hPa, i.e., the period of westerly winds at 50 hPa is referred to as westerly phase and the period of easterly winds at 50 hPa is referred to as easterly phase.

The QBO in the equatorial zonal wind, however, does not directly imply any vertical transport of aerosols, which is necessary to obtain the distributions shown in Figs. 1 and 2. The potential key to this problem lies in the secondary meridional circulation (SMC) that is associated with the QBO (e.g., Baldwin et al. 2001; Choi et al. 2002). The sketch in Fig. 3b describes (in line with Baldwin et al. (2001) and references therein) the basic features of the SMC related tracer transport. Schematically it shows two simplified situations of Fig. 3a in an altitude(z)-latitude(y) diagram. For instance, the conditions observed in October 2003 at pressure levels around 20 hPa are described in the left panel of Fig. 3b. In the lower altitude layers we find an easterly zonal wind and a westerly zonal wind at higher altitudes. This situation reflects a so-called westerly wind shear of the QBO. In October 2004, for instance, we have the opposite wind situation shown in the right panel of Fig. 3b, which is referred to as an easterly wind shear.

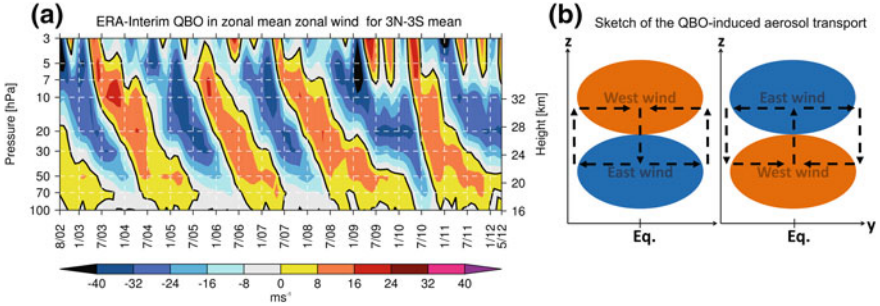

Fig. 3 **a** Time series of the ERA-Interim zonal-mean zonal wind averaged between 3°N and 3°S from August 2002 to April 2012 representing the quasi-biennial oscillation of the equatorial stratosphere. The *reddish* colours indicate westerly zonal wind (positive wind speeds) and the *bluish* colours easterly zonal wind (negative wind speeds). The *black contour line* is the wind transition. **b** Scheme of special wind periods of the QBO and effects on the aerosol transport in the stratosphere marked by the *black dashed arrows*. The westerly shear involves an equatorial downwelling (*left*) and the easterly shear an equatorial upwelling (*right*), both relative to the mean upwelling associated with the residual mean meridional circulation in the stratospheric

According to the thermal wind balance at the equator, which basically says that the vertical gradient in the zonal wind is compensated by temperature anomalies (e.g., Andrews et al. 1987; Randel et al. 1999), strong equatorial westerly (easterly) wind shears are accompanied by positive (negative) temperature anomalies (on the order of ±4 K, see Baldwin et al. 2001). The positive (negative) temperature anomalies induce adiabatic warming (cooling) of sinking (rising) air (e.g., Baldwin et al. 2001), which preserves these temperature anomalies. Thus, vertical motions relative to the upwelling of the mean meridional circulation (MMC) occur. In addition, the equatorial temperature anomalies are linked to anomalies in the MMC in the tropics. A negative anomaly in the Northern Hemisphere MMC and a positive anomaly in the Southern Hemisphere MMC at the same time induce a secondary meridional motion towards the equator and vice versa (Baldwin et al. 2001; Ribera et al. 2004). Due to mass continuity, the equatorial sinking (rising) motion during westerly (easterly) wind shear periods and the related meridional motion lead to subtropical rising (sinking) air (Baldwin et al. 2001). This finally completes the SMC in the tropical and subtropical stratosphere.

The SMC modulates the large-scale tracer transport in the stratosphere that is associated with the MMC. Based on a microphysical model of the life-cycle of stratospheric aerosols, Hommel et al. (2014) showed in detail how the stratospheric aerosol layer is lofted by the SMC during the QBO easterly shear. This lofting is followed by a slow descent over about a quarter QBO period, with a subsequent stronger descent under the influence of the emerging QBO westerly wind shear. This motion of aerosols in the equatorial stratosphere is pretty well reflected in the vertically-resolved time series of SCIAMACHY observed aerosol extinction coefficients at 750 nm (Fig. 2). Furthermore, the SCIAMACHY aerosol record nicely shows the hemispheric asymmetry in the QBO modulated meridional aerosol transport (Fig. 1), which is stronger in the Northern Hemisphere, where the wave driving in the stratosphere is stronger (e.g., Andrews et al. 1987).

The zonal-mean zonal winds in Fig. 3a indicate that an easterly shear between 10–30 hPa often coincides with strong easterly winds at about 5–10 hPa. Thus, we can use the wind at 10 hPa as a proxy for the underlying wind shear period and the resulting direction of the aerosol transport by the SMC in order to examine the correlation between the aerosol load at 30 km and the wind shear period. Figure 4 shows the relationship between the zonal wind at 10 hPa (≈31 km) and the aerosol load at 30 km altitude in two different ways. Figure 4a is a latitude-time cross section and shows that easterly winds stronger than −30 m/s occur at the same time as maximum aerosol loads. Figure 4b illustrates the time series of the aerosol extinction at 30 km (monthly mean averaged between 5°N and 5°S) and the zonal wind speed at 10 hPa (averaged between 3°N and 3°S). In both figures, a correlation between easterly wind (which has negative sign) and the aerosol extinction is clearly visible.

Finally, the lower aerosol load at 30 km during the last few years (mid-2009–2012) of the SCIAMACHY measurements should be discussed. We explain it as follows. Figure 3a shows that from about April 2008 to February 2010, a relatively long westerly phase in the lower stratosphere occurs. The next westerly phase starts in

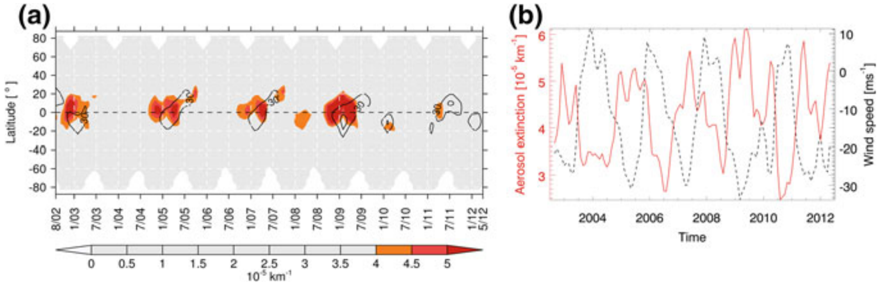

Fig. 4 **a** The same as Fig. 1, but all extinctions lower than 4×10^{-5} km^{-1} are shown in *gray*. The *black contour lines* indicate the ERA-Interim zonal wind lower or equal −30 m/s at a pressure level of 10 hPa. **b** Time series of the zonal monthly mean aerosol extinction at 30 km in *red* and time series of the zonal-mean zonal wind at 10 hPa (≈31 km). Both panels show the correlation between maximum easterly winds and maximum aerosol load at about 30 km altitude

September 2010 and does not end by the end of the time series. Hence, these last two westerly phases are longer than the first three westerly phases of the time series. Furthermore, at pressure levels near 8 hPa, the zonal-mean zonal winds show westerly winds of the semi-annual oscillation (SAO, a dominant variability mode in the mesosphere and upper stratosphere (e.g., Baldwin et al. 2001)), which reach in 2009 and 2011 relatively low altitudes compared with the years 2003–2008. The high aerosol load around January 2009 results from the strong easterly wind around 10 hPa in combination with the wind transition at about 20 hPa. These two features provide optimal conditions for high aerosol loads around 30 km. Shortly afterwards, the wind transition line sinks down to 40–50 hPa and the mentioned SAO westerly winds occur at 8 hPa. The combination of these two features, in contrast, leads to descent around 10–20 hPa, because the SAO induces a westerly shear and thus a reduced aerosol load at 30 km altitude. Almost the same happens in 2011 in addition to a relatively short time slot (Jan–May 2011) for an aerosol increase at 30 km. These observations explain that in 2011 the aerosol layer does not reach the same level of extension as in the years 2003, 2005, 2007, and 2009. Moreover, the delay of the last equatorial aerosol maximum in the sequence of biennially enhanced aerosol extinction results from the mentioned longer westerly phase ending in February 2010.

4 Conclusions

The ten-year SCIAMACHY limb stratospheric aerosol data record provides information about the variability of the global stratospheric aerosol load from the tropopause up to about 33 km with a vertical resolution of about 4 km. The analysis presented in this study is based on gridded aerosol extinction coefficients at 750 nm wavelength of the retrieval version 1.1. We focused on the tropical aerosol distribution at 30 km altitude, which shows variability on a biennial timescale. In agreement with other studies (e.g., Trepte and Hitchman 1992; Baldwin et al. 2001; Choi et al. 2002), this biennial variation was explained by the secondary meridional circulation (SMC) of the quasi-biennial oscillation (QBO). The vertical extension of the aerosol layer is affected by the SMC depending on the wind shear period of the QBO in the stratosphere. In order to demonstrate this, ECMWF ERA-Interim reanalysis data of the zonal-mean zonal wind were used.

We found that the wind speed at 10 hPa is representative for the underlying wind shear period and we showed that it anticorrelates with the aerosol extinction coefficients at 30 km altitude. Furthermore, a delayed and reduced maximum in the aerosol extinction in 2011 was explained by two longer westerly phases during the last four years of the time series in combination with more deeply penetrating westerly winds of the semi-annual oscillation (SAO) that occurs in the mesosphere and upper stratosphere.

Acknowledgments SCIAMACHY is jointly funded by Germany, the Netherlands and Belgium. This work was in part funded by the State and the University of Bremen, the European Space Agency (ESA), and the German Aerospace Agency (DLR). The ERA-Interim reanalysis data were provided by ECMWF. RH is funded by the BMBF through the ROSA project (funding reference code 01LG1212A). CvS was supported by the Ernst-Moritz-Arndt-University of Greifswald. Thanks to Claudia Timmreck from the Max Planck Institute (MPI) Hamburg for helpful discussions.

References

Andrews DG, Holton JR, Leovy CB (1987) Middle atmosphere dynamics. Academic Press, San Diego

Baldwin MP, Gray LJ, Dunkerton TJ, Hamilton K, Haynes PH, Randel WJ, Holton JR, Alexander MJ, Hirota I, Horinouchi T, Jones DBA, Kinnersley JS, Marquardt C, Sato K, Takahashi M (2001) The quasi-biennial oscillation. Rev Geophys 39(2):179–229

Bingen C, Fussen D, Vanhellemont F (2004) A global climatology of stratospheric aerosol size distribution parameters derived from SAGE II data over the period 1984–2000: 1. Methodology and climatological observations. J Geophys Res 109:D06201

Bourassa AE, Degenstein DA, Gattinger RL, Llewellyn EJ (2007) Stratospheric aerosol retrieval with optical spectograph and infrared imaging system limb scatter measurements. J Geophys Res 112:D10217

Bovensmann H, Burrows JP, Buchwitz M, Frerick J, Noël S, Rozanov VV, Chance KV, Goede APH (1999) SCIAMACHY: mission objectives and measurement modes. J Atmos Sci 56 (2):127–150

Burrows JP, Hölzle E, Goede APH, Visser H, Fricke W (1995) SCIAMACHY—scanning imaging absorption spectrometer for atmospheric chartography. Acta Astronaut 35:445–451

Butchart N (2014) The Brewer-Dobson circulation. Rev Geophys 52:157–184. doi:10.1002/2013RG000448

Choi W, Lee H, Grant WB, Park JH, Holton JR, Lee K-M, Naujokat B (2002) On the secondary meridional circulation associated with the quasi-biennial oscillation. Tellus 54B:395–406

Deshler T (2008) A review of global stratospheric aerosol: measurement, importance, life cycle, and local stratospheric aerosol. Atmos Res 90:223–232

Erle F, Grendel A, Perner D, Platt U, Pfeilsticker K (1998) Evidence of heterogeneous bromine chemistry on cold stratospheric sulphate aerosols. Geophys Res Lett 25(23):4329–4332

Ernst F, von Savigny C, Rozanov A, Rozanov V, Eichmann K-U, Brinkhoff LA, Bovensmann H, Burrows JP (2012) Global stratospheric aerosol extinction profile retrievals from SCIAMACHY limb-scatter observations. Atmos Meas Tech Discuss 5:5993–6035

Ernst F (2013) Stratospheric aerosol extinction profil retrievals from SCIAMACHY limb-scatter observations. PhD thesis, University of Bremen, Bremen, p 180

Fussen D, Bingen C (1999) A volcanism dependent model for the extinction profile of stratospheric aerosols in the UV-visible range. Geophys Res Lett 26(6):703–706

Gottwald M, Bovensmann H (2011) SCIAMACHY—exploring the changing Earth's atmosphere. Springer, New York

Hamill P, Jensen EJ, Russell PB, Bauman JJ (1997) The life cycle of stratospheric aerosol particles. Bull Am Meteorol Soc 78(7):1395–1410

Hofmann DJ, Solomon S (1989) Ozone destruction through heterogeneous chemistry following the eruption of el chichón. J Geophys Res 94(D4):5029–5041

Hommel R, Timmreck C, Giorgetta M, Graf H-F (2014) Quasi-biennial oscillation of the tropical stratospheric aerosol layer. Atmos Chem Phys Discuss 14:16243–16290 www.atmos-chem-phys-discuss.net/14/16243/2014/. doi:10.5194/acpd-14-16243-2014

Junge CE, Chagnon CW, Manson JE (1961) Stratospheric aerosols. J Atmos Sci 18(1):81–108

Kawatani Y, Hamilton K (2013) Weakened stratospheric quasibiennial oscillation driven by increased tropical mean upwelling. Nature 497:478–481

Lacis A, Hansen J, Sato M (1992) Climate forcing by stratospheric aerosols. Geophys Res Lett 19 (15):1607–1610

Llewellyn EJ, Lloyd ND, Degenstein DA et al (2004) The OSIRIS instrument on the Odin spacecraft. Can J Phys 82(6):411–422

McCormick MP, Hamill P, Pepin TJ, Chu WP, Swissler TJ, McMaster LR (1979) Satellite studies of the stratospheric aerosol. Am Meteorol Soc 60(9):1038–1046

Randel WJ, Wu F, Swinbank R, Nash J, O'Neill A (1999) Global QBO circulation derived from UKMO stratospheric analyses. J Atmos Sci 56(4):457–474

Ribera P, Peña-Ortiz C, Garcia-Herrera R, Gallego D, Gimeno L, Hernández E (2004) Detection of the secondary meridional circulation associated with the quasi-biennial oscillation. J Geophys Res 109:D18112. doi:10.1029/2003JD004363

Rodgers CD (2000) Inverse methods for atmospheric sounding: theory and practice. World Scientific, Singapore

Rosen JM (1971) The boiling point of stratospheric aerosols. J Appl Meteorol 10(5):1044–1046

Rozanov VV, Rozanov AV, Kokhanovsky AA, Burrows JP (2014) Radiative transfer through terrestrial atmosphere and ocean: software package SCIATRAN. J Quant Spectrosc Radiat Transfer 133:13–71

Solomon S, Daniel JS, Neely RR III, Vernier JP, Dutton EG, Thomason LW (2011) The persistently variable "background" stratospheric aerosol layer and global climate change. Science 333:866–870

Timmreck C, Graf H-F, Lorenz SJ, Niemeier U, Zanchettin D, Matei D, Jungclaus JH, Crowley TJ (2010) Aerosol size confines climate response to volcanic super-eruptions. Geophys Res Lett 37:L24705

Thomason LW, Peter T (2006) SPARC Assessment of Stratospheric Aerosol Particals, World Climate Research Programme (WCRP) SPARC Project Report (4), pp 29–76

Trepte CR, Hitchman MH (1992) Tropical stratospheric circulation deduced from satellite aerosol data. Nature 355:626–628

Valero FPJ, Pilewskie P (1992) Latitudinal survey of spectral optical depths of the Pinatubo volcanic cloud–derived particle sizes, columnar mass loadings, and effects on planetary albedo. Geophys Res Lett 19(2):163–166

Vernier JP, Thomason LW, Pommereau JP, Bourassa A, Pelon J, Garnier A, Hauchecorne A, Blanot L, Trepte C, Degenstein D, Vargas F (2011) Major influence of tropical volcanic eruptions on the stratospheric aerosol layer during the last decade. J Geophys Res 38:L12807

Investigating the Link Between Glyoxal and Biogenic Activities

Leonardo M.A. Alvarado, Andreas Richter, Mihalis Vrekoussis, Folkard Wittrock, Andreas Hilboll, Stefan F. Schreier and John P. Burrows

Abstract Measurements by the Ozone Monitoring Instrument (OMI) on board the Aura satellite have been used to retrieve global maps of glyoxal (CHOCHO) columns by applying the Differential Optical Absorption Spectroscopy (DOAS) method. Large amounts of glyoxal are found over regions with high biogenic emissions and vegetation fires, as well as over highly populated areas with large anthropogenic emissions. This paper focuses on investigating the link between CHOCHO columns and biogenic emissions during 2005–2012. The largest correlations are observed over the Southeastern US and the North of Africa, where large vegetation areas are found. Moreover, negative correlation are found over African regions where large fire events occur.

Keywords Correlation coefficients · VOC · Glyoxal · OMI · DOAS

1 Introduction

Volatile organic compounds (VOC) are emitted from a wide variety of natural and anthropogenic sources, as well as by geochemical processes (Kansal 2009). VOC have significant impacts on atmospheric chemistry and climate change (Vrekoussis et al. 2010; Williams 2004), due to their contribution in the formation of tropospheric ozone (O_3) in combination with nitrogen oxides NO_x (Houweling et al. 1998); they also contribute to the formation of secondary organic aerosols (SOA) (Fu et al. 2008). The biogenic global emissions of VOC exceed the anthropogenic ones with annual releases of about 1,150 $TgCyr^{-1}$ (Guenther et al. 2000).

L.M.A. Alvarado (✉) · A. Richter · F. Wittrock · A. Hilboll · S.F. Schreier · J.P. Burrows
Institute of Environmental Physics, University of Bremen, Bremen, Germany
e-mail: lalvarado@iup.physik.uni-bremen.de

M. Vrekoussis
Energy, Environment and Water Research Center, The Cyprus Institute, Nicosia, Cyprus

G. Lohmann et al. (eds.), *Towards an Interdisciplinary Approach in Earth System Science*, Springer Earth System Sciences,
DOI 10.1007/978-3-319-13865-7_7

Nevertheless, the uncertainties in total emissions are large due to their dependence on several parameters, including condition and species of plants, humidity, and also temperature (Guenther et al. 2000). Anthropogenic emissions are around 10 times lower globally than biogenic emissions, while 50 $TgCyr^{-1}$ are emitted from pyrogenic sources, however the uncertainties of estimation are high (Stavrakou et al. 2009b). In the last years, interest in the large variability of VOC fluxes into the atmosphere led to investigation of the spatial and temporal distribution of molecules such as formaldehyde (HCHO) and CHOCHO, because these are intermediate products in the oxidation of most VOC. Moreover, CHOCHO is an indicator of secondary aerosol formation (Fu et al. 2008; Sinreich et al. 2007; Vrekoussis et al. 2009) and has a short lifetime in the atmosphere, caused by photolysis (Tadi et al. 2006), and oxidation mechanisms in the presence of hydroxyl radicals (Setokuchi 2011). Additionally, wet and dry deposition are sinks of CHOCHO in the atmosphere (Fu et al. 2008). In recent years, a number of retrievals of global distribution of CHOCHO from satellite measurements has been reported including the SCanning Imaging spectroMeter Atmospheric CHartographY (Bovensmann et al. 1999; Burrows et al. 1995), the second Global Ozone Monitoring Experiment (GOME-2) (Callies et al. 2000), and OMI (Levelt et al. 2006) by using the DOAS method in the visible spectral region (Alvarado et al. 2014; Kurosu et al. 2007; Lerot et al. 2010; Chan Miller et al. 2014; Vrekoussis et al. 2009; Vrekoussis et al. 2010; Wittrock et al. 2006). In these studies, the largest amounts of CHOCHO were observed over tropical and sub-tropical regions with a large spatial and temporal variability, mainly as result of vegetation and fire emissions.

In this study, a short description of the CHOCHO retrieval approach applied to OMI measurements, as well as an investigation of the link between glyoxal and biogenic emissions during 2005–2012 are presented.

2 Glyoxal Retrieval

DOAS is frequently applied for the remote sensing of trace gases concentrations in the troposphere and stratosphere. This technique allows the determination of amounts of trace gases with narrow absorption bands in the ultraviolet and visible spectral range. DOAS is based on the Beer-Lambert law in the atmosphere by analyses the intensity of absorption bands (Platt and Stutz 2008),

$$\begin{aligned}\frac{I(\lambda)}{I_0(\lambda)} = \exp\Bigg[-\int ds\Bigg(\sum_i \rho_i(s)\sigma_i(\lambda,s) + \rho_{Ray}(s)\sigma_{Ray}(\lambda,s) \\ +\rho_{Mie}(s)\sigma_{Mie}(\lambda,s) + \rho_{Ring}(s)\sigma_{Ring}(\lambda,s)\Bigg)\Bigg]\end{aligned} \tag{1}$$

where $I_0(\lambda)$ represents the initial intensity (extra-terrestrial solar spectrum), $I(\lambda)$ the intensity after passing through the atmosphere, λ the wavelength, $\rho_{i,Ray,Mie,Ring}(s)$ are the number density of the absorbers and the scattering molecules and particles, s the light path, and $\sigma_{i,Ray,Mie,Ring}(\lambda)$ are the absorption and scattering cross sections, which are specific to each species. The so-called Ring effect is related to rotational Raman scattering on air molecules, this produce wavelength shifts in the ultraviolet and visible comparable to the width of Fraunhofer lines, which result in an apparent filling-in of the Fraunhofer lines. In Eq. 1 and not taking into account any dependence of the cross sections on distance (ds), we can exchange the integral with the sum and define the slant column (SC) as, $S_i = \int \rho_i(s)ds$. The cross section can be decomposed now into a component that varies “slowly” with wavelength, σ_i^0, and another component, σ_i', that shows a “fast” variation with wavelength $\left(\sigma_i = \sigma_i' + \sigma_i^0\right)$. The rapidly varying part σ_i' is representative of narrow bands in the absorption of trace gases, while σ_i^0 includes low frequency variations of the spectrum. The latter together with the Rayleigh scattering $\left(\sigma_{Ray} \sim \lambda^{-4}\right)$, and Mie scattering $\left(\sigma_{Mie} \sim \lambda^{-k}, 0 \leq k \leq 2\right)$ can be substituted by a low-order polynomial. With these considerations we obtain, $I(\lambda) = I_0(\lambda)\exp\left[-\sum_i \sigma_i'(\lambda)S_i - \sum_p a_p\lambda^p\right]$. If $I(\lambda)$, $I_0(\lambda)$, and the absorption cross sections σ_i are known, the slant columns density, S_i, can be determined by a linear least-squares method. As slant column depends on observation geometry, the vertical column (VC) is computed which is related with the SC by the air mass factor (AMF). The AMF depends on different parameters such as the priory trace gas profile, temperature, air pressure, surface albedo, aerosol and ozone profiles, and clouds, as well as solar zenith angle.

In this work, CHOCHO SCs have been retrieved from OMI measurements and converted to VCs using AMFs computed by the radiative transfer model SCIATRAN (Rozanov et al. 2005) and assuming typical glyoxal profiles as used in (Wittrock 2006). Briefly, OMI is a nadir viewing spectrometer providing the spectral coverage and resolution needed for DOAS retrievals of atmospherics trace gases. The instrument measures the light scattered by the atmosphere and surface in the ultraviolet and visible range. The spatial resolution of OMI is 13 km × 24 km at nadir. The Aura satellite has an equator crossing time of 13:45 LT (ascending node), and global coverage by OMI is achieved in 1 day (Levelt et al. 2006).

CHOCHO is retrieved in the spectral window between 433 and 458 nm and a polynomial of third order for removal of broad band signatures is used (Alvarado et al. 2014). Interfering species such as O_3 (Bogumil et al. 2003), NO_2 (220 and 294 K) (Vandaele et al. 1998), O_4 (Thalman and Volkamer 2013), water vapour (Rothman et al. 2005), and liquid water (Pope and Fry 1997) also absorb in the CHOCHO fitting window and are therefore included in the fit. Moreover, a synthetic ring spectrum (Vountas et al. 1998) accounting for the effect of rotational Raman scattering in the atmosphere is included in the retrieval.

3 Results and Discussion

It is well known that one of main source of trace gases into the atmosphere are biogenic emissions. The global maps of glyoxal show that high values are found over regions such as south America, continental Africa, and south of Asia and, to lesser extend, southeastern US, which correspond to areas with dense vegetation (see Fig. 1). Around 55 % of global glyoxal amounts released to the atmosphere results from the oxidation of biogenic VOC, where isoprene oxidation is responsible of 90 %, while the remaining sources are ethane and monoterpenes (Stavrakou et al. 2009a).

In order to investigate the link between glyoxal and biogenic activities, temporal and spatial correlation coefficients between CHOCHO and enhanced vegetation index (EVI) are computed, where EVI represents a measure of vegetation greenness, a composite property of leaf chlorophyll, and canopy cover, which can be retrieved from the MODerate resolution Imaging Spectroradiometers (MODIS) on board NASAs Aqua satellite (Justice et al. 2002). Assuming a linear relationship between CHOCHO VCs and EVI, monthly mean values of OMI CHOCHO VCs and EVI MODIS with a grid resolution of 1.0° × 1.0° were used in the calculations. Figure 2, top–left, shows a global map of correlation coefficients for the time period 2005–2012. The highest correlations between CHOCHO and EVI were found for two regions (southeastern US and north of Africa), even correlation coefficients larger than 0.8 were found over these areas (see Fig. 2, top–right). Also, time series of spatially averaged monthly means were computed for the two regions and are shown in the Fig. 2 (bottom). The seasonal behaviour of glyoxal and EVI are in a good

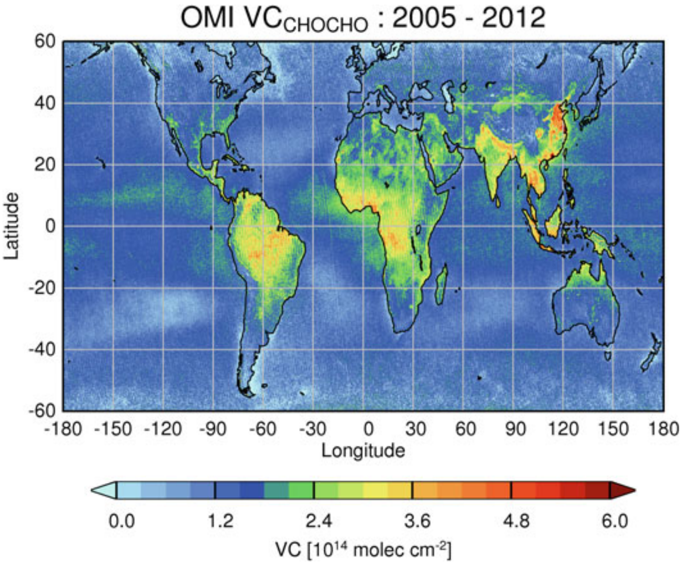

Fig. 1 Global map of CHOCHO VCs retrieved from OMI measurements between 2005 and 2012

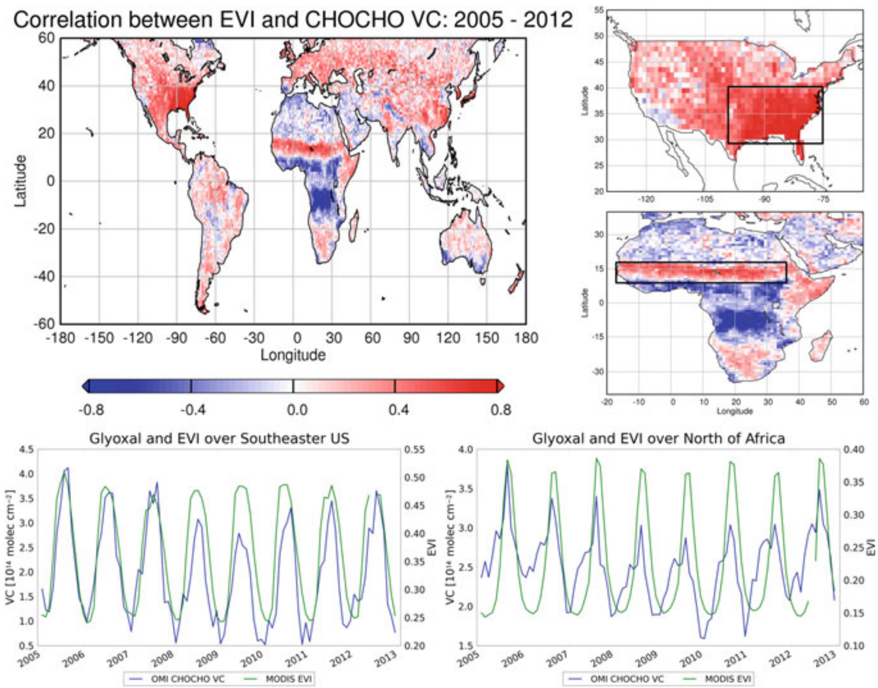

Fig. 2 Pearson coefficient correlation map between CHOCHO VC and EVI over continental regions (*top*) and temporal variation (*bottom*) over two selected regions with high correlation during 2007 and 2012 (Southeastern US and North Africa, *black boxes*)

correspondence for both regions, which leads to the conclusion that the dominant source of glyoxal are the biogenic emissions, this is in a good agreement with the results obtained for one year of analysis of SCIAMACHY CHOCHO VCs and EVI by (Vrekoussis et al. 2009). Moreover, maxima of glyoxal are found in the warm seasons, caused by the increase isoprenes emissions, which also corresponds to the major growth phase of plants. Additionally, negative correlations between CHOCHO VCs and EVI were found over regions in the continental Africa, which are characterized by high pyrogenic emissions as described in Alvarado et al. (2014).

4 Conclusions

We conclude that satellite observations during 8 years allow to infer a strong connection between the CHOCHO amounts in the atmosphere and the biogenic activities. Correlation coefficients between EVI and CHOCHO columns larger than 0.8 have been found over two regions (southeastern US and north Africa), where the computed time series of EVI and glyoxal columns show strong and in-phase seasonal variations. Moreover, the maxima of glyoxal were found during the warm seasons, as consequence of increase in the isoprene emissions. Additionally, strong negative correlation between glyoxal columns and EVI were found over Africa caused by large fires events over these regions, which mainly occur outside the growing season.

Acknowledgments Leonardo Alvarado gratefully acknowledges funding by the German Academic Exchange Service (DAAD). We acknowledge financial support provided by the University of Bremen and the Earth System Science Research School (ESSReS), an initiative of the Helmholtz Association of German Research Centres (HGF) at the Alfred Wegener Institute for Polar and Marine Research (AWI). OMI lv1 and EVI MODIS data have been provided by NASA.

References

Alvarado LMA, Richter A, Vrekoussis M, Wittrock F, Hilboll A, Schreier SF, Burrows JP (2014) An improved glyoxal retrieval from OMI measurements. Atmos Meas Tech 7(12):4133–4150

Bogumil K, Orphal J, Homann T, Voigt S, Spietz P, Fleischmann OC, Vogel A, Hartmann M, Kromminga H, Bovensmann H, Frerick J, Burrows JP (2003) Measurements of molecular absorption spectra with the SCIAMACHY pre-flight model: instrument characterization and reference data for atmospheric remote-sensing in the 2302380 nm region. J Photochem Photobiol A 157(23):167–184

Bovensmann H, Burrows JP, Buchwitz M, Frerick J, Nol S, Rozanov VV, Chance KV, Goede APH (1999) SCIAMACHY: mission objectives and measurement modes. J Atmos Sci 56 (2):127–150

Burrows JP, Hlzle E, Goede APH, Visser H, Fricke W (1995) SCIAMACHY scanning imaging absorption spectrometer for atmospheric chartography. Acta Astronaut 35(7):445–451

Callies J, Corpaccioli E, Eisinger M, Hahne A, Lefebvre A (2000) GOME-2-metop's second-generation sensor for operational ozone monitoring. ESA Bull 102:28–36

Chan Miller C, Abad GG, Wang H, Liu X, Kurosu T, Jacob DJ, Chance K (2014) Glyoxal retrieval from the ozone monitoring instrument. Atmos Meas Tech 7(11):3891–3907

Fu TM, Jacob DJ, Wittrock F, Burrows JP, Vrekoussis M, Henze DK (2008) Global budgets of atmospheric glyoxal and methylglyoxal, and implications for formation of secondary organic aerosols. J Geophys Res Atmos 113(D15303)

Guenther A, Geron C, Pierce T, Lamb B, Harley P, Fall R (2000) Natural emissions of non-methane volatile organic compounds, carbon monoxide, and oxides of nitrogen from North America. Atmos Environ 34(1214):2205–2230

Houweling S, Dentener F, Lelieveld J (1998) The impact of nonmethane hydrocarbon compounds on tropospheric photochemistry. J Geophys Res Atmos 103(D9):10673–10696

Justice CO, Giglio L, Korontzi S, Owens J, Morisette JT, Roy D, Descloitres J, Alleaume S, Petitcolin F, Kaufman Y (2002) The MODIS fire products. Remote Sens Environ 83(12):244–262

Kansal A (2009) Sources and reactivity of NMHCs and VOCs in the atmosphere: a review. J Hazard Mater 166(1):17–26

Kurosu TP, Chance K, Liu X, Volkamer R, Fu TM, Millet D, Jacob DJ (2007) Seasonally resolved global distributions of glyoxal and formaldehyde observed from the ozone monitoring instrument on EOS aura. In Proceeding of Anais XIII Simpsio Brasileiro de Sensoriamento Remoto

Lerot C, Stavrakou T, De Smedt I, Mller J-F, Van Roozendael M (2010) Glyoxal vertical columns from GOME-2 backscattered light measurements and comparisons with a global model. Atmos Chem Phys 10(24):12059–12072

Levelt PF, van den Oord GHJ, Dobber MR, Malkki A, Visser H, de Johan J, Stammes P, Lundell JOV, Saari H (2006) The ozone monitoring instrument. IEEE Trans Geosci Remote Sens 44 (5):1093–1101

Platt U, Stutz J (2008) Differential optical absorption spectroscopy: principles and applications. Springer, Berlin

Pope RM, Fry ES (1997) Absorption spectrum (380–700 nm) of pure water. II. integrating cavity measurements. Appl Opt 36(33):8710–8723

Rothman LS, Jacquemart D, Barbe A, Chris Benner D, Birk M, Brown LR, Carleer MR, Chackerian C Jr, Chance K, Coudert LH, Dana V, Devi VM, Flaud JM, Gamache RR, Goldman A, Hartmann JM, Jucks KW, Maki AG, Mandin JY, Massie ST, Orphal J, Perrin A, Rinsland CP, Smith MAH, Tennyson J, Tolchenov RN, Toth RA, Vander Auwera J, Varanasi P, Wagner G (2005) The HITRAN 2004 molecular spectroscopic database. J Quant Spectrosc Radiat Trans 96(2):139–204

Rozanov A, Rozanov V, Buchwitz M, Kokhanovsky A, Burrows JP (2005) SCIATRAN 2.0 a new radiative transfer model for geophysical applications in the 1752400 nm spectral region. Adv Space Res 36(5):1015–1019

Setokuchi O (2011) Trajectory calculations of OH radical- and cl atom-initiated reaction of glyoxal: atmospheric chemistry of the HC(o)CO radical. Phys Chem Chem Phys 13(13):6296–6304

Sinreich R, Volkamer R, Filsinger F, Frie U, Kern C, Platt U, Sebastin O, Wagner T (2007) MAX-DOAS detection of glyoxal during ICARTT 2004. Atmos Chem Phys 7(5):1293–1303

Stavrakou T, Mller JF, De Smedt I, Van Roozendael M, Kanakidou M, Vrekoussis M, Wittrock F, Richter A, Burrows JP (2009a) The continental source of glyoxal estimated by the synergistic use of spaceborne measurements and inverse modelling. Atmos Chem Phys 9(21):8431–8446

Stavrakou T, Mller JF, De Smedt I, Van Roozendael M, van der Werf GR, Giglio L, Guenther A (2009b) Evaluating the performance of pyrogenic and biogenic emission inventories against one decade of space-based formaldehyde columns. Atmos Chem Phys 9(3):1037–1060

Tadi J, Moortgat GK, Wirtz K (2006) Photolysis of glyoxal in air. J Photochem Photobiol A 177 (23):116–124

Thalman R, Volkamer R (2013) Temperature dependent absorption cross-sections of O_2O_2 collision pairs between 340 and 630 nm and at atmospherically relevant pressure. Phys Chem Chem Phys 15(37):15371–15381

Vandaele AC, Hermans C, Simon PC, Carleer M, Colin R, Fally S, Mrienne MF, Jenouvrier A, Coquart B (1998) Measurements of the NO_2 absorption cross-section from 42,000 cm^{-1} to 10,000 cm^{-1} (238–1000 nm) at 220 K and 294 K. J Quant Spectrosc Radiat Transfer 59 (35):171–184

Vountas M, Rozanov VV, Burrows JP (1998) Ring effect: impact of rotational raman scattering on radiative transfer in earth’s atmosphere. J Quant Spectrosc Radiat Trans 60(6):943–961

Vrekoussis M, Wittrock F, Richter A, Burrows JP (2009) Temporal and spatial variability of glyoxal as observed from space. Atmos Chem Phys 9(13):4485–4504

Vrekoussis M, Wittrock F, Richter A, Burrows JP (2010) GOME-2 observations of oxygenated VOCs: what can we learn from the ratio glyoxal to formaldehyde on a global scale? Atmos Chem Phys 10(21):10145–10160

Williams J (2004) Organic trace gases in the atmosphere: an overview. Environ Chem 1 (3):125–136

Wittrock F (2006) The retrieval of oxygenated volatile organic compounds by remote sensing techniques. PhD thesis, University of Bremen, Bremen

Wittrock F, Richter A, Oetjen H, Burrows JP, Kanakidou M, Myriokefalitakis S, Volkamer R, Beirle S, Platt U, Wagner T (2006) Simultaneous global observations of glyoxal and formaldehyde from space. Geophys Res Lett 33(L16804)

Estimates of NO_x Emission Factors from GOME-2 Measurements for the Major Types of Open Biomass Burning

Stefan F. Schreier, Andreas Richter and John P. Burrows

Abstract Vegetation fires across the globe, either started by lightning strikes or caused by humans, have various impacts on Earth systems such as the atmosphere and biosphere. A simple statistical approach to estimate emission factors (EFs) of NO_x, based on the empirical relationship between satellite-observed tropospheric NO_2 vertical columns (TVC NO_2) and fire radiative power (FRP), is presented. The great advantage of the method is the partitioning of different NO_x emission sources and the application to various biomes and regions. The estimated NO_x EFs are 1.83, 1.48, 2.96, and 0.72 g kg^{-1} for tropical forest, savanna and grassland, crop residue, and boreal forest, respectively. There is overall agreement between the satellite-derived EFs and comparable values reported in the literature, suggesting that the assumptions made in the approach are reasonable. However, a substantial discrepancy is found for savanna and grassland, which is the most frequently burned land cover type on Earth. Possible implications of these differences for fire emission inventories are discussed.

Keywords Satellite measurements · GOME-2 · Nitrogen dioxide · MODIS · Fire radiative power · Emission factors · Biomass burning

1 Introduction

Nitrogen oxides ($NO_x = NO + NO_2$) enter the atmosphere from a large number of natural and anthropogenic processes. Nitric oxide (NO) and nitrogen dioxide (NO_2) are coupled in the atmosphere as NO_2 is photolyzed to produce NO and an oxygen atom (O), which then reacts with molecular oxygen (O_2) to produce ozone (O_3).

S.F. Schreier (✉) · A. Richter · J.P. Burrows
Institute of Environmental Physics, University of Bremen, Bremen, Germany
e-mail: schreier@iup.physik.uni-bremen.de

G. Lohmann et al. (eds.), *Towards an Interdisciplinary Approach in Earth System Science*, Springer Earth System Sciences,
DOI 10.1007/978-3-319-13865-7_8

Major sources of NO_x are attributed to anthropogenic activities (e.g. high temperature combustion processes), biomass burning (intentional and accidental), soil microbial production, and lightning strikes (Lee et al. 1997).

Since the launch of the Global Ozone Monitoring Experiment (GOME) on board ESA's European Remote Sensing (ERS)-2 satellite (Burrows et al. 1999), NO_2 total and tropospheric vertical columns have been retrieved from nadir measurements by applying the Differential Optical Absorption Spectroscopy (DOAS) method, introduced by Perner and Platt (1979). The GOME-2 on board the Meteorological Operational (MetOp) satellites is an improved version of GOME (Callies et al. 2004) and was launched in October 2006 (MetOp-A) and in September 2012 (MetOp-B).

Large vegetation fires, which are known to occur every single month on our planet, emit large amounts of trace species into the atmosphere, among them NO_x. During the combustion process, nitrogen (N) present in the fuel is converted in part into oxides and N present in amino acids is converted to NO. However, NO_x may also result from the reaction of molecular nitrogen (N_2) with O_2 at very high temperatures (Andreae and Merlet 2001).

Fire radiative power (FRP) is a parameter describing the radiant component of energy release from a fire and is quantified in the infrared spectral range (Kaufman et al. 1998). First analyses of satellite-based FRP measurements have indicated clear spatio-temporal differences in the energy radiated by active fires (Wooster and Zhang 2004). Moreover, Wooster et al. (2005) have found proportionality between FRP and the combustion rate, which quantitatively links FRP to dry matter combustion rate.

Emission factors (EFs) of NO_x are used in bottom-up emission inventories for the translation of biomass burned into trace gas emissions (e.g. van der Werf et al. 2010; Kaiser et al. 2012). These parameters have been mainly derived from laboratory-controlled combustion experiments and field measurements (Andreae and Merlet 2001; Akagi et al. 2011).

Recently, satellite measurements of NO_2 have been used for the evaluation of fire emission rates (FERs) and EFs of NO_x for different biomes and regions (Mebust and Cohen 2013; Castellanos et al. 2014; Schreier et al. 2014a, b). These studies provide an important complementary collection of EFs for the community.

In this study, the satellite-based estimation of FERs and EFs of NO_x is demonstrated in a summarized form and EFs of NO_x as obtained from GOME-2 measurements are presented for the major land cover types burned.

2 Data and Methods

2.1 Satellite Measurements of TVC NO_2

As in most recent studies, the retrieval of tropospheric NO_2 vertical columns (TVC NO_2) from the GOME-2 measurements is achieved in four steps.

In the first step, the trace gas concentration integrated along the light path (slant column density or SCD) is determined by applying the Differential Optical

Absorption Spectroscopy (DOAS) method, based on Beer-Lambert's law. Here, we use SCDs from an improved NO_2 retrieval for GOME-2 (Richter et al. 2011).

In the second step, the reference sector method (Richter and Burrows 2002) and simulated stratospheric profiles (Hilboll et al. 2013) are used for removing the stratospheric part from the NO_2 SCDs over tropical/subtropical regions and over boreal regions, respectively.

Thirdly, measurements with cloud fraction greater than 0.2 are removed via cloud screening by using the improved version of the Fast REtrieval Scheme for Clouds from the Oxygen A-band (FRESCO+) algorithm (Wang et al. 2008).

Finally, the tropospheric SCDs are converted into TVC NO_2 by applying airmass factors (AMFs), which are derived using the radiative transfer model SCIATRAN (Rozanov et al. 2005) by taking into account the viewing geometry and scattering, absorption, and reflection within the atmosphere and the Earth's surface. Monthly means of TVC NO_2 between 2007 and 2011 (tropical and subtropical regions) and for the period 2007–2012 (boreal regions) are binned to a horizontal resolution of 1 × 1°.

2.2 Satellite Measurements of FRP

Accordingly, monthly data of FRP (Kaufman et al. 1998) from the MODIS instrument on board Terra have been downloaded at a horizontal resolution of 1 × 1° and for the given time period from ftp://neespi.gsfc.nasa.gov/data/s4pa/Fire/.

2.3 Land Cover Type Product

The Collection 5 MODIS Global Land Cover Type product (Friedl et al. 2010), which has been spatially aggregated to a 1° × 1° resolution applying a majority filter, is used for the definition of biomes evaluated in this study.

2.4 Production Rate of NO_x from Fire

The retrieved TVC NO_2 is converted into the production rate of NO_x from fire (P_f) by assuming that the background level of TVC NO_2 has no seasonal variation. A further assumption made in the approach is the constant value for the NO_x lifetime (6 h) following the findings of Beirle et al. (2011). While the NO_2/NO_x ratio is held constant (0.75) for the tropical and subtropical regions (Alvarado and Prinn 2009), it is derived from the MACC reanalysis data set of atmospheric composition (Inness et al. 2013) for the boreal regions. As the scientific community is interested in the production rate of NO_x rather than the number density of NO_2 molecules in the vertical column, we compute P_f as shown in the following equations:

$$\mathrm{TVC}_f[\mathrm{NO_2}] = \mathrm{TVC}[\mathrm{NO_2}] - \mathrm{TVC}_b[\mathrm{NO_2}]$$

Here, TVC_f NO_2 is the number density of NO_2 molecules produced by fires (in molecules cm^{-2}) as obtained from the subtraction of TVC_b NO_2 (y-intercepts or background NO_2) from TVC NO_2. The y-intercepts have been obtained from a linear regression analysis of the gridded monthly means of TVC NO_2 and FRP.

$$P_f = \frac{TVC_f[\mathrm{NO_2}] * M\left(1 + \frac{\mathrm{NO}}{\mathrm{NO_2}}\right)A_p}{N_A * \tau}$$

The term 1 + NO/NO_2 accounts for the above stated ratio (without units), M is the molar mass of NO (in g mol^{-1}) and A_p is the respective pixel area (in cm^2). N_A denotes Avogadro's number (in molecules mol^{-1}) and τ is the assumed lifetime of NO_x (in seconds). According to the described conversion of TVC NO_2, the FRP values have also been multiplied by A_p. Further details about the conversion are given in Schreier et al. (2014a, b).

2.5 *Estimation of NO_x Emission Factors*

In a next step, a linear regression model is used for the computation of gradients between P_f and FRP, here referred to as fire emission rates (FERs) of NO_x, for all pixels with a correlation coefficient between TVC NO_2 and FRP higher than 0.3.

In the final step, the FERs are translated into emission factors (EFs) of NO_x by applying a conversion factor of 0.41 kg MJ^{-1} as suggested by Vermote et al. (2009), following the findings of Wooster et al. (2005).

3 Results and Discussion

The correlation coefficients as obtained from the linear regression between TVC NO_2 and FRP are shown in Fig. 1. The global map is quite revealing in several ways. First, a very strong relationship between the two time series is found for the major biomass burning regions. Hence, the seasonal variation of TVC NO_2 is explained by the seasonal cycle of FRP to a large degree. Second, the empirical relationship forms the basis of the approach to estimate FERs of NO_x as it is a reasonable tool to separate between different NO_x sources. In order to assess NO_x from vegetation fires, the y-intercepts (background NO_2) of the linear regression model (not shown here) have been used for the conversion of TVC NO_2 into P_f as described earlier.

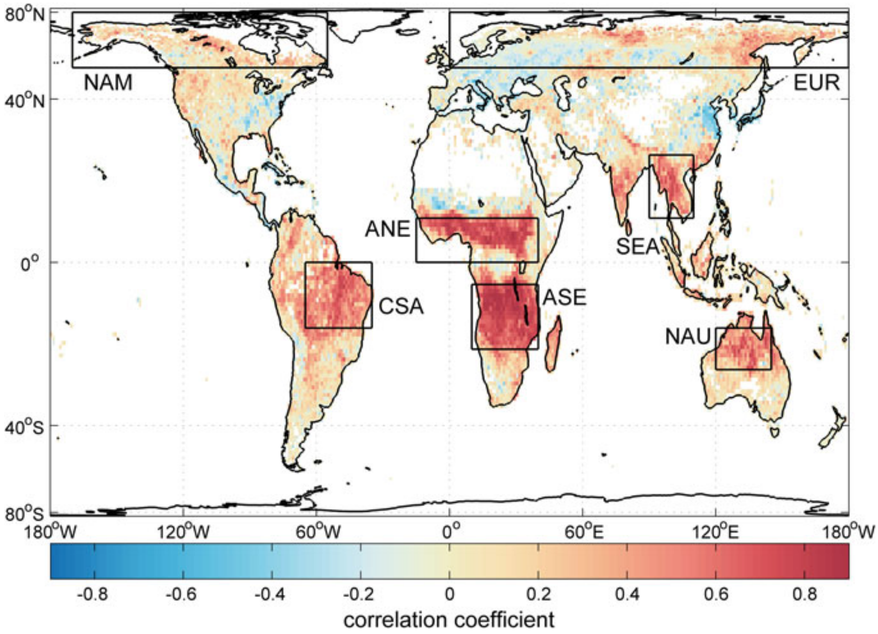

Fig. 1 Correlation coefficients (r) of the temporal relationship between TVC NO_2 and FRP based on monthly averages from 2007–2012 on a 1 × 1° grid. Schreier et al. (2014a) have derived FERs of NO_x for the tropical and subtropical regions ANE, Africa south of Equator (ASE), central South America (CSA), northern Australia (NAU), and southeast Asia (SEA). The boreal regions Eurasia (EUR) and North America (NAM) were the focus of Schreier et al. (2014b)

The evaluation of FERs of NO_x has been carried out for five tropical and subtropical and two boreal regions (see Fig. 1) as well as for eight different land cover types as defined by the UMD classification scheme (see Schreier et al. 2014a, b).

In Fig. 2, typical fits of the linear regression are shown for different types of open biomass burning within Africa north of Equator (ANE).

The calculated FERs of NO_x for the other selected biomes and regions are reported in Schreier et al. (2014a, b) and possible uncertainties are discussed in detail.

In order to make the satellite-derived EFs comparable to the values reported in the emission factor compilations by Andreae and Merlet (2001) and Akagi et al. (2011), the EFs of NO_x are derived for tropical forest (evergreen broadleaf forest), savanna and grassland (open shrublands, woody savannas, and savannas), crop residue (croplands), and boreal forest (evergreen needleleaf forest, deciduous needleleaf forest, mixed forest, and woody savannas).

Figure 3 provides the arithmetic means of EFs as obtained from satellite data as well as arithmetic means of EFs reported by Andreae and Merlet (2001) and Akagi et al. (2011). While the error bars denote one standard deviation of the arithmetic mean in the two latter studies, they indicate the minimum and maximum values obtained for the different regions as highlighted in Fig. 1. The satellite-based EFs of

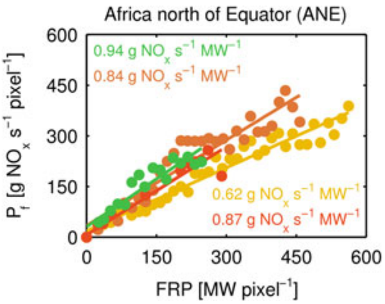

Fig. 2 Best fitting least-squares regression lines for evergreen broadleaf forest (*light green*), woody savannas (*orange*), savannas (*yellow*), and croplands (*red*) within Africa north of Equator (ANE)

NO_x are estimated at 1.83, 1.48, 2.96, and 0.72 g kg^{-1} for tropical forest, savanna and grassland, crop residue, and boreal forest, respectively.

From the data in Fig. 3 it is apparent that the arithmetic means of satellite-based EFs for tropical forest, crop residue, and boreal forest fall within one standard deviation of means reported by Andreae and Merlet (2001) and/or Akagi et al. (2011). However, the EFs for savanna and grassland obtained in this study are lower by a factor of 2.5 when compared to the other two values. A possible explanation for this might be the seasonal cycle in NO_x emissions rates (Mebust and Cohen 2013). It is possible that the fuel for laboratory-controlled combustion experiments has been mainly taken during that part of the fire season, where the highest emission rates are expected. In contrast, the satellite-derived EFs are based on the entire fire season, and thus, represent rather average values.

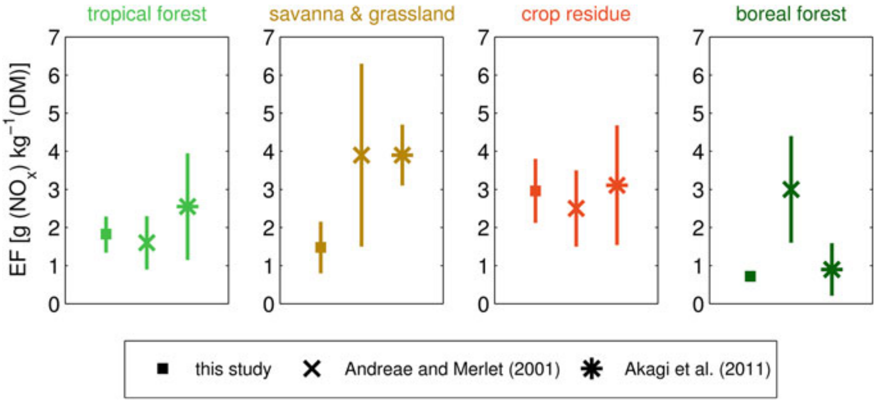

Fig. 3 Emission factors (EFs) of NO_x (g kg^{-1}) for tropical forest (*light green*), savanna and grassland (*ochre*), crop residue (*red*), and boreal forest (*dark green*). Satellite-based EFs are represented by *squares*, reported values from Andreae and Merlet (2001) are indicated by *a cross*, and the *asterisk* denotes EFs from Akagi et al. (2011)

One of the issues that emerge from these findings is that recent fire emission inventories might have overestimated NO_x emissions from savanna and grassland fires by a factor of 2.5.

We note that the results obtained in this study might be affected by errors in the satellite-based retrieval of TVC NO_2 and FRP as well as in the few assumptions made. A detailed discussion on the possible errors can be found in Schreier et al. (2014a, b).

4 Conclusions and Outlook

A simple statistical approach has been developed to estimate fire emission rates (FERs) and emission factors (EFs) of NO_x from fires using the strong correlation between satellite-derived parameters tropospheric NO_2 vertical column (TVC NO_2) and fire radiative power (FRP). After the conversion of TVC NO_2 into production rates of NO_x from fire (P_f), slopes of the linear regression between P_f and FRP, here referred to as FERs of NO_x, have been derived for different biomes and regions. The subsequent conversion of FERs into EFs of NO_x is based on the quantitative link between FRP and dry matter combustion rate.

The EFs of NO_x are estimated at 1.83, 1.48, 2.96, and 0.72 g kg^{-1} for tropical forest, savanna and grassland, crop residue, and boreal forest, respectively. The EFs presented here fall within one standard deviation of the mean EFs as reported by Andreae and Merlet (2001) and/or Akagi et al. (2011). While there is overall agreement between the EFs and the comparable values presented in the literature for tropical forest, crop residue, and boreal forest, we found substantial differences for savanna and grassland.

Consequently, recent fire emission inventories could have overestimated NO_x emissions from savanna and grassland fires by a factor of 2.5. As savanna and grassland is one of the major land cover types burned on Earth, this would have a significant effect on the estimation of open biomass burning emissions of NO_x on the global scale.

Further work needs to be done to establish whether other satellite sensors (e.g. SCIAMACHY and SEVIRI) reveal similar results as those reported here for GOME-2 and MODIS on board Terra.

References

Akagi SK, Yokelson RJ, Wiedinmyer C, Alvarado MJ, Reid JS, Karl T, Crounse JD, Wennberg PO (2011) Emission factors for open and domestic biomass burning for use in atmospheric models. Atmos Chem Phys 11:4039–4072

Alvarado MJ, Prinn RG (2009) Formation of ozone and growth of aerosols in young smoke plumes from biomass burning: 1. Lagrangian parcel studies. J Geophys Res Atmos 114

Andreae MO, Merlet P (2001) Emission of trace gases and aerosols from biomass burning. Glob Biogeochem Cycles 15:955–966

Beirle S, Boersma KF, Platt U, Lawrence MG, Wagner T (2011) Megacity emissions and lifetimes of nitrogen oxides probed from space. Science 333:1737–1739

Burrows JP, Weber M, Buchwitz M, Rozanov VV, Ladstaetter-Weissenmayer A, Richter A, DeBeek R, Hoogen R, Bramstedt K, Eichmann KU, Eisinger M (1999) The global ozone monitoring experiment (GOME): mission concept and first scientific results. J Atmos Sci 56:151–175

Callies J, Corpaccioli E, Eisinger M, Lefebvre A, Munro R, Perez-Albinana A, Ricciarelli B, Calamai L, Gironi G, Veratti R, Otter G, Eschen M, Van Riel L (2004) GOME-2 ozone instrument on-board the European METOP satellites. Weather and Environemental Satellites. In: Proceedings of SPIE—The International Society for Optical Engineering, Denver, CO, pp 60–70

Castellanos P, Boersma KF, van der Werf GR (2014) Satellite observations indicate substantial spatiotemporal variability in biomass burning NO_x emission factors for South America. Atmos Chem Phys 14:3929–3943

Friedl MA, Sulla-Menashe D, Tan B, Schneider A, Ramankutty N, Sibley A, Huang X (2010) MODIS collection 5 global land cover: algorithm refinements and characterization of new datasets. Remote Sens Environ 114:168–182

Hilboll A, Richter A, Rozanov A, Hodnebrog Ø, Heckel A, Solberg S, Stordal F, Burrows JP (2013) Improvements to the retrieval of tropospheric NO_2 from satellite—stratospheric correction using SCIAMACHY limb/nadir matching and comparison to Oslo CTM2 simulations. Atmos Measur Tech 6:565–584

Inness A, Baier F, Benedetti A, Bouarar I, Chabrillat S, Clark H, Clerbaux C, Coheur P, Engelen RJ, Errera Q, Flemming J, George M, Granier C, Hadji-Lazaro J, Huijnen V, Hurtmans D, Jones L, Kaiser JW, Kapsomenakis J, Lefever K, Leitão J, Razinger M, Richter A, Schultz MG, Simmons AJ, Suttie M, Stein O, Thépaut J-N, Thouret V, Vrekoussis M, Zerefos C (2013) The MACC reanalysis: an 8 yr data set of atmospheric composition. Atmos Chem Phys 13:4073–4109

Kaiser JW, Heil A, Andreae MO, Benedetti A, Chubarova N, Jones L, Morcrette JJ, Razinger M, Schultz MG, Suttie M, Van Der Werf GR (2012) Biomass burning emissions estimated with a global fire assimilation system based on observed fire radiative power. Biogeosciences 9:527–554

Kaufman YJ, Justice CO, Flynn LP, Kendall JD, Prins EM, Giglio L, Ward DE, Menzel WP, Setzer AW (1998) Potential global fire monitoring from EOS-MODIS. J Geophys Res D: Atmos 103:32215–32238

Lee DS, Köhler I, Grobler E, Rohrer F, Sausen R, Gallardo-Klenner L, Olivier JGJ, Dentener FJ, Bouwman AF (1997) Estimations of global NO(x) emissions and their uncertainties. Atmos Environ 31:1735–1749

Mebust AK, Cohen RC (2013) Observations of a seasonal cycle in NO_x emissions from fires in African woody savannas. Geophys Res Lett 40:1451–1455

Perner D, Platt U (1979) Detection of nitrous acid in the atmosphere by differential optical absorption. Geophys Res Lett 93:917–920

Richter A, Burrows JP (2002) Tropospheric NO_2 from GOME measurements. Adv Space Res 29:1673–1683

Richter A, Begoin M, Hilboll A, Burrows JP (2011) An improved NO_2 retrieval for the GOME-2 satellite instrument. Atmos Meas Tech 4:1147–1159

Rozanov A, Rozanov VV, Buchwitz M, Kokhanovsky A, Burrows JP (2005) SCIATRAN 2.0—a new radiative transfer model for geophysical applications in the 175–2,400 nm spectral region. Adv Space Res 36:1015–1019

Schreier SF, Richter A, Kaiser JW, Burrows JP (2014a) The empirical relationship between satellite-derived tropospheric NO_2 and fire radiative power and possible implications for fire emission rates of NO_x. Atmos Chem Phys 14:2447–2466

Schreier SF, Richter A, Schepaschenko D, Shvidenko A, Hilboll A, Burrows JP (2014b) Differences in satellite-derived NO_x emission factors between Eurasian and North American boreal forest fires. Atmos Environ. doi: 10.1016/j.atmosenv.2014.08.071

Van Der Werf GR, Randerson JT, Giglio L, Collatz GJ, Mu M, Kasibhatla PS, Morton DC, Defries RS, Jin Y, Van Leeuwen TT (2010) Global fire emissions and the contribution of deforestation, savanna, forest, agricultural, and peat fires (1997-2009). Atmos Chem Phys 10:11707–11735

Vermote E, Ellicott E, Dubovik O, Lapyonok T, Chin M, Giglio L, Roberts GJ (2009) An approach to estimate global biomass burning emissions of organic and black carbon from MODIS fire radiative power. J Geophys Res D: Atmos 114

Wang P, Stammes P, van der AR, Pinardi G, van Roozendael M (2008) FRESCO+: an improved O_2 A-band cloud retrieval algorithm for tropospheric trace gas retrievals. Atmos Chem Phys 8:6565–6576

Wooster MJ, Zhang YH (2004) Boreal forest fires burn less intensely in Russia than in North America. Geophys Res Lett 31:20501–20503

Wooster MJ, Roberts G, Perry GLW, Kaufman YJ (2005) Retrieval of biomass combustion rates and totals from fire radiative power observations: FRP derivation and calibration relationships between biomass consumption and fire radiative energy release. J Geophys Res D: Atmos 110:1–24

The Use of FTIR-Spectrometry in Combination with Different Biosphere-Atmosphere Flux Measurement Techniques

Hella van Asperen, Thorsten Warneke and Justus Notholt

Abstract Qualitative biosphere-atmosphere flux measurements are of great importance for future climate predictions. Multiple flux measurement techniques exist, all having its own advantages and disadvantages. We present a method wherein FTIR-spectrometry is connected to a flux gradient system and to flux chambers, which enables us to study different (greenhouse) gases and different ecosystem scales simultaneously. The method was tested in a peatland in Northern Germany (Himmelmoor, Quickborn). The application of the method, detection limits and first results are presented and the application of the method is evaluated. The results showed that the different techniques capture different ecosystem processes, therefore complementing each other. We believe that the developed method could be valuable for field campaigns and can help further improve our understanding of biosphere-atmosphere gas exchange dynamics.

Keywords FTIR-spectrometry · Biosphere-atmosphere gas exchange · Field measurements · Flux measurement techniques · Carbon dioxide

1 Introduction

The understanding of the greenhouse gas fluxes and their response to a changing climate is vital for future climate predictions. Greenhouse gas fluxes between the biosphere and atmosphere can be obtained via a top-down approach, modeling the exchange based on spatial and temporal concentration-variation in the atmosphere, and by a bottom-up approach, the upscaling of flux estimates, e.g. from field measurements of biosphere-atmosphere gas exchange. Field measurements are of

---

H. van Asperen (✉) · T. Warneke · J. Notholt
Institute of Environmental Physics, University of Bremen, Bremen, Germany
e-mail: v_asperen@iup.physik.uni-bremen.de

G. Lohmann et al. (eds.), *Towards an Interdisciplinary Approach in Earth System Science*, Springer Earth System Sciences,
DOI 10.1007/978-3-319-13865-7_9

great importance; they provide the opportunity to study greenhouse gas dynamics and its (feedback) mechanics in detail. In the following the most important methods for quantifying biosphere-atmosphere gas fluxes will be described.

Micrometeorological techniques, such as the Eddy Covariance (EC) technique, use the covariance between the vertical air velocity and concentration of an entity to calculate the flux of this entity. For EC-measurements, fast (10 Hz) wind and concentration measurements are required. Fast analyzers for CO_2 and H_2O are worldwide available and recent technology developments resulted in fast analyzers for other gases, such as CH_4 and N_2O. However, due to usual low CH_4- and N_2O- concentrations and -exchange, high quality EC-measurements for these gases are difficult (McDermitt et al. 2011; Zona et al. 2013). In contrast, accumulation techniques are suitable for measurement of minor fluxes (Griffith and Galle 2000). An example is the flux gradient method, which was used in this study.

Flux chamber techniques are based on the principle of sealing an area by placing a ‘chamber’ on top. Fluxes are derived from the change in gas concentration in the chamber headspace. Flux chamber designs vary and have been evaluated extensively (Pumpanen et al. 2004). In our study, a dynamic flux chamber system is used. In Table 1, the advantages (underlined) and disadvantages of micrometeorological and flux chamber methods are summarized.

Both methods can complement each other; therefore systems combining different flux measurement methods are recommended (Myklebust et al. 2008; Sturm et al. 2012). In this paper, a setup is described in which a Fourier Transform Infrared Spectrometer (FTIR) is connected to two flux measurement techniques which enables the measurement of different (greenhouse) gas emissions simultaneously, frequently and continuously.

Table 1 Advantages (*underlined*) and disadvantages of the micrometeorological and flux chamber methods (Burba and Anderson 2005; Foken and Nappo 2008; Myklebust et al. 2008)

	Micrometeorological methods	Flux chamber methods
Terrain and conditions	Difficult in hilly terrain	Possible in all terrains
	Specific atmospheric conditions required	Possible in all weather conditions
	Less suitable for low fluxes	Suitable for low fluxes
Deployment	Technical knowledge required	Easy in use
	Not labor intensive	Labor intensive
Results and representativeness	Demanding data processing	High precision
	Large footprint	Small footprint
	Suitable for frequent long term measurements	Potentially influences fluxes in measured area

2 Experimental Setup

We used a newly developed spectroscopic technique, and applied it for two flux measurement methods. In the following the setup is described in some detail. The analyzer used in this study is a FTIR-spectrometer, being able to measure CO_2, CH_4, N_2O, CO and $\delta^{13}CO_2$ [for details, see Griffith et al. (2012)]. We designed an external manifold box, which allowed us to connect the FTIR to a flux gradient setup and to 2 flux chambers simultaneously (Fig. 1). The designed setup was tested in peatland Himmelmoor (Quickborn, Germany).

2.1 The Flux Gradient Technique

The flux gradient technique concept is based on the relationship between the gas flux and the atmospheric concentration gradient (Griffith and Galle 2000). Fluxes can be calculated by:

$$F = K\frac{\delta c}{\delta z} \tag{1}$$

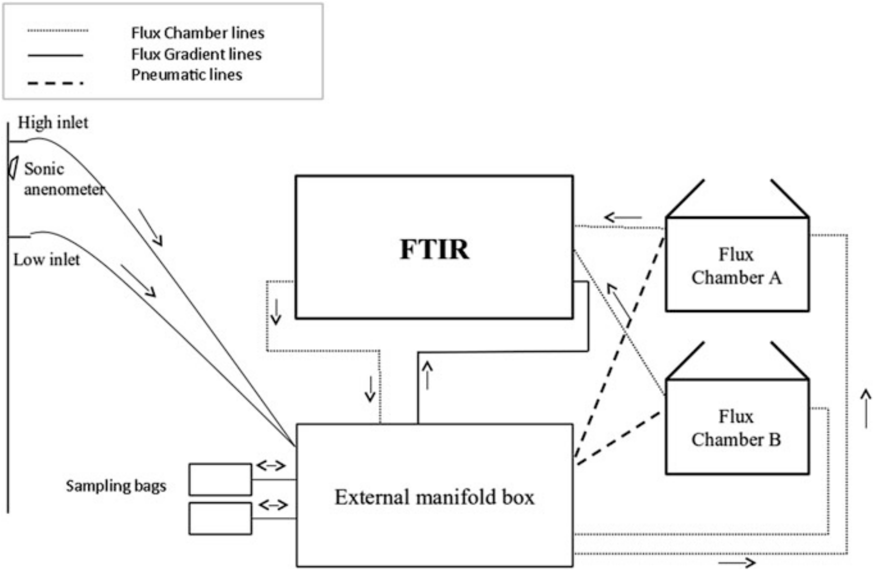

Fig. 1 Schematic figure of the used setup, combining two flux measurement techniques

Table 2 Estimated minimum detectable fluxes based on instrument precision (for flux gradient, diffusion coefficient = 0.1 $m^2\ s^{-1}\ m^{-1}$, $\delta z = 1.5$ m, spectra time 3 min; for flux chamber, spectra time 2 min)

	FTIR-precision (1σ, 10 min)	Estimated FTIR-precision (1σ) for 3 and 2 min spectra	Minimum detectable flux 'flux gradient method'	Minimum detectable flux 'flux chamber method'
CO_2	0.02 μmol mol^{-1}	0.04 and 0.05 μmol mol^{-1}	0.2 μmol $m^{-2}\ s^{-1}$	0.003 μmol $m^{-2}\ s^{-1}$
			9.7 μg $m^{-2}\ s^{-1}$	0.12 μmol $m^{-2}\ s^{-1}$
CH_4	0.2 nmol mol^{-1}	0.36 and 0.45 nmol mol^{-1}	2.0 nmol $m^{-2}\ s^{-1}$	0.09 nmol $m^{-2}\ s^{-1}$
			35.6 ng $m^{-2}\ s^{-1}$	1.3 ng $m^{-2}\ s^{-1}$
CO	0.2 nmol mol^{-1}	0.36 and 0.45 nmol mol^{-1}	2.2 nmol $m^{-2}\ s^{-1}$	0.3 nmol $m^{-2}\ s^{-1}$
			62.2 ng $m^{-2}\ s^{-1}$	7.6 ng $m^{-2}\ s^{-1}$
N_2O	0.06 nmol mol^{-1}	0.11 and 0.13 nmol mol^{-1}	0.67 nmol $m^{-2}\ s^{-1}$	0.02 nmol $m^{-2}\ s^{-1}$
			29.4 ng $m^{-2}\ s^{-1}$	0.02 ng $m^{-2}\ s^{-1}$

where in δC is the difference in concentration of gas x (μmol mol^{-1}) at two fixed different inlet-heights (δz(m)) and K is the diffusion coefficient ($m^2\ s^{-1}$), and F the flux (μmol $m^{-2}\ s^{-1}$). The diffusion coefficient can be parameterized using the data from a sonic anemometer.

Considering the FTIRs concentration detection limits (Table 2), an increased inlet-height difference can give higher concentration differences and decreases the method's detection limits. However, a too high distance between the inlets may lead to a different footprint per inlet (e.g. measuring distinctive types of soil, ecosystems or environmental conditions). Also, the lower inlet position should be higher than nearby vegetation or other disturbances. The sonic anemometer should be placed between the 2 inlets (Baldocchi 2003).

Air sampling was done continuously. For 30 min per hour, the airflows were directed to air sampling bags, after that the bag inlet was closed until analysis. Before analysis, the measurement-cell was evacuated. Afterwards, the cell and sample lines were flushed with sample air to avoid contamination. For each air sample, a 3 min-spectrum was taken.

2.2 The Flux Chamber Technique

Six soil collars (50 cm × 50 cm) were inserted up to 10 cm depth a week before the start of the experiment. Positions for soil collars were selected to be undisturbed and representative. Two transparent flux chambers (50 cm × 50 cm × 50 cm) were switched between collars every few days to avoid major environmental disturbance. The flux chambers (open dynamic chambers) were tightened by use of clamps and rubber air strips. Two fans per flux chamber were continuously running, ensuring well-mixed headspace air. Automatic chamber closure (once per hour) was made possible by use of a pneumatic system regulated by the valve manifold box. Air flow between the chamber and the FTIR was initiated by a pump placed behind the measurement cell and set to 1 L min^{-1} per minute. The air from the flux chamber was measured every 2 min (2 min-spectra) for 20 min. The flux chamber closed and opened after respectively 4 and 18 min. Gas fluxes were calculated by:

$$F = \frac{VP}{RST}\frac{\delta C}{\delta z} \tag{2}$$

wherein V is the volume of the chamber (m^3), P the chamber air pressure (Pa), R the gas constant (8.314 $\text{m}^3\,\text{Pa}\,\text{K}^{-1}\text{mol}^{-1}$), S the soil area ($\text{m}^2$), T the chamber air temperature (K) and $\delta C/\delta t$ is the gas concentration change over time ($\mu\text{mol mol}^{-1}\,\text{s}^{-1}$).

3 Flux Gradient- and Flux Chamber Measurements

The FTIR measurement precisions for 10-minute average values are given in Table 2 (Griffith and Galle 2000). Precisions for spectra with shorter averaging times are estimated (Table 2). Measurement of greenhouse gas fluxes by flux chambers, as well as by the flux gradient, are based on concentration differences, where an eventual instrumental drift plays a minor role. For reliable flux gradient measurements, a minimum concentration difference of 2σ is needed. Typical diffusion coefficient values under unstable conditions (Obhukov-length < 0) range between 0.1 and 0.4 $\text{m}^2\text{s}^{-1}\text{m}^{-1}$ (Foken and Nappo 2008). For reliable flux chamber measurements, also a minimum difference of 2σ between measurements is required. Minimum detectable fluxes for the flux gradient technique (3 min-spectra) and for the flux chamber technique (2 min-spectra) are given in Table 2. Increasing the time per spectrum decreases the required minimum concentration difference and could be considered in small magnitude flux-ecosystems.

Flux chambers can disturb fluxes during chamber closure, due to altering the concentration gradient and the air pressure (Hutchinson and Livingston 2002; Pumpanen et al. 2004). To minimize these effects, tall, well mixed chambers were chosen. During data evaluation, concentration increase was checked for logarithmic behavior and only linear regression fits with $R^2 > 0.9$ were used.

From August to November 2012, the setup (a flux gradient system and two flux chambers) was tested in the restored peatland Himmelmoor (Quickborn, Germany). The flux chambers were placed on a dry position in the wetland, but later in the experiment were moved to a wet location. The flux gradient system overlooked an area with mostly wet locations. In Fig. 2, hourly CO_2-fluxes (from flux chamber- and

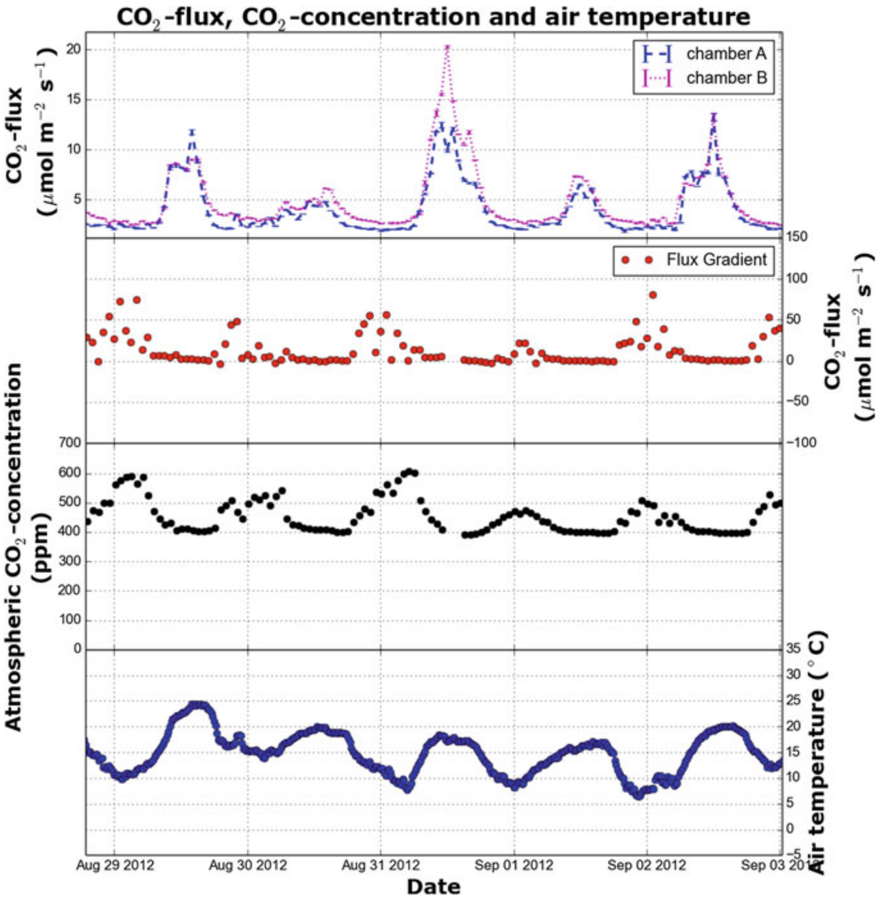

Fig. 2 Flux chamber CO$_2$-fluxes, flux gradient CO$_2$-fluxes, atmospheric CO$_2$-concentration and air temperature over 5 days in Himmelmoor in August and September 2012

flux gradient method), atmospheric CO$_2$-concentrations and air temperatures for 5 days in August and September are shown. The flux chambers (on a dry position in the wetland), being 20 m apart, showed very similar flux quantities and a clear diurnal pattern. The CO$_2$-fluxes, as measured by the flux gradient technique, originated from dry as well as from wet regions. It shows similar quantities to the flux chamber data, but a very different diurnal pattern indicating different (dominating) ecosystem processes in different parts of the wetland, such as photosynthesis, respiration or decomposition. Atmospheric CO$_2$-concentrations showed clear concentration buildup at night, indicating the presence of a nocturnal boundary layer (NBL). Additional NBL-height measurements would make boundary layer budget calculations possible, complementing the flux gradient technique during stable night conditions. Figure 2 also shows a clear diurnal air temperature pattern, which (not shown) correlates well with chamber CO_2-fluxes over the whole measurement period.

4 Discussion and Conclusion

The developed technique consisting of a FTIR connected to a flux measurement technique has multiple advantages. The combination of two different flux methods synchronically provides the opportunity to study different ecosystem processes and scales at the same time. The setup is flexible and easily adapted when research focus is shifted (requirement of higher precision or higher frequency) and can easily be expanded by different concentration or flux measurement techniques such as the boundary layer method or by concentration profile measurements. A possible disadvantage of using an FTIR for field measurements is the high power demand, the costs and the size of the instrument. An advantage of the use of FTIR-spectrometry is the opportunity to study different (greenhouse) gas species simultaneously. Conclusively, the new setup gives the opportunity to study biosphere-atmosphere exchange in detail and its application can improve our understanding of biosphere-atmosphere exchange dynamics.

Acknowledgments We would like to thank the Torfwerke Quickborn and David Holl, Norman Rüggen, Christian Wille and Lars Kutzbach from the university of Hamburg for their help and cooperation during the field campaign in Himmelmoor. Also, we are grateful for the support of the InGOS-project (European Community Seventh Framework Programme (FP7/2007–2013)). Furthermore, we would like to thank the two reviewers for their comments on the subject.

References

Baldocchi DD (2003) Assessing the eddy covariance technique for evaluating carbon dioxide exchange rates of ecosystems: past, present and future. Glob Change Biol 9(4):479–492

Burba G, Anderson D (2005) Introduction to the eddy covariance method: general guidelines and conventional workflow. LI-Cor Bio Sci 141

Foken T, Nappo CJ (2008) Micrometeorology. Springer, New York

Griffith DWT, Galle B (2000) Flux measurements of NH_3, N_2O and CO_2 using dual beam FTIR spectroscopy and the flux-gradient technique. Atmos Environ 34(7):1087–1098

Griffith DWT, Deutscher NM, Caldow C, Kettlewell G, Riggenbach M, Hammer S (2012) A fourier transform infrared trace gas and isotope analyser for atmospheric applications. Atmos Measur Tech 5(10):2481–2498

Hutchinson GL, Livingston GP (2002) 4.5 soil-atmosphere gas exchange. Methods Soil Anal: Part 4 Phys Methods, (methods of soil an4):1159–1182

McDermitt D, Burba G, Xu L, Anderson T, Komissarov A, Riensche B, Schedlbauer J, Starr G, Zona D, Oechel W et al (2011) A new low-power, open-path instrument for measuring methane flux by eddy covariance. Appl Phys B 102(2):391–405

Myklebust MC, Hipps LE, Ryel RJ (2008) Comparison of eddy covariance, chamber, and gradient methods of measuring soil CO_2 efflux in an annual semi-arid grass, *Bromus tectorum*. Agric For Meteorol 148(11):1894–1907

Pumpanen J, Kolari P, Ilvesniemi H, Minkkinen K, Vesala T, Niinistö S, Lohila A, Larmola T, Morero M, Pihlatie M et al (2004) Comparison of different chamber techniques for measuring soil CO_2 efflux. Agric For Meteorol 123(3):159–176

Sturm P, Eugster W, Knohl A (2012) Eddy covariance measurements of CO_2 isotopologues with a quantum cascade laser absorption spectrometer. Agric For Meteorol 152:73–82

Zona D, Janssens IA, Aubinet M, Gioli B, Vicca S, Fichot R, Ceulemans R (2013) Fluxes of the greenhouse gases (CO_2, CH_4 and N_2O) above a short-rotation poplar plantation after conversion from agricultural land. Agric For Meteorol 169:100–110

Near-Infrared Lunar Absorption Spectroscopy for the Retrieval of Column Averaged CO_2 and CH_4

Matthias Buschmann, Nicholas M. Deutscher, Mathias Palm, Thorsten Warneke, Tine Weinzierl and Justus Notholt

Abstract High resolution Fourier-Transform InfraRed (FTIR) absorption spectroscopic measurements are used to retrieve trace gas abundances in the atmosphere at a number of sites throughout the world. Typically, the sun is used as an infrared light source above the atmosphere of the Earth, however, at polar sites, such as our measurement site at Spitsbergen, sunlight is not available during polar night (October–March). Instead, the moon can be used as a substitute infrared light source. In this article we present a proof of concept for the usage of a thermoelectrically cooled InGaAs (Indium-Gallium-Arsenide) near infrared detector to measure the column averaged trace gas abundances by lunar absorption spectroscopy based on trial measurements made in Bremen. These measurements demonstrate the potential of using lunar measurements for retrieval of atmospheric columns of CO_2 and CH_4. The resulting data can be used to fill a crucial gap in the seasonal cycle at polar sites.

1 Introduction

The measurement of the carbon cycle is important in order to understand the complex relationships of its sources and sinks [e.g. Ciais et al. (2013)]. Within the measurement network Total Carbon Column Observing Network (TCCON), solar absorption spectra are taken with high resolution Fourier-Transform InfraRed (FTIR) spectrometers. Since the start of the TCCON program in 2004 measurements have been taken at an increasing number of stations around the globe (approximately 20 sites in the beginning of 2014). The measured spectra provide information on column-averaged mole fractions of CO_2, CH_4 and other gases.

M. Buschmann (✉) · N.M. Deutscher · M. Palm · T. Warneke · T. Weinzierl · J. Notholt
Institute of Environmental Physics, University of Bremen, Bremen, Germany
e-mail: m_buschmann@iup.physik.uni-bremen.de

G. Lohmann et al. (eds.), *Towards an Interdisciplinary Approach in Earth System Science*, Springer Earth System Sciences,
DOI 10.1007/978-3-319-13865-7_10

The rather strict network policy assures inter-comparability between the different sites and provides a valuable dataset for satellite validation and model comparisons (Wunch et al. 2011).

At our measurement site in Ny-Ålesund, Svalbard, Norway (78° 55′ 23″ N, 11° 55′ 22″ E), during Polar Night the sun is permanently below the horizon from October to March and solar absorption measurements are not possible. Consequently there is no information from solar absorption FTIR measurements of the polar atmosphere during winter. However, during full moon, the moon can be used as a substitute infrared light source above the atmosphere, as shown by Notholt (1994) in the middle infrared region. However, the much lower intensity of the moon light in the near-infrared results in a lower signal, which we mitigate by using a new detector with increased sensitivity. In Fu et al. (2014) it was shown that a similar detector setup can be used to measure spectra of sunlight reflected by the ground from a mountaintop site.

In this article we will first present the proof of concept for using a thermo-electrically cooled InGaAs detector to measure near-infrared (NIR) lunar spectra and retrieve column averaged mole fractions of trace gases during a full moon period at our site in Bremen (53° 6′ 13″ N, 8° 50′ 58″ E). Example spectra taken with the new instrument setup are shown and we conclude with the presentation of first retrievals of total column Carbon Dioxide and Methane (denoted xCO_2 and xCH_4).

2 Ground-Based Column Averaged Trace Gas Retrieval

There are two fundamentally different methods to assess the atmospheric composition and its change over time: In situ and remote sensing techniques. In situ measurements are able to observe the desired quantity with high precision and accuracy and high temporal resolution. However, they can only obtain localised measurements, which might be influenced by small scale processes and disturbances. This can be circumvented by installation of the in situ instrument on a moving platform (e.g. a balloon or an aircraft). Unfortunately this can mostly only be done on a campaign basis. The alternative is to use remote sensing. In case of ground-based remote sensing of trace gases in the atmosphere, we are able to retrieve information about the whole atmospheric column. Limitations are the inherent dependency on clear sky conditions and the fixed location of the instrument. Figure 1 shows a visualisation of the different measurement approaches and highlights the viewing geometry of the ground-based FTIR setup.

Several trace gases absorb sunlight in the near infrared spectral region and the incident solar radiation is therefore attenuated by the presence of the gases' molecules. The absorption lines are unique in their spectral position and can be non-ambiguously associated with the target gas. The individual line shapes and intensities are then used to retrieve the amount of gas along the lightpath.

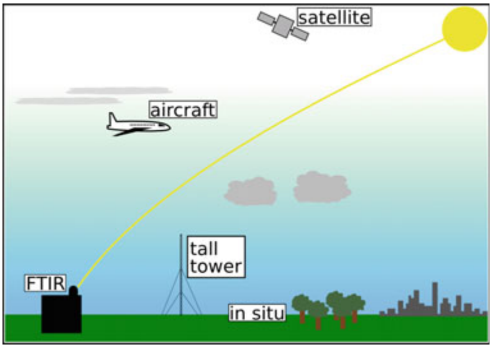

Fig. 1 An overview of the different current methods for atmospheric sounding of CO_2 and CH_4. The FTIR spectrometer has a viewing geometry similar to (nadir-viewing) satellites, sampling the whole atmosphere. In situ instruments and tall towers can only sample their immediate surroundings and the boundary layer, respectively

The standard TCCON retrieval is done by a least-square-fitting method, which scales an a priori profile (i.e. an initial guess of the atmospheric profile of the target gas) in order to minimize a cost function. This approach yields the vertical scaling factor (VSF) of the target gas, which is multiplied with the viewing geometry dependent airmass and the a priori column to yield the retrieved gas column.

Simultaneously (i.e. from the same measurement/spectrum) O_2 is retrieved in the same way and because the atmospheric content of O_2 is uniform and well known (20.95 %), we can normalise the retrieved target gas by the retrieved O_2 value to obtain the column-average dry-air mole fraction, e.g. for CO_2:

$$\mathrm{xCO_2} = \frac{\mathrm{column}_{\mathrm{CO_2}}}{\mathrm{column}_{\mathrm{O_2}}} \cdot 0.2095 \tag{1}$$

3 Spectra from the Bremen Instrument Setup

After characterisation and performance tests of the newly obtained InGaAs detector, it was installed in the Bremen FTIR instrument and spectra were taken on several consecutive nights around the full moon in July 2013.

Figure 2 shows two example spectra from July 21, 2013. The solar spectrum (green) was taken using the standard TCCON setup, the lunar spectrum (blue overlay) was taken the following night. The y-scale is arbitrary and dependent on preamplifier settings of the detectors and thus not comparable. However, one can identify the lower signal-to-noise (S/N) ratio of the lunar spectrum. The difference in the 4,000–5,500 cm^{-1} region originates from the different sensitivity ranges of the two detectors. The solar InGaAs detector has a lower cut cut-on wavenumber.

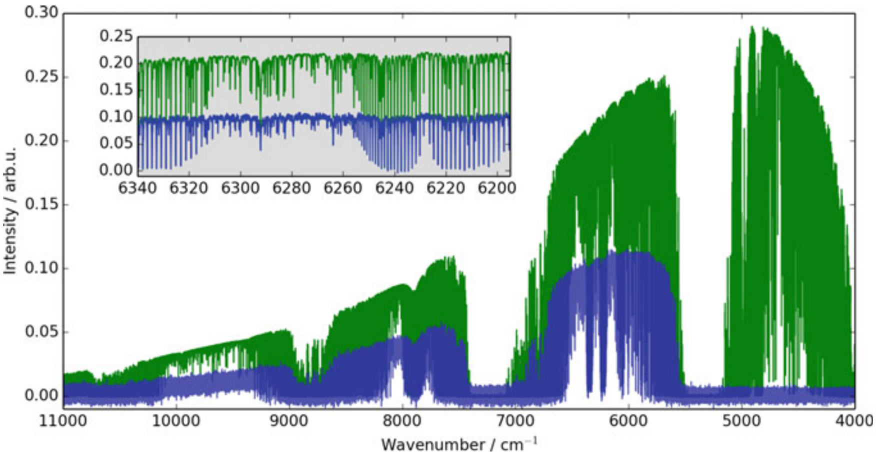

Fig. 2 A solar (*green*) and a lunar (*blue*) absorption spectrum, both taken on July 21, 2013 with the FTS in Bremen. *Note* the better signal-to-noise ratio of the solar spectrum, visible in the *blacked-out* regions, e.g. at 5,400 cm^{-1}. The *inset* shows some of the CO_2 absorption lines of the 1.6 μm band

Part of the CO_2 band can be seen in the inset in Fig. 2. Both spectra have a high spectral resolution of 0.014 cm^{-1} in the standard and 0.08 cm^{-1} in the lunar case, which allows the analysis of individual spectral lines. The lower resolution enables a larger number of spectra to be taken during an equal amount of time, to improve the signal-to-noise ratio. In case of the lunar spectra, 32 spectra were added, compared to 2 in case of the solar measurements. This results in an overall integration time per spectrum of 6 min for lunar and 4 min for solar spectra.

4 xCO_2 and xCH_4 from Lunar Absorption Spectroscopy

We now apply the standard TCCON retrieval approach (as described in Sect. 2) to the (solar and lunar) spectra taken in Bremen in July 2013, i.e. we calculate for each spectrum the column averaged dry air mole fraction of the two target gases xCO_2 and xCH_4.

The results can be seen in Fig. 3, were values retrieved from solar spectra (green) cover most of the days and those from lunar spectra cover most of the nights. Shown are in both cases 30-minute-averages, i.e. arithmetic mean of all measurements within 30 min. The error bars are given by the standard deviation of that half-hourly mean. Note that the error bars for the solar data are mostly too small to be seen on this scale. As a first measure of the precision of the lunar measurements, the mean standard deviation of the 30 min averages is smaller than 4 ppm for xCO_2 and smaller than 18 ppb in case of xCH_4. This can be compared to smaller than 0.3 ppm (xCO_2) and smaller than 1.4 ppb (XCH_4) for the standard TCCON solar measurements.

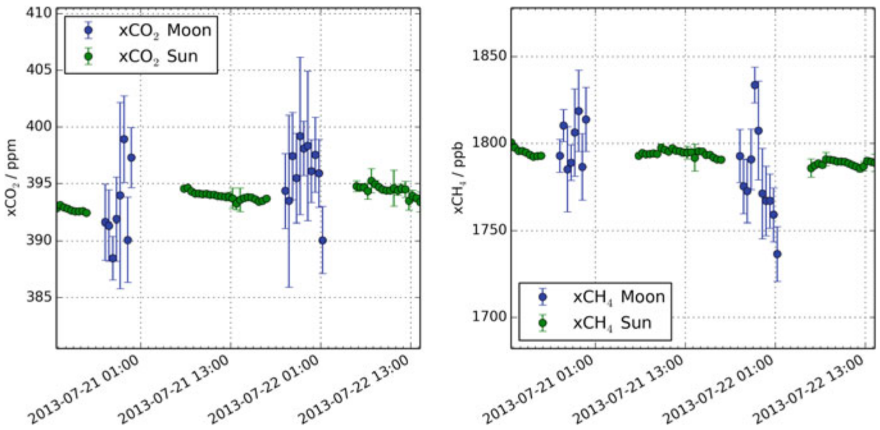

Fig. 3 The retrieved column averaged dry-air mole fractions of CO_2 (*left*) and CH_4 (*right*) for 3 consecutive days in July 2013. *Note* the difference in scatter for the lunar absorption measurements (*blue*) compared to the solar ones (*green*) due to the increased noise in the spectrum (see Fig. 2)

Especially in the lunar case clear sky conditions are very important and times with too dense cloud cover have been removed. Additionally the measurements of lunar spectra are removed at times, when the solar zenith angle is smaller than 95° because the sky is too bright to ensure accurate pointing of the solar/lunar tracking system.

The origin of the apparent draw down in both xCO_2 and xCH_4 on the early morning of July 22 still has to be investigated but is considered an artifact and not real at this point.

5 Conclusions

We presented the first high resolution near-infrared lunar absorption spectra for the retrieval of xCO_2 and xCH_4 from Bremen. Despite the decreased resolution of $0.08\ \mathrm{cm}^{-1}$ with an integration time of about 6 min, we observe an increase in scatter by a factor of 10 compared to the solar absorption spectra. This in turn leads to a lower precision (higher standard deviation of the mean) of the lunar measurements in the order of one magnitude compared to the solar data. The daily cycle in mid-latitudes is estimated in Keppel-Aleks et al. (2011) as peak-to-trough diurnal amplitude of CO_2 of about 0.5–0.75 ppm. The seasonal cycle is more pronounced in the mid and high-latitudes. Warneke et al. (2005) found a seasonal cycle amplitude of CO_2 of 11 ppm for the Ny-Ålesund site. In this study, the scatter of the lunar retrievals (4 ppm) prevents a column averaged daily cycle from easily being seen. Further studies and longer time series are needed to investigate if a daily cycle can be derived from the lunar measurements.

However, with further averaging of the retrieved total column amounts over a longer time period, e.g. daily means, we are confident in gaining information about the seasonal cycle of the column averaged mole fractions of CO_2 and CH_4 in the final measurement setup at our site in Ny Ålesund.

Acknowledgements We thankfully acknowledge funding by the German Research Foundation (DFG).

References

Ciais P, Sabine C, Bala G, Bopp L, Brovkin V, Canadell J, Chhabra A, DeFries R, Galloway J, Heimann M, Jones C, Le Qur C, Myneni RB, Piao S, Thornton P (2013) Climate change 2013: the physical science basis. In: Contribution of Working Group I to the Fifth Assessment Report of the Intergovernmental Panel on Climate Change, chapter Carbon and Other Biogeochemical Cycles. Cambridge University Press, Cambridge

Fu D, Pongetti TJ, Blavier J-FL, Crawford TJ, Manatt KS, Toon GC, Wong KW, Sander SP (2014) Near-infrared remote sensing of los angeles trace gas distributions from a mountaintop site. Atmos Measur Tech 7(3):713–729

Keppel-Aleks G, Wennberg PO, Schneider T (2011) Sources of variations in total column carbon dioxide. Atmos Chem Phys 11(8):3581–3593

Notholt J (1994) The moon as a light source for FTIR measurements of stratospheric trace gases during the polar night: application for HNO_3 in the arctic. J Geophys Res Atmos (1984–2012), 99(D2):3607–3614

Warneke T, Yang Z, Olsen S, Krner S, Notholt J, Toon GC, Velazco V, Schulz A, Schrems O (2005) Seasonal and latitudinal variations of column averaged volume-mixing ratios of atmospheric CO_2. Geophys Res Lett 32(3)

Wunch D, Toon GC, Blavier JFL, Washenfelder RA, Notholt J, Connor BJ, Griffith DWT, Sherlock V, Wennberg PO (2011) The total carbon column observing network. Philos Trans Royal Soc Math Phys Eng Sci 369(1943):2087–2112

A New Method to Filter Out Radio-Frequency Interference (RFI) from SMOS Level 1C Data for Sea Ice Applications

Marcus Huntemann and Georg Heygster

Abstract The Soil Moisture and Ocean Salinity (SMOS) satellite carries a passive microwave radiometer working at 1.4 GHz (L-Band). A unique synthetic aperture antenna consisting of several small antennas allows SMOS to observe a single geographic location under various incidence angles within single overflights. Here we present a preprocessing method starting from SMOS Level 1C data for sea ice applications which reduces the instrumental noise and filters radio frequency interference while preserving valuable data better than previously suggested methods in cryospheric applications. The filter employs binning on incidence angles, so that the filtered data can be used for comparison with surface emissivity models or may serve as input to retrieval procedures.

1 Introduction

Microwave (MW) radiometers on-board satellites are important tools for observing the ocean, atmosphere and cryosphere. For more than 40 years several MW radiometers have been observing the earth, especially providing valuable information on the sea ice cover. Since the beginning of 2010 the SMOS satellite has been operational. Its payload, the Microwave Imaging Radiometer with Aperture Synthesis Microwave Imaging Radiometer with Aperture Synthesis (MIRAS) extends the existing MW radiometers to 1.4 GHz (L-band), the lowest microwave frequency used for satellite passive microwave remote sensing so far. Even though the SMOS satellite was engineered for remote sensing of soil moisture and ocean salinity (name SMOS), its low frequency observations also carry information on the sea ice properties like Sea Ice Thickness (SIT) (Huntemann et al. 2014) and depth of the snow cover (Maaß et al. 2013).

M. Huntemann (✉) · G. Heygster
Institute of Environmental Physics, University of Bremen, Otto-Hahn-Allee 1,
28359 Bremen, Germany
e-mail: marcus.huntemann@uni-bremen.de

G. Lohmann et al. (eds.), *Towards an Interdisciplinary Approach in Earth System Science*, Springer Earth System Sciences,
DOI 10.1007/978-3-319-13865-7_11

2 Data Description

The SMOS satellite observes the earth surface by taking so called snapshots. One snapshot is acquired every 1.3 s and extends more than 1,000 km along and cross track, so that the obtained snapshots overlap to a large extent. This overlap means that every location is observed at several incidence angles during one single overflight. The SMOS Level 1C data product is organized swath-wise but gridded into the Snyder equal area grid (Sahr et al. 2003) with a grid spacing of 15 km. As common in microwave remote sensing, the data are expressed as brightness temperatures (*TB*) which is defined as the temperature a black body would have to have, if it emits this amount of radiation at a given frequency. The brightness temperature is essentially the product of the emissivity, a material constant, and the physical temperature.

Since mid 2010 SMOS is in full polarization mode, i.e., it obtains all four components of the Stokes vector. However, it needs several snapshots to create the whole Stokes vector for a single geographical point since the instrument switches between the polarisations each snapshot. These data still have to be converted from the satellite reference (X, Y) frame into the earth reference frame (horizontal, vertical) or often just (H, V) (Martin-Neira et al. 2002). The corresponding horizontal and vertical polarized brightness temperatures are denoted as *TBh* and *TBv* respectively. After this transformation the data are ready to serve as, e.g., input for retrievals of surface parameters like sea ice thickness.

One major problem with SMOS is the Radio Frequency Interference (RFI) contamination of the data especially in the early phase of SMOS (Oliva et al. 2012). It originates from anthropogenic L-band transmitters from the earth surface mostly from radar or communication devices. Even though mostly located on land, some RFI can also be traced back to ships. In addition, since SMOS uses a synthetic aperture antenna with a Fourier transform based reconstruction of one snapshot, strong RFI may extend over the whole snapshot producing ringing effects. In the current L1C v5.05 data product RFI is flagged sparsely and ringing effects are not addressed.

3 Filtering Procedure

For current snow- and sea ice thickness retrieval algorithms using SMOS data, a rather simple RFI filter is sufficient. Whenever a single observation in one snapshot exceeds 300 K, the whole snapshot is discarded. This leads to a considerably large data loss of potentially unaffected data, especially when the RFI is not strong enough to cause ringing effects in the whole snapshot. This loss of data is not an issue on daily averages and averages over large incidence angle ranges as used by Huntemann et al. (2014), Kaleschke et al. (2012), Tian-Kunze et al. (2014) and Maaß et al. (2013).

However, if an acquisition of brightness temperatures for a smaller incidence angle range is desired or sub-daily changes are to be observed, then the number of available observations is much smaller and a more careful processing is suggested.

A single overflight is sufficient to observe an area from different incidence angles as consecutive SMOS snapshot overlap considerably. We start converting the L1C data into the earth reference frame (Huntemann et al. 2014), averaging the observations into single degree incidence angle bins and derive the standard deviation for each bin, representing the variability of brightness temperatures for a given grid cell within the few seconds the grid cell is observed by SMOS under an incidence angle ±1° segment. The surface conditions will not change within this temporal scale. Therefore, if this variation is high, a non-geophysical influence on the brightness temperatures is detected and the data point is discarded. From the resulting data set, also wider incidence angle range averages like the 40–50° averages used in Huntemann et al. (2014) for a SIT retrieval can be calculated.

Due to the aperture synthesis step of the SMOS image generation process, RFI sources propagate in a ringing structure throughout the snapshot along specific lines. Therefore, the values from the different snapshots of one overflight falling into an incidence angle bin of one grid cell may show a large variability in brightness temperature. As compromise between data quality and loss of data due to filtering we use 10 K standard deviation as a threshold, i.e. bins with a standard deviation above 10 K are discarded. In addition we require at least 3 data points for a valid average. The detailed statistics of an example day, the 25 Dec 2010, are shown in Fig. 1. The upper plot (a) shows the 3 data point criterion in a histogram as a red line. On the left axis the number of data points is shown while the right axis shows the percentage of remaining data points when applying the data point requirement as a lower threshold. The criterion of having at least 3 data points is fulfilled in a 63.3 % of the cases as can be read from this axis. The hatched area shows data where the criterion is not fulfilled. The shape of the histogram originates from the incidence angle distribution within a single snapshot, where some incidence angles have more observations in one overflight than others (Martin-Neira et al. 2002).

For incidence angle bins with more than 3 data points, the standard deviation is calculated. The histogram of standard deviations of *TBh* per incidence angle is shown in Fig. 1b. The standard deviation seems relatively evenly distributed over all incidence angles with a peak at about 1–4 K standard deviation and 30–60° incidence angle. However, allowing just a maximum standard deviation of 4 K would discard about 50 % of all data. Since the radiometric accuracy of MIRAS varies not with the incidence angle but with the position of the point within one snapshot (Khazaal and Anterrieu 2009; Martin-Neira et al. 2002), we define for our application a required standard deviation of less than 10 K. In the example day of Fig. 1b about 87 % of the data remain. Again, the red hatches mark the data regime not fulfilling this criterion.

A brightness temperature example of thin sea ice of 1 Oct 2010 is shown in Fig. 2. The left (a) shows *TBh* and *TBv* of an overflight at 7:36 UTC. The moderate

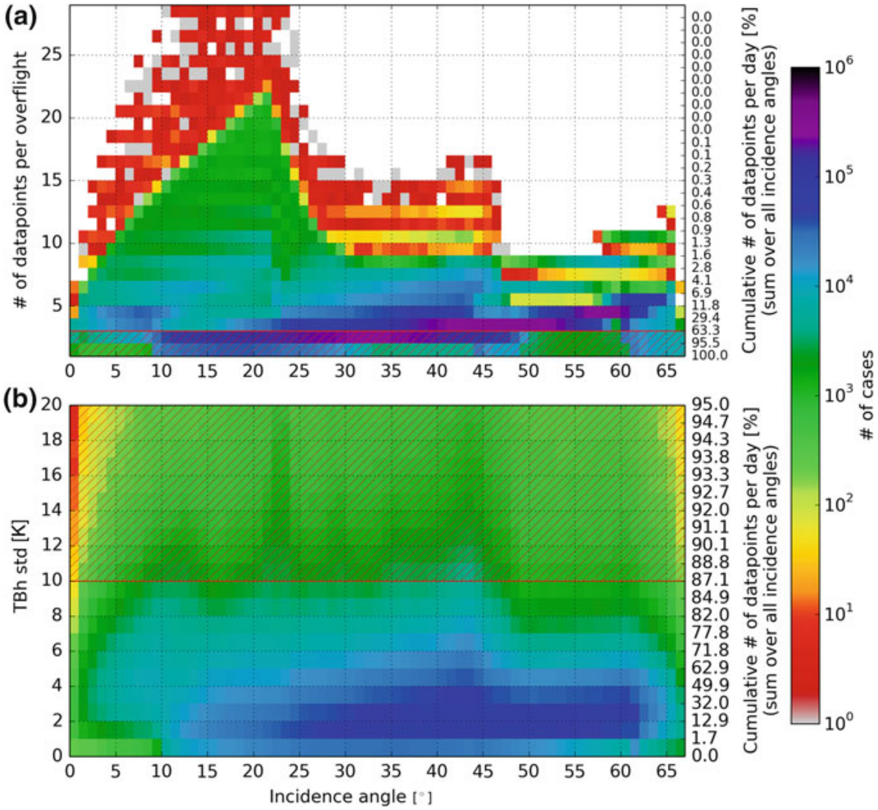

Fig. 1 Statistical overview on SMOS L1C data higher than 50° N on 25 Dec 2010. The *upper plot* (**a**) illustrates the number of all observations per incidence angle bin per grid cell per overflight. The *color* shows the number of occurrences. The *red line* marks the threshold of at least 3 data point for a valid average brightness temperature. The *lower plot* (**b**) illustrates the standard deviation criteria on all cases which fulfilled the 3 data point criteria. The chosen threshold of 10 K for the standard deviation is marked by the *red line*. *Red hatched areas* mark discarded data

change of brightness temperature with the incidence angle leads to a smooth curve of average brightness temperatures with low standard deviations. The threshold of 10 K is exceeded at no incidence angle bin. In contrast, on the right (b) the result is much less homogeneous even though it is the same grid cell on the same day, but at a later overflight (12:32 UTC). The strong variations especially between 40 and 50° in *TBv* cause high standard deviations in many incidence angle bins exceeding the 10 K threshold. An averaging of brightness temperatures will not give representative values as the strong variations are not caused by natural surface emissions but most probably by RFI.

On 25 Dec 2010 the Kara and Barents Seas are highly affected by RFI, which are influencing the brightness temperatures and therefore the retrieved thin SIT values (Huntemann et al. 2014). Figure 3 demonstrates the RFI filter qualities of this

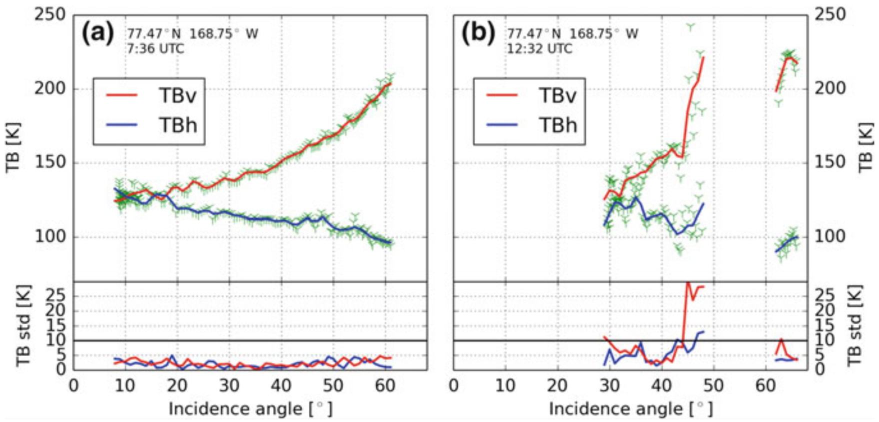

Fig. 2 *TBh* and *TBv* versus incidence angle on 1 Oct 2010 7:36 UTC (**a**) and 12:32 UTC (**b**) for a location on thin sea ice. *Green triangles* are single observations, *blue* (TBh) and *red* (TBv) *lines* show the averaging. Lower parts show the standard deviation with the *black horizontal line* marking the 10 K threshold

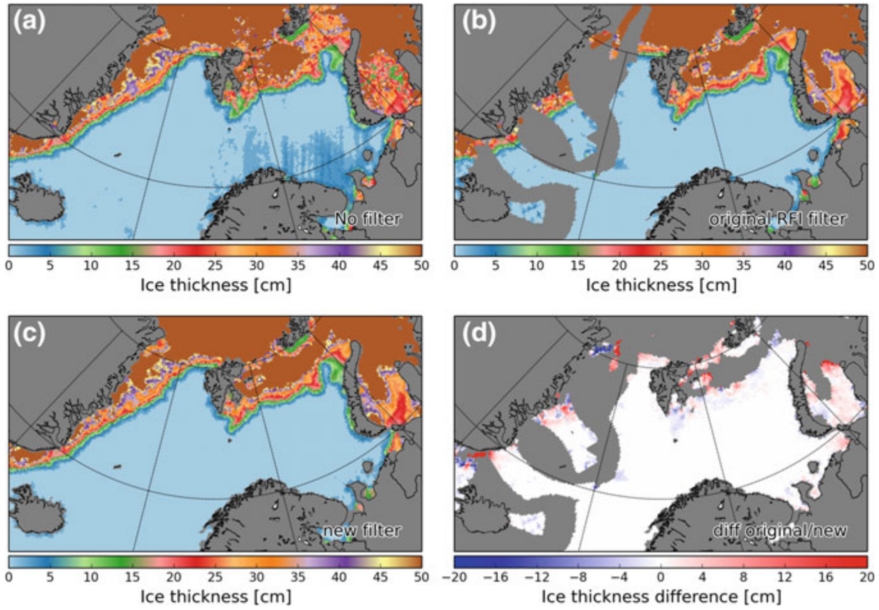

Fig. 3 Sea ice thickness (up to 50 cm) retrieved from differently preprocessed datasets; unfiltered data (**a**) show strong RFI influence, original RFI filtered data (**b**) show more homogeneous results. New RFI filter (**c**) keeps high data coverage and obtains stability. Difference between original and new RFI filter (**d**)

averaging method. In Fig. 3a the SIT retrievals based on unfiltered L1C data are spatially inhomogeneous in the Kara and Barents seas on that day due to RFI. Figure 3b shows the result after applying the original RFI filtering method of discarding complete snapshots. The SIT in the Kara and Barents seas seem more reasonable and more spatially consistent compared to the unfiltered version. However, this strict filter also filters obviously useful data east of Greenland where the SIT looks undistorted in the unfiltered data. Figure 3c shows the results after applying the new filter masking out all data from a single overflight where the standard deviation is higher than 10 K within each single incidence angle bin. The SIT in the Kara and Barents seas look reasonable and very similar to the SIT in the original filter in Fig. 3b. In addition the SIT east of Greenland is preserved and show reasonable values as in the unfiltered version before. The difference between the two filters is shown in Fig. 3d. Results after the two filters mostly agree well. The highest values in the difference map are from SIT values of 30–50 cm, where the retrieval is more sensitive to small changes in the brightness temperatures. The small SIT offset of a few cm in the thin ice area in the Kara sea stem from the averaging over several overflights, i.e., a later overflight of that day contains RFI somewhere in the snapshot. In the old filter these data are discarded, where the new filter uses these data as long as they show only small variability within the few seconds of acquisition. An obvious interpretation is that this SIT difference, which is positive almost everywhere, originates from the ice thickness increase by freezing within that day.

4 Conclusion

A new data filter and averaging method of SMOS brightness temperatures for Level 1C data have been introduced, filtering for unphysical changes of brightness temperatures within small incidence angle and temporal variations. The filtered, incidence angle binned data may serve as stable comparison to model data or as input for a retrievals of geophysical parameters like ice thickness. However, also retrievals of other parameters might profit from this technique.

Thresholds of 3 observations at least with a standard deviations of 10 K or less per overflight of one grid cell per incidence angle bin are suggested as filter criteria. This way, the influence of RFI on an example of sea ice thickness retrieval was eliminated preserving most of the data while achieving better data coverage than with the previously used RFI filter discarding complete snapshots. The given conditions leave about 3 to 20 valid observations for a single average. The proposed method might miss RFI in case of small RFI effects, which could introduce an offset to the brightness temperatures. This effect can be reduced further by tuning the parameters of minimum number of observations and of standard deviation. Since globally the RFI reduced since the beginning of the SMOS mission, for more recent data a more strict criteria for the standard deviation is suggested.

As we expect a normal distribution, other methods than just the standard deviation as criteria could be employed, such as Dixon's Q test (Dean and Dixon 1951) or Grubbs' test (Grubbs 1950) for outlier elimination or replacing the currently taken mean by median. An alternative filter method would be to fit the brightness temperature as a function of incidence angle potentially based on the Fresnel equations and define an additional parameter to reflect the quality of each fit. However, for the purpose of RFI removal, the described filtering procedure has proved satisfactory for the 3 month of Oct–Dec 2010.

Acknowledgments Financial support of the Federal Ministry of Education and Research/Bundesministerium für Bildung und Forschung (BMBF) MiKliP project Climate Model Validation by confronting globally Essential Climate Variables from models with observations (ClimVal) is gratefully acknowledged. We also thank the reviewers for their valuable comments and suggestions.

References

Dean RB, Dixon WJ (1951) Simplified statistics for small numbers of observations. Anal Chem 23 (4):636–638. doi:10.1021/ac60052a025, URL http://pubs.acs.org/doi/abs/10.1021/ac60052a025 (ISSN 0003-2700)

Grubbs FE (1950) Sample criteria for testing outlying observations. Annals Math Stat 21(1):27–58. doi:10.1214/aoms/1177729885, URL http://projecteuclid.org/euclid.aoms/1177729885 (ISSN 0003-4851)

Huntemann M, Heygster G, Kaleschke L, Krumpen T, Mäkynen M, Drusch M (2014) Empirical sea ice thickness retrieval during the freeze-up period from SMOS high incident angle observations. The Cryosphere 8(2):439–451. doi:10.5194/tc-8-439-2014. URL http://www.the-cryosphere.net/8/439/2014/ (ISSN 1994-0424)

Kaleschke L, Tian-Kunze X, Maaß N, Mäkynen M, Drusch M. Sea ice thickness retrieval from SMOS brightness temperatures during the Arctic freeze-up period. Geophys Res Lett 39(5). doi:10.1029/2012GL050916, URL http://www.agu.org/pubs/crossref/2012/2012GL050916.shtml (ISSN 0094-8276)

Khazaal A, Anterrieu E (2009) SMOS image reconstruction algorithm: extension of the band limited approach to the fully-polarimetric mode of MIRAS. In: 2009 international conference on advances in computational tools for engineering applications. IEEE, New York, pp 180–185. doi:10.1109/ACTEA.2009.5227912, URL http://ieeexplore.ieee.org/lpdocs/epic03/wrapper.htm?arnumber=5227912 (ISBN 978-1-4244-3833-4)

Maaß N, Kaleschke L, Tian-Kunze X, Drusch M (2013) Snow thickness retrieval over thick Arctic sea ice using SMOS satellite data. The Cryosphere 7(6):1971–1989. doi:10.5194/tc-7-1971-2013, URL http://www.the-cryosphere.net/7/1971/2013/ (ISSN 1994-0424)

Martin-Neira M, Ribo S, Martin-Polegre AJ (2002) Polarimetric mode of MIRAS. IEEE Trans Geosci Remote Sens 40(8):1755–1768. doi:10.1109/TGRS.2002.802489 (ISSN 0196-2892)

Oliva R, Daganzo E, Kerr YH, Mecklenburg S, Nieto S, Richaume P, Gruhier C (2012) SMOS radio frequency interference scenario: status and actions taken to improve the RFI environment in the 1400–1427-MHz passive band. IEEE Trans Geosci Remote Sens 50(5):1427–1439. doi:10.1109/TGRS.2012.2182775, URL http://ieeexplore.ieee.org/lpdocs/epic03/wrapper.htm?arnumber=6148276 (ISSN 0196-2892)

Sahr K, White D, Kimerling AJ (2003) Geodesic discrete global grid systems. Cartogr Geogr Inf Sci 30(2):121–134. doi:10.1559/152304003100011090, URL http://www.tandfonline.com/doi/abs/10.1559/152304003100011090 (ISSN 1523-0406)

Tian-Kunze X, Kaleschke L, Maaß N, Mäkynen M, Serra N, Drusch M, Krumpen T (2014) SMOS-derived thin sea ice thickness: algorithm baseline, product specifications and initial verification. The Cryosphere 8(3):997–1018. doi:10.5194/tc-8-997-2014, URL http://www.the-cryosphere.net/8/997/2014/ (ISSN 1994-0424)

Arctic Multiyear Ice Concentration Retrieval from SSM/I Data Using the NASA Team Algorithm with Dynamic Tie Points

Yufang Ye and Georg Heygster

Abstract We retrieve multiyear ice concentration with the NASA Team algorithm and a modified NASA Team algorithm with dynamic tie points. The latter is used to compensate the temporal impact of brightness temperature variations. To assess the performance of both methods, analyses were made for all winters from 1989 to 2012. The method with dynamic tie points yields higher estimates in most years. Both methods show a clear declining trend of the multiyear ice area from 1989 to 2012, which is consistent with the decrease of the annual minimum ice extent. Furthermore, the ice extent of multiyear ice in most years decreases during each winter, reflecting the expected loss of multiyear ice by export to lower latitudes. A sensitivity study to evaluate the influence of each tie point on multiyear ice concentration retrieval shows that the retrieval is most sensitive to the tie points of multiyear ice and first year ice at 19 GHz vertical polarization. Therefore, these tie points need to be determined more precisely if dynamic tie points are used for multiyear ice retrieval with the NASA Team algorithm.

Keywords Multiyear ice concentration · SSM/I · Dynamic tie points · NASA team algorithm

1 Introduction

Arctic sea ice is a sensitive climate indicator (Serreze and Francis 2006). Its area has declined dramatically over the past 30 years. The decrease is most pronounced in September when the annual sea ice minimum occurs, so that the area of multiyear ice (ice which has survived at least one summer) is decreasing (Nghiem et al. 2007; Perovich and Richter-Menge 2009; Stroeve et al. 2005). Multiyear ice is important because it differs from first year ice in physical and biological aspects. Multiyear ice

---

Y. Ye (✉) · G. Heygster
Institute of Environmental Physics, University of Bremen, Bremen, Germany
e-mail: yufang@iup.physik.uni-bremen.de

G. Lohmann et al. (eds.), *Towards an Interdisciplinary Approach in Earth System Science*, Springer Earth System Sciences,
DOI 10.1007/978-3-319-13865-7_12

is thicker and therefore conducts less heat from the ocean to the atmosphere. It is stronger and thus has more resistance against the deforming forces of wind and currents. Furthermore, it is populated by microorganisms which are at the top of the food chain (Thomas and Dieckmann 2009). Therefore there is a need for accurate observation of multiyear ice area changes.

The data used in this study are obtained from the Defense Meteorological Satellite Program (DMSP) Special Sensor Microwave/Imager (SSM/I), provided by the National Snow and Ice Data Center (NSIDC), with daily averaged brightness temperatures projected in a polar stereographic grid of 25 km grid cell size.

2 Method

In the past three decades, sea ice has been monitored with microwave radiometers, scatterometers and other satellite sensors. These datasets allows determination of total sea ice extent and area quite reliably from space. However, discrimination of multiyear ice from first year ice and other ice types poses many more difficulties. Several methods to retrieve multiyear ice concentration from passive microwave radiometers have been suggested, i.e. the NASA Team, Bootstrap and Lomax algorithms (Comiso et al. 1997; Lomax et al. 1995; Steffen and Schweiger 1991; Wang et al. 2009). In this study, we present a modified version of the NASA Team algorithm with dynamic tie points.

The NASA Team algorithm uses brightness temperatures of three channels, namely the 19 GHz horizontally (H) and vertically (V) polarized channels and the vertically polarized 37 GHz channel. The brightness temperatures for 100 % multiyear ice, first year ice and open water are regarded as tie points. For the original NASA Team algorithm, the tie points are a set of fixed values, based on experimental and statistical studies. However, the temporal and spatial variability in brightness temperature of the three surface types introduces errors in the estimates of multiyear ice and first year ice concentration. We propose to use dynamic tie points to minimize the error associated with this variability.

The brightness temperatures of sea ice and open water at different frequencies and polarizations vary considerably as shown in the scatter plot in Fig. 1, which shows SSM/I 19 and 37 GHz brightness temperature data at vertical polarization. The cluster of data points near OW represents open water and those around MYI and FYI represents multiyear ice and first year ice, respectively. For the dynamic NASA Team algorithm, dynamic tie points are derived daily using the following technique:

First, two regions are defined for taking samples. One is generally ice-covered, the other one is open water at most time. The ice covered region is the region of the minimum ice extent of the previous September. The “ice free” region is not without ice the whole year but the region where monthly total ice concentration is zero for at least 1 month from the previous October to that September. Thus, it may be partly or completely ice covered in other months. This region is assumed to contain a

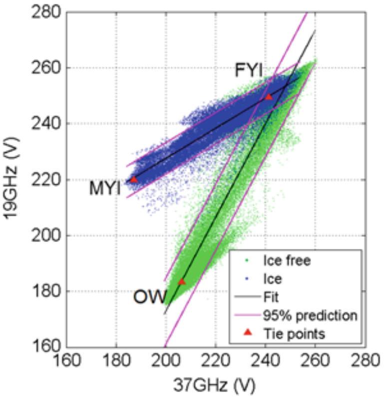

Fig. 1 Scatter plot of brightness temperatures at 37 and 19 GHz vertical polarization on 1st Jan. 2007. *Green* data points are taken from the region which is ice free in summer, *blue* data points from the region that has ice in summer, *red triangle* points are the dynamic tie points derived from the scatter plot

mixture of open water and first year ice. Data from each day along with the previous and following 3 days are taken from the defined regions and plotted as shown in Fig. 1. In order to exclude noisy data points, the number density is calculated in each 1 K by 1 K bin, in a 2-D histogram of the 19 GHz and 37 GHz V channels. Data points in the grid where the number density is below five are eliminated. With a linear regression, data points that are outside 95 % prediction of the regression lines are removed. It is assumed that the data points are randomly sampled from a Gaussian distribution. 95 % of the samples will lie within the 95 % prediction lines.

Second, based on the remaining data points, a linear regression is made again, used for generating a set of lines perpendicular to the regression line. For each data point, there is a corresponding perpendicular line with a certain intercept on the 19 GHz V axis. The average of the ice region data points of which the intercept is between 0.1 and 0.4 % (threshold range for multiyear ice tie points) of the largest intercept are regarded as the tie points for multiyear ice. The average of the ice free data points of which the intercept is between 20 and 25 % (threshold range for open water tie points) of the largest intercept are regarded as the tie points for open water. The average of the ice region data points located between the lines that are parallel to the regression line of ice free data points and have an intercept between 90 and 110 % (threshold range for first year ice tie points) of the regression intercept are regarded as the tie points for first year ice. Another possible solution of deriving tie points for first year ice could be the intercept of the two regression lines. However, the latter method will lead to big difference between the dynamic and fixed tie points.

The fixed tie points of open water correspond to calm water under dry atmosphere. Tie points of first year ice and multiyear ice correspond to 100 % first year ice and multiyear ice respectively. Dynamic tie points are derived with the empirical method described above. Threshold ranges of the method are selected according to

Table 1 Average difference between dynamic tie points and fixed tie points

Surface type	Threshold range (%)	19 GHz H (K)	19 GHz V (K)	37 GHz V (K)	Sum of absolute difference
OW	15–20	−1.85	−2.83	0.17	4.85
	20–25	0.53	−1.60	1.23	3.36
	25–30	3.13	−0.24	2.43	5.80
MYI	0.1–0.4	2.56	−2.50	−0.36	5.42
	0.4–0.7	3.18	−1.82	0.87	5.87
	0.7–1	3.65	−1.36	1.71	6.72
FYI	85–115	−4.08	−2.45	−2.50	9.03
	90–110	−2.11	−0.86	0.74	3.71
	95–105	0.08	0.97	4.28	5.33

the idea that averages of the dynamic tie points in all the winter months from 1998 to 2007 are close to the fixed tie points. That means we select the threshold range for each surface type with the smallest average difference between dynamic and fixed tie points, which corresponds to the smallest sum of absolute differences at the three channels. More threshold ranges than those in Table 1 were tried in this study. We only show those with relatively small average difference.

Figure 2 shows the fixed and dynamic tie points for ice and open water at all the three channels from 1998 to 2007 (October–May). Compared to the dynamic tie points for first year ice and multiyear ice, those for open water have much less seasonal variations. It indicates that the influence of the atmosphere is much less than that of ice. In each year, the dynamic tie points of first year ice and multiyear ice have high values at the beginning of November and end of May, as the high temperature of air and ice increases the contribution to the observed brightness temperature through high snow wetness and high surface temperature. Dynamic tie points in October and May are shown in Fig. 2 but not included in this study as the thin ice in October and the high air temperature in May would cause errors of multiyear ice concentration retrieval. It is known that the influence of thin ice is much larger at 19 GHz H than that at 19 and 37 GHz V, with an increase of 45 K at 19 GHz H when ice thickness increases from 10 to 50 cm, while the increase is 9 and 5 K at 19 GHz V and 37 GHz V (Heygster et al. 2014). This causes large variations of tie points for first year ice however has no influence on those for multiyear ice and open water, leading to unexpected retrieval. Besides, the high air temperature in May could cause snow melt on ice, leading to errors of multiyear ice retrieval.

In addition to the seasonal variations, the inter-annual variations of tie points for first year ice and multiyear ice are much larger than those of open water. In warm winters such as the winter of 2002/2003, 2005/2006 and 2006/2007, tie pointes for multiyear ice at 37 GHz V channel are larger than those in other years, since the emissivity of ice increases when there is an increase of snow wetness on ice (Ulaby et al. 1986). The warm weather could cause increasing snow wetness and lead to increase of brightness temperature consequently, which is more pronounced at 37 GHz than at 19 GHz (Drobot and Anderson 2001).

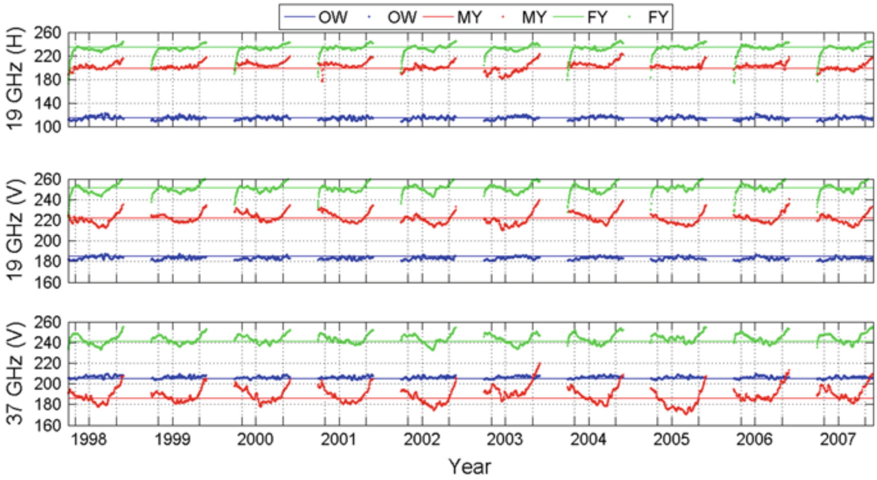

Fig. 2 Dynamic tie points from 1998 to 2007 (October–May). *Vertical bars* show beginnings of November, January and May of each winter

Table 2 Average daily change of dynamic tie points from 1998 to 2007 (November–April)

Surface type	19 GHz H (K)	19 GHz V (K)	37 GHz V (K)
	$T_{B,aag}$	$T_{B,aag}$	$T_{B,aag}$
OW	0.51	0.26	0.22
MYI	0.41	0.26	0.37
FYI	0.24	0.20	0.24

The average absolute daily change $T_{B,aag}$ of the dynamic tie points from 1998 to 2007 (November–April) are shown in Table 2. The small daily change of tie points in all channels and surface types confirms the tie points deriving procedure.

3 Time Series Results

Using fixed and dynamic tie points, both total and multiyear ice concentrations are retrieved daily with the NASA Team algorithm for all winters (November–April) from 1989 to 2012. Figure 3 shows the multiyear ice extent, defined as the sum of the area covered by grid cells that have 30 % or higher multiyear ice concentration (Comiso 2012). Both multiyear ice retrievals show lower multiyear ice extent than the annual minimum of the total ice extent in September. There are two reasons for the differences. Firstly, the multiyear ice extent is extracted by ignoring pixels with multiyear ice concentration below 30 %. Secondly, first year ice is already formed at the time of the annual ice extent minimum in September.

In the NASA Team algorithm, polarization ratio (PR) and gradient ratio (GR) are calculated as below:

$$PR = \frac{T_{B,19V} - T_{B,19H}}{T_{B,19V} + T_{B,19H}}, \tag{1}$$

$$GR = \frac{T_{B,37V} - T_{B,19V}}{T_{B,37V} + T_{B,19V}}, \tag{2}$$

where $T_{B,19V}$, $T_{B,19H}$ and $T_{B,37V}$ are the brightness temperature at 19 GHz V, 19 GHz H and 37 GHz V channel. Multiyear ice concentration retrieval is mainly determined by GR in the GR/PR space because of its high sensitivity for multiyear ice concentration retrieval. Based on the average brightness temperature differences between dynamic and fixed tie points in Table 2, GR of averaged dynamic tie points for first year ice and multiyear ice are:

$$GR_{FY} = \frac{T_{BFY,37V} - T_{BFY,19V} + 0.74 + 0.86}{T_{BFY,37V} + T_{BFY,19V} + 0.74 - 0.86}, \tag{3}$$

$$GR_{MY} = \frac{T_{BMY,37V} - T_{BMY,19V} - 0.36 + 2.5}{T_{BMY,37V} + T_{BMY,19V} - 0.36 - 2.5}, \tag{4}$$

where $T_{BMY,37V}$ and $T_{BMY,19V}$ are the brightness temperature of fixed tie points for first year ice at 37 and 19 GHz V, T_{BFY} are those for multiyear ice. They are larger than GR of the fixed tie points. In addition, the GR differences between that of fixed and dynamic tie points for multiyear ice are bigger than those for first year ice, which makes GR of second year ice closer to that of multiyear ice. As a consequence, the method using dynamic tie points yields higher estimates than that using fixed tie points in most winters, which is shown in Fig. 3.

There is a slightly declining trend of minimum ice extent as shown in Fig. 1, which is consistent with the multiyear ice extent retrieved from both methods. In most winters, multiyear ice extent decreases as expected. One reason for the multiyear ice reduction is the export to more southern regions. Figure 4 shows the reduction of multiyear ice area and the ice outflow through Fram Strait (Kwok 2009) from 1988 to 2007. It is noted that the multiyear ice area takes the pixels with multiyear ice concentration below 30 % into account. In all, the multiyear ice reduction is larger than however not highly correlated to the ice export through Fram, with a correlation coefficient of 0.15 and 0.22 for the retrieval from original and dynamic NASA Team algorithm respectively. The difference between Fram strait export and multiyear ice area could be caused discrepancy in considered periods and the export through regions like Canadian archipelago.

In Fig. 3, multiyear ice extent retrieved from both methods increases during some winters, such as the winter of 1999/2000. It could be caused by the ice drift from central Arctic, which is not covered by SSM/I data. Besides, the multiyear ice extent changes rapidly from day to day, which could be caused by the sensor noise.

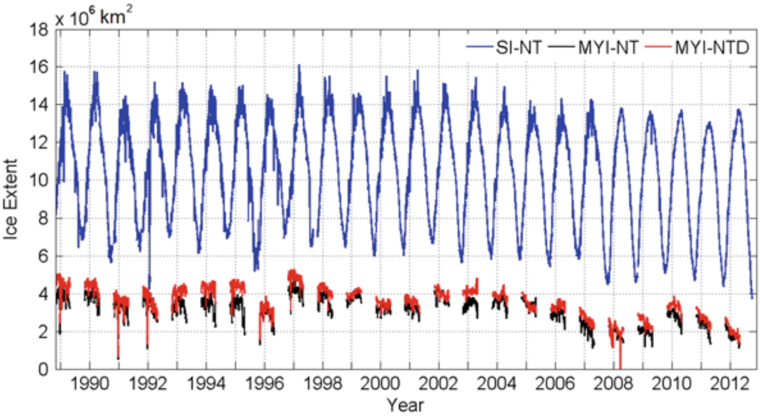

Fig. 3 Total sea ice extent retrieved with NASA Team algorithm, multiyear ice extent retrieved with NASA Team algorithm and dynamic NASA Team algorithm from 1989 to 2012. SI-NT: total sea ice extent retrieval with NASA Team algorithm, MYI-NT: multiyear ice extent retrieved with NASA Team algorithm, MYI-NTD: multiyear ice extent retrieval with dynamic NASA Team algorithm

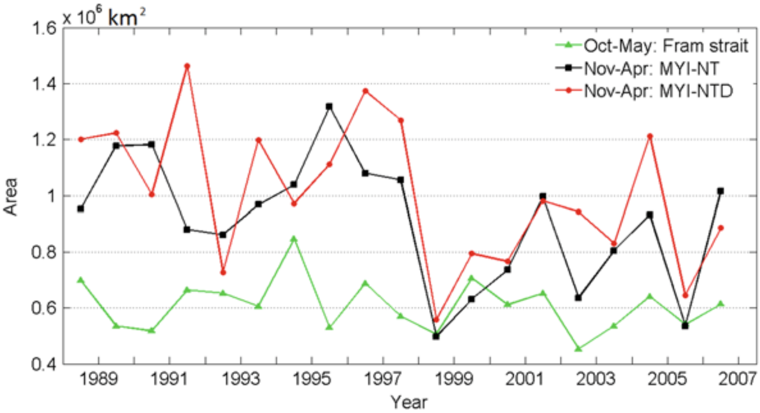

Fig. 4 Arctic sea ice outflow through Fram Strait (October–May) (Kwok 2009) and multiyear ice reduction (November–April) from 1988 to 2007

4 Sensitivity Study and Conclusion

A sensitivity study was conducted to see the influence of each tie point on the multiyear ice concentration retrieval. The standard deviation $T_{B,std}$ and average difference $T_{B,diff}$ are introduced to measure the stability of the dynamic tie points and the difference from fixed tie points. $T_{B,diff}$ is calculated as:

Table 3 Standard deviation and average difference of dynamic tie points

Surface type	19 GHz H (K)		19 GHz V (K)		37 GHz V (K)	
	$T_{B,diff}$	$T_{B,std}$	$T_{B,diff}$	$T_{B,std}$	$T_{B,diff}$	$T_{B,std}$
OW	0.53	2.47	−1.60	1.30	1.23	1.12
MYI	2.56	4.65	−2.50	3.71	−0.36	5.60
FYI	−2.11	2.62	−0.86	2.80	0.74	3.53

$$T_{B,diff} = avg\left(T_{B,dyn}\right) - T_{B,fix}, \tag{5}$$

where $T_{B,dyn}$ is the dynamic tie point, $T_{B,fix}$ is the fixed tie point.

Table 3 lists the standard deviation and average difference of all the dynamic tie points in winters from 1998 to 2007. It shows that the average difference $T_{B,diff}$ between the average dynamic tie point $\mathrm{T_{B,dyn}}$ and the fixed tie point $\mathrm{T_{B,fix}}$ for open water at 19 and 37 GHz V is larger than one standard deviation, which means tie points for open water at the two channels are not well estimated. Among all the tie points, those for multiyear ice are most unstable. For first year ice and multiyear ice, the average difference $T_{B,diff}$ is smaller than $T_{B,std}$ in all channels, which means tie points for first year ice and multiyear ice are estimated well.

In order to evaluate the sensitivity of ice concentrations to changes in the tie points, we define two parameters, the first one is

$$C_{SEN1} = \frac{avg(C_{MY+} - C_{MY-})}{2}, \tag{6}$$

this is half of the average change of ice concentration if two modified sets of tie points are used, where C_{MY+} and C_{MY-} are the multiyear ice concentration retrieved with the tie points increased and decreased by one standard deviation respectively. For three used channels and three surface types, this results in nine sensitivity parameters C_{SEN1} given in Table 4. There, in addition the sensitivity C_{SEN2} is given,

$$C_{SEN2} = C_{SEN1} \times T_{B,diff}/T_{B,std}, \tag{7}$$

which describes the difference of multiyear ice concentration caused by the difference of tie points.

Table 4 Sensitivity parameters of the dynamic tie points

Surface type	19 GHz H (%)		19 GHz V (%)		37 GHz V (%)	
	C_{SEN1}	C_{SEN2}	C_{SEN1}	C_{SEN2}	C_{SEN1}	C_{SEN2}
OW	0.027	0.006	−0.26	0.32	0.07	0.08
MYI	0.26	0.14	−2.46	1.66	1.48	−0.10
FYI	0.39	−0.31	−6.32	1.94	2.94	0.61

Table 4 shows that multiyear ice retrieval is most sensitive to the tie points at 19 GHz V channel and least sensitive to those at 19 GHz H channel. In the NASA Team algorithm, 19 GHz H is only used in PR. As mentioned above, multiyear ice concentration retrieval is mainly determined by the gradient ratio (GR) in the GR/PR space. The low sensitivity of horizontal channel (shown in Table 4) confirms the weak influence of polarization ratio. Besides, tie points of multiyear ice and first year ice are more sensitive than those of open water as expected. To sum up, tie points of multiyear ice and first year ice at 19 GHz V are the most sensitive thus need to be determined as precisely as possible if the dynamic NASA Team algorithm is used.

To conclude, dynamic tie points improve the retrieval of multiyear ice concentration with the NASA Team algorithm by taking the temporal variation of brightness temperature into account. However, because of the high sensitivity of tie points and the impact of spatial variation of brightness temperature, much further work could be done to further improve the retrieval of multiyear ice with the NASA Team algorithm. For example, we could define three regions for deriving tie points of open water, first year and multiyear ice instead of two (shown in Fig. 1). Furthermore, better weather filters could improve the retrieval as well.

Acknowledgements Financial support of the China Scholarship Council is gratefully acknowledged. We also thank the reviewers for their valuable comments and suggestions.

References

Comiso JC (2012) Large decadal decline of the arctic multiyear ice cover. J Clim 25

Comiso JC, Cavalieri DJ, Parkinson CL, Gloersen P (1997) Passive microwave algorithms for sea ice concentration: a comparison of two techniques. Remote Sens Environ 60:357–384

Drobot SD, Anderson MR (2001) An improved method for determining snowmelt onset dates over Arctic sea ice using scanning multichannel microwave radiometer and special sensor microwave/imager data. J Geophy Res Atmos (1984–2012) 106:24033–24049

Heygster G, Huntemann M, Ivanova N, Saldo R, Pedersen LT (2014) Response of passive microwave sea ice concentration algorithms to thin ice. In: 2014 IEEE international on geoscience and remote sensing symposium (IGARSS), pp. 3618–3621

Kwok R (2009) Outflow of Arctic Ocean sea ice into the Greenland and Barents Seas: 1979–2007. J Clim 22:2438–2457

Lomax AS, Lubin D, Whritner RH (1995) The potential for interpreting total and multiyear ice concentrations in SSM/I 85.5 GHz imagery. Remote Sens Environ 54:13–26

Nghiem S, Rigor I, Perovich D, Clemente-Colón P, Weatherly J, Neumann G (2007) Rapid reduction of Arctic perennial sea ice. Geophy Res Lett 34

Perovich DK, Richter-Menge JA (2009) Loss of sea ice in the arctic. Annu Rev Mar Sci 1:417–441

Serreze MC, Francis JA (2006) The Arctic amplification debate. Clim Change 76:241–264

Steffen K, Schweiger A (1991) NASA team algorithm for sea ice concentration retrieval from defense meteorological satellite program special sensor microwave imager: comparison with Landsat satellite imagery. J Geophys Res Oceans (1978–2012) 96:21971–21987

Stroeve J, Serreze M, Fetterer F, Arbetter T, Meier W, Maslanik J, Knowles K (2005) Tracking the Arctic's shrinking ice cover: another extreme September minimum in 2004. Geophys Res Lett 32

Thomas DN, Dieckmann GS (2009) Sea ice. Wiley, Hoboken

Ulaby FT, Moore RK, Fung AK (1986) Microwave remote sensing active and passive-volume III: from theory to applications

Wang H, Heygster G, Shuzong H, Bin C (2009) Arctic multiyear ice concentration retrieval based on AMSR-E 89 GHz data. Chin J Polar Res 21:186–196

Detecting CDOM Fluorescence Using High Spectrally Resolved Satellite Data: A Model Study

Aleksandra Wolanin, Vladimir Rozanov, Tilman Dinter and Astrid Bracher

Abstract Absorption and fluorescence of CDOM are widely used to characterize its concentration and composition, both in situ and with remote sensing techniques. As fluorescence is an inelastic scattering process, it can potentially be observed in filling-in of Fraunhofer lines with the DOAS method in high spectrally resolved satellite data. Here, we perform a theoretical model study and preliminary DOAS retrieval on SCIAMACHY data in order to test the feasibility of such an approach. Our results show that retrieving CDOM fluorescence is difficult, due to its relatively weak signal in global oceans (in comparison to Raman scattering of clear water) and varying broad spectral features. Detailed studies of the synergistic use of narrow and broad fluorescence features, and an appropriate scheme to account for disturbance effects of Raman scattering, are needed for further investigating the retrieval of CDOM fluorescence.

1 Introduction

Colored or chromophoric dissolved organic matter (CDOM) is part of the dissolved organic matter (DOM) pool, which significantly absorbs light in the UV and blue region of the light spectrum. CDOM plays a role in many physical, chemical and biological processes in aquatic systems. Primarily, it reduces potentially harmful UV radiation within the water column, but on the other hand—when abundant—limits the amount of light available for photosynthesis.

Optical parameters of CDOM are widely used to characterize it both qualitatively and quantitatively. Absorbance and fluorescence of bulks of CDOM are measured

---

A. Wolanin (✉) · V. Rozanov · T. Dinter · A. Bracher
Institute of Environmental Physics, University of Bremen, Bremen, Germany
e-mail: ola@iup.physik.uni-bremen.de

A. Wolanin · A. Bracher
Alfred Wegener Institute Helmholtz Centre for Polar and Marine Research,
Bremerhaven, Germany

G. Lohmann et al. (eds.), *Towards an Interdisciplinary Approach in Earth System Science*, Springer Earth System Sciences,
DOI 10.1007/978-3-319-13865-7_13

locally and globally to examine water quality, chemical composition of dissolved organic matter, trace water masses and study dynamical processes involving CDOM. CDOM fluorescence is a significant inelastic process in natural waters, along with vibrational Raman scattering (VRS) and chlorophyll fluorescence.

Between processes of absorption and emission some energy is dissipated, so the energy emitted is lower than the energy absorbed. The wavelengths at which a photon is absorbed and emitted depend mainly on the molecule itself, but can also depend on several environmental factors, e.g. pH, temperature, a presence of certain metals (Hudson et al. 2007). Fluorescent CDOM is a complex mixture of many fluorescent compounds, and individual fluorophores are hard to identify.

Because of the shift of wavelength in the fluorescence process, its effect on the backscattered radiation at the top of atmosphere is possibly identified in the filling-in of Fraunhofer lines, which are spectrally narrow, often saturated absorption features in the solar spectrum. Other inelastic processes have been already retrieved from hyperspectral satellite data with the Differential Optical Absorption Spectroscopy (DOAS) method (e.g. Vountas et al. 1998, 2003, 2007). In this work we test the use of the filling-in signal originating from CDOM fluorescence to characterize CDOM composition and concentration independent from chlorophyll. This method would also help to improve chlorophyll retrievals in regions of high CDOM concentrations.

2 Methods

2.1 DOAS Retrieval Technique

Different variants of the DOAS technique have been applied for several years for the retrieval of atmospheric trace gases from satellite measurements (e.g. Burrows et al. 1999; Richter et al. 2005), and have lately been extended to the aquatic domain as PhytoDOAS (Vountas et al. 2007: Bracher et al. 2009; Sadeghi et al. 2012). The DOAS method is based on Beer-Lambert's law (e.g. Rozanov and Rozanov 2010) and determines the amount of molecular absorbers along the effective optical light path by fitting and scaling spectra within a given wavelength window. The broad-band effects (e.g. Rayleigh and Mie scattering) are removed by a low-degree polynomial that is also fitted. The fitting in the DOAS method is formalized as a least-squares minimization and is described by the following equation:

$$\left\|\tau(\lambda)-\sum_{n=1}^{N}\sigma_n(\lambda)S_n-\sigma_R(\lambda)S_R-\sigma_V(\lambda)S_V-\sigma_f(\lambda)S_f-\sum_{m=0}^{M}a_m\lambda^m\right\|^2\rightarrow min. \quad (1)$$

Here, $\tau(\lambda)=-\ln\frac{I(\lambda)}{I_0(\lambda)}$ is the so-called slant optical density, $I(\lambda)$ and $I_0(\lambda)$ are the measured backscattered radiance and extraterrestrial irradiance, respectively;

$\sigma_n(\lambda)$ is the absorption cross-section of the nth atmospheric absorber; N is the number of absorbers; $\sigma_R(\lambda)$, $\sigma_V(\lambda)$, and $\sigma_f(\lambda)$ are reference spectra of rotational Raman scattering (RRS), VRS and CDOM fluorescence, respectively; $\sum_{m=0}^{M} a_m \lambda^m$ is the low order polynomial, typically of the order $M \leq 4$.

The minimization is carried out with S_n, S_R, S_V, S_f and polynomial coefficients as the fitted parameters. The parameter S_n is the integrated number density of the nth atmospheric absorber along the slant optical path, which is generally related to the concentration of a given absorber. Parameters S_R, S_V, and S_f are called scaling or fit factors and carry information about the strength of the corresponding inelastic process.

2.2 CDOM Fluorescence Modeling

In order to perform the CDOM fluorescence retrieval with the DOAS method, an adequate fluorescence spectrum has to be used as a priori information, which is then scaled in the fitting procedure. The reference spectrum for CDOM fluorescence is calculated as the difference between the optical density modeled without and with CDOM fluorescence (after Vountas et al. 1998):

$$\sigma_f\ (\lambda) = \ln \frac{I^+(\lambda)}{I^-(\lambda)}, \tag{2}$$

where $I^+(\lambda)$ and $I^-(\lambda)$ are modeled radiances calculated including and excluding inelastic processes, respectively.

The radiances $I^+(\lambda)$ and $I^-(\lambda)$ at the top of the atmosphere have been calculated by using the coupled ocean-atmosphere radiative transfer model SCIATRAN (Rozanov et al. 2014; Blum et al. 2012). Atmospheric conditions, namely the pressure, temperature, and water vapor profiles were set as default in the model for April and latitude of 45°, according to a climatological database obtained using a 2D chemical transport model developed at the University of Bremen (Sinnhuber et al. 2009). The solar zenith angle was set to 45°. Fluorescence was implemented using the spectral volume inelastic function $\beta(z;\xi' \rightarrow \xi;\lambda' \rightarrow \lambda)$, after Mobley (1994):

$$\beta(z;\xi' \rightarrow \xi;\lambda' \rightarrow \lambda) = a(z;\lambda')R(\lambda' \rightarrow \lambda)\tilde{\beta}(\xi' \rightarrow \xi)[m^{-1}sr^{-1}nm - 1], \tag{3}$$

where $a(z;\lambda')$ is an absorption coefficient at the depth z and wavelength λ', usually expressed as a product of a specific absorption coefficient $a^*(\lambda')$ and concentration $C(z)$. $R(\lambda' \rightarrow \lambda)$ is a wavelength redistribution function from excitation wavelength λ' to emission wavelength λ. $\tilde{\beta}(\xi' \rightarrow \xi)$ is a phase function for the radiance emitted from a direction ξ' to a direction ξ, which is assumed to be isotropic. The CDOM fluorescence was implemented into the SCIATRAN radiative transfer model on the base of two different approaches as described below.

2.2.1 CDOM as Mixture of Humic and Fulvic Acids

In his work, Hawes (1992) assumed that fulvic and humic acids comprise the sum of total CDOM (although it is not usually true). Hawes (1992) isolated humic and fulvic acids from several samples and measured their absorption and fluorescence; $a^*(\lambda')$ and spectral fluorescence quantum efficiency functions $\eta(\lambda' \rightarrow \lambda)$ were converted into mathematical functions with linear regression in order to use the data in optical models. He used $\eta(\lambda' \rightarrow \lambda)$ (formulated in numbers of photons), from which we obtained $R(\lambda' \rightarrow \lambda)$ (formulated in terms of energy), according to Mobley (1994). For the purpose of our study, absorption and fluorescence parameters of samples numbered FA7 (of fulvic acids) and HA6 (of humic acids) from Hawes (1992) were used. Specific absorption spectra and fluorescence quantum efficiency functions for these components are shown in Fig. 1. For the investigation of fluorescence structures in the whole spectral range, concentrations of fulvic and humic acids were set separately to 1 and 10 g m^{-3} in the 100 m deep water column. For narrow-band modeling in the spectral region of Fraunhofer line $H\beta$ at 486 nm (see Sect. 3) concentrations of fulvic and humic acids were set simultaneously to 1, 10, 50 and 100 g m^{-3}.

CDOM abundance is typically quantified by its absorption coefficient at a given wavelength (e.g. 443 or 355 nm). For most of the ocean a(443 nm) is below 0.1 m^{-1} (Morel and Gentili 2009), but can be much higher for coastal waters. In European coastal waters a(443 nm) ranges approximately between 0.01 and 1 m^{-1} (Babin, 2003). In our case, 1 g m^{-3} of fulvic or humic acids corresponds to a(443 nm) of 0.075 m^{-1} for FA7 and 0.011 m^{-1} for HA6.

2.2.2 Excitation-Emission Matrices Approach

In the second approach of implementing CDOM fluorescence into SCIATRAN we used a PARAFAC (PARAllel FACtor analysis) model. Nowadays, PARAFAC is

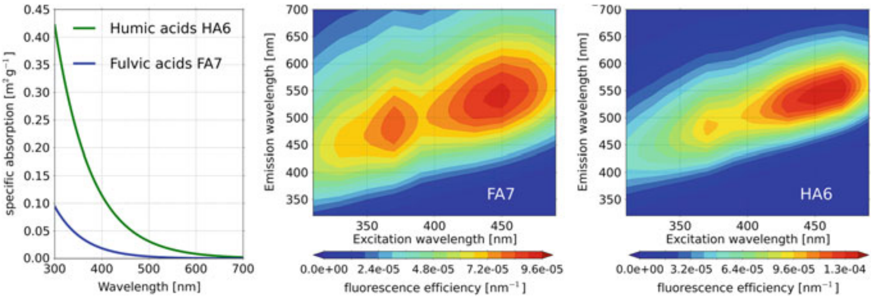

Fig. 1 Specific absorption spectra and fluorescence quantum efficiency functions for samples numbered FA7 (of fulvic acids) and HA6 (of humic acids). Redrawn from Hawes (1992)

widely applied to excitation-emission matrices (EEMs) and enables qualitative and quantitative characterization of CDOM samples (Ishii and Boyer 2012).

The PARAFAC model is similar to a principal component analysis (PCA), but decomposes the data matrix into a set of trilinear terms and a residual array:

$$x_{ijk} = \sum_{f=1}^{F} b_{if} c_{jf} d_{kf} + \varepsilon_{ijk}, \qquad i = 1,\ldots,I; \quad j = 1,\ldots,J; \quad k = 1,\ldots,K \tag{4}$$

According to Stedmon et al. (2003), when applying the PARAFAC model to EEMs, x_{ijk} is the intensity of fluorescence for the ith sample at emission wavelength j and excitation wavelength k; b_{if} is directly proportional to the concentration of the fth component in sample i; c_{jf} is linearly related to the fluorescence quantum efficiency of the fth component at emission wavelength j, d_{kf} is linearly proportional to the specific absorption coefficient at excitation wavelength k. F defines the number of components in the model, and a residual ε_{ijk} represents the variability not accounted for by the model. The parameters of the PARAFAC model are found by the process of minimizing the sum of squared residuals.

For our study we used the data from a paper by Jørgensen et al. (2011), who conducted a broad analysis of CDOM fluorescence on a global scale and identified seven components with the PARAFAC model, using split half analysis for validation (introduction to the PARAFAC technique and description of its application to CDOM fluorescence are presented in more detail in Stedmon and Bro (2008)). Jørgensen et al. (2011) characterized these components by comparing their spectral characteristics to components identified in earlier studies and pure fluorophores. Spectral characteristics (product of matrices **c** and **d**) of seven PARAFAC components are shown in Fig. 2. Jørgensen et al. (2011) identified components 1 and 4 as humic-like DOM. Components 2, 3, 5 and 7 were characterized as amino acid-like DOM, which had spectra similar to phenylalanine, tryptophan and tyrosine. Component 6 had characteristics similar to both groups.

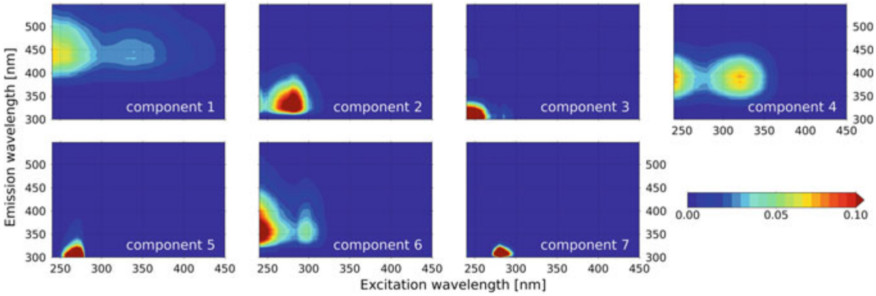

Fig. 2 Fluorescence characteristics of the seven components identified by the PARAFAC analysis and included into radiative transport model SCIATRAN. Redrawn from Jørgensen et al. (2011)

Because it is not known what the fluorescent components are, the molar absorbance, quantum efficiency and concentration cannot be calculated correctly. Hence, the terms of the PARAFAC model are only proportional to the molar absorbance, quantum efficiency and concentration. We decided to scale the matrices in order to obtain values that are realistic and comparable to the first approach we used for CDOM modeling. Fluorescence quantum yields of CDOM were previously reported to range from 0.005 up to 0.025 (Green and Blough 1994). The values obtained by Hawes (1992), used in the first approach of modeling CDOM fluorescence, vary within these limits (0.009 to 0.019). In order to obtain fluorescence yields of the same order for the PARAFAC components, we scaled matrix **c** by a factor of 0.001, after which the fluorescence yields varied between 0.009 and 0.024.

The absorption of the PARAFAC components is calculated as a product of matrices **b** and **d**. We decided to scale these matrices so that we obtain absorption similar to the first modeling approach. In case of humic and fulvic acids, we set their concentrations to 1 and 10 g m^{-3}, and the sum of 1 g m^{-3} of fulvic and 1 g m^{-3} of humic acids lead to the absorption at 443 nm of 0.086 m^{-1}. To be consistent, we scaled the product of matrices so that the final absorption of all components at 443 nm would be similar. In fact, it is only component 1 that absorbs at this wavelength region, and its absorption after applied scaling equaled 0.088 m^{-1} at 445 nm. The scaled matrices were used to calculate R and then the form of spectral volume inelastic scattering function β was derived (Eq. 3). Just like in case of the first modeling approach, we also simulated scenarios for ten times higher concentrations of PARAFAC components. It is important to bear in mind, that we could only scale matrices to realistic values, but their correct values remain unknown.

3 Results and Discussion

With the methods described above, the reference spectra were calculated for fulvic and humic acids (according to Hawes 1992) and for seven PARAFAC components identified by Jørgensen et al. (2011). We investigated the spectral characteristics of different CDOM components, particularly in terms of their possible application in the satellite DOAS retrieval technique. In particular, we looked into the narrow sharp features resulting from filling-in of Fraunhofer lines.

We present reference spectra for fulvic and humic acids and PARAFAC components, calculated according to Eq. 2, in Fig. 3a–c. The noticeable sharp and narrow features correspond to filling-in of Franuhofer lines or telluric absorption lines. Among the amino-acid like PARAFAC components (Fig. 3c), fluorescence of component 2 is noticeably stronger than the others at wavelengths above 310 nm. This component was identified as trypthophan-like (Jørgensen et al. 2011). Components 3 and 7 have very weak fluorescence, and component 5 did not produce any fluorescence signal. In general, amino acid-like components have much smaller (up to three orders of magnitude) reference spectra than the humic-like (Fig. 3b).

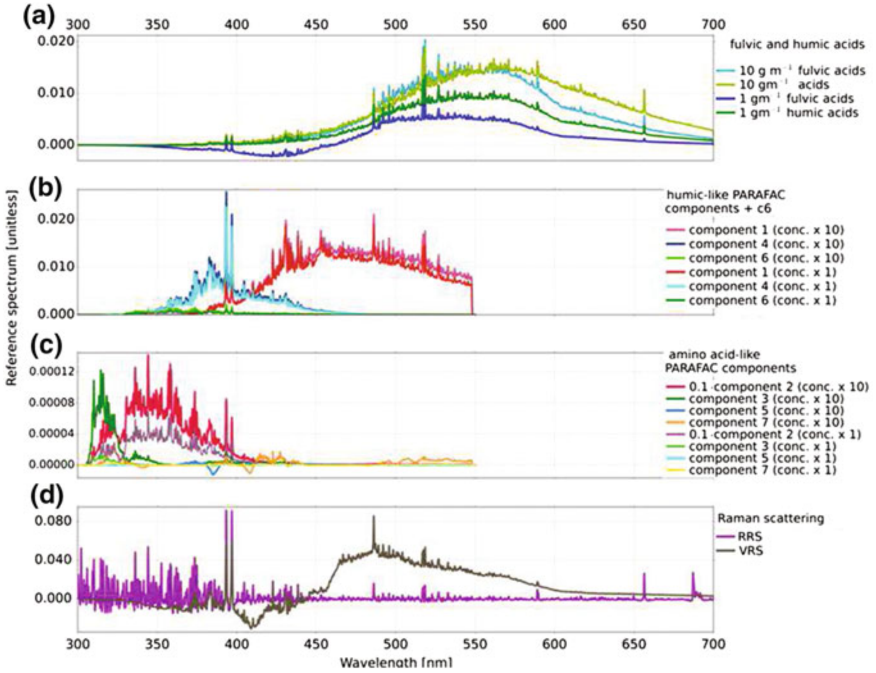

Fig. 3 Calculated reference spectra for: **a** fulvic and humic acids (Hawes 1992), **b**, **c** PARAFAC components (Jørgensen et al. 2011) **d** RRS and VRS

Amino acid-like components exhibit the fluorescence excitation at shorter wavelengths, usually below 300 nm (Jørgensen et al. 2011). Due to this, when it is measured with active techniques, the fluorescence signal is strong; however, it is much weaker in natural conditions as there is little electromagnetic radiation reaching the ocean surface in this wavelengths region. One reason is the shape of the solar spectrum, which has its maximum irradiance in longer wavelengths near 500 nm, and is rapidly decreasing towards shorter wavelengths. The second reason is the strong absorption of ozone in the UV region. Humic-like components of CDOM show stronger fluorescence features under natural conditions, as their excitation spectral region is in longer wavelengths, above 300 nm, where more light is available in the water column.

The spectral shape of humic-like PARAFAC components differs significantly from the spectra of humic acids obtained using the Hawes (1992) approach (Fig. 3a). In case of the latter, their fluorescence emissions start in longer wavelengths and reach further up to 700 nm, which is not the case for the PARAFAC measurements. This difference is probably due to the techniques used by Hawes (1992) to separate and measure humic and fulvic acids absorption and fluorescence. It was shown in previous studies that CDOM extracted with C-18 cartridges (which were used in this case) did not always retain the optical properties of the original water sample (e.g. Vodacek 1989). This conclusion is supported by the results of Green and Blough (1994), which indicate that this isolation procedure preferentially extracts longer wavelength absorbing and fluorescing material that also exhibits higher quantum yields. However, EEMs from oligotrophic waters might also underestimate absorption and fluorescence at longer wavelengths. We can also note, that a ten fold increase in the concentration of CDOM leads to a much smaller increase in filling-in of Fraunhofer lines. This is true in case of both modeling approaches.

In the following, the fluorescence reference spectra were compared to the reference spectra for RRS and VRS, which also lead to filling-in of Fraunhofer lines (Grainger and Ring 1962; Kattawar and Xu 1992). These features can be observed in the whole spectral region of the CDOM fluorescence (Fig. 3d). We can detect that RRS produces especially strong signature in the short wavelength region, where the amino acid-like part of DOM produces weak fluorescence. However, we have to bear in mind, that the PARAFAC components were calculated using a scaling introduced by us and hence the values obtained might deviate from the correct values.

In Fig. 4 the differential parts (after subtracting the polynomial in the spectral region of interest) of the reference spectra, calculated according to Eq. 2, for different inelastic processes are shown. Their structures originate from filling-in of two Fraunhofer lines: Fe I lines at 344 nm (region of relatively strong fluorescence of amino acid-like DOM) and Hβ at 486 nm (the region of fluorescence of humic like DOM). Fraunhofer line Hβ at 486 nm also lies close to the CDOM fluorescence maximum reported in previous studies at 490 nm (e.g. Vodacek et al. 1994; Pozdnyakov et al. 2002). For CDOM spectra we summed up contributions from all defined components of either model. Filling-in of those Fraunhofer lines due to the CDOM fluorescence is relatively weak when compared to filling-in resulting from Raman scattering (RRS, VRS for clear water) for both spectral ranges. For the short-wave fluorescence of amino acid-like components (Fe I lines at 344 nm), the strength of RRS is absolutely dominant over all other inelastic processes (Fig. 4, left panel).

In case of longer wavelengths (Hβ at 486 nm), all processes lead to filling-in of the similar strength (Fig. 4, right panel). In addition, we investigated the effect of

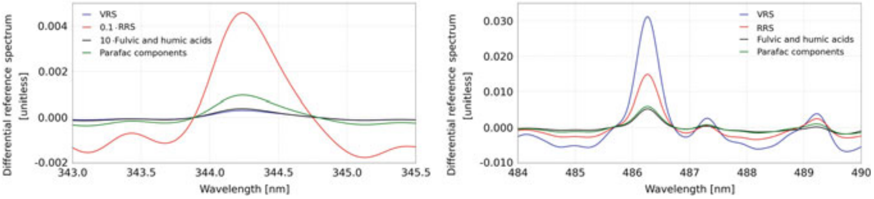

Fig. 4 The differential parts of the reference spectra calculated according to Eq. 2 and Sect. 2.2 for different inelastic processes in the spectral region of Fraunhofer lines Fe I at 344 nm (*left panel*) and Hβ at 486 nm (*right panel*)

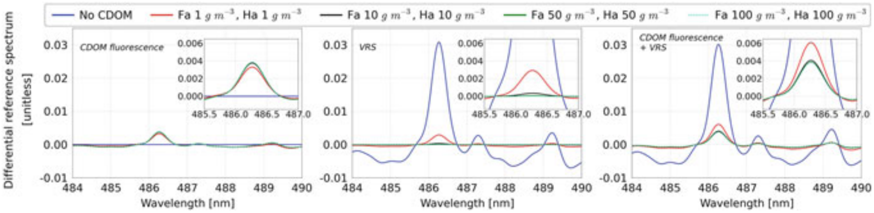

Fig. 5 The differential part of the reference spectra calculated according to Eq. 2 in the spectral region of Fraunhofer line Hβ at 486 nm calculated for different concentrations of humic and fulvic acids and for different inelastic processes: CDOM fluorescence (*left panel*), VRS (*middle panel*), CDOM fluorescence and VRS simultaneously (*right panel*)

varying concentration of fulvic and humic acids (from none to 100 g m^{-3} of each) on the differential reference spectra of CDOM and VRS. In this wavelength region it is more likely to observe the CDOM fluorescence with satellite measurements. However, in clear waters, the VRS signal is dominant, but is weakening with increasing CDOM concentrations (Fig. 5 middle panel). In case of CDOM concentration of 1 g m^{-3} fulvic and 1 g m^{-3} humic acids, both CDOM fluorescence and VRS lead to similar filling-in. In case of CDOM being a mixture of 50 g m^{-3} of fulvic and 50 g m^{-3} humic acids, VRS signal is one order of magnitude weaker than CDOM fluorescence, and for 100 g m^{-3} of fulvic and 100 g m^{-3} of humic acids, the VRS signal is negligible (Fig. 5). However, the filling-in due to CDOM fluorescence itself remains almost constant through all the scenarios of different CDOM concentrations (Fig. 5 left panel). It is due to the fact that with increasing CDOM concentration, light is absorbed stronger and does not penetrate that deep into the water column, hence the bulk CDOM fluorescence signal originates from thinner surface layer of the ocean and is not significantly higher. Our results agree with the previous studies by Pozdnyakov et al. (2002), who showed that VRS is negligible for waters with high CDOM concentrations. Their results also indicate that the CDOM fluorescence signal does not increase substantially with much higher CDOM concentrations, even though it becomes relatively more significant, as in general the upwelling radiance decreases. However, contrary to their results, we found that the VRS in clear waters is stronger than CDOM fluorescence in waters of high CDOM concentration. These discrepancies might be due to the fact that while we are investigating the impact of inelastic process on the filling-in of Fraunhofer lines at the top of the atmosphere, Pozdnyakov et al. (2002), focused on the water volume reflectance. Furthermore, we used the coupled ocean-atmosphere radiative transfer model, while Pozdnyakov et al. (2002), used simple hydrooptical models, which calculate the volume reflectance arising from CDOM fluorescence directly from optical properties of water and CDOM. For scenarios of simultaneous CDOM fluorescence and VRS, we observe that the combined filling-in signal is in fact getting weaker with increasing CDOM concentration (Fig. 5 right panel).

Hence, filling-in signals due to CDOM fluorescence and VRS are coupled: when there is no CDOM, the VRS signal is strong. On the other hand, when CDOM concentrations are high and VRS signal is very weak, there is still significant CDOM fluorescence signal. It follows, that the filling-in signal can be due to strong CDOM fluorescence or strong VRS. However, the VRS is in general a stronger process and filling-in originating from CDOM fluorescence does not increase strongly with increasing CDOM concentration, so in the regions of high CDOM we see in fact weaker filling-in due to absorption of CDOM and weakening of VRS.

As an example, we have run two simple DOAS retrievals for June and July 2009 on the SCIAMACHY (Bovensmann et al. 1999) data in the spectral regions of those Fraunhofer lines (343–345.5 nm and 484–490 nm). For each retrieval we fitted only one reference spectrum, which was a sum of reference spectra of all the PARAFAC components for a respective spectral window. In fact, due to spectral similarities of the filling-in of Fraunhofer lines caused by different processes, the fitted spectra correspond to the contribution from all inelastic processes. We focused on the Atlantic area close to the river mouth of the Amazon, where loading of the terrestrial CDOM into the ocean is generally very high, and where the highest CDOM absorption in the surface waters of open ocean was found in a study by Nelson and Siegel (2013). In Fig. 6 results of fit factors for the two spectral windows are compared to the MODIS-Aqua absorption coefficient for dissolved and detrital particulate matter at 443 nm derived from the Garver-Siegel-Maritorena algorithm (Garver and Siegel 1997; Maritorena et al. 2002). In case of using the filling-in of Hβ line in the retrieval (Fig. 6b), in the area of high CDOM concentration, where we expect strong CDOM fluorescence, the retrieved filling-in of Fraunhofer lines is in fact weaker. It is due to weaker VRS, as described above. For the CDOM fluorescence retrieval in shorter wavelengths (Fig. 6a), when preliminarily examined, the spatial structure of the Amazon plum is not seen and the results are completely dominated by RRS (which is stronger towards higher solar zeniths angle hence higher latitudes). However, these results do not include correction for Raman scattering contribution to filling-in of Fraunhofer lines, which would be necessary for a solid comparison.

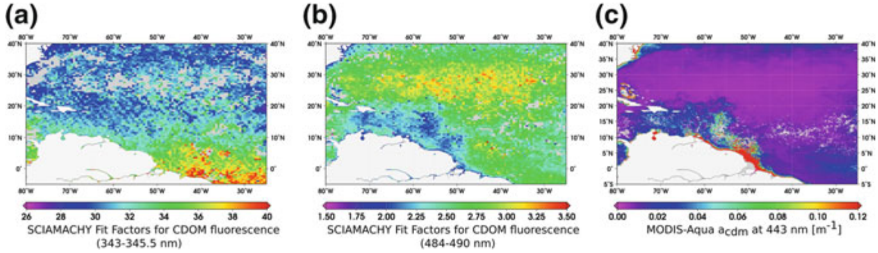

Fig. 6 Maps of retrieved CDOM fluorescence fit factors for 2 months (June and July 2009) in two different spectral regions (**a**, **b**) compared with MODIS-Aqua absorption coefficient for dissolved and detrital particulate matter a_{cdm} at 443 nm $[m^{-1}]$ (**c**)

4 Conclusions and Outlook

Our study shows that although it was possible to estimate inelastic processes with the DOAS method (Vountas et al. 1998, 2003, 2007), it is difficult to use this approach to retrieve CDOM fluorescence from hyperspectral satellite data, mainly because of dominant effects of other inelastic processes (RRS, VRS). However, our modeling studies prove that for coastal areas, where VRS is weak, fluorescence of humic-like CDOM is a significant source of filling-in. Hence, selection of waters with high CDOM concentration should be further studied with satellite or airborne sensor providing much smaller footprints, as well as the good choice of wavelength regions. It is even more difficult to study the composition of CDOM and retrieve fluorescence for the amino acid-like components of DOM, which have excitation and emission in UV-wavelengths. It is due to stronger RRS for shorter wavelengths, very low electromagnetic radiation reaching the surface in the excitation wavelengths, and similar effects in filling-in of Fraunhofer lines. In addition to looking at filling-in of individual Fraunhofer lines, it could be possible to compare broader structures, as filling-in spectra of different CDOM components have spectra distinct from RRS and VRS (Fig. 3). However, due to various composition of CDOM worldwide, those structures vary significantly in time and space, and are not known a priori. Additional precise EEM measurements accompanied by correctly calculated molar absorbance, quantum efficiency and concentration, are needed for improving the modeling of CDOM fluorescence. Combined use of narrow and broad fluorescence features and an appropriate method to account for inelastic processes are as well necessary for further investigating the retrieval of CDOM fluorescence.

Acknowledgments Aleksandra Wolanin gratefully acknowledges financial support provided by the Earth System Science Research School (ESSReS), an initiative of the Helmholtz Association of German Research Centres (HGF) at the Alfred Wegener Institute for Polar and Marine Research (AWI) and HGF Innovative Network Fund (PHYTOOPTICS project). Authors thank DLR and ESA for SCIAMACHY level-1 data. We also acknowledge the MODIS mission scientists and associated NASA personnel for the production of the data used in this research effort. Analyses and visualizations were produced with the Giovanni online data system, developed and maintained by the NASA GES DISC. We also thank C. Stedmon and K. Carder for providing CDOM data and their helpful comments throughout the development of this chapter.

References

Babin M (2003) Variations in the light absorption coefficients of phytoplankton, nonalgal particles, and dissolved organic matter in coastal waters around Europe. J Geophys Res 108(C7)

Blum M, Rozanov V, Burrows J, Bracher A (2012) Coupled ocean-atmosphere radiative transfer model in the framework of software package SCIATRAN: selected comparisons to model and satellite data. Adv Space Res 49(12):1728–1742

Bovensmann H, Burrows JP, Buchwitz M, Frerick J, Noël S, Rozanov VV, Chance KV, Goede APH (1999) SCIAMACHY: mission objectives and measurement modes. J Atmos Sci 56 (2):127–150

Bracher A, Vountas M, Dinter T, Burrows J, Röttgers R, Peeken I (2009) Quantitative observation of cyanobacteria and diatoms from space using PhytoDOAS on SCIAMACHY data. Biogeosciences 6:751–764

Burrows JP, Weber M, Buchwitz M, Rozanov V, Ladstätter-Weißenmayer A, Richter A, DeBeek R, Hoogen R, Bramstedt K, Eichmann K-U (1999) The global ozone monitoring experiment (GOME): mission concept and first scientific results. J Atmos Sci 56(2):151–175

Garver SA, Siegel DA (1997) Inherent optical property inversion of ocean color spectra and its biogeochemical interpretation: 1. time series from the Sargasso Sea. J Geophys Res 102 (C8):18607

Grainger JF, Ring J (1962) Anomalous Fraunhofer line profiles. Nature 193(4817):762

Green SA, Blough NV (1994) Optical absorption and fluorescence properties of chromophoric dissolved organic matter in natural waters. Limnol Oceanogr 39(8):1903–1916

Hawes SK (1992) Quantum fluorescence efficiencies of marine fulvic and humic acids. M.Sc. thesis. University of South Florida, Tampa

Hudson N, Baker A, Reynolds D (2007) Fluorescence analysis of dissolved organic matter in natural, waste and polluted waters-a review. River Res Appl 23(6):631–649

Ishii SKL, Boyer TH (2012) Behavior of reoccurring PARAFAC components in fluorescent dissolved organic matter in natural and engineered systems: a critical review. Environ Sci Technol 46(4):2006–2017

Jørgensen L, Stedmon CA, Kragh T, Markager S, Middelboe M, Søndergaard M (2011) Global trends in the fluorescence characteristics and distribution of marine dissolved organic matter. Mar Chem 126(1–4):139–148

Kattawar GW, Xu X (1992) Filling in of Fraunhofer lines in the ocean by Raman scattering. Appl Opt 31(30):6491

Maritorena S, Siegel D, Peterson A (2002) Optimization of a semianalytical ocean color model for global-scale applications. Appl Opt 41(15):2705–2714

Mobley CD (1994) Light and water: radiative transfer in natural waters. Academic Press, San Diego (u.a.)

Morel A, Gentili B (2009) A simple band ratio technique to quantify the colored dissolved and detrital organic material from ocean color remotely sensed data. Remote Sens Environ 113 (5):998–1011

Nelson NB, Siegel DA (2013) The global distribution and dynamics of chromophoric dissolved organic matter. Annu Rev Mar Sci 5(1):447–476

Pozdnyakov D, Grassl H, Lyaskovsky A, Pettersson L (2002) Numerical modelling of transspectral processes in natural waters: Implications for remote sensing. Int J Remote Sens 23(8):1581–1607

Richter A, Burrows JP, Nüß H, Granier C, Niemeier U (2005) Increase in tropospheric nitrogen dioxide over China observed from space. Nature 437(7055):129–132

Rozanov V, Rozanov A, Kokhanovsky A, Burrows J (2014) Radiative transfer through terrestrial atmosphere and ocean: software package SCIATRAN. J Quant Spectrosc Radiat Transfer 133:13–71

Rozanov VV, Rozanov AV (2010) Differential optical absorption spectroscopy (DOAS) and air mass factor concept for a multiply scattering vertically inhomogeneous medium: theoretical consideration. Atmos Meas Tech 3:751–780

Sadeghi A, Dinter T, Vountas M, Taylor B, Altenburg-Soppa M, Bracher A (2012) Remote sensing of coccolithophore blooms in selected oceanic regions using the PhytoDOAS method applied to hyper-spectral satellite data. Biogeosciences 9:2127–2143

Sinnhuber B-M, Sheode N, Sinnhuber M, Chipperfield MP, Feng W (2009) The contribution of anthropogenic bromine emissions to past stratospheric ozone trends: a modelling study. Atmos Chem Phys 9:2863–2871

Stedmon C, Markager S, Bro R (2003) Tracing dissolved organic matter in aquatic environments using a new approach to fluorescence spectroscopy. Mar Chem 82(3–4):239–254

Stedmon CA, Bro R (2008) Characterizing dissolved organic matter fluorescence with parallel factor analysis: a tutorial. Limnol Oceanogr Methods 6:572–579

Vodacek A (1989) Synchronous fluorescence spectroscopy of dissolved organic matter in surface waters: application to airborne remote sensing. Remote Sens Environ 30(3):239–247

Vodacek A, Green SA, Blough NV (1994) An experimental model of the solar-stimulated fluorescence of chromophoric dissolved organic matter. Oceanography 39(1)

Vountas M, Dinter T, Bracher A, Burrows JP, Sierk B (2007) Spectral studies of ocean water with space-borne sensor SCIAMACHY using differential optical absorption spectroscopy (DOAS). Ocean Sci 3(3):429–440

Vountas M, Richter A, Wittrock F, Burrows JP (2003) Inelastic scattering in ocean water and its impact on trace gas retrievals from satellite data. Atmos Chem Phys 3(5):1365–1375

Vountas M, Rozanov V, Burrows J (1998) Ring effect: impact of rotational Raman scattering on radiative transfer in Earth’s atmosphere. J Quant Spectrosc Radiat Transfer 60(6):943–961

Part III
Physical Oceanography

The Flow of Dense Water Plumes in the Western Weddell Sea Simulated with the Finite Element Ocean Model (FEOM)

Mathias Rucker van Caspel, João Marcelo Absy, Qiang Wang, Hartmut H. Hellmer and Michael Schröder

Abstract Ocean simulations performed with the Finite Element Ocean Model (FEOM) were used to show the relevance of the location of the dense water plume source on the western Weddell Sea continental shelf. When the plume starts close to the tip of the Antarctic Peninsula it flows into Bransfield Strait, but if it is found further south it can flow down the slope and contribute to Weddell Sea Deep Water (WSDW). The influence of density on the spreading was also tested indicating that a denser plume reaches greater depths while lighter plumes do not interact with the WSDW.

Keywords Plume · Larsen ice shelf · Weddell Sea Deep Water · Ocean modelling · Bransfield strait

1 Introduction

The shelf waters from the northwestern Weddell Sea contribute to the production of Weddell Sea Deep Water (WSDW) (e.g. Absy et al. 2008), which is one important source of the water mass that fills most of the world ocean abyss, the Antarctic Bottom Water (AABW) (e.g. Orsi et al. 1999). Besides of this global relevance, part of the water contours the Antarctic Peninsula (AP) and enters the Bransfield Strait, playing an important role for the circulation of this region (e.g. Gordon et al. 2000; García et al. 2002).

WSDW is transported by the clockwise circulation of Weddell Gyre and is formed by the mixture of Weddell Sea Bottom Water with Warm Deep Water

---

Scholarship from CNPq/DAAD (Process 290034/2011-6).

M.R. van Caspel (✉) · J.M. Absy · Q. Wang · H.H. Hellmer · M. Schröder
Alfred Wegener Institute, Helmholtz Centre for Polar and Marine Research,
Bremerhaven, Germany
e-mail: mcaspel@awi.de

G. Lohmann et al. (eds.), *Towards an Interdisciplinary Approach in Earth System Science*, Springer Earth System Sciences,
DOI 10.1007/978-3-319-13865-7_14

(WDW) or by the interaction of shelf waters with WDW (e.g. Nicholls et al. 2009). As the current flows north along the isobaths, dense waters observed on the continental shelf in front of the Larsen Ice Shelf (LIS) flow down the slope mixing with the ambient waters and increasing the volume of WSDW (e.g. Absy et al. 2008).

As the current reaches the tip of the AP it turns east along the South Scotia Ridge and forms the northern branch of the gyre. Through a passage in the Powell Basin, the Philip Passage, or one of the deep gaps in the South Scotia Ridge, Orkney Passage, Bruce Passage, and Discovery Passage, the WSDW escapes from the Weddell Sea to form AABW (e.g. Naveira Garabato et al. 2002).

As mentioned before, part of the shelf water is deviated to the west and enters the Bransfield Strait. There, the relatively cold and salty Weddell Sea waters mix with water masses from the Antarctic Circumpolar Current and from the Bellingshausen Sea, filling almost the entire Strait. One assumes that the Bransfield Deep Water is a mixture of Weddell shelf waters with WDW modified by in situ winter conditions (García et al. 2002).

In the present work we investigate how changes in the characteristics of the dense shelf waters observed off LIS may impact the neighboring basins. To reach this goal we used numerical simulations performed with the Finite Element Ocean Model (FEOM).

2 Model Setup and Experiments

FEOM is a 3D finite-element primitive equation ocean circulation model based on an unstructured horizontal mesh. The version used in this study is fully described by Wang et al. (2008a). For our experiments a triangular grid that goes from 25 to 80°S and encircles the Antarctic Continent was created. The surface mesh resolution varies from 1/15° (approx. 3.3 km) in the area of investigation, i.e. the western Weddell Sea, to 2° in the remaining areas. 21 terrain-following (σ) vertical levels with increased resolution close to the bottom and in the surface mixed layer were used (Wang et al. 2008b). The bathymetry was derived from the 2-Minute Gridded Global Relief Data (ETOPO2 2001).

To the south the continent limits the domain, and for the northern open boundary a restoring of temperature and salinity to climatological values from the World Ocean Atlas 1994 (WOA01) (Levitus and Boyer 1994) was used along 15° of latitude. The model was initialized with mean temperature and salinity fields extracted from WOA01 and forced with the wind stress from the National Centers for Environmental Predictions (NCEP) reanalysis (see e.g. Trenberth et al. 1990), and sea surface temperature and salinity were relaxed to the WOA01 values. After 4.5 years of integration the model was stable and we initialized the outflow experiments.

Two sensitivity tests were performed: task (a) to assess the importance of the latitude were the dense water plume is formed and task (b) to study the effects of initial density on the spreading of the plume. All simulations start on the first day of June and run for 8 months with a 6-minutes time-step. In each case, a plume source occupying half of the water column was placed on the continental shelf for 2 months. Afterwards the integrations continued without any further adjustments. The plumes were marked with a passive tracer.

For the first task two experiments were carried out: the dense water source was placed where (a) the former LIS A and B were located (experiment L1) and (b) in front of LIS C (L2). The temperature (−1.92 °C) and salinity (34.64) values used were obtained from observations (station 301 in Absy et al. 2008).

The second task consisted of two experiments with the plume starting at the same position of L2. In the first run, the density of the water (σ_0) was reduced from 27.89 kg/m^3, L1 and L2, to 27.73 kg/m^3 using an increased temperature (−1.69 °C) and lower salinity (34.45) (S1). In the second simulation the density was raised to 27.97 kg/m^3 by increasing the salinity to 34.75 (S2).

3 Results

The plume starting at L1 leads to a major flow into Bransfield Strait (BS) (Fig. 1). The spreading path bifurcates at the tip of the AP. The southern branch flows southwest along the Strait southern slope of BS and then turns north-northeast to spread along the opposite margin. This path agrees well with the circulation scheme

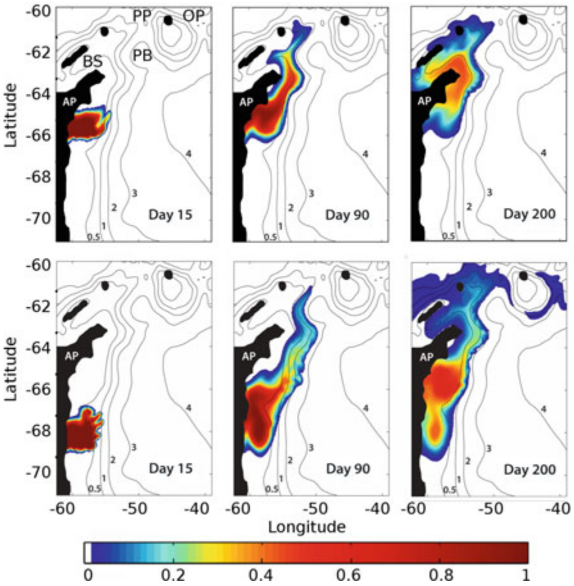

Fig. 1 Tracer concentration in simulations L1 (*upper panels*) and L2 (*lower panels*) after 15 (*left*), 90 (*middle*) and 200 (*right*) days. The abbreviations in the upper left panel represent Bransfield Strait (*BS*), Orkney Passage (*OP*), Powell Basin (*PB*), and Philip Passage (*PP*)

proposed for this region (e.g. García et al. 2002). The other branch flows along the northern rim of Powell Basin, leaving the Weddell Sea at the western margin of Philip Passage.

In L2, part of the plume flows down the slope and is carried by the Weddell Gyre, while the water that remains on shelf flows north with smaller velocities (Fig. 1). The portion transported by the gyre enters Powell Basin, flows around South Orkney Island and leaves the Weddell Sea through the South Orkney Passage, with some leakage of dense water through Philip Passage. The waters remaining on the continental shelf follow the same path as described in L1.

In simulation S2 the spreading paths are similar to L2, but the dilution by the surrounding ambient takes a longer time (distance) and the plume water reaches greater depths than in the other runs. When lighter water is prescribed (S1), the northward flow is restricted to the continental shelf and the upper part of the slope, and the dilution below the shelf break is higher. When the traced water gets closer to the tip of the AP a behavior analogous to the first 90 days of L1 is observed, but the simulation period ends before the southwestward flow into BS can occur.

4 Summary and Conclusions

Our experiments have shown that dense water found close to the tip of the Antarctica Peninsula flows mainly into Bransfield Strait, while if it is located further south, it can flow down the slope and contribute to the WSDW that might be converted into AABW. The importance of the waters from the northwestern Weddell Sea for the fringing basins is already known, but we showed that the location where the plume starts defines whether it will flow into Bransfield Strait or into the Scotia Sea.

This result support the idea that the freshening of the deep waters from BS (Garcia and Mata 2005) is associated with the freshening observed on the northwestern Weddell Sea (Hellmer et al. 2011). Further investigation of this subject will be carried out using the Finite Element Sea Ice-Ocean Model (FESOM) (Wang et al. 2013), a model that simulate sea-ice formation and the interaction with the fringing ice shelf, both crucial for the dense water production.

Another crucial factor for the spreading of the LIS plume is its initial density. Lighter water mixes faster with the ambient waters and does not influence the WSDW while denser water sinks to greater depth. Due to the lack of data, the variability of the plume is not known. Modelling attempts will be made to illuminate this issue, but in situ measurements are indispensable for understanding this region, its influence on the fringing basins, and its importance for the World Ocean.

Acknowledgments We would like thank Mauricio Mata and Oliver Huhn (reviewers) for their comments to improve this manuscript and the suggestions for the future work. The first author was supported by CNPq grant 290034/2011-6.

References

Absy JM, Schröder M, Muench R, Hellmer HH (2008) Early summer thermohaline characteristics and mixing in the western Weddell Sea. Deep Sea Res Part II 55:1117–1131

ETOPO2 (2001) Global gridded 2-minute database. National Geophysical Data Center, National Oceanic and Atmospheric Administration, U.S. Dept. of Commerce

García M, Castro C, Ríos A, Doval M, Rosón Gomis D (2002) Water masses and distribution of physico-chemical properties in the Western Bransfield Strait and Gerlache Strait during Austral summer 1995/96. Deep Sea Res Part II 49:585–609

Garcia CAE, Mata MM (2005) Deep and bottom water variability in the central basin of Bransfield Strait (Antarctica) over the 1980–2005 period. Clivar Exchanges 10(4):48–50

Gordon AL, Mensch M, Zhaoqian D, Smethie WM Jr, de Bettencourt J (2000) Deep and bottom water of the Bransfield Strait eastern and central basins. J Geophys Res 105(C5):11337–11346

Hellmer HH, Huhn O, Gomis D, Timmermann R (2011) On the freshening of the northwestern Weddell Sea continental shelf. Ocean Sci 7:305–316

Levitus S, Boyer P (1994) World Ocean Atlas 1994: temperature. NOAA, NESDIS, Washington, DC, p 117

Naveira Garabato AC, Heywood KJ, Stevens DP (2002) Modification and pathways of southern ocean deep waters in the Scotia Sea. Deep Sea Res Part I 49:681–705

Nicholls KW, Østerhus S, Makinson K, Gammelsrød T, Fahrbach E (2009) Ice-ocean processes over the continental shelf of the southern Weddell Sea, Antarctica: a review. Rev Geophys 47: RG3003

Orsi AH, Johnson GC, Bullister JL (1999) Circulation, mixing, and production of Antarctic Bottom Water. Prog Oceanogr 43:55–109

Trenberth KE, Large WG, Olson JG (1990) The mean annual cycle in global ocean wind stress. J Phys Oceanogr 20:1742–1760

Wang Q, Danilov S, Schröter J (2008a) Finite element ocean circulation model based on triangular prismatic elements, with application in studying the effect of topography representation. J Geophys Res 113(C05015):21

Wang Q, Danilov S, Schröter J (2008b) Comparison of overflow simulations on different vertical grids using the finite element ocean circulation model. Ocean Model 20(4):313–335

Wang Q, Danilov S, Sidorenko D, Timmermann R, Wekerle C, Wang X, Jung T, Schröter J (2013) The finite element sea ice-ocean model (FESOM): formulation of an unstructured-mesh ocean general circulation model. Geoscientific Model Dev Discuss 6:3893–3976

Data Analysis and Modeling of the Amundsen Sea Embayment

Yoshihiro Nakayama, Ralph Timmermann, Michael Schröder
and Hartmut H. Hellmer

Abstract The Pine Island Ice Shelf (PIIS) is melting rapidly, which may have a large impact on ice sheet dynamics, sea-level rise, and changes in water mass properties of the surrounding ocean. The reason for the PIIS melting is the relatively warm (~ 1.2 °C) Circumpolar Deep Water (CDW) that approaches the PIIS cavity through two submarine glacial troughs located on the Amundsen Sea continental shelf. Since CDW causes melting of some other glaciers in West Antarctica in a similar way, understanding the PIIS melting helps to understand the impact of ocean-ice sheet interaction on the mass balance of the West Antarctic ice sheet and the impact of climate change in the Southern Ocean. Thus, in my PhD study, we investigate the CDW intrusion onto the Amundsen Sea continental shelf by (a) analyzing hydrographic data obtained during ANTXXVI/3 in 2010 and (b) using the Finite Element Sea ice-Ocean Model (FESOM). We focus on the intruding CDW properties and demonstrate the difficulties of modeling CDW intrusion onto the Amundsen Sea continental shelf. We further show that the choice of forcing is not the reason for the difficulties in reproducing the CDW intrusions.

1 Introduction

Pine Island Ice Shelf (PIIS) and Thwaites Glacier (TG) are the major ice streams of the West Antarctic Ice Sheet (WAIS), draining around 393,000 km^2, and driving the largest ice loss of the Antarctic ice sheet (e.g. Shepherd et al. 2001; Rignot et al. 2002, 2008, 2011, 2013; Wingham et al. 2009; Joughin and Alley 2011; Shepherd et al. 2012). The reason for the large ice loss is increased basal melting due to the interaction of deep-drafted ice shelves with Circumpolar Deep Water (CDW) which is about 3 °C warmer than the in situ freezing point (e.g. Jacobs et al. 2011;

Y. Nakayama (✉) · R. Timmermann · M. Schröder · H.H. Hellmer
Alfred Wegener Institute Helmholtz Centre for Polar and Marine Research, Bremerhaven, Germany
e-mail: Yoshihiro.Nakayama@awi.de

G. Lohmann et al. (eds.), *Towards an Interdisciplinary Approach in Earth System Science*, Springer Earth System Sciences,
DOI 10.1007/978-3-319-13865-7_15

Pritchard et al. 2012). This relatively warm water flows onto the continental shelf through submarine glacial troughs (Jacobs et al. 2011). When this warm water reaches the grounding line, it melts basal ice and forms a buoyant plume of CDW mixed with meltwater. This plume flows out from the ice shelf cavity and drives the continuous intrusion of CDW into the PIIS cavity. Recent results show that the averaged melt rates for PIIS in 2009 and 2010 are estimated to be about 30 m year^{-1} (Jacobs et al. 2011; Nakayama et al. 2013).

The melting of PIIS and other ice shelves of the WAIS can have large impacts on the global ocean. First, 10 % of the observed sea level rise has been attributed to the thinning of the WAIS (Rignot et al. 2008)—the WAIS has the potential to raise global sea level by about 3.3 m (Bamber et al. 2009). Second, it may cause the freshening of the shelf water locally in the Amundsen Sea as well as remotely in the Ross Sea (Jacobs et al. 2002). This may lead to a change in the characteristics of the Antarctic Bottom Water (AABW) formed in the Ross Sea (Jacobs et al. 2002; Rintoul 2007) and thus may influence the global thermohaline circulation. Therefore, investigations related to the PIIS melting and its impact on the ocean is crucial for understanding climate change in the Southern Ocean.

In this study, we show hydrographic data obtained during Polarstern cruise ANTXXVI/3 in 2010 with focus on the CDW intrusion. Then, we discuss the difficulties of modeling the CDW intrusions into the Amundsen Sea embayment and the sensitivity of CDW intrusion to the different model forcings.

2 Hydrographic Data Analysis

Sampling was carried out during ANTXXVI/3 from the research ice breaker RV Polarstern (Gohl 2010). In total 62 conductivity-temperature-depth (CTD) profiles were collected on this cruise including one Heli-CTD measurement Fig. 1a. The details of the measurements are summarized in Nakayama et al. (2013).

The vertical distribution of potential temperature for Sects. 1, 2 (Fig. 1) mainly show Winter Water (WW) with the potential temperature minimum at 100–300 m and warm CDW from 300–400 m to the bottom. The potential temperature section for the north–south Sect. 2 (Fig. 1c), which connects the deepest stations of each east-west section, shows that CDW clearly dominates the lower part of the water column, and that CDW is present all along the bottom towards the PIIS cavity. A similar result is presented in Jacobs et al. (2011) from their observations in 2009. Along the surface-referenced isopycnal of 27.7, CDW with the potential temperature of 1 °C, salinity of 34.5, and dissolved oxygen of 4.2 ml kg^{-1} flows onto the continental shelf and into the PIIS cavity (Jacobs et al. 2011; Nakayama et al. 2013). The maximum isopycnal that reaches PIIS is ~27.79 (not shown), while the 27.8-isopycnal only advances to the center of Pine Island Trough (PIT). When compared with the previous observations, the bottom CDW properties do not change largely within the last two decades [e.g. the temporal variability of potential temperature in PIT is small (~0.2 °C) (Nakayama et al. 2013)].

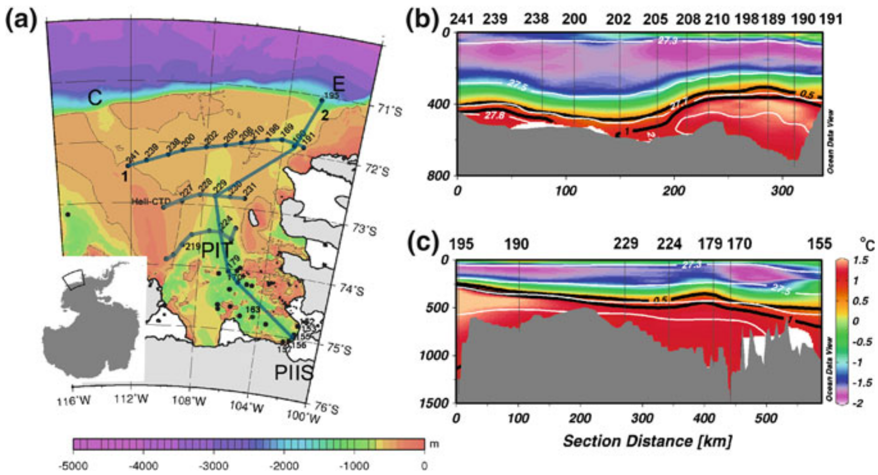

Fig. 1 **a** Distribution of CTD stations in the eastern Amundsen Sea of the cruise ANTXXVI/3 in 2010 with bathymetry, ice shelf, and coastline (*gray shade*). The 500-m contour is also shown (*thin gray*). The *lower-left inlet* figure shows Antarctica with the enclosed region denoting the location of the enlarged portion. *Solid dots* indicate the position of CTD stations and *lines marked 1–2* are the sections discussed in this paper. The location of Pine Island Ice Shelf (PIIS) and Pine Island Trough (PIT) are shown. Letters *E* and *C* mark the submarine glacial troughs located on the eastern and central Amundsen Sea continental shelf. **b** Vertical section of potential temperature of Sect. 1 shown by *colors* and *thick black* contours. Surface referenced potential density is indicated by *white contours*. The *vertical black lines* mark the location of CTD profiles with station numbers shown at the *top*. *Bottom* topography is based on RTopo-1 (Timmermann et al. 2010). **c** Same as b but along Sect. 2

3 Modeling of the Amundsen Sea

Several approaches have been conducted to simulate the CDW intrusion onto the Amundsen Sea continental shelf in regional and global models (Thoma et al. 2008; Timmermann et al. 2009, 2012; Schodlok et al. 2012; Assmann et al. 2013; Kusahara and Hasumi 2013). Although regional models have been successful, global models have not yet reproduced a realistic CDW flow onto the continental shelf.

In this study, we analyze the results of the global Finite-Element Sea ice-ice shelf-Ocean Model (FESOM) and focus on the CDW intrusion onto the Amundsen Sea continental shelf. Details of this model are summarized in Timmermann et al. (2009, 2012). We use a tetrahedral mesh with a horizontal length scale of 50 km along non-Antarctic coasts, which is refined to ~10 km along the Antarctic coast, 7 km under the larger ice shelves in the Ross and Weddell Seas, and ~5 km in the central Amundsen and Bellingshausen seas. To allow for an adequate representation of ice shelf cavities, we apply a hybrid vertical-coordinate system with 36 layers where the top 23 layers are terrain-following in a region along the Antarctic coast for depth shallower than 2,500 m. The model is forced with daily data from NCEP/NCAR reanalysis and ERA-interim reanalysis (Kalnay et al. 1996; Dee et al. 2011) for the period of 1979–1988. We refer to these two cases as NCEP and ERA.

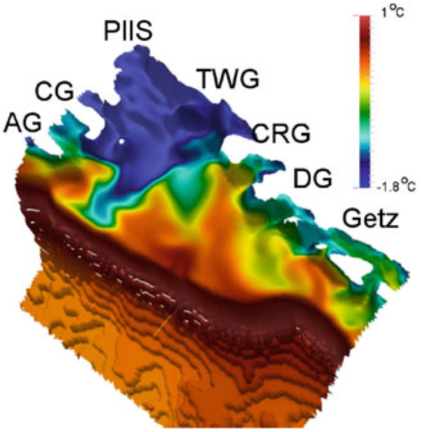

Fig. 2 Modeled bottom potential temperature in the Amundsen Sea for January 1984 in the NCEP case (*AG* Abbot Glacier, *CG* Cosgrove Glacier, *PIIS* Pine Island Ice Shelf, *TWG* Thwaites Glacier, *CRG* Crosson Glacier, *DG* Doston Glacier, *Getz* Getz Glacier)

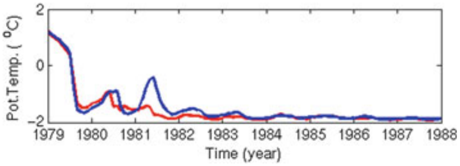

Fig. 3 Time series of PIIS ice front bottom potential temperature with NCEP reanalysis (*red*) and ERA-interim (*blue*) forcings

In the NCEP case as shown by Timmermann et al. (2012), the Amundsen Sea remains cold throughout this model run, and potential temperature at the bottom becomes nearly equal to −1.8 °C after 3–4 years of model simulation (Fig. 2), while observations show a watermass warmer than 1 °C at the bottom near the PIIS ice front Sect. 1. Timmermann et al. (2012) indicate that the large difference is caused by a cold bias in NCEP reanalysis winter temperature, as demonstrated by Assmann et al. (2005). In the ERA case, however, CDW temperature at the PIIS ice front remains cold and no significant change can be seen compared to the NCEP case (Fig. 3). This indicates that the forcing is not the only reason for the difficulties in reproducing CDW intrusion onto the Amundsen Sea continental shelf.

4 Discussion and Outlook

In this paper, we show the data from hydrographic observations in 2010 (RV Polarstern cruise, ANTXXVI/3) and discuss the two FESOM simulations with different atmospheric forcing. As shown by previous studies, CDW intrudes onto the eastern Amundsen Sea continental shelf through the submarine glacial troughs located at the shelf break (Nakayama et al. 2013; Assmann et al. 2013). Along the surface-referenced isopycnal of 27.7, CDW with the potential temperature of 1 °C, salinity of 34.5, and dissolved oxygen of 4.2 ml kg^{-1} flows towards and into the PIIS cavity Fig. 1b.

The model result presented by Timmermann et al. (2012) is not realistic in the Amundsen Sea, showing a bottom potential temperature of ~ -1.8 °C with almost no CDW intrusion (Fig. 2). Although Timmermann et al. (2012) suggest that NCEP reanalysis forcing is the reason for the cold Amundsen Sea condition, the simulation with ERA-interim forcing cannot reproduce the CDW intrusion either, indicating that the forcing is not the only reason for the cold conditions on the Amundsen Sea continental shelf in FESOM.

The reason for the difficulties of simulating CDW intrusion onto the Amundsen Sea continental shelf is published in Nakayama et al. (2014).

References

Assmann KM, Hellmer HH, Jacobs SS (2005) Amundsen sea ice production and transport. J Geophys Res Oceans (1978–2012) 110:C12

Assmann KM, Jenkins A, Shoosmith DR, Walker DP, Jacobs SS, Nicholls KW (2013) Variability of circumpolar deep water transport onto the amundsen sea continental shelf through a shelf break trough. J Geophys Res Oceans 118(12):6603–6620

Bamber JL, Riva REM, Vermeersen BLA, LeBrocq AM (2009) Reassessment of the potential sea-level rise from a collapse of the west antarctic ice sheet. Science 324(5929):901–903

Dee DP, Uppala SM, Simmons AJ, Berrisford P, Poli P, Kobayashi S, Andrae U, Balmaseda MA, Balsamo G, Bauer P et al (2011) The ERA-Interim reanalysis: configuration and performance of the data assimilation system. Q J R Meteorol Soc 137(656):553–597

Gohl K (2010) The expedition of the research vessel polarstern to the amundsen sea. Rep Polar Mar Res 617:173

Jacobs SS, Giulivi CF, Mele PA (2002) Freshening of the ross sea during the late 20th century. Science 297(5580):386

Jacobs SS, Jenkins A, Giulivi CF, Dutrieux P (2011) Stronger ocean circulation and increased melting under pine island glacier ice shelf. Nat Geosci 4(8):519–523

Joughin I, Alley RB (2011) Stability of the west antarctic ice sheet in a warming world. Nat Geosci 4(8):506–513

Kalnay E, Kanamitsu M, Kistler R, Collins W, Deaven D, Gandin L, Iredell MO, Saha S, White G, Woollen J et al (1996) The NCEP/NCAR 40-year reanalysis project. Bull Am Meteorol Soc 77 (3):437–471

Kusahara K, Hasumi H (2013) Modeling antarctic ice shelf responses to future climate changes and impacts on the ocean. J Geophys Res Oceans 118(5):2454–2475

Nakayama Y, Schröder M, Hellmer HH (2013) From circumpolar deep water to the glacial meltwater plume on the eastern Amundsen Shelf. Deep Sea Res Part I: Oceanographic Research Papers 77:50–62, hdl:10013/epic.41617, doi:10.1016/j.dsr.2013.04.001

Nakayama Y, Timmermann R, Schröder M, Hellmer HH (2014) On the difficulty of modeling circumpolar deep water intrusions onto the amundsen sea continental shelf. Ocean Model 84:26–34, hdl:10013/epic.44341, doi:10.1016/j.ocemod.2014.09.007

Pritchard HD, Ligtenberg SRM, Fricker HA, Vaughan DG, Van den Broeke MR, Padman L (2012) Antarctic ice-sheet loss driven by basal melting of ice shelves. Nature 484(7395):502–505

Rignot E, Vaughan DG, Schmeltz M, Dupont T, MacAyeal D (2002) Acceleration of pine Island and thwaites glaciers. Ann Glaciol 34(1):189–194

Rignot E, Bamber JL, den Broeke MRV, Davis C, Li Y, de Berg WJV, Meijgaard EV (2008) Recent antarctic ice mass loss from radar interferometry and regional climate modelling. Nat Geosci 1(2):106–110

Rignot E, Mouginot J, Scheuchl B (2011) Ice flow of the antarctic ice sheet. Science 333 (6048):1427–1430

Rignot E, Jacobs SS, Mouginot J, Scheuchl B (2013) Ice-shelf melting around antarctica. Sci Express 341:226–270

Rintoul SR (2007) Rapid freshening of antarctic bottom water formed in the indian and pacific oceans. Geophys Res Lett 34(6):L06606

Schodlok MP, Menemenlis D, Rignot E, Studinger M (2012) Sensitivity of the ice shelf ocean system to the sub-ice shelf cavity shape measured by NASA icebridge in pine island glacier. Ann Glaciol 53:156–162

Shepherd A, Wingham DJ, Mansley JAD, Corr HFJ (2001) Inland thinning of pine island glacier. Science 291(5505):862

Shepherd A, Ivins ER, Geruo A, Barletta VR, Bentley MJ, Bettadpur S, Briggs KH, Bromwich DH, Forsberg R, Galin N et al (2012) A reconciled estimate of ice-sheet mass balance. Science 338(6111):1183–1189

Thoma M, Jenkins A, Holland D, Jacobs S (2008) Modelling circumpolar deep water intrusions on the amundsen sea continental shelf. Geophys Res Lett 35(18)

Timmermann R, Danilov S, Schröter J, Böning C, Sidorenko D, Rollenhagen K (2009) Ocean circulation and sea ice distribution in a finite element global sea ice–ocean modelOcean Model 27(3):114–129

Timmermann R, Brocq AL, Deen T, Domack E, Dutrieux P, Galton-Fenzi B, Hellmer H, Humbert A, Jansen D, Jenkins A et al (2010) A consistent data set of antarctic ice sheet topography, cavity geometry, and global bathymetry. Earth Syst Sci Data 2(2):261–273

Timmermann R, Wang Q, Hellmer H (2012) Ice shelf basal melting in a global finite-element sea ice/ice shelf/ocean model. Ann Glaciol 53(60)

Wingham DJ, Wallis DW, Shepherd A (2009) Spatial and temporal evolution of pine island glacier thinning. Geophys Res Lett 36(17):L17501

Part IV
Sea-ice Physics

Impact of Sea-Ice Bottom Topography on the Ekman Pumping

Giulia Castellani, Rüdiger Gerdes, Martin Losch and Christof Lüpkes

Abstract Sea-ice elevation profiles and thickness measurements have been collected during summer 2011 in the Central Arctic. These two different data sets have been combined in order to obtain surface and bottom topography of the sea-ice. From the bottom profile, the keels of ridges are detected. Then, a parameterization of oceanic drag coefficients that accounts for the keels depth and density is applied. The calculated oceanic drag coefficients are highly variable (between about 2×10^{-3} and about 8×10^{-3}) within the range of observed values. In order to estimate the contribution of variable drag coefficients on the Ekman pumping, the calculated drag coefficients are used in an idealized model experiment, where sea ice is drifting at constant velocity on an ocean at rest. The resulting variations of the Ekman vertical velocity are in the same order of magnitude as for variable ice velocity at the surface. In most state-of-the-art general circulation models, the variations of drag coefficients are not taken into account. The simple experiment carried out in the present study suggests that neglecting this contribution can lead to an incorrect representation of the momentum exchange between ice and ocean and to an underestimation of the Ekman pumping, with consequences for the large scale ocean circulation.

G. Castellani (✉) · R. Gerdes · M. Losch · C. Lüpkes
Alfred Wegener Institute Helmholtz Center for Polar and Marine Research,
Bussestrasse 24, 27570 Bremerhaven, Germany
e-mail: giulia.castellani@awi.de

R. Gerdes
e-mail: ruediger.gerdes@awi.de

M. Losch
e-mail: martin.losch@awi.de

C. Lüpkes
e-mail: christof.luepkes@awi.de

G. Castellani
Jacobs University, Bremen, Germany

G. Lohmann et al. (eds.), *Towards an Interdisciplinary Approach in Earth System Science*, Springer Earth System Sciences,
DOI 10.1007/978-3-319-13865-7_16

1 Introduction

The sea ice in the Arctic Ocean has a surface and bottom topography that is characterized by many different scales from small hummocks and piles of ice to large ridges. A pressure ridge consists of a part that extends into the atmosphere (sail) and a part that extends into the ocean (keel).

The sails are usually above one meter, sometimes they can be as high as 2 m. In order to satisfy the hydrostatic equilibrium, the keels usually extend much deeper into the ocean and may reach depths of 30 m (Pite et al. 1995). The formation of these topographic features depends on the ice motion. In particular, large pressure ridges are formed when the ice is exposed to strong convergence.

The main forces that govern the ice motion are the internal forces (Steele et al. 1989), the local winds and the ocean currents (Thorndike and Colony 1982). In the momentum balance equation that describes the ice motion, the interactions between air, ice and water are parameterized by drag coefficients. These drag coefficients must account for sea-ice surface characteristics on the near-surface transport of momentum. The sea-ice surface is spatially and temporally inhomogeneous and thus we can expect spatial and temporal variations of the drag coefficients as well.

Many studies addressed the dependence of the drag coefficients on the surface topography of the ice. In particular, for the atmospheric drag coefficients, parameterizations for numerical models have been developed (see, e.g., Birnbaum and Lüpkes 2002; Garbrecht et al. 2002; Lüpkes and Birnbaum 2005; Lüpkes et al. 2012, 2013). In these parameterizations the atmospheric drag coefficients are a function of surface characteristics of the ice (i.e., melt ponds, pressure ridges, floe edges). Only very few studies focused on the oceanic drag coefficients. Among these few, the studies by Steiner et al. (1999) and Steiner (2000) relate the drag coefficients to the roughness of the ice, whereas in Lu et al. (2011) the oceanic drag coefficients are expressed as a function of observable geometric parameters of the sea ice such as the depth of keels, the mean separation between ridges, and the floe edges.

The momentum transferred by wind or ice to the ocean is redistributed by vertical turbulent mixing from the surface to a certain depth. The layer with turbulence, that is where the vertical variations of the surface stress are not negligible, is called the *Ekman layer*. The fluxes of momentum lead to the formation of a velocity field in the surface layer of the ocean. Associated with the induced velocity is the vertical *Ekman pumping* (when directed downwards) or *Ekman suction* (when directed upwards). The Ekman pumping (suction) depends on the wind stress applied at the upper surface and represents the amount of volume pumped from below into (or from above out of) the Ekman layer. It was also shown (Rabe et al. 2011) that variations in Ekman pumping affect the depth of the 34-isohaline with consequences for the entire ocean circulation. In most state-of-the-art global circulation models, the stress at the ice-ocean interface depends on the variability of the wind field, while variations in the drag coefficients are usually not taken into account. In the present study we calculate oceanic drag coefficients as function of observed ice topography. These drag coefficients are then used to illustrate the effects on Ekman pumping when only the spatial variations of the oceanic drag are considered.

2 Data and Methods

The data used for this study were collected by helicopter flights over the Arctic Ocean during a campaign with the ice breaker *RV Polarstern* in summer 2011. The map with the tracks along which the data have been collected is shown in Fig. 1.

During the campaign, two different types of data have been collected: sea-ice surface elevation profiles using a laser altimeter and sea-ice thickness using the so-called EM-bird. The laser altimeter profiles are collected using a Riegel LD90-3100HS that was introduced in 2001. This instrument has a wavelength of 905 nm, a sampling frequency of 100 Hz and an accuracy of ±1.5 cm. The point spacing is about 30–40 cm. The profiles recorded by the laser altimeter show an altitude variation due to the surface roughness of the ice and a variation at a lower frequency due to the movement of the helicopter. In order to remove this movement, a combination of low and high pass filters is used (Hibler 1972).

The EM-bird is a device to measure the sea-ice thickness directly using electromagnetic induction (Haas 2004; Haas et al. 2009). The EM-bird contains two coils for transmission and receptions of electromagnetic fields and can measure the distance between the instrument and the ice-ocean interface by using the electromagnetic field generated by induction in the conductive sea water. In addition, a

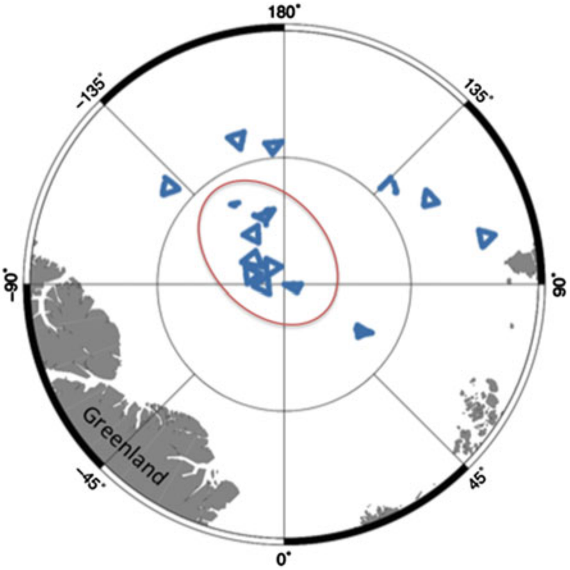

Fig. 1 Map of the Arctic Ocean with the location of the laser altimeter and EM-bird measurements. The *red circle* encloses the measurements taken in the area that in the present study is referred to as the Central Arctic

laser altimeter (as described above) gives the distance of the instrument to the surface (ice or snow), hence the thickness is obtained by the difference between laser and EM measurements. The sea-ice thickness is sampled at 10 Hz, which leads to an average point spacing of ~4 m. The footprint of the instrument is about 40 m (Kovacs et al. 1995; Redi et al. 2006). Ice thickness samples thinner than 0.1 m are considered as open water. Since sea ice surface and underside profiles are recorded at the same time we can have a complete description of the ice topography on the surface and underneath the ice.

In order to obtain information about the bottom topography of the ice, in each point where both measurements are available, the thickness recorded with the EM-bird is subtracted from the filtered laser altimeter profiles. The spatial resolution is lower than the one for the upper surface (30–40 cm) since the thickness measurements are recorded every ~4 m. A routine is then applied to the filtered profile to select minima that are deeper than a certain threshold value. The procedure is the same as used in other studies for the detection of sails from surface ice profiles (e.g. Von Saldern et al. 2006; Rabenstein et al. 2010). Values ranging from −5 to –9 m can be used as thresholds for keel detection (Davis and Wadhams 1996; Williams et al. 1975). Here we assume a sail height to keel depth ratio of 4 (Timco and Burden 1997). In the studies by, e.g., Rabenstein et al. (2010), Von Saldern et al. (2006) a sail height of 0.8 m is used as threshold value for the identification of sails. This gives a threshold value for the keel depth equal to −3.2 m. Since the EM-bird underestimates the real thickness of ridges by up to 50–60 % (Haas 2004), we

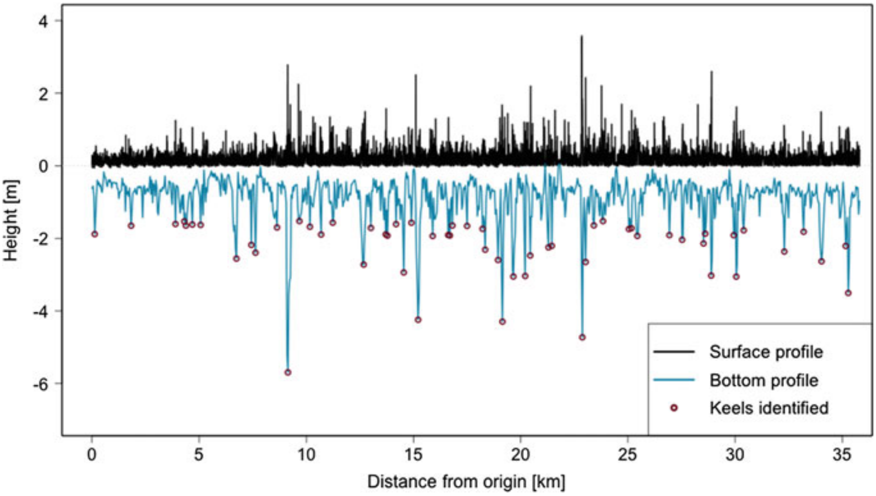

Fig. 2 An example of a sea ice profile of ca. 35 km length. The *black line* shows the upper surface profile obtained by the filtered laser altimeter data. The *light blue line* represents the bottom profile of the ice obtained by subtracting the thickness from the laser altimeter profiles. The *circles* represent the detected keels. The depth of the keels is then multiplied by a factor of 2 as described in Sect. 2

finally choose a cut-off depth of −1.5 m. Moreover, two adjacent keels have to satisfy the Rayleigh criterion: the minimum points must be separated by a point whose depth is less than half of the depth of the keel in order to be resolved as separate entity (Hibler 1975; Wadhams and Horne 1980; Wadhams and Davy 1986). An example of a final profile is shown in Fig. 2. The depth of the keels that are detected and shown in Fig. 2 are then multiplied by a factor of 2 in order to account for the systematic underestimation of the maximum draft by a factor of 2 due to the EM technique (Haas 2004; Martin 2007).

3 Calculation of Oceanic Drag Coefficients

In order to calculate the oceanic drag coefficients we make use of a parameterization presented in Lu et al. (2011). This parameterization is based on a partitioning concept that was already introduced for atmospheric drag coefficients in Arya (1973, 1975). The parameterization in Lu et al. (2011) distinguishes between the influence of small scale roughness (skin drag) and larger obstacles such as the keels associated with ridges and the edges of the ice floes (form drag). Since we focus our analysis on areas with 100 % sea-ice cover, the contribution of floe edges can be neglected.

The oceanic drag coefficient c_w is then the sum of the skin drag c_w^s and the form drag due to ridges c_w^r:

$$c_w = c_w^s + c_w^r. \tag{1}$$

The drag contributions, in the case of sea-ice concentration A equal to 1, are calculated as following:

$$c_w^s = C_s\left(1 - m\frac{H_r}{D_r}\right), \tag{2}$$

$$c_w^r = \frac{C_r H_r}{\pi D_r}\left[1 - \left(\frac{H_r}{D_r}\right)^{1/2}\right]^2. \tag{3}$$

H_r and D_r are the mean depth of the keels and the mean separation between them respectively. The remaining constants are: $m = 1$, $C_r = 0.5$ and $C_s = 2 \times 10^{-3}$.

For the calculation of the drag coefficients we need to compute the mean depth of the keels H_r and the mean separation D_r between them as obtained from the available data. We focus on the Central Arctic region (see Fig. 1). There, we have 320 profiles. The length of each profile varies between ca. 10 km and 30 km for a total of more than 700 km of data. For each profile we detect the keels as described in Sect. 2 and we calculate the mean depth and the mean spacing between them.

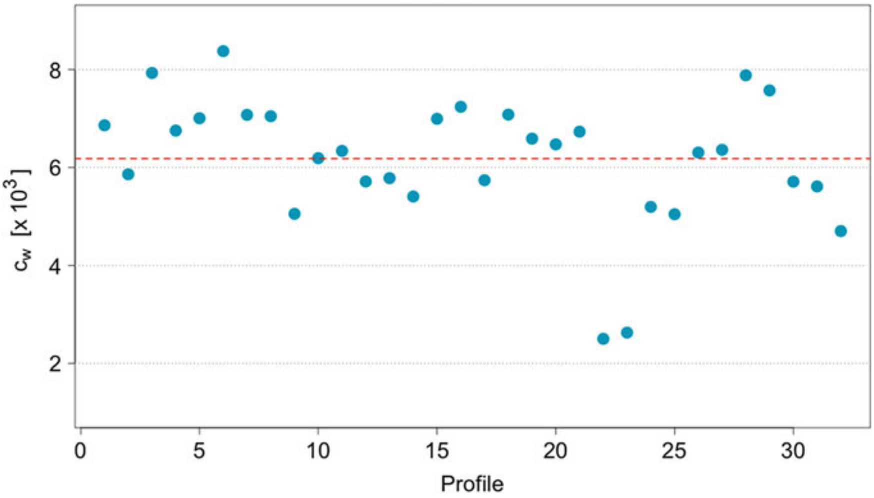

Fig. 3 Values of the oceanic drag coefficients c_w calculated for the Central Arctic. The *red line* represents the mean value

With this information we can calculate the drag coefficients for each profile. The results are shown in Fig. 3.

Only a few measurements of oceanic drag coefficients are available for comparing the results obtained with Eqs. 2 and 3. Lu et al. (2011) showed (see their Table 1) that oceanic drag coefficients can vary from 1×10^{-3} to even 22×10^{-3}. Our calculated values lie within this range. We stress that the oceanic drag coefficients vary strongly with the sea-ice topography and that the choice of a constant value used in global circulation models might imply a bias in the estimation of the momentum exchange between the ice and the ocean.

4 Ekman Pumping

Ekman pumping in the ocean depends on the spatial variation of the stress applied at the surface. This spatial variation is a consequence of variations in both the velocity field and the drag coefficients. In this section we want to evaluate the contribution to Ekman pumping that is caused only by variations of the drag coefficients. We thus set up a very simple experiment. 32 grid cells aligned along y, each 20 km wide, form a domain of 20 km × 640 km. This domain is covered completely with sea ice (100 % sea-ice cover). The surface and bottom properties of the ice are varying from one cell to the other, so that the drag coefficients are also different. In particular, to each grid cell we assign a value for the drag coefficient that was calculated (see Sect. 3) on the basis of real sea-ice topography. We assume that the ice is in motion along x with a constant velocity $v_{\mathrm{ice}} = 0.05$ m/s while the ocean is at rest. We then compute the Ekman pumping with:

$$w_{\mathrm{E}} = \hat{z} \cdot \nabla \times \frac{\tau}{\rho_0 f}, \tag{4}$$

where ρ_0 is the mean density of the sea water, τ is the stress at the surface, f is the Coriolis parameter. The stress term τ is given by:

$$\tau = \rho_0 c_w |\mathbf{v}_{\mathrm{ice}}| \mathbf{v}_{\mathrm{ice}}. \tag{5}$$

The formulation (Eq. 4) of the Ekman vertical velocity is only valid for large domains in a steady state and our 20 km grid axes may be too small. Nevertheless we can use such a simplified formulation because we are not primarily interested in quantifying actual Ekman pumping, but we would like to illustrate the importance of variations in the value of oceanic drag coefficients alone on the Ekman pumping. The results of our calculations are shown in Fig. 4. In this simple experiment there would not be Ekman pumping if the drag coefficients were constant in the whole domain. The range of variations of the vertical velocity is between −20 and 30 cm/day. Simulated variations in the Ekman vertical velocity based on variations of the surface stress when no keels are taken into account are shown in Rabe et al. (2011) (their Fig. 6): Here the range of variations of annual mean vertical velocities over different regions in the Arctic is between −5 and 3 cm/day. In Rabe et al. (2011) the variations in the ocean-surface stress are caused by variations only in the wind field and not by variations in the drag coefficients. In our study we see a much higher variation than in Rabe et al. (2011) but we stress once more that their result shows variations averaged over the entire basin while here we focus on local variations.

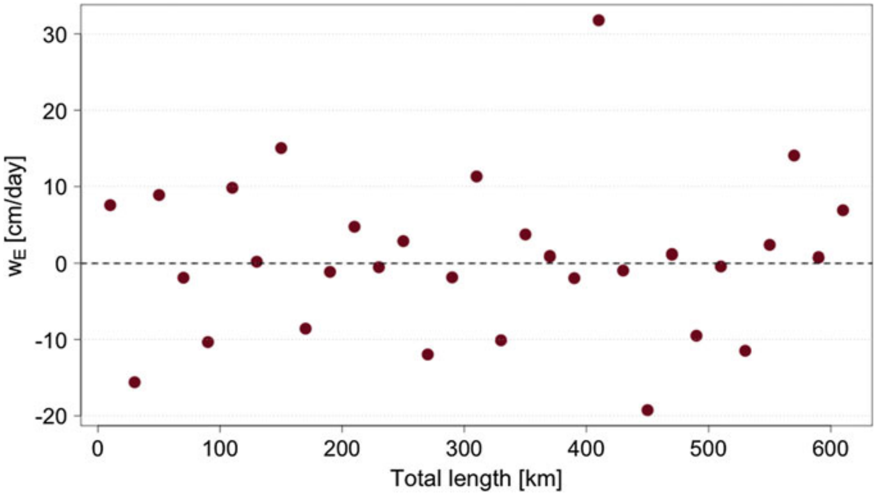

Fig. 4 Ekman pumping calculated for the idealized situation described in Sect. 4

From the results of this calculation we can conclude that the variations in Ekman pumping associated with variable oceanic drag coefficients is at least in the same order of magnitude as the variations due to changes in the surface velocity of the ice. Even though the strong local effect might be damped when averages are taken over a larger area, we can still assume that the effect will remain of the same order of the velocity variations shown by Rabe et al. (2011). Thus we speculate that the presence of different sea-ice regimes on a large scale may induce a basin-scale variation in Ekman pumping that then would have consequences for the Ekman transport and the large scale ocean circulation. Numerical experiments and simulations with large scale sea ice-ocean models could help to investigate the effect on an Arctic basin scale ocean circulation.

5 Summary and Conclusion

Airborne altimetry and EM-bird observations have been used in the present study to reconstruct the surface and bottom topography of the sea-ice in the Arctic Ocean.

From the obtained profiles we detected the keels and calculated keel mean depth and keel mean separation along profiles of different length. This information is then used to calculate the oceanic drag coefficients. These coefficients are calculated by applying a parameterization presented in Lu et al. (2011) to a hypothetical situation of 100 % sea-ice cover. The calculated drag coefficients are in the range of values obtained by in situ observations. The range of variability is large and this suggests that the choice of a constant drag in sea-ice numerical models might lead to a misrepresentation of the actual ice-ocean momentum transfer.

The calculated oceanic drag coefficients have been used for a rough calculation of Ekman pumping. The results provide an insight into the expected magnitude of Ekman pumping caused by the variability of the oceanic drag coefficients. The upper layer vertical velocity generated by variations in drag coefficients is on the same order of magnitude as for variable ice velocity at the surface. In order to better understand the importance of the variable drag coefficients on the large scale oceanic circulation, Pan Arctic simulations with global circulation models are required. The results shown here suggest that neglecting the contribution of variable oceanic drag coefficients in the momentum transfer between ice and ocean can lead to considerable errors in numerical models or data analysis.

Acknowledgments We would like to thank the crew of the RV Polarstern and the HeliService International GmbH. Moreover we thank all the people who contributed to collect the laser altimeter data and EM-bird data, in particular Stefan Hendricks. We are also very thankful to Michael Karcher for the interesting and constructive discussions. Finally we thank the Earth System Science Research School (ESSReS) for any support to this study and to the PhD project.

References

Arya SPS (1973) Contribution of form drag on pressure ridges to the air stress on Arctic ice. J Geophys Res 78(30):7092–7099

Arya SPS (1975) A drag partitioning theory for determining the large-scale roughness parameter and wind stress on the Arctic pack ice. J Geophys Res 80(24):3447-–3454

Birnbaum G, Lüpkes C (2002) A new parameterization of surface drag in the marginal sea ice zone. Tellus 54A:107–123

Davis N, Wadhams P (1996) A statistical analysis of Arctic pressure ridge morphology. J Geophys Res 100:10915–10925

Garbrecht T, Lüpkes C, Hartman J, Wolf M (2002) Atmospheric drag coefficients over sea ice—validation of a parameterization concept. Tellus 54(2):205–219

Haas C (2004) EM ice thickness measurements during GreenICE 2004 field campaign. Tech Rep EU project GreenICE (EVK2-2001-00280), Alfred Wegener Institute, Bremerhaven

Haas C, Lobach J, Hendricks S, Rabenstein L, Pfaffling A (2009) Helicopter-borne measurements of sea ice thickness, using a small and lightweight, digital EM system. J Appl Geophys 67:234–241

Hibler WD III (1972) Removal of aircraft altitude variation from laser profiles of the Arctic pack. J Geophys Res 77(36):7190–7195

Hibler WD III (1975) Characterization of cold-regions terrain using airborne laser profilometry. J Geophys Res 77(36):7190–7195

Kovacs A, Holladay J, Bergeron C Jr (1995) The footprint altitude ratio for helicopter electromagnetic sounding of sea-ice thickness: comparison of theoretical and field estimates. Geophysics 60(2):374–380. doi:10.1190/1.1443773

Lu P, Li Z, Cheng B, Leppäranta M (2011) A parameterization of the ice-ocean drag coefficient. J Geophys Res 116:C07019

Lüpkes C, Birnbaum G (2005) Surface drag in the Arctic marginal sea-ice zone: a comparison of different parameterisation concepts. Bound-Layer Meteorol 117:179–211. doi:10.1007/s10546-005-1445-8

Lüpkes C, Gryanic VM, Hartmann J, Andreas EL (2012) A parameterization, based on sea ice morphology, of the neutral atmospheric drag coefficients for weather prediction and climate models. J Geophys Res 117:D13112

Lüpkes C, Gryanic V, Rösel A, Birnbaum G, Kaleschke L (2013) Effects of sea ice morphology during Arctic summer on atmospheric drag coefficients used in climate models. Geophys Res Lett doi:10.1029/2012GL054354

Martin T (2007) Arctic sea ice dynamics: drift and ridging in numerical models and observations. Ber Polarforsch Meeresforsch 563 (PhD thesis, ISSN 1618-3193)

Pite HD, Topham DR, Hardenberg JV (1995) Laboratory measurements of the drag force on a family of two-dimensional ice keel models in a two-layer flow. J Phys Oceanogr 25(12):3008–3031

Rabe B, Karcher M, Schauer U, Toole JM, Krishfield RA, Pisarev S, Kauker F, Gerdes R, Kikuchi T (2011) An assessment of Arctic Ocean freshwater content changes from the 1990s to the 2006–2008 period. Deep Sea Res Part I: Oceanogr Res Pap 58(2):173–185

Rabenstein L, Hendricks S, Martin T, Pfaffhuber A, Haas C (2010) Thickness and surface-properties of different sea-ice regimes within the Arctic Trans Polar Drift: data from summers 2001, 2004 and 2007. J Geophys Res 115. doi:10.1029/2009JC005846

Redi J, Pfaffling A, Vrbancich M (2006) Airborne electromagnetic footprints in 1D earths. Geophysics 71:G63–G72

Steele M, Morison JH, Untersteiner N (1989) The partition of air-ice-ocean momentum exchange as a function of ice concentration, floe size, and draft. J Geophys Res 94(C9):12739–12750

Steiner N (2000) Introduction of variable drag coefficients into sea-ice models. Ann Glaciol 33:181–186

Steiner N, Harder M, Lemke P (1999) Sea-ice roughness and drag coefficients in a dynamic–thermodaynamic sea-ice model for the Arctic. Tellus 51A:964–978

Thorndike AS, Colony R (1982) Sea ice motion in response to geostrophic winds. J Geophys Res 87:5845–5852

Timco M, Burden RP (1997) An analysis of the shape of sea ice ridges. Cold Reg Sci Technol 25:65–77

Von Saldern C, Haas C, Dierking W (2006) Parameterization of Arctic sea-ice surface roughness for application in ice type classification. Ann Glaciol 44:224–230

Wadhams P, Davy T (1986) On the spacing and draft distributions for pressure ridges keels. J Geophys Res 91(C9):10697–10708. doi:10.1029/JC09p10697

Wadhams P, Horne R (1980) An analysis of ice profiles obtained by submarine sonar in the Beaufort Sea. J Glaciol 25:401–424

Williams E, Swithinbank C, de Robin GQ (1975) A submarine sonar study of Arctic pack ice. J Glaciol 15(73):349–362

Classification of CryoSat-2 Radar Echoes

Robert Ricker, Stefan Hendricks, Veit Helm and Rüdiger Gerdes

Abstract Sea-ice thickness at global scale is an important variable in the polar climate system. Only satellite altimeters such as onboard the CryoSat-2 mission allow us to obtain sea-ice thickness on hemispherical scale. Accurate CryoSat-2 altimeter range measurements provide surface elevations which have to be referenced to the local sea level to obtain sea-ice freeboard that can be converted into sea-ice thickness assuming hydrostatic equilibrium. The local sea-surface height is determined by careful detection of leads in the ice surface using the specific characteristics of the radar signal. Off-nadir reflections from leads can significantly affect the range retracking and hence bias the surface elevations of leads and sea ice. This can finally lead to a negative freeboard and hence also affects the thickness and volume retrieval. We present a method for the classification of CryoSat-2 radar echoes to correctly discriminate between valid and off-nadir biased echoes. We apply our classification to a CryoSat-2 track from December 15 where 50 leads over a distance of 2,300 km are identified. Overall 22 % of the surface elevations are associated with biased radar echoes.

R. Ricker (✉) · S. Hendricks · R. Gerdes
Helmholtz Centre for Polar and Marine Research, Alfred Wegener Institute,
Bussestrasse 24, 27570 Bremerhaven, Germany
e-mail: Robert.Ricker@awi.de

S. Hendricks
e-mail: Stefan.Hendricks@awi.de

R. Gerdes
e-mail: Ruediger.Gerdes@awi.de

V. Helm
Helmholtz Centre for Polar and Marine Research, Alfred Wegener Institute,
Am Alten Hafen 26, 27568 Bremerhaven, Germany
e-mail: Veit.Helm@awi.de

G. Lohmann et al. (eds.), *Towards an Interdisciplinary Approach in Earth System Science*, Springer Earth System Sciences,
DOI 10.1007/978-3-319-13865-7_17

1 Introduction

Several studies have shown considerable evidence that the Arctic sea ice is thinning during the last decades (Haas et al. 2010; Kwok et al. 2009; Rothrock et al. 1999). When combined with the observed rapid reduction of the ice covered area (Comiso 2002; Comiso et al. 2008; Stroeve et al. 2012) this leads to a decline in sea-ice volume (Laxon et al. 2013). The only remote sensing technique capable of quantifying this ice-volume decrease at global scale is satellite altimetry. This method is based on the retrieval of the sea-ice freeboard, which is the height of the ice-surface above the local sea level (Fig. 1a). Assuming hydrostatic equilibrium the freeboard can be converted into sea-ice thickness (Giles et al. 2008; Kwok et al. 2009; Wadhams et al. 1992) and with additional information into sea-ice volume (Laxon et al. 2013).

Satellite altimeters are operated in different electromagnetic wavelength ranges. The laser altimeter onboard the ICESat mission featured a small footprint (70 m) but was affected by clouds. Radar altimeters on the other hand are not affected by clouds but have a larger footprint of several kilometres. CryoSat-2 is the current

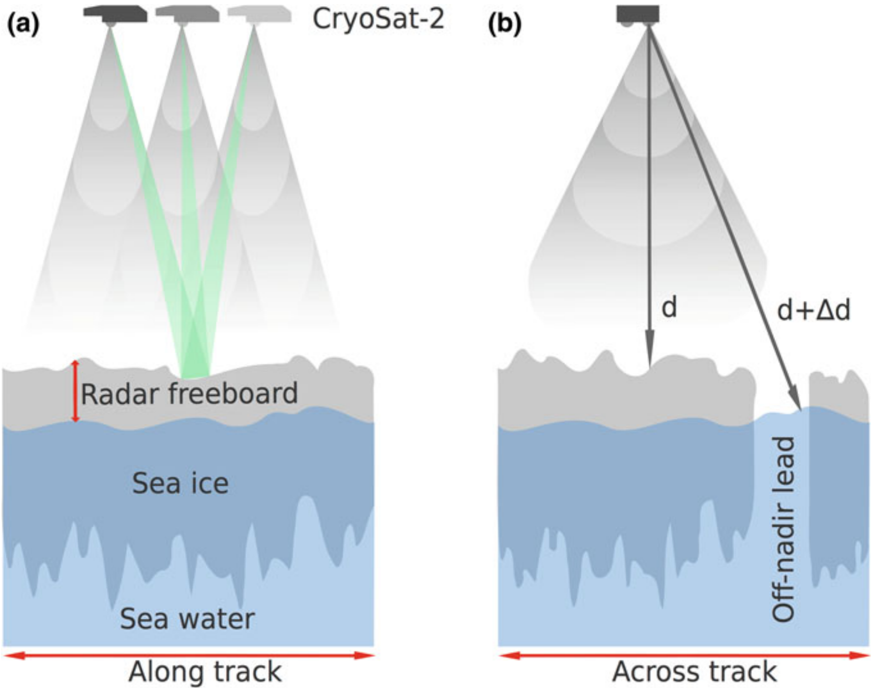

Fig. 1 **a** Scheme of CryoSat-2 measurements along track. The *green* illuminated area illustrates a Doppler cell. **b** Scheme of CryoSat-2 measurement across track with an off-nadir lead at the edge of the main radar lobe, causing a range bias of Δd

satellite altimeter mission of the European Space Agency (ESA) and was launched in April 2010, with special emphasis on Arctic sea ice. It is equipped with a Ku-Band SAR radar altimeter synthetic aperture interferometric radar altimeter (SIRAL) that uses along-track beam sharpening (Wingham et al. 2006) to reduce footprint size compared to previous radar altimeter missions (ERS1/2, Envisat). By using the effect of the *Doppler shift* the radar footprint can be divided into stripes called *Doppler cells* (for CryoSat-2 approximately 250 m). Each cell is illuminated from different incident angles as the satellite passes by (Fig. 1a). The echoes of each illumination are stacked to reduce noise. This method results in a higher resolution than pulse-limited radar altimeters like onboard ERS1/2 and Envisat.

Since the uncertainties of freeboard can easily reach the magnitude of freeboard itself, optimized algorithms that reduce errors and uncertainties in CryoSat-2 freeboard retrieval are necessary. The first step in obtaining sea-ice freeboard is to determine the main scattering horizon to receive geolocated surface elevations (Kurtz et al. 2014; Ricker et al. 2014). In this study a *threshold first-maximum retracker* with a 40 % threshold (TFMRA40) (Helm et al. 2014; Ricker et al. 2014) is applied to the geolocated radar echoes (waveforms) that are provided by the European Space Agency. Within this retracker algorithm the waveform is oversampled and smoothed. We compute the derivative to find the first maximum of the waveform and assign the main scattering horizon at 40 % of this first peak. The effects of different thresholds and retrackers on the freeboard retrieval can be substantial and have been investigated in Ricker et al. (2014) and Kurtz et al. (2014). In the second step the geolocated CryoSat-2 elevations have to be referenced to the sea level to obtain the freeboard. We apply a waveform classification algorithm (Ricker et al. 2014) in order to detect leads which are narrow open water areas in the ice surface. At leads the sea level can directly be obtained by the CryoSat-2 range measurement. The lead elevations are interpolated along the CryoSat-2 ground tracks to receive the actual sea-surface height which is then subtracted from the sea-ice elevations to get the sea-ice freeboard.

Armitage and Davidson (2014) have shown that off-nadir reflections from leads can bias the range retrieval since elevation retrievals are based on the assumption that the main reflector is in the nadir of the satellite. They typically occur when specular reflection on the edge of the main radar lobe still dominate the return signal (Figs. 1b and 2). These biased waveforms are mostly a composition of reflections of leads and sea ice. They can potentially affect elevations of leads if classified as leads as well as ice elevations if classified as sea ice and cause a range bias of Δd (Fig. 1b). In this study we present our method to discriminate waveforms that are biased by off-nadir reflections from leads and valid sea-surface height information. In addition the waveform classification scheme is extended to also discriminate different ice types.

2 Methods

Before referencing the ice elevations to the local sea level we have to assign waveforms to surface types. In this study we only focus on sea-ice and lead waveforms. Leads show an almost specular reflection due to the absence of surface waves in ice covered areas, because the surface of narrow open water areas is usually smooth. In contrast, reflections from sea ice have diffuse characteristics. Hence the echo power of a lead waveform is significantly higher than for a radar return from sea ice (Fig. 2a). Radar returns from the open ocean can be also considered as tie points for the sea surface height but are less relevant in referencing the ice elevations because this surface type mostly occurs in the marginal ice zone. Ocean waveforms are highly affected by waves and have different characteristics.

We here use the findings of Zygmuntowska et al. (2013) and Ricker et al. (2014) and use different waveform characteristics to discriminate between first-year ice (FYI) and multi-year ice (MYI). The pulse peakiness PP is described in Peacock and Laxon (2004) and indicates the shape of the power distribution of the waveform. Since waveforms from leads show specular returns, their PP is higher than those for sea ice with the waveform widened by diffuse reflections. The echo power contribution of an off-nadir lead is registered after the return from the nadir area but is of specular nature. Thus the retracker algorithm will fix the main scattering horizon at the leading edge of the lead. In order to identify those biased waveforms we introduce a *left*- and *right*-peakiness PP_l and PP_r (Ricker et al. 2014). They are defined as:

$$PP_r = \frac{\max(WF)}{\text{mean}\left(\left[WF_{i_{max}-3}, WF_{i_{max}-1}\right]\right)} \cdot 3 \qquad (1)$$

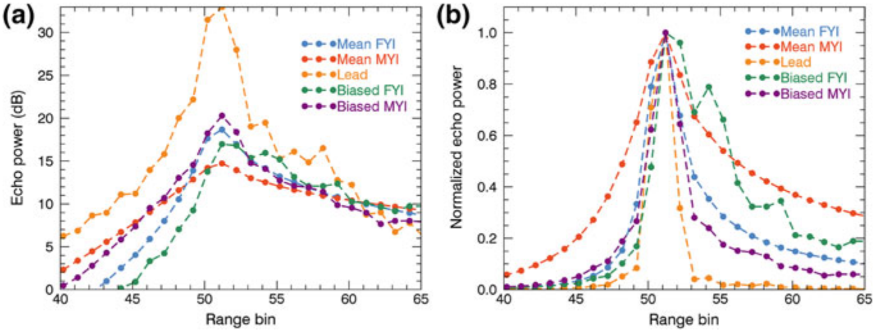

Fig. 2 CryoSat-2 waveforms from different surface types for the CryoSat-2 ground track in Fig. 3. The mean first-year ice (FYI) and multi-year ice (MYI) waveforms are an average of all FYI (MYI) waveforms along the track. **a** Shows all waveforms aligned to the peak power in dB. **b** Shows all waveforms normalized and aligned to the peak power

Table 1 Waveform parameter and ice concentration thresholds used in the CryoSat-2 processing to identify the surface types *Lead* and *multi-year* (MYI) and *first-year* ice (FYI)

Surface type	PP	K	SSD	PP_l	PP_r	IC (%)
Lead	≥40	≥40	≤4	≥40	≥30	≥70
Sea ice (FYI)				≤ 60	≤ 25	≥ 70
Sea ice (MYI)				≤ 18	≤ 15	≥ 70

Pulse peakiness PP, stack kurtosis K, stack standard deviation SSD, peakiness PP_l left of the power maximum, peakiness PP_r right of the power maximum and sea-ice concentration IC

$$PP_l = \frac{\max(WF)}{\mathrm{mean}\left(\left[WF_{i_{\max}+1}, WF_{i_{\max}+3}\right]\right)} \cdot 3 \tag{2}$$

where WF_i is the echo power at range bin i and max(WF) the peak power of the waveform. PP_l and PP_r are a measure for the peakiness *left* and *right* of the power maximum as we consider the ratio of the maximum power to the mean power of only three range bins left and right of the maximum. In the case of a nadir lead the waveform power distribution is narrow and shows a high maximum echo power as well as high PP_r and PP_l values (Fig. 2a, b).

For the lead identification we further use the parameter *stack kurtosis* (K), also a measure of peakiness (Wingham et al. 2006), and the *stack standard deviation* (SSD), which is a measure of the variation in surface backscatter depending on the incident angle (Wingham et al. 2006). The term *stack* refers to the multi-look SAR processing (Wingham et al. 2006). Leads are associated with a high K and a low SSD because of their specular reflection. Table 1 shows a set of waveform parameters used for the discrimination between sea ice and leads. The threshold values were determined by test-processing of CryoSat-2 ground tracks. All waveforms that do not comply with these constraints are discarded.

After the identification of leads, the actual sea level can be interpolated and subtracted from the CryoSat-2 elevations that were identified as sea ice. As a result we receive the radar freeboard according to (Ricker et al. 2014).

3 Results

Here we show exemplary results from a CryoSat-2 ground track from December 15. The track is directed south-east and first passes the MYI region north of Greenland before it passes over FYI in the marginal ice zone in the Fram Strait (Fig. 3). For the ice-type discrimination we use the OSI SAF ice-type product (Eastwood 2012).

Figure 4a reveals the range retrieval after subtracting the mean sea-surface height. Applying the waveform discrimination according to Table 1 we find 50 leads over a distance of 2,300 km. Radar echoes with waveform parameters that do not comply with the thresholds in Table 1 were discarded. Overall 22 % of the FYI and 21 % of the MYI waveforms are discarded. The fraction of detected leads is 0.7 % for FYI and 0.5 % for MYI. The difference of waveform characteristics

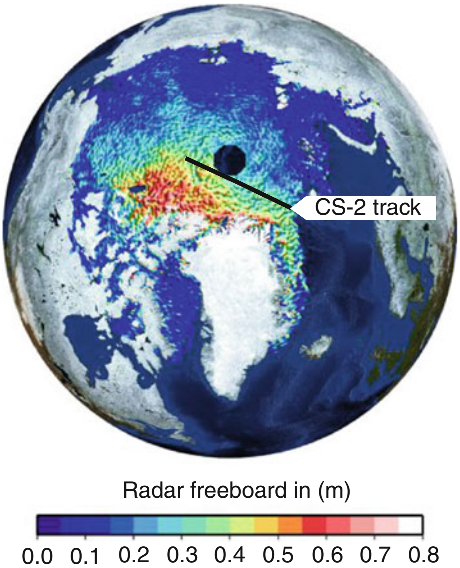

Fig. 3 CryoSat-2 monthly mean radar freeboard from December 2013, using a 40 % retracker threshold. The *black line* shows the CryoSat-2 ground track that is considered in this study

between FYI and MYI can be seen in the fact that if we use the MYI thresholds for FYI we discard 86 % of the FYI waveforms.

Figure 4b shows the left- and right-peakiness along the CryoSat-2 track. Within the MYI the left-peakiness reveals a mean value of 9.0 (Table 2) whereas for FYI we find a mean PP_l of 32.0. Furthermore the scattering for FYI is higher than for MYI. The right-peakiness PP_r shows overall less scattering compared to PP_l. It reveals mean values of 5.6 for MYI and 10.1 for FYI. The mean difference between FYI and MYI is lower than for PP_l but also shows higher values for FYI (Table 2). In coincidence with negative outliers in the MYI zone in Fig. 4a we find increased values for PP_r and PP_l.

Considering the biased waveforms in Table 2 we find PP_l values of 21.5 for FYI and 38.7 for MYI. These values are significantly higher than the mean value for MYI, but in the range of the mean PP_l for FYI. On the other hand, the PP_r for MYI is close to the mean PP_r of the unbiased MYI waveforms.

4 Discussion

Waveforms from FYI and MYI are of significantly different nature, which has been already investigated in Zygmuntowska et al. (2013). Surface properties of MYI, involving snow cover and surface roughness, cause a shallow echo power distribution in the waveform whereas for FYI we find a steeper leading edge (Fig. 2) which results in increased left- and right peakiness values (Fig. 4b).

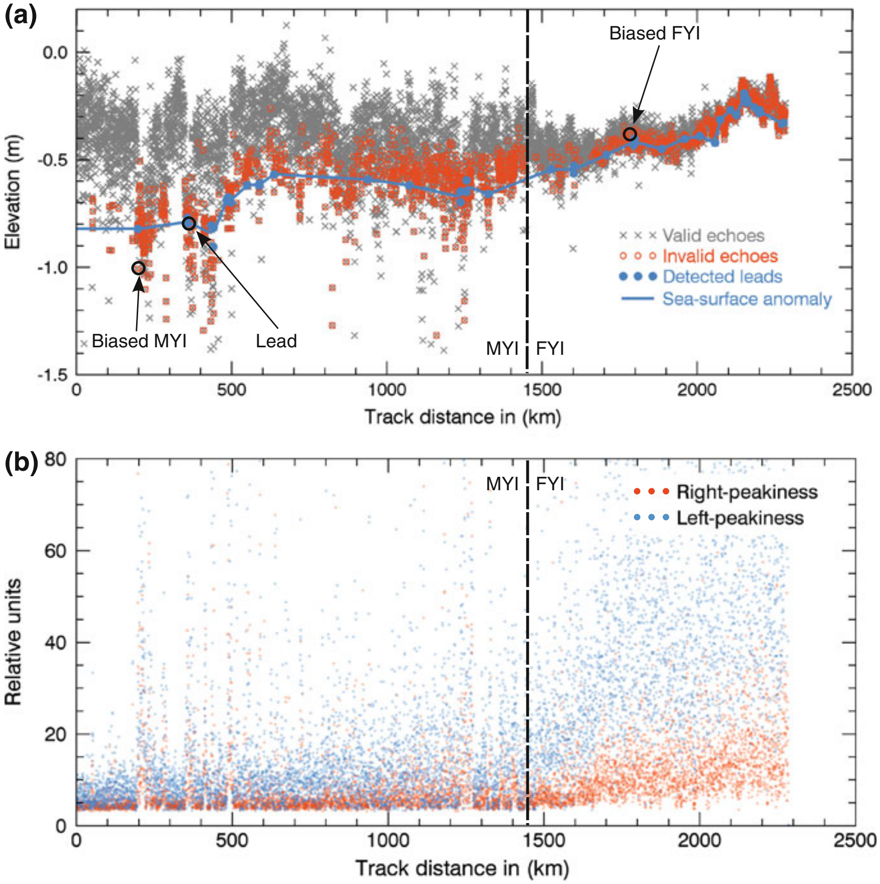

Fig. 4 **a** Geolocated CryoSat-2 surface elevations after retracking with a 40 % threshold and subtraction of the mean sea-surface height which has been interpolated along the CryoSat-2 ground track. Highlighted points belong to the waveforms in Fig. 2. **b** Right- and left-peakiness along the CryoSat-2 ground track. The *dashed vertical line* marks the boundary between first- and multi-year ice

Table 2 Values of left-peakiness (PP_l) and right-peakiness (PP_l) for the different surface types that are shown in Fig. 2

Waveform parameter	Mean FYI	Mean MYI	Lead	Biased FYI	Biased MYI
PP_l	32.0	9.0	87.2	21.5	38.7
PP_r	10.1	5.6	109.0	15.1	5.2

This finding has direct consequences for the classification of off-nadir reflections from leads that can either bias the interpolation of the sea-surface, if classified as leads, or affect the surface elevations of the sea ice, if classified as sea ice. In the first case high thresholds for the peakiness are necessary to exclude off-nadir leads. In the second case off-nadir leads cause decreased ice elevations which is shown in Fig. 4a for example between 200 and 400 km. In the FYI zone, we do not observe a similar effect. Figure 2 shows biased waveforms of FYI and MYI. Both are a composition of an off-nadir lead reflection and reflections from sea ice. The biased MYI waveform shows a high left-peakiness of 38.7 while the right-peakiness is 5.2 which is close to the value for mean MYI. Here the off-nadir lead seems to dominate the peak power. Thus the waveform is dominated by the off-nadir lead reflection and the range is tracked at the leading edge of the lead waveform contribution, resulting in a range bias $\varDelta$d (Fig. 1b). Considering PP_l and PP_r allows us to characterize waveforms and to identify biased waveforms.

FYI waveforms can exhibit similar shapes and properties as biased MYI. As a consequence, FYI waveforms might be discarded if they are classified as MYI in the OSI SAF ice type.

We also note that for FYI we find fewer outliers than for MYI (Fig. 4a). We can speculate that the backscatter from FYI is usually higher than from MYI (Fig. 2a). An off-nadir lead reflection is then in certain cases still distinguishable from the sea-ice echo as shown in Fig. 2 (green line). We can identify two peaks where the first represents the sea-ice reflection and the second the off-nadir lead that is well separated from the ice waveform. Therefore the retracker algorithm captures the leading edge of the sea-ice echo correctly and hence a range bias does not occur. Therefore we can use higher thresholds of PP_l and PP_r for FYI than for MYI to avoid discarding FYI waveforms erroneously. However, another reason for fewer outliers in the FYI zone could be a different pattern and distribution of leads in the considered FYI area.

The uncertainties of the range retrieval are discussed in more detail in Ricker et al. (2014). Besides a bias due to the choice of the retracker, the uncertainty is dominated by the speckle noise (Laxon et al. 2013; Wingham et al. 2006) that is around 0.1 m for a single measurement. Using the OSI SAF ice-type product for the waveform classification also induces a classification uncertainty (Eastwood 2012) and might lead to an underrepresentation of FYI within the MYI zone. Therefore a combined ice-type classification using the CryoSat-2 waveforms as well as the OSI SAF ice-type product might be a reasonable approach for the future. The thresholds in Table 1 for FYI and MYI are empirical and where chosen considering the distribution of PP_l and PP_r in Fig. 4b. Valid outliers in Fig. 4a could not be identified as biased waveforms and still affect the freeboard retrieval.

5 Conclusion

In this study we present a method to classify CryoSat-2 waveforms using a combination of parameters that characterize the radar echo. We use a *left*- and *right*-peakiness to characterize surface types and to identify waveforms that are biased by off-nadir-leads. Those waveforms can cause a decrease in surface elevation, especially for multi-year ice while for first-year ice this bias does not have a significant effect. Therefore we used higher threshold values for the left- and right-peakiness for first-year ice to avoid discarding first-year ice waveforms erroneously. Overall we discarded 22 % of the radar echoes of a CryoSat-2 ground track from December 15, 2013. Using the multi-year ice thresholds of left- and right-peakiness for FYI would lead to a rejection of 86 % of the first-year ice waveforms because the shape of first-year ice waveforms is similar to invalid waveforms from multi-year ice that are biased by off-nadir leads. However, since we rely on the OSI SAF ice-type product valid first-year might be underrepresented if indicated as multi-year ice.

Acknowledgments We thank the European Space Agency for providing the CryoSat-2 data. We further thank the Earth-System Science Research-School (ESSRES) for any support during this Phd project. The work of S. Hendricks and V. Helm was funded by the 268 Federal Ministry of Economics and Technology (Grant 50EE1008). For the usage of images of *The Blue Marble: Next Generation* we thank NASAs Earth Observatory.

References

Armitage T, Davidson M (2014) Using the interferometric capabilities of the esa cryosat-2 mission to improve the accuracy of sea ice freeboard retrievals. Geosci Remote Sens IEEE Trans 52 (1):529–536. doi:10.1109/TGRS.2013.2242082

Comiso JC (2002) A rapidly declining perennial sea ice cover in the arctic. Geophys Res Lett 29 (20): 17–1. doi:10.1029/2002GL015650

Comiso JC, Parkinson CL, Gersten R, Stock L (2008) Accelerated decline in the Arctic sea ice cover. Geophys Res Lett 35(L01703). http://www.agu.org/pubs/crossref/2008/2007GL031972.shtml

Eastwood S (2012) OSI SAF sea ice product manual, v3.8 edn. http://osisaf.met.no

Giles KA, Laxon SW, Ridout AL (2008) Circumpolar thinning of arctic sea ice following the 2007 record ice extent minimum. Geophys Res Lett 35(22):L22502. doi:10.1029/2008GL035710

Haas C, Hendricks S, Eicken H, Herber A (2010) Synoptic airborne thickness surveys reveal state of arctic sea ice cover. Geophys Res Lett 37(9):L09501. doi:10.1029/2010GL042652

Helm V, Humbert A, Miller H (2014) Elevation and elevation change of greenland and antarctica derived from cryosat-2. Cryosphere 8(4):1539–1559. doi:10.5194/tc-8-1539-2014. http://www.the-cryosphere.net/8/1539/2014/

Kurtz NT, Galin N, Studinger M (2014) An improved cryosat-2 sea ice freeboard and thickness retrieval algorithm through the use of waveform fitting. Cryosphere Discuss 8(1):721–768. http://www.thecryospherediscuss.net/8/721/2014/. doi:10.5194/tcd-8-721-2014

Kwok R, Cunningham GF, Wensnahan M, Rigor I, Zwally HJ, Yi D (2009) Thinning and volume loss of the arctic ocean sea ice cover: 2003-2008. J Geophys Res 114(C7):C07005. doi:10.1029/2009JC005312

Laxon SW, Giles KA, Ridout AL, Wingham DJ, Willatt R, Cullen R, Kwok R, Schweiger A, Zhang J, Haas C, Hendricks S, Krishfield R, Kurtz N, Farrell S, Davidson M (2013) Cryosat-2 estimates of arctic sea ice thickness and volume. Geophys Res Lett 40(4):732–737. doi:10.1002/grl.50193

Peacock NR, Laxon SW (2004) Sea surface height determination in the arctic ocean fromers altimetry. J Geophys Res: Oceans 109(C7):C07001. doi:10.1029/2001JC001026

Ricker R, Hendricks S, Helm V, Skourup H, Davidson M (2014) Sensitivity of cryosat-2 arctic sea-ice freeboard and thickness on radar-waveform interpretation. Cryosphere 8(4):1607–1622. http://www.thecryosphere.net/8/1607/2014/. doi:10.5194/tc-8-1607-2014

Rothrock DA, Yu Y, Maykut GA (1999) Thinning of the arctic sea-ice cover. Geophys Res Lett 26 (23):3469–3472. doi:10.1029/1999GL010863

Stroeve J, Serreze M, Holland M, Kay J, Malanik J, Barrett A (2012) The arctic's rapidly shrinking sea ice cover: a research synthesis. Climatic Change 110(3–4):1005–1027. doi:10.1007/s10584-011-0101-1

Wadhams P, Tucker WB, Krabill WB, Swift RN, Comiso JC, Davis NR (1992) Relationship between sea ice freeboard and draft in the arctic basin, and implications for ice thickness monitoring. J Geophys Res 97(C12):20325–20334. doi:10.1029/92JC02014

Wingham D, Francis C, Baker S, Bouzinac C, Brockley D, Cullen R, de Chateau-Thierry P, Laxon S, Mallow U, Mavrocordatos C, Phalippou L, Ratier G, Rey L, Rostan F, Viau P, Wallis D (2006) Cryosat: a mission to determine the fluctuations in earth's land and marine ice fields. Adv Space Res 37(4):841–871. doi:10.1016/j.asr.2005.07.027

Zygmuntowska M, Khvorostovsky K, Helm V, Sandven S (2013) Waveform classification of airborne synthetic aperture radar altimeter over arctic sea ice. Cryosphere 7(4):1315–1324. http://www.the-cryosphere.net/7/1315/2013/ . doi:10.5194/tc-7-1315-2013

Part V
Earth System Modelling and Data Analysis

Integration of Passive Tracers in a Three-Dimensional Ice Sheet Model

Johannes Sutter, Malte Thoma and Gerrit Lohmann

Abstract Components of the climate system, such as ice sheets and marine sediments serve as invaluable archives, which can be tapped into, to reconstruct paleoclimate conditions. The relative abundance of hydrogen and oxygen isotopes in ice cores is a proxy for past local temperature evolution. However the translation of these proxies into temperature is not straightforward. Complex interdependencies in the climate system can hide or override the local climate signal at which the ice core was drilled. Using 3D ice sheet modelling in concert with passive tracer advection one can simulate the isotopic distribution in ice sheets and compare them to ice core data. Combining this method in a coupled climate model environment, containing atmosphere and ocean components, one can theoretically simulate the isotopic cycle from the source to the actual ice record. Such an approach would greatly support the interpretation of proxy data whilst constraining the output of 3D ice sheet models (ISMs). We present the implementation of passive tracer advection in our 3D ISM RIMBAY (Thoma et al. in Geosci Model Dev 1:1–21, 2014, Goeller et al. in Cryosphere 7:1095–1106, 2014) and asses the potential of the method to reproduce chronologies of the polar ice sheets.

1 Introduction

The polar ice sheets contain information on past climate conditions conserved in the form of relative abundances of hydrogen and oxygen isotopes. This information can be tapped by drilling ice cores. Snow precipitating on the surface of an ice sheet

---

J. Sutter (✉) · M. Thoma · G. Lohmann
Alfred-Wegener-Institute, Bussestrasse 24, 27570 Bremerhaven, Germany
e-mail: johannes.sutter@awi.de

M. Thoma
e-mail: malte.thoma@awi.de

G. Lohmann
e-mail: gerrit.lohmann@awi.de

G. Lohmann et al. (eds.), *Towards an Interdisciplinary Approach in Earth System Science*, Springer Earth System Sciences,
DOI 10.1007/978-3-319-13865-7_18

contains a distinct isotopic signature which depends on the respective temperature during condensation (Dansgaard 1964). In theory it is possible to reconstruct the local surface temperature from isotope ratios. However many other processes apart from the condensation at site can influence the relative isotope concentration of precipitation. Temperature variations at the source or even a change in the source area might significantly change isotope concentrations (Jouzel et al. 1997). Circulation pathways might undergo dynamic changes as well, which complicates the relationship between temperature and isotope concentrations. The present day temperature-isotope relationship can be estimated, by measuring the isotope content in snow and fitting it to the observed temperatures at site (Dansgaard 1964; Jouzel et al. 1997). This relationship can then be used to reconstruct past temperature variations. To put this reconstruction into perspective, it is necessary to establish a timeline for the ice core's isotope variations, which can be derived from annual layer counting in the upper part of the ice core or via mass spectrometry of the deep part. Close to the bedrock it is often impossible to decipher a meaningful chronology due to complicated flow patterns of the ice which fold and heavily compress the local stratigraphy.

3D ice sheet modelling combined with tracer advection can provide a modeled stratigraphy for Antarctica and Greenland, which can then be compared to the available proxy data (Goelles et al. 2014; Lhomme et al. 2005; Clarke and Marshall 2002). We developed a passive tracer module for the 3D ISM RIMBAY (RIMTRACE) to reproduce the stratigraphy and isotope distribution of Greenland and Antarctica. RIMTRACE is first tested on simplified model environments based on the EISMINT geometry (Huybrechts and Payne 1996) and further validated against the analytical Nye-Haefeli age-depth relation (Nye 1963; Haefeli 1963).

2 Methods

The 3D ISM RIMBAY forming the framework for the passive tracer advection module is a "multi physics" higher order ice sheet model based on the 3D ISM of Pattyn (2003). The model includes all major features of the polar ice sheets [ice shelves, nunataks, fast flowing glaciers, basal hydrology etc. (see Fig. 1)]. Tracer simulations are carried out on a regular grid with a variable resolution. In the experiments discussed in this paper a resolution of 50 km is chosen. The ice sheet was run with a combination of the shallow ice (SIA) and shallow shelf (SSA) solution to the Navier-Stokes equation. The shallow ice approximation neglects all stresses except for the vertical stress term. Ice flow is governed by the overburden pressure of the ice and the surface and bedrock slope. Equation (1) highlights the equation for the lateral velocity according to the SIA.

$$\mathbf{u}(z) = -2(\rho g)^n |\nabla|^{n-1} \nabla s \int_b^z A(\theta^*)(s-z)^n dz + \mathbf{u}_b \qquad (1)$$

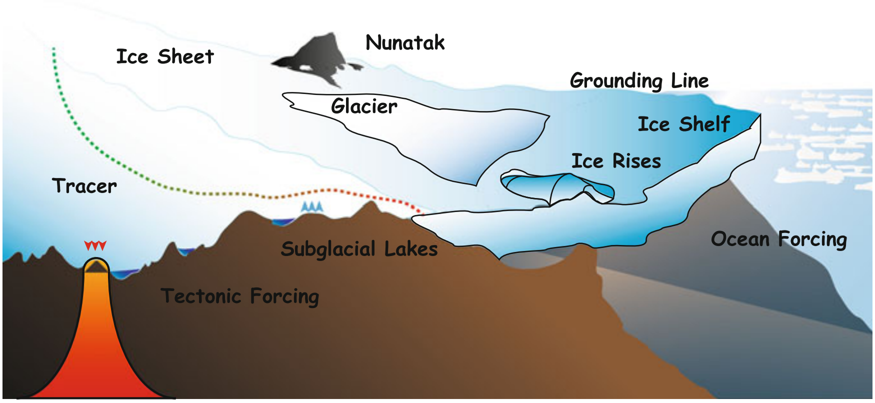

Fig. 1 Physical components of RIMBAY. The 3D ice sheet model RIMBAY, used in this study, represents all major physical components of Antarctica, such as ice shelves, subglacial hydrology, ice streams as well as including external forcings such as sea level and ocean temperatures as well as topographic and hydrologic features like nunataks and subglacial lakes

where n is the exponent found in the Glen flow law (Cuffey and Paterson 2010) set to the empirical value of 3 (some ice sheet models use n as a variable parameter for tuning purposes. For the sake of simplicity, here the empirical value is chosen), $A(\theta^*)$ is a temperature dependent flow rate factor and $\mathbf{u}_b$ the basal velocity, ρ and g are density of ice (910 kgm^{-3}) and gravitational force constant (9.81 ms^{-2}). The integral is evaluated from the bedrock (b) underneath the ice to ice surface (s). This approximation is valid for ice sheets with a small depth-to-width relationship, which applies to the interior of Greenland and Antarctica but not to the margins, where ice shelves and fast flowing ice streams govern ice dynamics. In the shallow shelf approximation basal friction is omitted while lateral velocities are assumed to be constant throughout the depth of the shelf ($\frac{\partial u}{\partial z}, \frac{\partial v}{\partial z} = 0$). Figure 2 illustrates the different stress field domains within the model domain.

Since tracer advection models simply utilize the velocity output of the underlying model, realistic velocity patterns are required for the reconstruction of age-depth distributions. To this end, model runs with present day boundary conditions where carried out to achieve an equilibrium ice sheet state comparable to the present day surface topography and mass balance. This approach involves the underlying postulate, that under PD-conditions the Antarctic ice sheet is close to equilibrium. Even though this is not the case it is a reasonable first estimate.

2.1 Present Day Control Run

One of the main drivers of ice sheet evolution in Antarctica (next to the surface mass balance), is the ocean-ice shelf interaction. The inflow of warm water masses

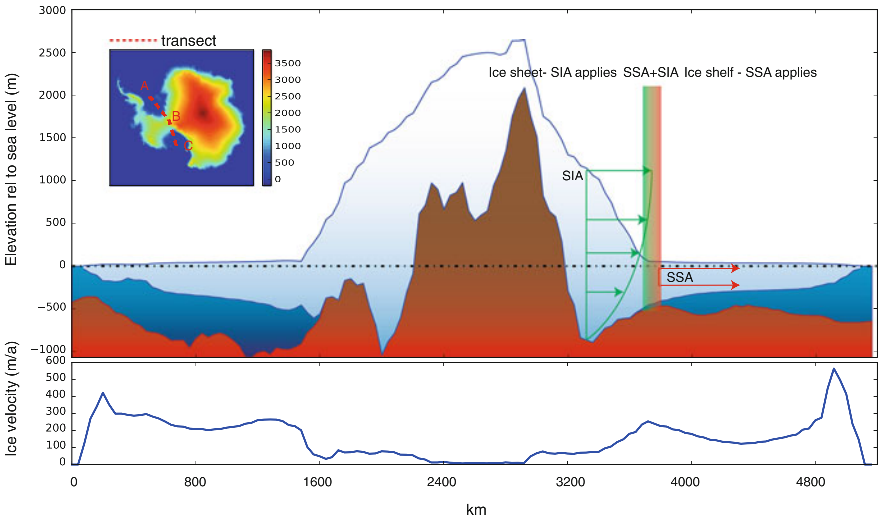

Fig. 2 Transition between the shallow shelf (SSH) and shallow ice (SIA) approximations. Where ice is grounded SIA applies and ice flow is governed by overburden pressure, surface slope and bedrock topography, floating shelf ice is governed by the SSH. Basal friction is set to zero and ice flow is governed by longitudinal stress. The area close to the grounding line is represented by a combined SSH+SIA term (depicted by the shaded coloring). *A* Transect through *ABC* present day topography/bathymetry starting from Larssen-Shelf through Filchner-Ronne and Ross-Shelf. *B* Velocities along the transect *ABC*

underneath the circumantarctic ice shelves can play an important role in the dynamics of the grounding line and the adjacent glaciers feeding the ice shelves (Hellmer et al. 2012; Joughin et al. 2014). Basal melting of the shelf is parametrized according to the approach of Beckmann and Goosse (2003). A 3D temperature distribution assembled from the World Ocean Atlas (2009) was compiled to drive the melting process at the respective depth of the ice shelf bottom. For the control run, Antarctic present-day (PD) geometry was used as a constraint to the equilibrium state. Even though PD Antarctica is not in equilibrium (Antarctica is loosing mass and will be subject to increased rates of mass loss based on climate projections) it is a reasonable zeroth order topographic constraint. Optimal parameterization was achieved by varying the parameter space spanned by basal friction, Beckmann-Goosse parameter and the flow enhancement factor. The parameter-set which corresponded to the closest representation of the PD surface topography and mass balance was chosen to be the default parameterization for the transient model runs. Even though it is unlikely, that basal conditions remained constant throughout glacial interglacial cycles, lack of proxy data shedding light on paleo-bedrock conditions prohibits a more elaborate approach. Figure 3 illustrates the climatological and topographic forcings used in the PD run. The PD run was carried out until ice volume reached a stable state, which took approximately 50,000 model years. Figure 4 exhibits the equilibrium topographic features of the tuned PD-run

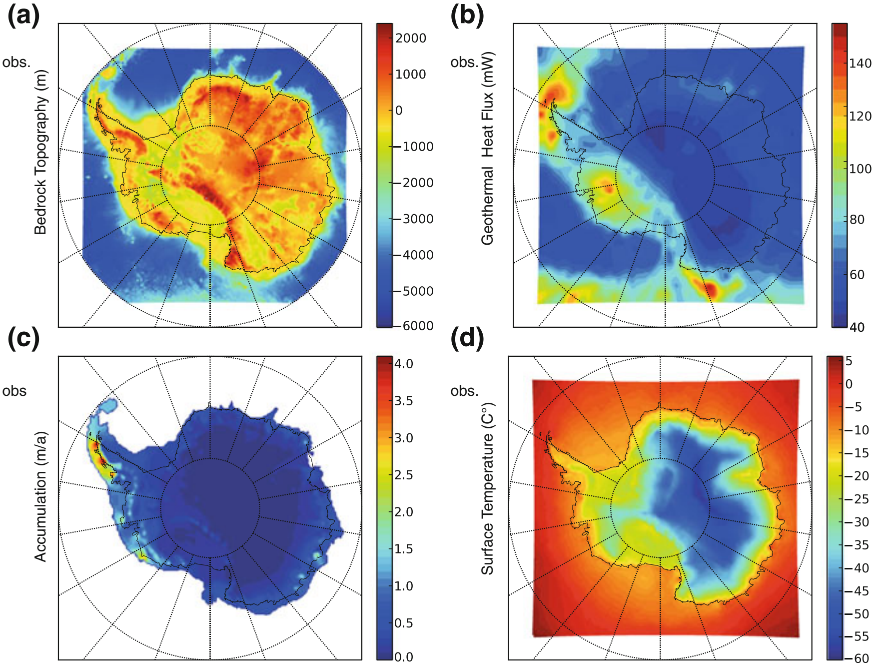

Fig. 3 Climatological and topographic forcings taken from observations used in the PD run. **a** Depicts the bedrock topography which was kept constant throughout the experiment (no visco-elastic response from the Earth's mantle), **b** geothermal heat flux distribution, **c** annually averaged accumulation based on (Arthern et al. 2006), **d** surface temperature field, **a**, **b** and **d** from ALBMAP data set (Le Brocq et al. 2010)

which equilibrium ice volume corresponds to the PD ice volume within one percent. Regardless of the good match of equilibrium volume, there are large discrepancies in ice thickness distribution. The East Antarctic Ice Sheet generally looses ice mass due to the low accumulation and outflow along the topographic gradient. The area around the Amery Ice Shelf gains considerable mass and hence increased ice thickness. This is due to the coarse 40 km resolution and the narrow topographic trough underneath the Amery shelf (represented in the model by 5 grid points or 200 km at the shelf front and narrowing to 1 grid cell or 40 km around the grounding line). This leads to a strong decrease in ice flow, and subsequent accumulation of ice mass.

2.2 *Passive Tracer Advection*

There are two widely used methods of transporting passive tracers in numerical simulations both implemented in the tracer advection model discussed below.

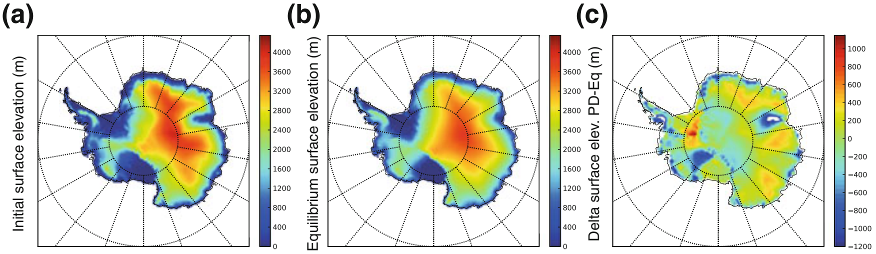

Fig. 4 **a** Antarctic present day topography (m) and **b** modeled equilibrium ice sheet elevation after 50,000 years of PD atmospheric forcing, **c** anomalies. Ice shelves are shown in *black/dark blue*. While most of the small circumantarctic ice shelves turned into grounded ice, the large ice shelves are reasonably well represented

The Lagrangian advection assumes the particle-perspective, which means that the particle is followed along its trajectory through the model grid. In contrast to the Lagrangian approach the Eulerian tracer advection solves the advection equation

$$\nabla_t A = \partial_t A + u\partial_x A + v\partial_y A + w\partial_z A = 0 \tag{2}$$

at every grid point covering the whole model domain, with the advantage of producing information at every grid point. A is the advected property with absolute and partial derivatives with respect to time and space (∇_t, ∂_{xyz}). The drawback of the Euler approach lies within the numerical diffusion arising from solving the advection equation in a finite differences environment. Furthermore it is impossible to trace back the trajectories of single tracers from their origin. This is a valuable feature of the Lagrangian transport, allowing detailed transport studies of any passive tracer object. The disadvantage of the Lagrangian transport lies in the sparse coverage of the model domain, which might be even reduced by dispersive flow as is the case in the lower parts of an ice sheet.

2.2.1 Validation of Tracer Modules

To ensure the capability of the tracer modules of reproducing realistic transport processes, tests are carried out in controlled model environments. The EISMINT project provides the perfect testing ground for this purpose. Both Lagrangian and Euler transport schemes are applied to simulations of spherical ice domes with radial accumulation pattern on flat bedrock. The ice sheet is run into equilibrium and subsequently the transport module is activated. The simulated age-depth relationship of both transport schemes is compared at the ice divide. Additionally both transport schemes are compared to the analytical age-depth distribution for a Nye-Vialov ice sheet, which is characterized as a radially symmetric ice dome with relatively steep flanks (see Fig. 5).

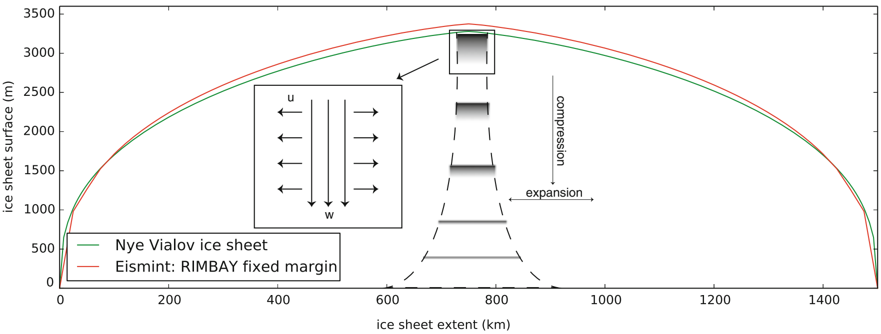

Fig. 5 Ice sheet equilibrium topography of the EISMINT Fixed Margin experiment compared to the analytical description of the Nye-Vialov ice sheet. The *shaded areas* illustrate the combined effect of compression and layer thinning (not to scale). The box depicts constant horizontal velocities along the *vertical axis* and constant vertical velocities along the *horizontal axis* close to the ice divide

2.2.2 Analytical Comparison to the Nye-Vialov Solution

The Nye-Vialov solution (Rybak and Huybrechts 2003) for an idealized ice sheet (Eq. 3) was used to compare the performance of the Lagrangian and Eulerian tracer advection approach (see Fig. 6). Utilizing the analytical age-depth relationship for an ice sheet without basal melting, no horizontal advection, and constant vertical strain rate we can directly compare both advection methods to a pre-defined age-depth relationship (Eq. 4):

$$H_0 = \left(\frac{20M}{A}\right)^{\frac{1}{2(n+1)}} \left(\frac{1}{\rho g}\right)^{\frac{1}{2(n+1)}} L^{\frac{1}{2}} \tag{3}$$

$$A = \frac{H_0}{G} \ln\left(\frac{z}{H_0}\right) \tag{4}$$

where H_0 is the ice sheet thickness at the divide, M the mass balance ($\frac{\mathrm{m}}{a}$), A is the time (years) it would take to get from the surface (divide position) to the location z within the ice sheet, g gravitational force (9.81 ms^{-2}) and ρ ice density (910 Kgm^{-3}), L denotes the characteristic length of the ice sheet, G is surface accumulation and z the depth inside the ice sheet. The basic assumption behind the Nye-Vialov solution is that ice inside glaciers or ice caps undergoes compression by overburden pressure (compaction) and, increasing with depth, layer thinning due to lateral extension. The horizontal velocity is assumed to be constant trough any vertical transect through the ice sheet while the vertical velocity is constant along any horizontal line (strip shaped ice sheet). In the standard configuration of 50 km lateral resolution and 41 vertical sigma layers (terrain following coordinates) the difference between both advection methods to the analytical solution is negligible in the upper domain of the ice divide. However, the solutions diverge in the lower part

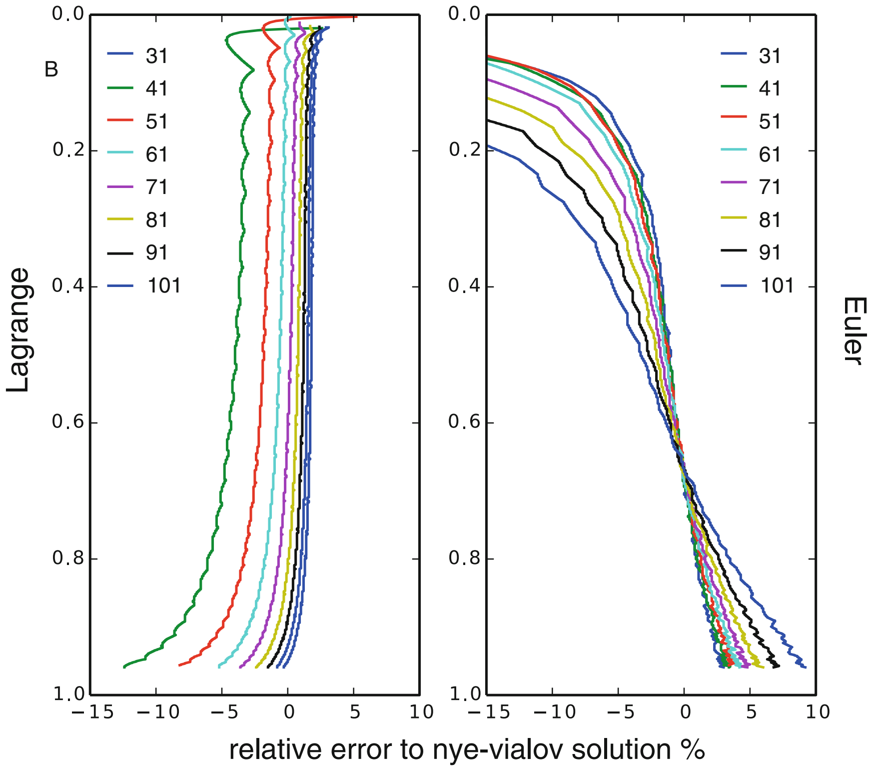

Fig. 6 Sensitivity of age depth relationship in an idealized Nye-Vialov ice sheet environment. Ice ages where calculated at the ice divide where an analytical solution to the age-depth problem exists. The figure compares two model runs with 31 and 101 sigma levels. Especially the Eulerian tracer method is highly sensitive to the number of sigma levels. The large error of both methods at the ice sheet surface, where the ice age should be zero is due to the very coarse resolution of the surface layers. This leads to an erroneous representation of velocities and hence to large discrepancies between the Eulerian solution and Nye-Vialov. Furthermore, Eulerian advection is a diffusive scheme leading to a time spread in the upper layers

of the ice sheet close to the bedrock. This is due to the cumulative interpolation error accumulated along the trajectory in case of the Lagrangian approach and due to the increasing impact of numerical diffusion in the Eulerian solution. Low vertical resolution results in considerable deviations of the Eulerian age-depth relation from the analytical solution, whilst the Lagrangian advection is less affected. Increasing the amount of sigma levels (finer vertical resolution), the performance of both advection methods can be instantly improved, reducing the discrepancy close to bedrock significantly. This approach is applicable in an idealized resource-friendly model-setup (such as the EISMINT environment, without shelves or complicated geometries as opposed to full scale simulations of the Antarctic ice sheet), however full scale simulations of large ice sheets limit the computationally feasible degree of resolution to around 50–100 sigma levels.

3 Discussion

The aim of this study was to asses the capability of the 3D ISM RIMBAY to reproduce ice sheet chronologies. To this end model validations against an analytical age-depth scale where carried out to test the accuracy of the implemented advective transport schemes. Both schemes exhibit excellent accuracy down to ≈85 % depth of the ice sheet. Below this depth high vertical resolutions are required to maintain a chronology within 5 % of the analytical solution. Computational cost is the main concern limiting the available number of vertical layers ($n \lesssim 100$). Taking into account the various unknowns in climate forcings when it comes to transient simulations of the Antarctic or Greenland ice sheet, a tracer age accuracy of 95 % relative to the analytical solution throughout the ice sheet, in an idealized setup, should be more than sufficient. To compare simulated chronologies to ice core data, transient simulations of ice sheet dynamics are necessary to reproduce realistic ice flow patterns. Sensitivity studies of the Antarctic ice sheet are carried out in which crucial flow parameters and boundary conditions were tuned to yield an equilibrium ice sheet comparable to the present day configuration available from observations. First results (not shown in this work) hint at a strong dependance of ice ages in the interior on variable boundary conditions such as basal shelf melting, sea level and accumulation effects. Following the validation of the tracer routine RIMTRACE, the next steps include the transient simulation of ice core chronologies in glacial-interglacial model runs. Comparing the results acquired in this fashion to ice core data, will provide an important constraint to the ISM model results. Fitting the ISM output to match the observed ice core chronologies will hopefully help in assessing past ice sheet geometries. The results from test runs of the Eulerian and Lagrangian advection methods, show that the Lagrangian scheme yields more accurate results and includes the advantage of backtracking tracers to their point of origin. However both schemes will be further improved. An additional implementation and comparison to the Semi-Lagrangian tracer scheme, as discussed in (Goelles et al. 2014) would complement the efforts to shed light on the polar climate archives. The last step in the puzzle will be the implementation of the RIMBAY-TRACE ISM into the coupled climate model COSMOS (Stepanek and Lohmann 2012) including a complete isotope cycle which would provide the first fully coupled model assessment of the isotope and age distribution of the polar ice sheets.

References

Arthern RJ, Winebrenner DP, Vaughan DG (2006) Antarctic snow accumulation mapped using polarization of 4.3-cm wavelength microwave emission. J Geophys Res Atmos 111:D06107

Beckmann A, Goosse H (2003) A parameterization of ice shelf-ocean interaction for climate models. Ocean Model 5:157–170

Clarke GKC, Marshall SJ (2002) Isotopic balance of the Greenland ice sheet: modelled concentrations of water isotopes from 30,000 BP to present. Quatern Sci Rev 21:419–430

Cuffey KM, Paterson WSB (2010) The physics of glaciers, vol 4. Elsevier, Oxford

Dansgaard W (1964) Stable isotopes in precipitation. Tellus B 16:436–468

Goeller S, Thoma M, Grosfeld K, Miller H (2014) RIMBAY a balanced water layer concept for subglacial hydrology in large-scale ice sheet models. Cryosphere 7:1095–1106

Goelles T, Grosfeld K, Lohmann G (2014) Semi-lagrangian transport of oxygen isotopes in polythermal ice sheets: implementation and first results. Geoscientific Model Dev 7:1137–1174

Haefeli R (1963) A numerical and experimental method for determining ice motion in the central parts of ice sheets. In: International Association of Scientific Hydrology Publication 61 (General Assembly of Berkeley 1963—Snow and Ice)

Hellmer HH, Kauker F, Timmermann R, Determann J, Rae J (2012) Twenty-first-century warming of a large Antarctic ice-shelf cavity by a redirected coastal current. Nature 485:225–228

Huybrechts P, Payne TA (1996) The EISMINT benchmarks for testing ice-sheet models. Ann Glaciol 23:1–12

Joughin I, Smith BE, Medley B (2014) Marine ice sheet collapse potentially underway for the thwaites glacier basin, West Antarctica. Science 344:735–738

Jouzel J, Alley RB, Cuffey KM, Dansgaard W, Grootes P, Hoffmann G, Johnsen SJ, Koster RD, Peel D, Shuman CA, Stievenard M, Stuiver M, White J (1997) Validity of the temperature reconstruction from water isotopes in ice cores. J Geophys Res Oceans 102:26471–26487

Le Brocq AM, Payne AJ, Vieli A (2010) An improved antarctic dataset for high resolution numerical ice sheet models (ALBMAP v1). Earth Syst Sci Data 2:247–260

Lhomme N, Clarke GKC, Marshall SJ (2005) Tracer transport in the Greenland ice sheet: three-dimensional isotopic stratigraphy. Quatern Sci Rev 24:155–171

Nye JF (1963) Correction factor for accumulation measured by the thickness of the annual layers in an ice sheet. J Glaciol 4:785–788

Pattyn F (2003) A new three-dimensional higher-order thermomechanical ice sheet model: basic sensitivity, ice stream development, and ice flow across subglacial lakes. J Geophys Res Solid Earth 108:2156–2202

Rybak O, Huybrechts P (2003) A comparison of Eulerian and Lagrangian methods for dating in numerical ice-sheet models. Ann Glaciol 37:150–158

Stepanek C, Lohmann G (2012) Modelling mid-Pliocene climate with COSMOS. Geosci Model Dev 5:1221–1243

Thoma M, Grosfeld K, Barbi D, Determann J, Goeller S, Mayer C, Pattyn F (2014) RIMBAY a multi-approximation 3D ice-dynamics model for comprehensive applications: model description and examples. Geosci Model Dev 1:1–21

Part VI
Climate Archives and Geotectonics

Bivalve Shells—Unique High-Resolution Archives of the Environmental Past

Lars Beierlein, Gernot Nehrke, Tamara Trofimova and Thomas Brey

Abstract Understanding the climate of the past is essential for anticipating future climate change. Palaeoclimatic archives are the key to the past, but few marine archives (including tropical corals) combine long recording times (decades to centuries) with high temporal resolution (decadal to intra-annual). In temperate and polar regions carbonate shells can perform the equivalent function as a proxy archive as corals do in the tropics. The bivalve *Arctica islandica* is a particularly unique bio-archive owing to its wide distribution throughout the North Atlantic and its extreme longevity (up to 500 years). This paper exemplifies how information at intra-annual and decadal scales is derived from *A. islandica* shells and combined into a detailed picture of past conditions. Oxygen isotope analysis ($\delta^{18}O$) provides information on the intra-annual temperature cycle while frequency analysis of shell growth records identifies decadal variability such as a distinct 5-year signal, which might be linked to the North Atlantic Oscillation.

Keywords Sclerochronology · *Arctica islandica* · Frequency analysis · Raman microscopy · Stable oxygen isotopes · Palaeoceanography · Intra-annual · Decadal

1 Introduction

Current predictions of future climate change (e.g., IPCC 2013) are based on global circulation models (GCM) to a large extent. Such models incorporate observational and instrumental data of the oceans, continents and atmosphere. Instrumental data are available for the last two centuries at best, but we need climate and

---

L. Beierlein (✉) · G. Nehrke · T. Brey
Alfred Wegener Institute Helmholtz Centre for Polar and Marine Research,
Bremerhaven, Germany
e-mail: Lars.Beierlein@awi.de

T. Trofimova
Saint Petersburg State University, St. Petersburg, Russia

G. Lohmann et al. (eds.), *Towards an Interdisciplinary Approach in Earth System Science*, Springer Earth System Sciences,
DOI 10.1007/978-3-319-13865-7_19

environmental data prior to the instrumental era in order to improve and verify such climate models. Therefore, climate sciences rely on climate archives such as sediment cores and ice cores. Such archives contain "*proxies*", i.e. physical, chemical or biological properties that correlate to certain environmental parameters and hence allow reconstructions of such parameters at the time of the formation of the archive. The relationship between water temperature and $\delta^{18}O$ is thought to be the most important relationship between an environmental parameter and its proxy.

Accretionally growing hard parts of aquatic organisms (e.g., corals, fish and squid otoliths, coralline algae, bivalve shells) are being used as climate archives

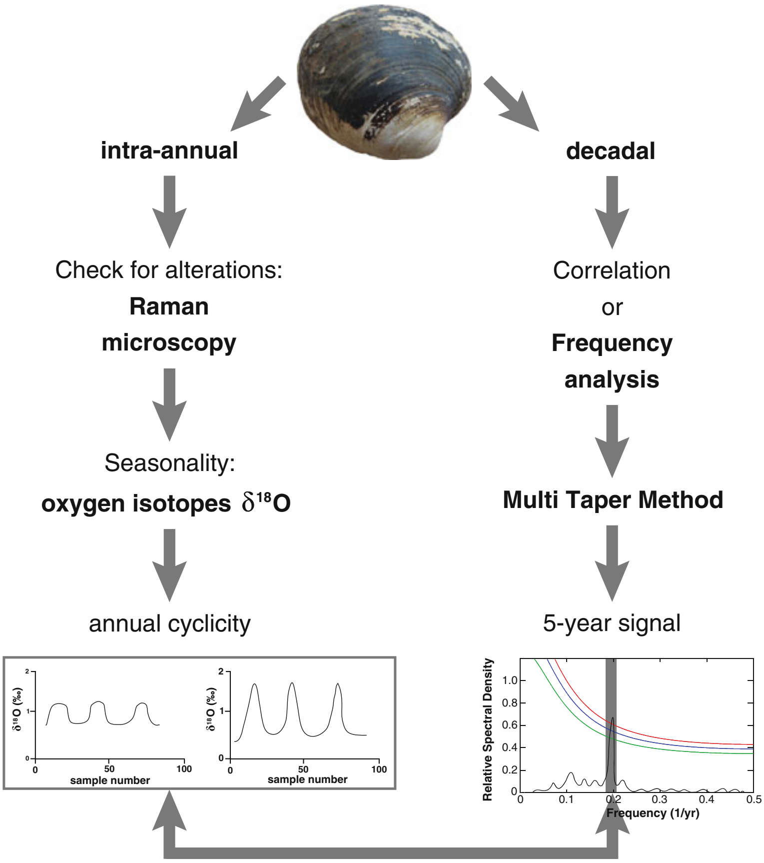

Fig. 1 Flow chart illustrating potential reconstruction techniques on various time-scales for bivalve shells. Geochemical analyses, such as $\delta^{18}O$ as a proxy for water temperatures, allow reconstructions on an intra-annual level. A test for preservation in fossil specimens—e.g., by using CRM—should be obligatory. The shell of *A. islandica* can additionally be used for a frequency analysis (e.g., Multi Taper Method) of the annual growth pattern, allowing the identification of decadal variabilities, such as a 5-year quasi-periodic signal

with increasing frequency, providing environmental information on daily to multi-centennial time-scales (Schöne et al. 2005b; Hallmann et al. 2009; Butler et al. 2010). For this purpose, analyses of the anatomical-morphological features of the skeletal hard parts—such as growth patterns and crystal structures—are commonly combined with geochemical analyses (e.g., stable isotopes, trace elements). Due to its wide distribution throughout the North Atlantic (Dahlgren et al. 2000) and its longevity (500 years and more, Butler et al. 2013), the bivalve *Arctica islandica* represents an exceptional bio-archive for northern temperate regions.

A. islandica forms annual growth rings (increments), which can be measured and used as a calendar (Jones 1980). However, when working with fossil specimens, the state of preservation is an essential aspect to consider prior to any kind of geochemical analysis (e.g., stable oxygen isotopes ($\delta^{18}O$) as a proxy for water temperature and salinity). Confocal Raman microscopy (CRM) is a non-destructive method, which allows a test for diagenetic alteration on the same sample that will later be used for the geochemical measurement.

The annual growth rate of bivalves mainly depends on ambient water temperature and food quality and availability (e.g., Witbaard et al. 1997) which vary on a regional scale, but may be affected by large-scale ocean-atmosphere phenomena, too (Schöne et al. 2003a), like the North Atlantic Oscillation (NAO). The frequency analysis of the growth record of just a single *A. islandica* shell can identify such decadal signals (several years to decades) in a time window corresponding to the animal's lifetime.

For demonstration purposes we combine the results from modern and fossil shell material to emphasise the unique character of the bio-archive *A. islandica*. We demonstrate its outstanding potential in terms of intra-annual (stable oxygen isotopes) as well as decadal (frequency analysis) climatic and environmental reconstructions and show how these can be combined to inform our understanding of climate in the past (Fig. 1).

2 Methods

2.1 Shell Origin and Laboratory Work

We use three *A. islandica* specimens of different geological age (see Table 1 for details) to demonstrate how sclerochronological analyses at intra-annual and decadal scale fit together. The CRM approach has been applied on Pliocene specimen AI-TjBe-01, which was removed from the biostratigraphically dated Tjörnes Bed formation, Iceland. Specimen AI-EgLo-02 has been found dead in beach deposits at the Lofoten, Norway, and used for the frequency analysis. Further, specimen

Table 1 Shell information

Shell ID	Length (mm)	Height (mm)	Width (mm)	Locality	Geological age	Ontogenetic age (years)	Applied method
Ai24568	86.7	82.0	23.2	Tromso, Norway	Modern	71	Oxygen isotope analysis
AI-EgLo-02	53.3	46.6	14.0	Lofoten, Norway	Found dead, beach deposit	45	Frequency analysis
AI-TjBe-01	57.2*	84.0	24.4*	Tjörnes, Iceland	Pliocene	Not determined	Raman microscopy

Information on shell morphology, shell origin, geological and ontogenetic ages as well as applied methods are given. Measurements marked with (*) for specimen AI-TjBe-01 give values for partly fragmented shell portions

Ai24568 has been live-collected in Tromsø, Norway in 2006 and used for the $\delta^{18}O$ approach.

In the laboratory, all specimens were cleaned using a paintbrush, deionized water and an ultrasonic bath. Afterwards, shells were externally strengthened with an epoxy resin and cut along the line of strongest growth (LSG, Fig. 2). The cut shell sections were glued onto glass slides and ground on sandpaper with varying grain sizes of 15, 10 and 5 µm respectively.

To improve the visibility of the individual growth increments, the thick-section intended for the frequency analysis (shell ID: AI-EgLo-02) was stained with Mutvei's solution (Schöne et al. 2005a). Digital images were taken under a stereo-microscope (Olympus, SZX12) attached to a CCD camera (Olympus) and

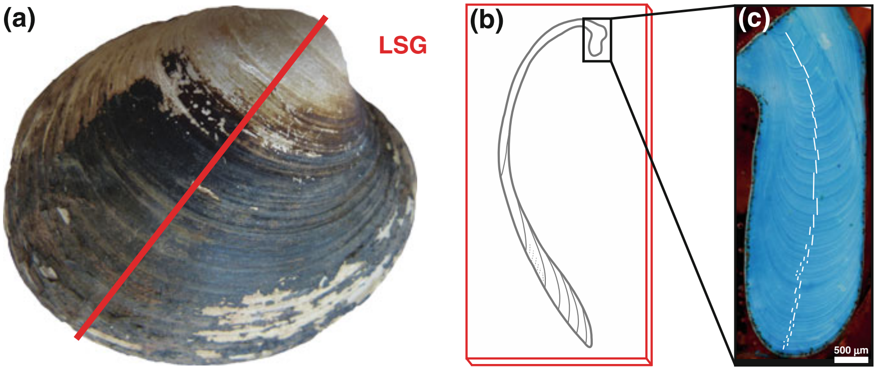

Fig. 2 Cutting axis and location of shell increments in *A. islandica*. **a** Right valve of an *A. islandica* specimen with line of strongest growth (LSG, equals cutting axis). **b** Graphical illustration of an *A. islandica* thick-section after cutting through the LSG (*red*). *Black box* indicates the umbonal area shown in **c**. **c** Magnification of the umbonal area, stained in Mutvei's solution and showing annual growth increments. Growth band widths are measured perpendicular to the increments, as indicated by the *white lines*

increment width was measured using the image processing software analySIS (Olympus, version 5.1).

2.2 State of Preservation

The shells of *A. islandica* consist of aragonite ($CaCO_3$), trace elements and organics (e.g., Schöne 2013). After burial and in terms of fossilisation, several factors such as heat and pressure at depth, as well as hydrothermal fluids, can cause alterations in the shell carbonate, e.g., recrystallization from pristine aragonite to the more stable $CaCO_3$ polymorph calcite (e.g., Bathurst 1964). In most cases the recrystallization process involves a dissolution and recrystallization process (*neomorphism*, e.g., Maliva 1998), which would replace the pristine stable oxygen isotope ratio within the carbonate and erase the associated environmental signal in the shell (e.g., Hendry et al. 1995).

Due to its high spatial resolution of a few hundred nm CRM provides an ideal tool for shell carbonate analysis. For our measurements on Pliocene specimen AI-TjBe-01 we used a WITec alpha 300 R instrument, equipped with a diode laser (excitation wavelength 532 nm) and a 20× Zeiss objective. Details on the measurements can be found in Nehrke et al. (2012).

2.3 Frequency Analysis

The growth record of shell AI-EgLo-02 was detrended using a cubic spline (JMP software, version 9.0.1 by SAS Institute Inc. 2007), and a standardized growth index (SGI) was calculated following Butler et al. (2010). The subsequent frequency analysis was conducted using kSpectra software (version 3.4 by SpectraWorks) with settings according to Ivany et al. (2011) and applying a Singular Spectrum Analysis (SSA) and the Multi Taper Method (MTM). Furthermore, we used wavelet transformation to examine whether quasi-periodic signals were stationary over time (http://ion.researchsystems.com/IONScript/wavelet/), following Torrence and Compo (1998). Growth records of specimens Ai24568 and AI-TjBe-01 have not been analysed.

2.4 Stable Oxygen Isotopes ($\delta^{18}O$)

During shell formation, *A. islandica* incorporates oxygen isotopes in equilibrium with the surrounding seawater (Weidman and Jones 1994). Since the incorporation of lighter oxygen isotopes is facilitated during higher temperatures (Grossman and Ku 1986), the oxygen isotope ratio $\delta^{18}O$ of most bivalve species provides information on water temperatures (e.g., Schöne et al. 2005c) and salinity (e.g., Schöne et al. 2003b) at the moment of shell formation. In general, the modified temperature equation by Dettman et al. (1999) is used for *A. islandica*, which is based on the empirically determined relationship between temperature and $\delta^{18}O$ for aragonite by Grossman and Ku (1986).

Carbonate samples were milled by hand (Dettman and Lohmann 1995) using a 700 µm drill bit (Komet/Gebr. Brasseler GmbH & Co. KG) mounted onto an industrial high precision drill (Minimo C121, Minitor Co., Ltd.) and attached to a binocular microscope. Measurements were performed on a Thermo Finnigan MAT 253 isotope ratio mass spectrometer and calibrated against a NBS-19 standard with a precision error of 0.08 ‰ for oxygen. Shell-derived water temperatures have been compared to SST measurements reported online (http://www.seatemperature.org/europe/norway/tromso.htm).

3 Results

3.1 State of Preservation

From the Raman scan it can be seen that the area of the fossil *A. islandica* shell (shell ID: AI-TjBe-01) marked in Fig. 3a consisted of both aragonite and calcite. An area scan of 520 × 500 µm (Fig. 3b), partly covering the potentially recrystallized shell portion, indicates the distribution of (pristine) aragonite and (recrystallized) calcite within the shell carbonate. Both polymorphs share carbonate-specific peaks at 155 and 1085 cm^{-1} in their Raman spectra (Fig. 3c). The aragonite-specific peak at ~206 cm^{-1} (blue line in Fig. 3c) is shifted towards ~280 cm^{-1} in (recrystallized) calcite (red line in Fig. 3c).

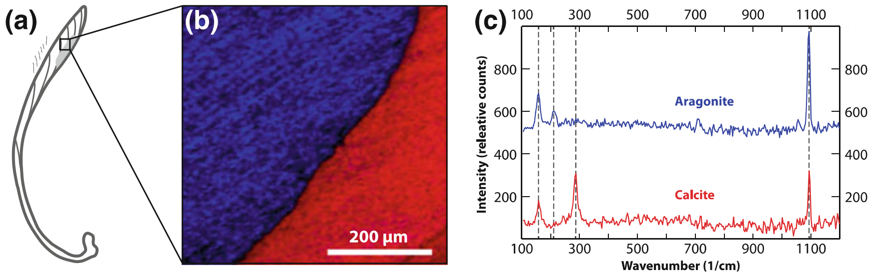

Fig. 3 State of preservation tested by confocal Raman microscopy. **a** Schematic illustration of a (fossil) *A. islandica* specimen. *Light grey colour* exemplary indicates area of potential recrystallization. **b** Areal CRM scan in specimen AI-TjBe-01 close to the altered shell portion and as indicated in **a**. Two different materials have been identified. **c** Raman spectra for two different polymorphs of calcium carbonate explaining colour coding in B. Intensity differences in liberation modes (peaks at ~206 cm^{-1} for aragonite and ~280 cm^{-1} for calcite) in single spot Raman spectra identify pristine aragonite (*blue*) and recrystallized calcite (*red*)

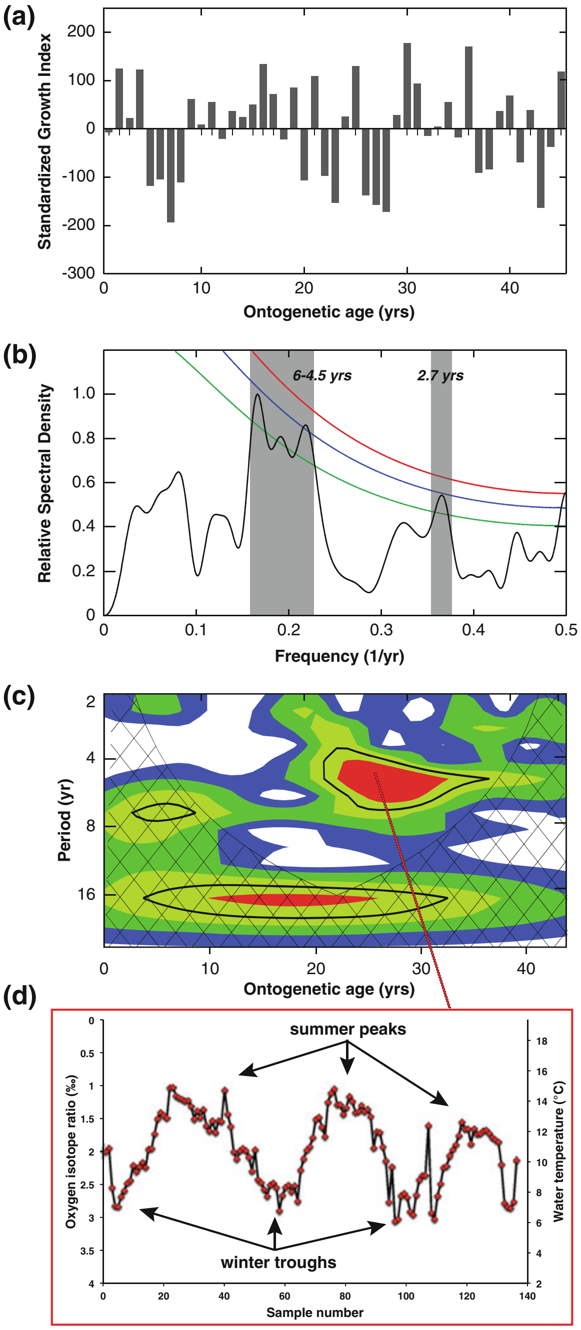

Fig. 4 Frequency analysis on *A. islandica* growth pattern. **a** Standardized growth index (SGI) giving relative information on positive (above 0) or negative (below 0) deviations from average shell growth. **b** Multi Taper Method (MTM) applied to the SGI shown in **a**. *Red*, *blue* and *green lines* represent significance levels of 99, 95 and 90 %, respectively. The significant (95 %) signal at the frequency of 0.197 (1/year) corresponds to a 5-year signal (combined SSA and MTM analysis). **c** Wavelet transformation giving information on the stationarity of quasi-periodic signals identified by SSA and MTM. The strength of the 5-year quasi-periodic signal varies over time, being more prominent from ontogenetic year 20 onwards. **d** Results for the $\delta^{18}O$ analysis in three ontogenetic years throughout the pronounced phase of the 5-year signal, as indicated in **c**. $\delta^{18}O$ values have been translated into water temperatures according to Dettman et al. (1999) assuming a $\delta^{18}O_{seawater}$ value of 0 ‰. *Arrows* indicate summer peaks and winter troughs

3.2 Frequency Analysis

The frequency analysis of the SGI (Fig. 4a) in specimen AI-EgLo-02 indicates a significant (95 % level) 5-year signal (Fig. 4b). Additionally, a signal at 2.7 years was significant at the 90 ‰ level. The wavelet transformation shows the variability of the indicated signals over time. Strength of the 5-year signal varies distinctly over time and is most prominent between ontogenetic years 20 and 30 (Fig. 4c).

3.3 Stable Oxygen Isotopes ($\delta^{18}O$)

Oxygen isotope ratios of three consecutively sampled ontogenetic years in modern *A. islandica* specimen Ai24568 show three distinct sinusoidal patterns (summer peaks and winter troughs) with amplitudes of about 2 ‰ each (Fig. 4d). Assuming a constant modern $\delta^{18}O_{seawater}$ ratio of 0 ‰ during shell formation, the measurements translate into water temperatures between 15 and 6 °C (Fig. 4d).

4 Discussion and Conclusions

When working on fossil shell material, the state of preservation must be evaluated prior to geochemical analysis (e.g., stable oxygen isotopes) to avoid serious errors and bias. Here, CRM represents a powerful, time-effective and non-destructive tool for the examination of shell carbonate polymorphs (Fig. 3).

In *A. islandica* shells it is possible to check the growth record for decadal variability throughout the life of the animal. In specimen AI-EgLo-02 (Lofoten, Norway) frequency analysis identified a significant 5-year signal, which, however, is not stationary over time (Fig. 4a–c). Since the date of death is unknown, a direct correlation to observational or instrumental time-series is not feasible. This would, however, be an essential step to unambiguously link our 5-year signal to the NAO (cf., Wunsch 1999). A number of studies have shown indeed *A. islandica* shell growth patterns to correlate with known ocean-atmosphere oscillations such as NAO (Schöne et al. 2003a; Wanamaker et al. 2009). Nevertheless, further investigations of additional shell material as well as of local forcing mechanisms are required.

$\delta^{18}O$ derived water temperatures (6–15 °C, Fig. 4d) in specimen Ai24568 correspond well to SST measurements (2.8–13.7 °C) for Tromsø, Norway. However, our temperature reconstruction does not account for seasonal changes in salinity and assumes a global average $\delta^{18}O_{seawater}$ value of 0 ‰, which would need verification by on-site measurements. Further, an assumed growing season from February/March to September (Schöne et al. 2004) in *A. islandica* might explain truncated winter minimum temperatures.

Conclusively, for demonstrating purposes, we combined the results from the frequency and $\delta^{18}O$ analyses from two different shell specimens to give an exemplary perspective on the potential of *A. islandica* as a recorder of the environmental past. Accordingly, if *A. islandica* growth increment series can be synchronized with the external forcing signal (e.g., NAO) intra-annual analysis techniques (such as $\delta^{18}O$) can be used to analyse whether intra-annual patterns differ between weak and strong phases of shell growth oscillation. In our example, $\delta^{18}O$ analysis allowed to link a seasonal water temperature amplitude of about 9 °C to the most prominent phase of the 5-year periodic signal (Fig. 4c, d). The high temporal resolution combined with an exceptional longevity distinguish *A. islandica* shells from all other marine archives and show the great potential and uniqueness of *A. islandica* for climatic and environmental reconstructions on various time-scales.

Acknowledgments We would like to thank Salma Begum (AWI Bremerhaven), Carin Andersson Dahl (Bjerknes Centre for Climate Research, Uni Research), Lovísa Ásbjörnsdóttir (Icelandic Institute of Natural History) for providing the shell material. Further, Andreas Mackensen, Lisa Schönborn and Kerstin Beyer (all AWI Bremerhaven) are thanked for their help and advice with the stable oxygen isotope measurements.

References

Bathurst RGC (1964) The replacement of aragonite by calcite in the molluscan shell wall. In: Imbrie J, Newell NO (eds) Approaches to paleoecology. Wiley, New York, pp 357–376

Butler PG, Richardson CA, Scourse JD, Wanamaker AD Jr, Shammon TM, Bennell JD (2010) Marine climate in the Irish Sea: analysis of a 489-year marine master chronology derived from growth increments in the shell of the clam *Arctica islandica*. Quater Sci Rev 29:1614–1632

Butler PG, Wanamaker AD Jr, Scourse JD, Richardson CA, Reynolds DJ (2013) Variability of marine climate on the North Icelandic Shelf in a 1357-year proxy archive based on growth increments in the bivalve *Arctica islandica*. Palaeogeogr Palaeoclimatol Palaeoecol 373:141–151

Dahlgren TG, Weinberg JR, Halanych KM (2000) Phylogeography of the ocean quahog (*Arctica islandica*): influences of paleoclimate on genetic diversity and species range. Mar Biol 137:487–495

Dettman D, Lohmann KC (1995) Microsampling carbonates for stable isotope and minor element analysis: physical separation of samples on a 20 Micrometer scale. J Sediment Res 65A:566–569

Dettman DL, Reische AK, Lohmann KC (1999) Controls on the stable isotope composition of seasonal growth bands in aragonitic fresh-water bivalves (Unionidae). Geochim Cosmochim Acta 63:1049–1057

Grossman EL, Ku T-L (1986) Oxygen and carbon isotope fractionation in biogenic aragonite: temperature effects. Chem Geol 59:59–74

Hallmann N, Burchell M, Schöne BR, Irvine GV, Maxwell D (2009) High-resolution sclerochronological analysis of the bivalve mollusk *Saxidomus gigantea* from Alaska and British Columbia: techniques for revealing environmental archives and archaeological seasonality. J Archaeol Sci 36:2353–2364

Hendry JP, Ditchfield PW, Marshall JD (1995) Two-stage neomorphism of Jurassic aragonitic bivalves: implications for early diagenesis. J Sediment Res 65:214–224

IPCC, Climate Change (2013) The physical science basis. Contribution of working group I to the 5th assessment report of the intergovernmental panel on climate change. Cambridge University Press, Cambridge

Ivany LC, Brey T, Huber M, Buick DP, Schöne BR (2011) El Niño in the Eocene greenhouse recorded by fossil bivalves and wood from Antarctica. Geophys Res Lett 38:L16709

Jones DS (1980) Annual cycle of shell growth increment formation in two continental shelf bivalves and its paleoecologic significance. Paleobiology 6:331–340

Maliva RG (1998) Skeletal aragonite neomorphism—quantitative modelling of a two-water diagenetic system. Sed Geol 121:179–190

Nehrke G, Poigner H, Wilhelms-Dick D, Brey T, Abele D (2012) Coexistence of three calcium carbonate polymorphs in the shell of the Antarctic clam *Laternula elliptica*. Geochem Geophys Geosyst 13:Q05014

Schöne BR (2013) *Arctica islandica* (Bivalvia): a unique paleoenvironmental archive of the northern North Atlantic Ocean. Global Planet Change 111:199–225

Schöne BR, Dunca E, Fiebig J, Pfeiffer M (2005a) Mutvei's solution: an ideal agent for resolving microgrowth structures of biogenic carbonates. Palaeogeogr Palaeoclimatol Palaeoecol 228:149–166

Schöne BR, Houk SD, Freyre Castro AD, Fiebig J, Oschmann W, Kroncke I, Dreyer W, Gosselck F (2005b) Daily growth rates in shells of *Arctica islandica*: assessing sub-seasonal environmental controls on a long-lived bivalve mollusk. Palaios 20:78–92

Schöne BR, Oschmann W, Rössler J, Castro ADF, Houk SD, Kröncke I, Dreyer W, Janssen R, Rumohr H, Dunca E (2003a) North Atlantic oscillation dynamics recorded in shells of a long-lived bivalve mollusk. Geology 31:1037–1040

Schöne BR, Pfeiffer M, Pohlmann T, Siegismund F (2005c) A seasonally resolved bottom-water temperature record for the period AD 1866–2002 based on shells of *Arctica islandica* (Mollusca, North Sea). Int J Climatol 25:947–962

Schöne BR, Tanabe K, Dettman DL, Sato S (2003b) Environmental controls on shell growth rates and δ^{18}O of the shallow-marine bivalve mollusk *Phacosoma japonicum* in Japan. Mar Biol 142:473–485

Schöne BR, Freyre Castro AD, Fiebig J, Houk SD, Oschmann W, Kröncke I (2004) Sea surface water temperatures over the period 1884–1983 reconstructed from oxygen isotope ratios of a bivalve mollusk shell (*Arctica islandica*, southern North Sea). Palaeogeogr Palaeoclimatol Palaeoecol 212:215–232

Torrence C, Compo GP (1998) A practical guide to wavelet analysis. Bull Am Meteorol Soc 79:61–78

Wanamaker A Jr, Kreutz K, Schöne B, Maasch K, Pershing A, Borns H, Introne D, Feindel S (2009) A late Holocene paleo-productivity record in the western Gulf of Maine, USA, inferred from growth histories of the long-lived ocean quahog (*Arctica islandica*). Int J Earth Sci 98:19–29

Weidman CR, Jones GA (1994) The long-lived mollusc *Arctica islandica*: a new paleoceanographic tool for the reconstruction of bottom temperatures for the continental shelves of the northern North Atlantic Ocean. J Geophys Res 99:18305–18314

Witbaard R, Franken R, Visser B (1997) Growth of juvenile *Arctica islandica* under experimental conditions. Helgolaender Meeresuntersuchungen 51:417–431

Wunsch C (1999) The interpretation of short climate records, with comments on the North Atlantic and Southern oscillations. Bull Am Meteorol Soc 80:245–255

Functional Diversity and Traits Assembly Patterns of Benthic Macrofaunal Communities in the Southern North Sea

Mehdi Ghodrati Shojaei, Lars Gutow, Jennifer Dannheim, Hendrik Pehlke and Thomas Brey

Abstract The study of ecosystem functioning—the fluxes of energy and material through biotic and abiotic components of an ecosystem—is becoming increasingly important in benthic ecological research. We investigated the functional structure of macrozoobenthic communities at four long-term sampling sites in the southern North Sea using biological traits assigned to life history, morphological and behavioural characteristics. The "typical" species of the macrofaunal assemblages at the sampling sites was characterized by small to medium body size, infaunal burrowing life style, deposit feeding habit, omnivory diet type, short to medium life span, gonochoristic sexual differentiation, <2 years age at maturity, high fecundity, and planktotrophic development mode. Functional diversity differed significantly among the four sites. As part of the present study, trait information for >330 macrofaunal taxa have been compiled in a comprehensive database.

Keywords Functional diversity · Biological traits · Macrozoobenthos · North sea

1 Introduction

Distribution, abundance and community composition of the North Sea macrozoobenthos are strongly influenced by a variety of physical, chemical and biological factors (Bremner et al. 2006; Franke and Gutow 2004; Kröncke et al. 2004). Temperature, water depth, food supply and sediment type have been shown to have critical, though sometimes variable effects on macrofaunal distribution

---

M. Ghodrati Shojaei (✉) · L. Gutow · J. Dannheim · H. Pehlke · T. Brey
Alfred Wegener Institute Helmholtz Centre for Polar and Marine Research,
Am Handelshafen 12, 27570 Bremerhaven, Germany
e-mail: Mehdi.Shojaei@awi.de

M. Ghodrati Shojaei
Department of Marine Biology, Faculty of Marine Science, Tarbiat Modares University,
Tehran, Iran

G. Lohmann et al. (eds.), *Towards an Interdisciplinary Approach in Earth System Science*, Springer Earth System Sciences,
DOI 10.1007/978-3-319-13865-7_20

(Dutertre et al. 2013; Hillebrand 2004; Posey et al. 1995). Additionally, biological interactions (e.g. competition, predation) among species influence the diversity of marine assemblages (Defeo and McLachlan 2005). Many benthic species constitute a food source for fish and other predators (Pinto 2011). Predatory fish may directly reduce epifaunal abundances while their effects on infaunal species may be limited (Schlacher and Wooldridge 1996).

Marine ecosystems are routinely subjected to a wide range of anthropogenic disturbances (Marques et al. 2009; van der Molen et al. 2013). Exposure to bottom trawling, aggregate extraction and pollution are responsible for alteration of bottom habitats and may contribute to changes in growth, mortality and recruitment rate of species (Bergman and Hup 1992; Dannheim et al. 2014; Worm et al. 2006). These changes have the potential to modify the structure and functioning of benthic communities (van der Linden et al. 2012; Worm et al. 2006).

Ecosystem functioning is a general concept that encompasses a variety of phenomena, including ecosystem processes (e.g. energy fluxes), properties (e.g. pools of carbon and organic matter) and services (e.g. human alimentation) as well as the resistance or resilience of these factors in response to fluctuating abiotic conditions (Bremner et al. 2006; Díaz et al. 2008; Hooper et al. 2005; Loreau et al. 2001; van der Linden et al. 2012). Ecosystem functioning mainly depends on traits or characteristics of the constituent functional groups of organisms (Snelgrove 1997). Traditional analytical procedures, which derive biodiversity and community structure from species abundance/biomass data, do not take into account functional features of species (van der Linden et al. 2012). However, functional diversity, i.e. the range and number of functional traits performed within an ecosystem (Díaz and Cabido 2001), is a useful indicator of ecosystem functioning (Hooper et al. 2005). Several methods based on species morphological and ecological traits have been proposed to describe and quantify functional diversity of benthic assemblages (Beche et al. 2006; Bremner et al. 2006; Pacheco et al. 2011; van der Molen et al. 2013). We used biological trait analysis (BTA) to explore the ecological functioning of benthic assemblages (Sigala et al. 2012; van der Linden et al. 2012) and to compare functional diversity across different assemblages. BTA combines quantitative structural data (e.g. abundance) with information on biological characteristics of the taxa (Shettleworth 2012) to functionally characterise species assemblages (Bremner et al. 2006). This method is suitable for analysing assemblage responses to environmental parameters (Paganelli et al. 2012; Shettleworth 2012). Hence, BTA provides a link between benthic assemblages, environment and ecosystem processes (Oug et al. 2012; Pacheco et al. 2011)

The objectives of this study were (a) to determine the dominant functional characteristics of the German Bight benthos and (b) to identify functional differences between benthic communities at different sites by comparing functional diversity.

2 Material and Methods

A database was generated from a long-term macro-zoobenthos time series at four sites in the German Bight (Fig. 1). Benthos samples were collected each spring from 1981 to 2011 (i.e. "taxa by station" matrix). The sites covered the dominant sediment types (FSd = fine sand, Slt = silt, SSd = silty sand and WB = White Bank with silty sand in deeper waters) in the south-eastern North Sea with the corresponding typical benthic associations (Salzwedel et al. 1985). At each station and sampling date, five 0.1 m^2 samples were taken with a van Veen grab. The samples were sieved over 0.5 mm mesh and fixed in 4 % buffered formalin. Macro-zoobenthic organisms were identified to species level as far as possible, counted and weighed (wet weight). In total we identified 334 species belonging to 235 genera and 157 families, respectively. After computing average abundance (N/m^{-2}) per sampling date and station from the five replicate samples, our basic data matrix consisted of 334 species × four stations × 31 sampling dates. From these data, we computed average abundance per species and station over the complete sampling period (1981–2011).

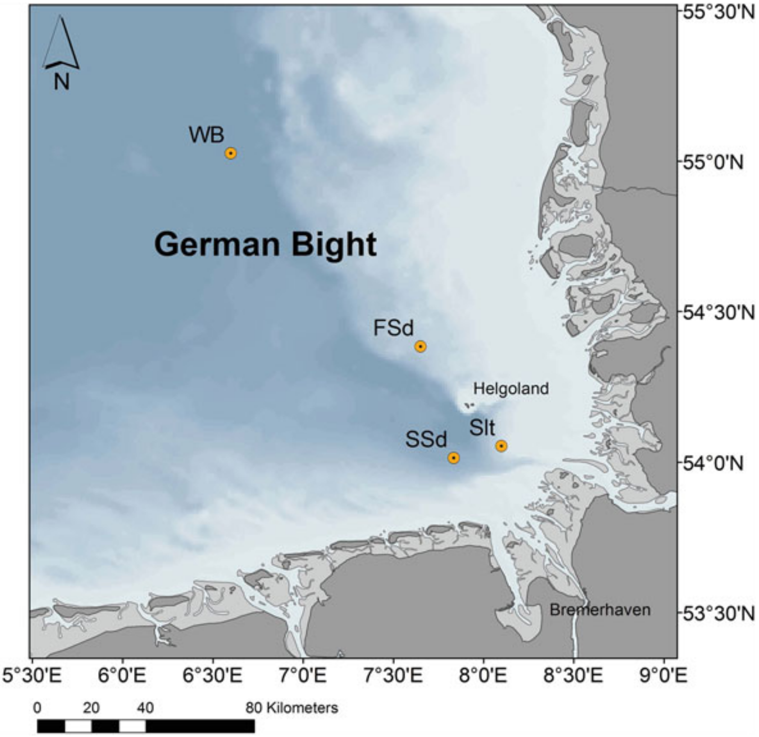

Fig. 1 Location of the four long-term monitoring sites (i.e. *Slt* silt; *SSd* silty sand, *FSd* fine sand, *WB* White Bank) for macro-zoobenthos in the German Bight

An autecological database (i.e. “trait by species” matrix) was generated from 10 different traits covering life history, behavioral characteristics, morphological attributes and environmental preferences of benthic species. Traits were selected either for their importance for the structure and functioning of the benthic system or for their sensitivity to changes in environmental variables. Each trait comprised qualitative or quantitative modalities, which allow for a functional characterization of individual taxa (Table 1). Specific trait modalities were assigned to individual taxa (i.e. species or genus) using a “fuzzy coding” procedure (Chevene et al. 1994) with a scoring range for affinities of zero to three. An affinity score of zero indicates no association of a taxon with a modality, whereas a score of three indicates highest affinity. For example, the polychaete *Pisione remota* mostly feeds as predator/scavenger but may also feed occasionally as deposit feeder. Accordingly, the species was coded 1 for “surface/subsurface deposit feeder” and 2 for “predator/scavenger” for the trait variable ‘feeding habit’. Information on biological traits of taxa was compiled from peer-reviewed literature, species identification guides, online databases (e.g. BIOTIC 2012) and from personal expert consultations. Missing data were supplemented by using information referring to closely related species. To give the same weight to each taxon and trait, the scores were standardized by scaling the sum of all scores for each trait of a taxon equal to 100. The standardized modality scores for each taxon were multiplied by the average species abundance at each station and summed up over all taxa. The results are a “trait by station matrix” providing the frequencies of occurrence of modalities in each year and at each station.

The complete trait dataset contained 10 traits subdivided into 43 modalities. The amount of information available differed markedly among traits. Information on feeding habit, environmental position and adult motility was abundant, whereas data on morphological traits (e.g. fragility) and fertilization type were not that readily available. The full data gathered on the species traits with an attributed reference list are available as Supplementary Material at PANGAEA—Network for Geological and Environmental Data (http://doi.pangaea.de/10.1594/PANGAEA.813419).

Functional diversity of an assemblage was calculated using the Quadratic entropy index (Rao 1982):

$$FD_{RAO} = \sum_{i=1}^{s} \sum_{j=1}^{s} d_{ij} p_i p_j$$

where s is the number of taxa in the community and p_i and p_j are the proportion of the ith and jth taxon in the community, respectively. d_{ij} is the trait dissimilarity between each pair of taxa i and j measured as Euclidean distance. Accordingly, $\mathrm{FD_{RAO}}$ is the sum of the trait dissimilarities among all possible pairings of taxa, weighted by the relative abundance of the taxa (de Bello et al. 2009). $\mathrm{FD_{RAO}}$ was calculated separately for each of the 11 biological traits and summed up for the entire assemblage of a site (Darr et al. 2014; van der Molen et al. 2013). $\mathrm{FD_{RAO}}$ was calculated using the ‘ADE-4’ (Thioulouse et al. 1997) and ‘VEGAN’ libraries

Table 1 Traits and their modalities used to assess functional composition

Traits	Modalities
Feeding habit	Surface deposit feeder
	Sub-surface deposit feeder
	Suspension feeder
	Interface feeder
	Predator
	Sand licker
	Grazer
	Parasite
Environmental position	Epifauna
	Infauna
	Epizoic
Adult movement	Swimmer
	Crawler
	Burrower
	Sessile
Diet type	Omnivore
	Carnivore
	Herbivore
Larval development	Direct
	Lecithotrophic
	Planktotrophic
Sexual differentiation	Gonochoric
	Synchronous hermaphrodite
	Sequential hermaphrodite
Adult longevity (years)	<1
	1–2
	3–10
	10+
Age at maturity (years)	<1
	1–2
	3–4
	4+
Fecundity	1–10
	10–100
	100–1,000
	100–10,000
	10,000–1 m
	1 m+

(continued)

Table 1 (continued)

Traits	Modalities
Maximum size of organism (cm)	<1
	1–10
	11–20
	20+

(Oksanen et al. 2013) for the open-source R software, version 3.0.1 (R Development Core Team 2009). Similarity in β-diversity (i.e. the variability in species composition among sampling sites for a given area at a given spatial scale) among the sampling sites were tested using a test for homogeneity of multivariate dispersions (PERMDISP routine, Permanova+ add-on in Primer 6; Anderson et al. 2008). The test was conducted on the basis of species composition (presence/absence) data in conjunction with compositional dissimilarity (i.e., Sorensen resemblance measures). Functional diversity was compared among sampling sites by means of a Monte-Carlo random permutation test (999 permutations). For each trait, the distribution of modalities was compared among the four sampling sites using contingency tables (Chi square tests).

3 Results

For each trait, the distribution of modalities differed significantly between the four sampling sites (each $p < 0.001$; Fig. 2). All benthic assemblages were dominated by infaunal organisms (Fig. 2a) with small to medium body size (1–10 cm; Fig. 2b). Small individuals (<1 cm) occurred mainly at stations Slt and WB. Most individuals were burrowers while sessile species were rare in all assemblages (Fig. 2c). Omnivorous organisms dominated the benthos whereas the proportion of purely herbivorous individuals was generally low (Fig. 2d). The reproductive mode was mainly gonochoric with development through a planktotrophic larval stage (Fig. 2e, f). The majority of the animals reached maturity within 2 years (Fig. 2g) and only few species had a life expectancy of more than 10 years (Fig. 2h). Only the assemblage at station WB had a higher proportion of individuals with a longevity >10 years. Feeding types were more heterogeneously distributed (Fig. 2i). Deposite feeders and interface feeders were generally the most common feeding types. However, predators/scavengers were also common at all sites. Fecundity mainly ranged between 10 and 10^6 ind. fem.$^{-1}$ (Fig. 2j). Only at station Slt a considerable proportion of the infaunal assemblage produced more than 10^6 ind. fem.$^{-1}$ while only few individuals produced less than 100 ind. fem.$^{-1}$ at all sites.

The average functional diversity of the benthic assemblages ranged from $FD_{RAO} = 1.66 \pm 0.16$ at site Slt to $FD_{RAO} = 2.01 \pm 0.06$ at site SSd. The functional diversity was significantly lower at site Slt than at all other sites ($p < 0.001$; Fig. 3). At site WB, the functional diversity was lower than at sites FSD and SSd ($p < 0.01$) which were not significantly different ($p > 0.05$).

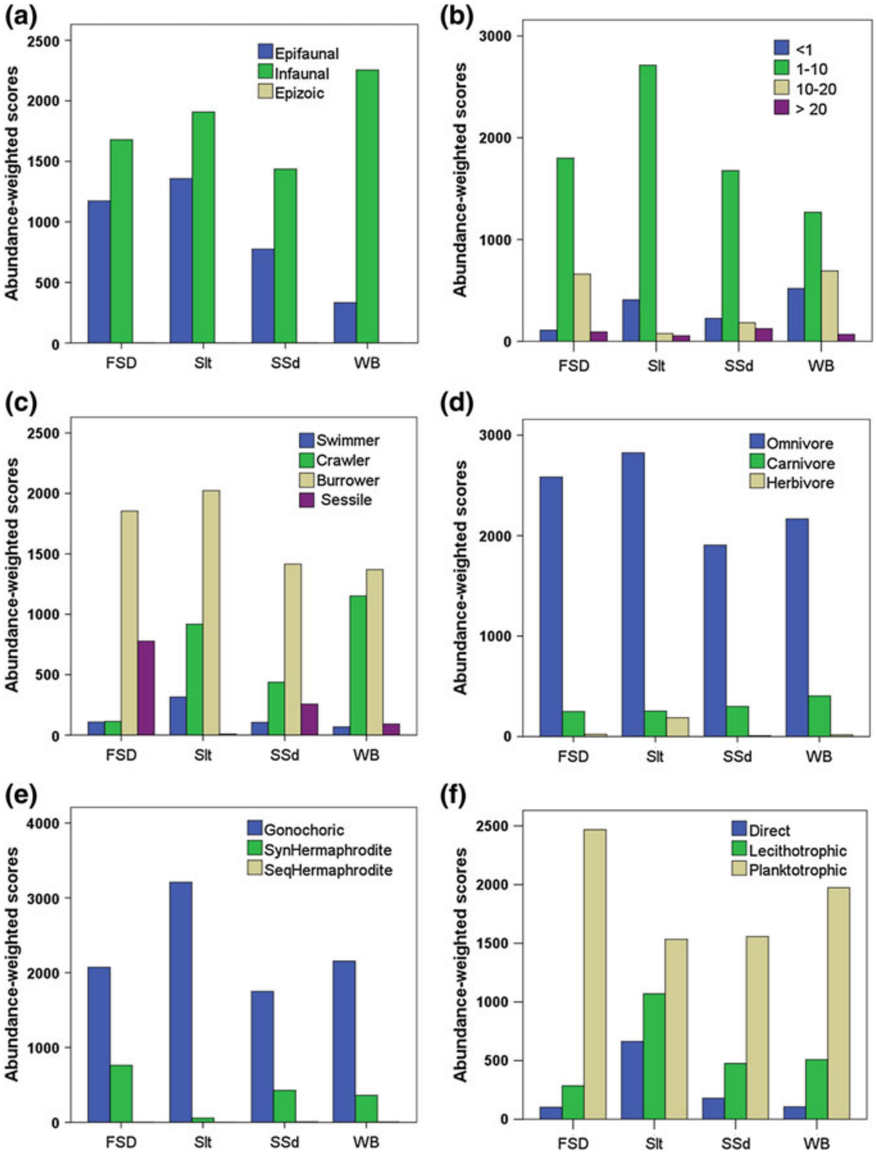

Fig. 2 Distribution of abundance-weighted modality scores (integrated over the entire 30 year period) within benthic infaunal assemblages at four sites in the German Bight: **a** environmental position, **b** size of organisms, **c** adult movement, **d** diet type, **e** sexual differentiation, **f** larval development, **g** age at maturity, **h** adult longevity, **i** feeding habit and **j** fecundity. Site names are *FSd* fine sand, *Slt* silt, *SSd* silty sand and *WB* White Bank. For each trait the distribution of modalities differed significantly between the four sampling sites ($p < 0.001$)

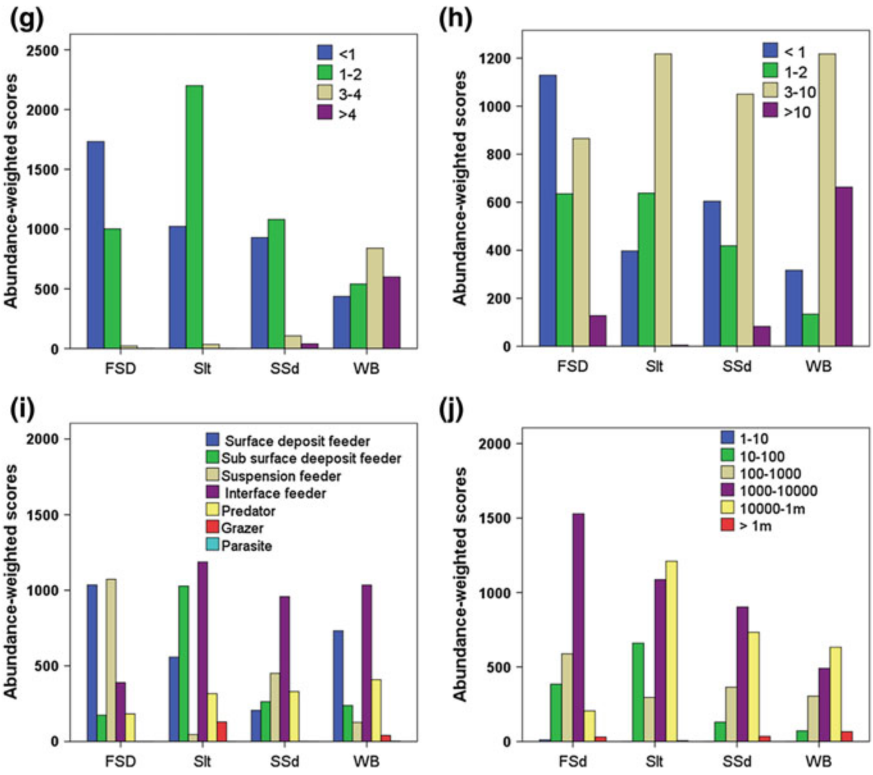

Fig. 2 (continued)

Fig. 3 Average (±SD) functional diversity of the benthic infaunal communities at four sites in the German Bight. *FSd* fine sand, *Slt* silt, *SSd* silty sand, *WB* White Bank

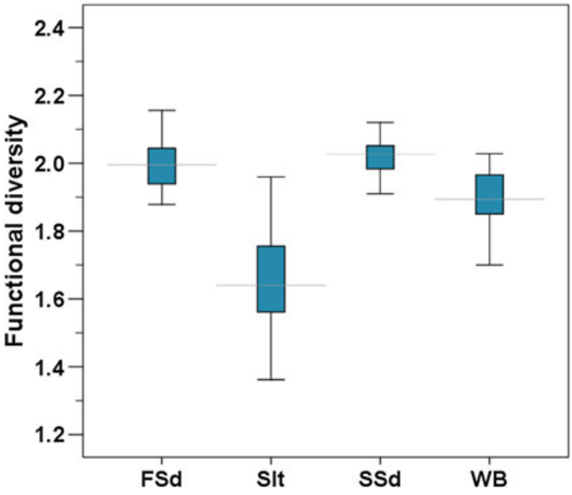

4 Discussion

The functional trait composition of the benthic assemblages in the German Bight indicates that the benthos of the south-eastern North Sea is generally dominated by small-sized and short-living opportunistic species. A dominance of opportunistic species is often characteristic for disturbed ecosystems (Borja et al. 2003; Thrush et al. 1998). In the North Sea various anthropogenic stressors (e.g. bottom trawling, eutrophication) have modified the benthic communities towards a suppression of large, long-living species, which were replaced by small, opportunistic species (Kaiser and Spencer 1996). For example, continuous physical disturbance of the seafloor by bottom trawling prevents the recovery of benthic species with multi-annual life spans, low recruitment and slow post-recruitment development (Kroger 2003). These organisms are out-competed by opportunistic taxa with high recruitment rates and are, thus, at high risk of regional extinction (Calabretta and Oviatt 2008).

The test for homogeneity of multivariate dispersions revealed no differences among the three sampling sites (i.e. FSd, SSd and WB; $p > 0.05$). Several environmental parameters may have contributed to the observed homogenization of benthic assemblages. However theoretical and empirical surveys have demonstrated that increased homogeneity mainly owing to anthropogenic and climatic disturbances (Passy and Blanchet 2007). Widespread anthropogenic and climatic pressures increase the harshness of habitat conditions and thus, reduce compositional heterogeneity among sites by decreasing the stochastic processes in structuring assemblages (Donohue et al. 2009; Olden and Poff 2004).

Pairwise test identified solely Slt as being significantly different ($p < 0.01$) from the other three sites in terms of variability in species composition. It is likely resulted from a lower species richness as well as from the numerical dominance of a few species (i.e., *Nucula* spp. and *Owenia fusiformis* constituted >50 % total benthic abundance). Numerical dominance of few species can be indicative of a highly stressed ecosystem (Méndez 2002). Slt was located in the innermost German Bight, in front of the mouths of the rivers Weser and Elbe. In addition to the role of the general large scale influences (e.g. bottom trawling) in the shaping of the entire German Bight ecosystem, it seems that some local scale drivers (e.g. river water run off), in particular, have caused drastic changes in the benthic assemblages at the Slt site. The possible effect of riverine discharge could be a function of the interaction between physical processes (e.g. sedimentation and advection) biological processes (e.g. losses via low-salinity intolerance) and chemical processes (e.g. nutrient enhancement) (Palmer et al. 2000). The functional trait composition were different among all four sampling sites (Fig. 2). For example, the benthic assemblage at the station WB showed a higher proportion of long-lived species suggesting more stable conditions and less disturbance in deeper offshore waters. Assembly theory for ecological communities suggests that two processes, i.e. competition and abiotic filtering (i.e. ecological filters that select individual taxa from a regional pool because they own a certain set of traits suitable for a given habitat (Díaz et al. 1998;

Maire et al. 2012) affect the distribution of trait values within assemblages (Cornwell et al. 2006). Within a local community, competition aims to ecological differentiation of coexisting species, whereas abiotic filtering reduces the spread of trait values, reflecting common ecological tolerances (de Bello 2012; Kang et al. 2014).

The results also revealed that not only functional composition but also functional diversity differed significantly among sampling sites (Fig. 3). Spatial differences in functional diversity of benthic assemblages may emerge as a result of the environmental variation as well as distinct behaviors, processes and functions that are known to prevail in each ecosystem type (Dimitriadis et al. 2012; Levin et al. 2001). In conclusion, two important results can be deduced from our results: First, changes in benthic assemblages (e.g. homogenization of benthic assemblages in this study) are not necessarily linked with changes in ecological functions played by organisms. Second, biological traits analysis (BTA) is sensitive method in identifying differences among benthic assemblages and, thus, can provide additional information of community distribution patterns (Alves et al. 2014). For example, this method has proven to be a very useful approach for determining changes in benthic assemblages exposed to different disturbances such as bottom trawling (Tillin et al. 2006), marine aggregate dredging (Newell et al. 2004; Robinson et al. 2005) and eutrophication (Paganelli et al. 2012).

Acknowledgments We are deeply indebted to all the persons who contributed in the sampling, sample sorting and taxonomic identification. We thank the crew of all research vessels especially "FS Heincke" and "FS Uthörn" for their help with sampling throughout the years. The authors are also grateful for the very valuable comments of three anonymous reviewers. MSh is funded by the Iranian Ministry of Sciences, Research and Technology. We gratefully acknowledge partial support through Earth System Sciences Research School (ESSReS).

References

Alves A, Veríssimo H, Costa M, Marques J (2014) Taxonomic resolution and biological traits analysis (BTA) approaches in estuarine free-living nematodes. Estuar Coast Shelf Sci 138:69–78

Anderson MJ, Gorley RN, Clarke KR (2008) PERMANOVA+ for primer: guide to software and statistical methods. PRIMER-E, Plymouth, p 214

Beche LA, Mcelravy EP, Resh VH (2006) Long term seasonal variation in the biological traits of benthic macroinvertebrates in two Mediterranean-climate streams in California, USA. Freshw Biol 51:56–75

Bergman M, Hup M (1992) Direct effects of beamtrawling on macrofauna in a sandy sediment in the southern North Sea. ICES J Mar Sci: J Conseil 49:5–11

Borja A, Muxika I, Franco J (2003) The application of a Marine Biotic Index to different impact sources affecting soft-bottom benthic communities along European coasts. Mar Pollut Bull 46:835–845

Bremner J, Rogers SI, Frid CLJ (2006) Matching biological traits to environmental conditions in marine benthic ecosystems. J Mar Syst 60:302–316

Calabretta CJ, Oviatt CA (2008) The response of benthic macrofauna to anthropogenic stress in Narragansett Bay, Rhode Island: a review of human stressors and assessment of community conditions. Mar Pollut Bull 56:1680–1695

Chevene F, Doléadec S, Chessel D (1994) A fuzzy coding approach for the analysis of long-term ecological data. Freshw Biol 31:295–309

Cornwell WK, Schwilk DW, Ackerly DD (2006) A trait-based test for habitat filtering: convex hull volume. Ecology 87:1465–1471

Dannheim J, Brey T, Schröder A, Mintenbeck K, Knust R, Arntz WE (2014) Trophic look at soft-bottom communities—short-term effects of trawling cessation on benthos. J Sea Res 85:18–28

Darr A, Gogina M, Zettler ML (2014) Functional changes in benthic communities along a salinity gradient—a western Baltic case study. J Sea Res 85:315–324

de Bello F (2012) The quest for trait convergence and divergence in community assembly: are null-models the magic wand? Glob Ecol Biogeogr 21:312–317

de Bello F, Thuiller W, Lepš J, Choler P, Clément JC, Macek P, Sebastià MT, Lavorel S (2009) Partitioning of functional diversity reveals the scale and extent of trait convergence and divergence. J Veg Sci 20:475–486

Defeo O, McLachlan A (2005) Patterns, processes and regulatory mechanisms in sandy beach macrofauna: a multi-scale analysis. Mar Ecol Prog Ser 295:1–20

Díaz S, Cabido M (2001) Vive la difference: plant functional diversity matters to ecosystem processes. Trends Ecol Evol 16:646–655

Díaz S, Cabido M, Casanoves F (1998) Plant functional traits and environmental filters at a regional scale. J Veg Sci 9:113–122

Díaz AM, Alonso MLS, Gutiérrez MRVA (2008) Biological traits of stream macroinvertebrates from a semi-arid catchment: patterns along complex environmental gradients. Freshw Biol 53:1–21

Dimitriadis C, Evagelopoulos A, Koutsoubas D (2012) Functional diversity and redundancy of soft bottom communities in brackish waters areas: local vs regional effects. J Exp Mar Biol Ecol 426:53–59

Donohue I, Jackson AL, Pusch MT, Irvine K (2009) Nutrient enrichment homogenizes lake benthic assemblages at local and regional scales. Ecology 90:3470–3477

Dutertre M, Hamon D, Chevalier C, Ehrhold A (2013) The use of the relationships between environmental factors and benthic macrofaunal distribution in the establishment of a baseline for coastal management. ICES J Mar Sci: J Conseil 70:294–308

Franke H-D, Gutow L (2004) Long-term changes in the macrozoobenthos around the rocky island of Helgoland (German Bight, North Sea). Helgol Mar Res 58:303–310

Hillebrand H (2004) Strength, slope and variability of marine latitudinal gradients. Mar Ecol Prog Ser 273:251–267

Hooper D, Chapin F, Ewel J, Hector A, Inchausti P, Lavorel S, Lawton J, Lodge D, Loreau M, Naeem S (2005) Effects of biodiversity on ecosystem functioning: a consensus of current knowledge. Ecol Monogr 75:3–35

Kaiser MJ, Spencer BE (1996) The effects of beam-trawl disturbance on infaunal communities in different habitats. J Anim Ecol pp 348–358

Kang M, Chang SX, Yan ER, Wang XH (2014) Trait variability differs between leaf and wood tissues across ecological scales in subtropical forests. J Veg Sci 25(3):703–714

Kroger K (2003) Recovery of subtidal benthic macroinvertebrate communities following natural and experimental disturbances. Victoria University of Wellington

Kröncke I, Stoeck T, Wieking G, Palojärvi A (2004) Relationship between structural and functional aspects of microbial and macrofaunal communities in different areas of the North Sea. Mar Ecol Prog Ser 282:13–31

Levin LA, Boesch DF, Covich A, Dahm C, Erséus C, Ewel KC, Kneib RT, Moldenke A, Palmer MA, Snelgrove P (2001) The function of marine critical transition zones and the importance of sediment biodiversity. Ecosystems 4:430–451

Loreau M, Naeem S, Inchausti P, Bengtsson J, Grime J, Hector A, Hooper D, Huston M, Raffaelli D, Schmid B (2001) Biodiversity and ecosystem functioning: current knowledge and future challenges. Science 294:804–808

Maire V, Gross N, Börger L, Proulx R, Wirth C, Pontes LDS, Soussana JF, Louault F (2012) Habitat filtering and niche differentiation jointly explain species relative abundance within grassland communities along fertility and disturbance gradients. New Phytologist 196:497–509

Marques J, Basset A, Brey T, Elliott M (2009) The ecological sustainability trigon—a proposed conceptual framework for creating and testing management scenarios. Mar Pollut Bull 58:1773–1779

Méndez N (2002) Annelid assemblages in soft bottoms subjected to human impact in the Urías estuary (Sinaloa, Mexico). Oceanol Acta 25:139–147

Newell R, Seiderer L, Simpson N, Robinson J (2004) Impacts of marine aggregate dredging on benthic macrofauna off the south coast of the United Kingdom. J Coastal Res 115–125

Oksanen J, Blanchet FG, Kindt R, Oksanen MJ, Suggests M (2013) Package 'vegan'. Community ecology package, version 2, 0–0

Olden JD, Poff NL (2004) Ecological processes driving biotic homogenization: testing a mechanistic model using fish faunas. Ecology 85:1867–1875

Oug E, Fleddum A, Rygg B, Olsgard F (2012) Biological traits analyses in the study of pollution gradients and ecological functioning of marine soft bottom species assemblages in a fjord ecosystem. J Exp Mar Biol Ecol 432:94–105

Pacheco AS, González MT, Bremner J, Oliva M, Heilmayer O, Laudien J, Riascos JM (2011) Functional diversity of marine macrobenthic communities from sublittoral soft-sediment habitats off northern Chile. Helgol Mar Res 65:413–424

Paganelli D, Marchini A, Occhipinti-Ambrogi A (2012) Functional structure of marine benthic assemblages using biological traits analysis (BTA): a study along the Emilia-Romagna coastline (Italy, North-West Adriatic Sea). Estuar Coast Shelf Sci 96:245–256

Palmer MA, Covich AP, Lake S, Biro P, Brooks JJ, Cole J, Dahm C, Gibert J, Goedkoop W, Martens K (2000) Linkages between aquatic sediment biota and life above sediments as potential drivers of biodiversity and ecological processes, a disruption or intensification of the direct and indirect chemical, physical, or biological interactions between aquatic sediment biota and biota living above the sediments may accelerate biodiversity loss and contribute to the degradation of aquatic and riparian habitats. Bioscience 50:1062–1075

Passy SI, Blanchet FG (2007) Algal communities in human-impacted stream ecosystems suffer beta-diversity decline. Divers Distrib 13:670–679

Pinto DFDBL (2011) Relationships between the structure of sublitoral assemblages and habitat complexity in a rocky shore in the Portugal coast

Posey M, Powell C, Cahoon L, Lindquist D (1995) Top down vs bottom up control of benthic community composition on an intertidal tideflat. J Exp Mar Biol Ecol 185:19–31

Rao CR (1982) Diversity and dissimilarity coefficients: a unified approach. Theor Popul Biol 21:24–43

R Development Core Team (2009) R: a language and environment for statistical computing. R Foundation for Statistical Computing, Viena. http://www.R-project.org

Robinson J, Newell R, Seiderer L, Simpson N (2005) Impacts of aggregate dredging on sediment composition and associated benthic fauna at an offshore dredge site in the southern North Sea. Mar Environ Res 60:51–68

Salzwedel H, Rachor E, Gerdes D (1985) Benthic macrofauna communities in the German Bight. Veröffentlichungen des Instituts für Meeresforschung Bremerhaven 20:199–267

Schlacher T, Wooldridge T (1996) Patterns of selective predation by juvenile, benthivorous fish on estuarine macrofauna. Mar Biol 125:241–247

Shettleworth SJ (2012) Do animals have insight, and what is insight anyway? Can J Exp Psychol 66:217–226

Sigala K, Reizopoulou S, Basset A, Nicolaidou A (2012) Functional diversity in three Mediterranean transitional water ecosystems. Estuar Coast Shelf Sci 110:202–209

Snelgrove PV (1997) The importance of marine sediment biodiversity in ecosystem processes. Ambio 578–583

Thioulouse J, Chessel D, Dole S, Olivier J-M (1997) ADE-4: a multivariate analysis and graphical display software. Stat Comput 7:75–83

Thrush S, Hewitt J, Cummings V, Dayton P, Cryer M, Turner S, Funnell G, Budd R, Milburn C, Wilkinson M (1998) Disturbance of the marine benthic habitat by commercial fishing: impacts at the scale of the fishery. Ecol Appl 8:866–879

Tillin H, Hiddink J, Jennings S, Kaiser M (2006) Chronic bottom trawling alters the functional composition of benthic invertebrate communities on a sea-basin scale. Mar Ecol Prog Ser 318:31–45

van der Linden P, Patrício J, Marchini A, Cid N, Neto JM, Marques JC (2012) A biological trait approach to assess the functional composition of subtidal benthic communities in an estuarine ecosystem. Ecol Ind 20:121–133

van der Molen J, Aldridge JN, Coughlan C, Parker ER, Stephens D, Ruardij P (2013) Modelling marine ecosystem response to climate change and trawling in the North Sea. Biogeochemistry 113:213–236

Worm B, Barbier EB, Beaumont N, Duffy JE, Folke C, Halpern BS, Jackson JB, Lotze HK, Micheli F, Palumbi SR (2006) Impacts of biodiversity loss on ocean ecosystem services. Science 314:787–790

Snow Accumulation in North Greenland over the Last Millennium

Stefanie Weißbach, Anna Wegner and Sepp Kipfstuhl

Abstract Knowledge of snow accumulation rates of the large polar ice sheets and their variability over time is crucial for mass budget studies and sea level predictions. Here we present mean long-term snow accumulation rates of 12 shallow ice cores drilled by the North Greenland traverse in the northern part of Greenland. The ice core records cover the last 500–1000 years. We find a trend of decreasing accumulation rate from the southwest (~180 mmWE/a) to northeast (~95 mmWE/a). Ice divide sites show higher accumulation rates but also higher variability (up to 20 %) than sites off the ice divides (less than 10 %). Unlike a recent modeling study our results indicate no change in the accumulation in the north of Greenland during the last 400 years.

Keywords Greenland · Accumulation rate · Polar ice sheet · Mass budget · North Greenland · Ice divide

1 Introduction

Polar ice sheets are unique archives of present and past climatic and environmental conditions. Ice cores drilled on the polar ice sheets provide not only extended records of the Earth's climate in the far past but give also insight into the most recent development in remote parts of the globe where instrumental records are sparse or not available at all. The polar ice sheets are not only unique paleo-archives they are also an important active component of the climate system. Changes in the accumulation rate affect the mass balance of the ice sheets but also reflect changes in the hydrological cycle and atmospheric circulation.

S. Weißbach (✉) · A. Wegner · S. Kipfstuhl
Alfred Wegener Institute Helmholtz Centre for Polar and Marine Research,
Bremerhaven, Germany
e-mail: Stefanie.Weissbach@awi.de

G. Lohmann et al. (eds.), *Towards an Interdisciplinary Approach in Earth System Science*, Springer Earth System Sciences,
DOI 10.1007/978-3-319-13865-7_21

Accumulation rates in Greenland were compiled first by Ohmura and Reeh (1991). Updated maps of the accumulation rate were then presented by Ohmura et al. (1999) and Bales et al. (2001, 2009). More recently, maps of the accumulation rate or estimates of the mass balance for varying periods are produced by modeling the precipitation over Greenland using regional atmospheric circulation models (e.g. Dethloff et al. 2002; Burgess et al. 2010; Hanna et al. 2011; Box et al. 2013). Box et al. (2013) reconstructed the accumulation history over the last 400 years and find for example that the Greenland ice sheet net snow accumulation rate increased by 12 % from the end of the Little Ice Age (1840 AD).

Due to the huge dimensions of the polar ice sheets data coverage is not at all evenly distributed (e.g. Ohmura and Reeh 1991; Box et al. 2013). Until the beginning of the era of deep cores in Greenland (GRIP, GISP2, NGRIP and NEEM) at about 1990 most work focused on the central and southern parts of Greenland (e.g. NEEM community members 2013). North Greenland was only covered sparsely, mainly by the PARCA activities (e.g. Mosley-Thompson 2001) and the North Greenland Traverse (NGT). The NGT started at the Summit of the Greenland ice sheet after the GRIP ice core was completed (in summer 1993) and ended at the NGRIP drill site about 350 km northwest of Summit in summer 1996. A total of 13 deep ice cores 70–175 m long were drilled during the NGT (see Fig. 1).

In this contribution within the ESSReS-framework we present an overview of the evolution of the accumulation in North Greenland over the last 500–800 years, the first such overview for the data sparse North Greenland region. The accumulation histories are derived by carefully aligning the time scale for the 13 NGT cores by volcanic matching, and subsequently using measured density data to convert average annual layer thickness between volcanic horizons to accumulation rate estimations.

2 Methods

The lengths of the investigated ice cores and the coordinates of the drill sites are given in Table 1. An overview of their positions is given in Fig. 1.

The drill sites of cores B21–B30 (except B22) are lying on the main ice divide leading from the Summit to the Northwest and then splitting north of site B29 into a branch towards the Northeast (B23 and B21). Core B22 has been drilled in the windward side and all other cores (B16–B20) in the lee-side of the ice divides.

The Di Electric Profiling (DEP)-records of the cores which reflect the impurity content in the ice are used to date the cores. The basis of the dating is the well know pattern of volcanic events present in DEP records (Fig. 2).

The accumulation rate, given here as equivalent height of a water column (mmWE/a), is derived from the deposited snow mass per time in a core. During the field campaign the length and weight of each single piece of core were measured. From these results and the known diameter of the cores an average density for each single piece was calculated. In the AWI cold room laboratories the density of the cores was additionally measured in millimeter resolution by γ absorption (Wilhelms 1996) or X-

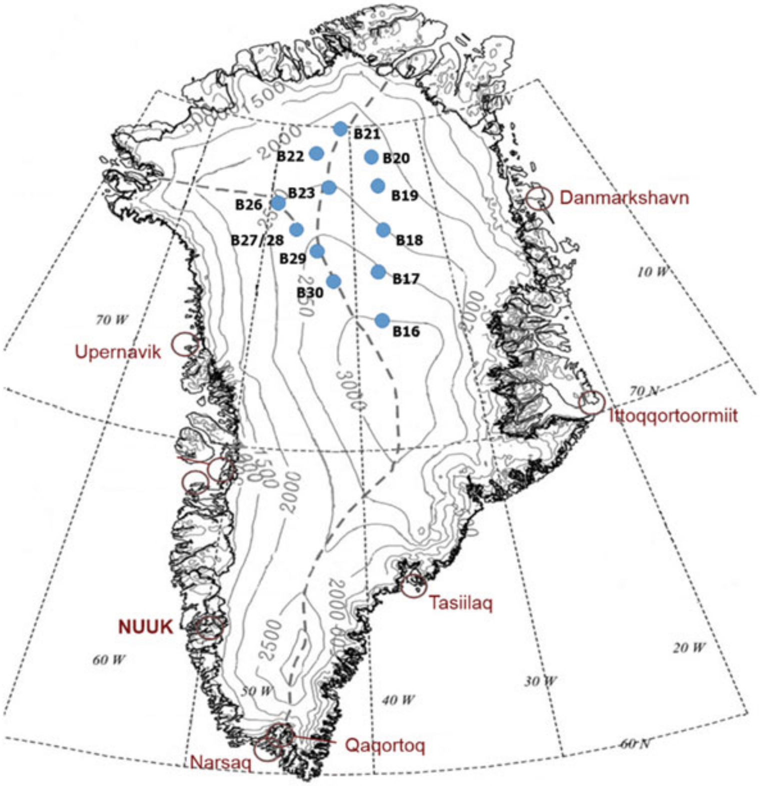

Fig. 1 Map of drill sites of the NGT cores (*blue dots*). The *dashed line* represents present ice divides whereas *solid lines* mark the surface topography

Table 1 Site information about the NGT drill locations

Core	Drill site	Core length (m)	Altitude (m)	Latitude °N	Longitude °W
B16	NGT 03	102.4	3,040	73.94	37.63
B17	NGT 06	100.8	2,820	75.25	37.63
B18	NGT 14	150.2	2,508	76.62	36.40
B19	NGT 19	150.4	2,234	78.00	36.40
B20	NGT 23	150.4	2,147	78.83	36.50
B21	NGT 27	100.6	2,185	80.00	41.14
B22	NGT 30	120.6	2,242	79.34	45.91
B23	NGT 33	150.8	2,543	78.00	44.00
B26	NGT 37	119.7	2,598	77.25	49.22
B27	NGT 39	175.0	2,733	76.66	46.82
B28	NGT 39	70.7	2,733	76.66	46.82
B29	NGT 42	110.5	2,874	76.00	43.50
B30	NGT 45	160.8	2,947	75.00	42.00

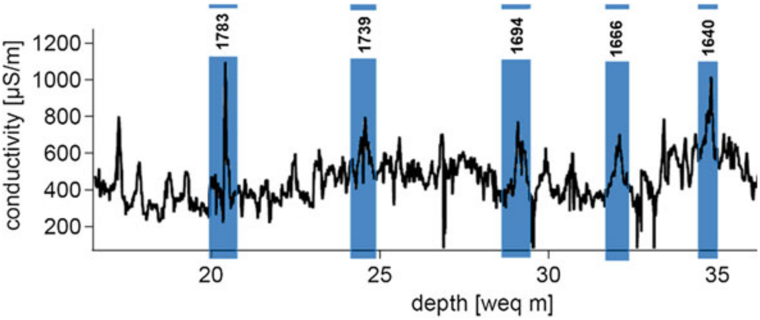

Fig. 2 Dating example. Volcanic marker horizons (*blue bars*) in the DEP record (here core B20 on water equivalent depth scale) provide ice core ages

ray imaging (Freitag et al. 2013). To account for the increase of density in the top 100 m of the ice sheet from about 300 kg/m^3 for the uppermost firn layers to the density of ice (920 kg/m^3) an exponential function was fit to the obtained density profiles.

3 Results

The mean accumulation rates at the 12 drill sites are presented in Table 2. They do not exceed 200 mmWE/a and show a west-east as well as a south-north trend (Fig. 3). The accumulation rates decrease northward from between 150 and 200 mm/a just north of the summit to less than 100 mm/a between 78°N and 79°N, and they are strongly influenced by the ice sheet topography (Fig. 3). The highest accumulation rates (180 and 176 mmWE/a) are found at the B27 and B26 drill sites on the ice divide. The cores with the lowest accumulation rates are B19 and B20 (94 and 98 mmWE/a) with the largest distance to the ice divides in the far northeast. This pattern in the accumulation results probably from a combination of factors. Besides temperature and humidity of the air the shape of the *coastline*, the topography and the inclination of the slopes west of the inland ice plateau play some role for the clouds moving on to the inland ice (Benson 1962). The moisture-

Table 2 Mean accumulation rates for North Greenland at the NGT drill sites

	B16	B17	B18	B19	B20	B21
mm/a	141	114	103	94	98	109
Period	1993–1640	1993–1479	1993–934	1993–934	1994–1179	1994–1514
	B22	B23	B26	B27	B29	B30
mm/a	145	121	176	180	149	166
Period	1994–1479	1994–1179	1995–1601	1995–1783	1995–1479	1995–1259

Given are mean values over the period from present (1993–1995) back to the time of the deepest volcanic event identified in the core

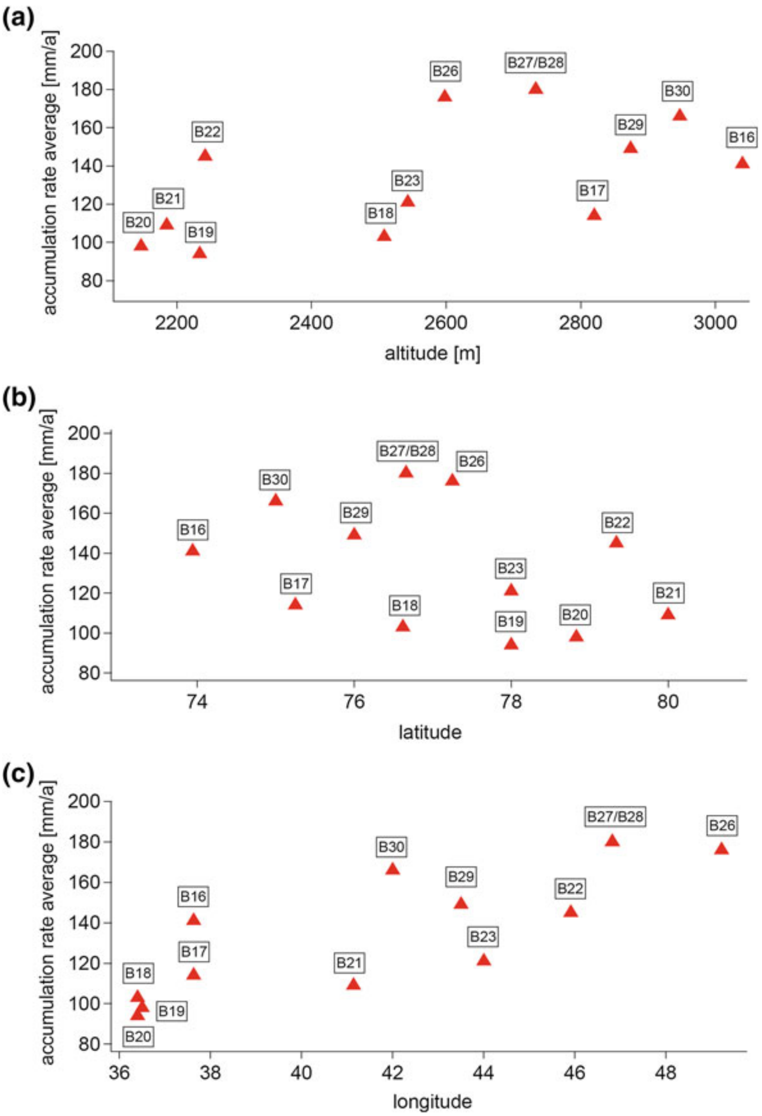

Fig. 3 Accumulation rates at NGT sites versus. **a** Altitude, **b** latitude and **c** longitude

bearing air masses come generally from the west or southwest originating in cyclones forming in the Hudson or Baffin Bay (Chen et al. 1997). They loose most moisture on the coast in front of and on the slopes to the inland ice plateau. East of the ice divide in its wind shadow and at similar or even slightly descending altitude the amount of precipitation is reduced.

Changes in the accumulation rates over the last 400–800 years are given in Table 3 and displayed in Fig. 4. Except for the 33 years lasting period between the

Table 3 Mean accumulation rates (mm/a) for periods between well dated volcanic eruptions of Tambora (1816), Laki (1783) Huyanaputina (1601), Mt. St. Helens (1479) and an unknown event at 1259

Period	B16	B17	B18	B19	B20	B21	B22	B23	B26	B27	B29	B30
1993–1816	138	115	107	95	97	110	144	121	176	174	146	168
1816–1783	148	119	107	96	93	110	154	132	190	184	161	178
1783–1601	143	114	105	95	101	109	144	121	173	171	148	166
1601–1479	142	114	105	90	103	107	144	120		172	152	169
1479–1259			101	90	98					167		161

Fields are blank, when the respective time interval was not covered by the core

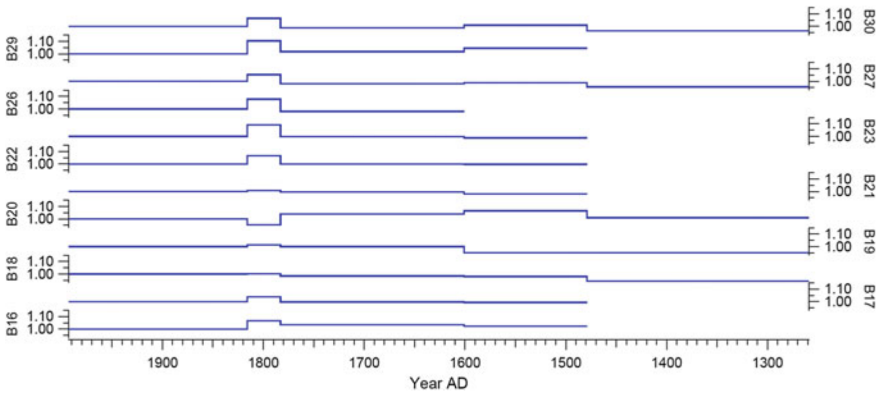

Fig. 4 Relative changes in the accumulation rates for periods between well dated volcanic eruptions (Tambora 1816; Laki 1783; Huyanaputina 1601; Mt. St. Helens 1479; unknown 1259). Reference for each core is the mean accumulation rates over the period between 1816 and present (1993–1995)

Laki and Tambora eruptions (1783–1816) the accumulation rates do not show any significant changes during the entire period of the last millennium. The changes are mostly around 1 % but never exceed 5 % relative to the mean since the Tambora eruption (1816–1993).

4 Discussion and Conclusion

The accumulation rates derived from 12 shallow ice cores in northern central Greenland indicate only little variability over the past millennium. The changes are generally less than 10 % for all sites. Except for the short period between the Laki and Tambora eruptions (1783 and 1816, respectively) the accumulation rates do not show clear trends, however, these changes may be caused by the shortness of this time period.

Our mean accumulation rates agree well with the results of Benson (1962) and Bales et al. (2009). Compared to our accumulation rates the values presented in the map of Ohmura and Reeh (1991) seem to overestimate the accumulation in central parts of North Greenland between 10 and up to more than 30 % (Fig. 5).

In future work the causes of these differences have to be investigated in more detail. They may be explained by the different interpolation techniques or differences in accumulation rates on shorter distances.

A direct comparison to the accumulation rates obtained by Box et al. (2013) is not possible as no details about regional distribution is given.

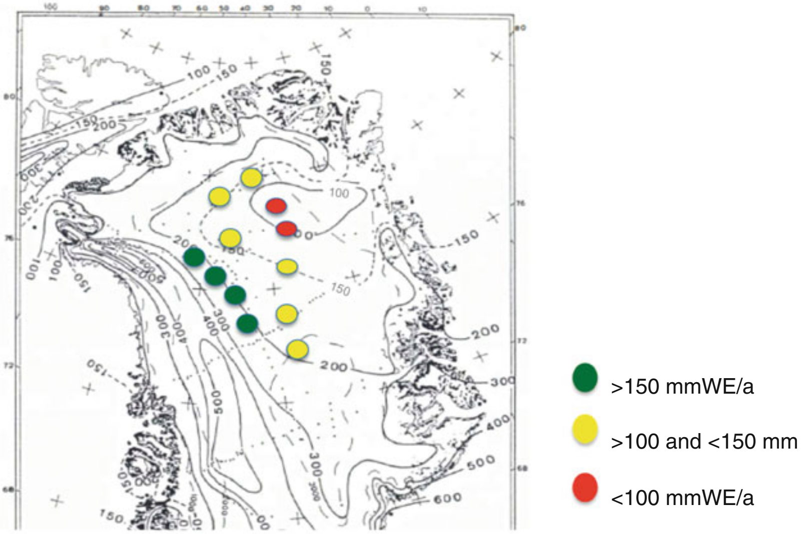

Fig. 5 Accumulation rates from NGT-cores compared to values by Ohmura and Reeh (1991). The color-coded dots represent the accumulation rates from this study, covering up to 1000 years (*red*<100 mmWE/a, *yellow*>100 and <150 mmWE/a, *green*>150 mmWE/a). The *contour line* give accumulation rates as given in Ohmura and Reeh (1991)

References

Bales RC, McConnell JR, Mosley-Thompson E, Csatho B (2001) Accumulation over the Greenland ice sheet from historical and recent records. J Geophys Res 106:33813-33826 (2001)

Bales RC, Guo Q, Shen D, McConnell JR, Du G, Burkhart JF, Spikes VB, Hanna E, Cappelen J (2009) Annual accumulation for Greenland updated using ice core data developed during 2000–2006 and analysis of daily coastal meteorological data. J Geophys Res 114:1–14

Benson CS (1962) Greenland snow pit and core stratigraphic data 1952, 1953, 1954, 1955. U.S. Army Corps Eng Snow Ice Permafrost Res 70:1-182

Box JE, Cressie N, Bromwich DH, Jung J-H, van den Broeke M, van Angelen JH, Forster RR, Miège C, Mosley-Thompson E, Vinther B, McConnell JR (2013) Greenland ice sheet mass balance reconstruction. Part I: net snow accumulation (1600–2009). J Clim 26:3919–3934

Burgess EW, Forster RR, Box JE, Mosley-Thompson E, Bromwich DH, Bales RC, Smith LC (2010) A spatially calibrated model of annual accumulation rate on the Greenland ice sheet (1958–2007). J Geophys Res Earth Surface 115:F02004

Chen QS, Bromwich DH, Bai L (1997) Precipitation over Greenland retrieved by a dynamic method and its relation to cyclonic activity. J Clim 10:839–870

Dethloff K, Schwager M, Christensen JH, Kiilsholm S, Rinke A, Dorn W, Jung-Rothenhäusler F, Fischer H, Kipfstuhl S, Miller H (2002) Recent Greenland accumulation estimated from regional climate model simulations and ice core analysis*. J Clim 15:2821–2832

Freitag J, Kipfstuhl S, Laepple T (2013) Core-scale radioscopic imaging: a new method reveals density-calcium link in Antarctic firn. J Glaciol 59:1009–1014

Hanna E, Huybrechts P, Cappelen J, Steffen K, Bales RC, Burgess E, McConnell JR, Peder Steffensen J, Van den Broeke M, Wake L, Bigg G, Griffiths M, Savas D (2011) Greenland ice sheet surface mass balance 1870 to 2010 based on twentieth century reanalysis, and links with global climate forcing. J Geophys Res 116:D24121

Mosley-Thompson E, McConnell JR, Bales RC, Li Z, Lin P-N, Steffen K, Thompson LG, Edwards R, Bathke D (2001) Local to regional-scale variability of Greenland accumulation from PARCA cores. J Geophys Res (Atmos) 106(D24):33839–33852

NEEM community membery (2013) Eemian interglacial reconstructed from a Greenland folded ice core. Nature 493:489–494

Ohmura A, Reeh N (1991) New precipitation and accumulation maps for Greenland. J Glaciol 37:140–148

Ohmura A, Calanca P, Wild M, Anklin M (1999) Precipitation, accumulation and mass balance of the Greenland ice sheet. Zeitschrift für Gletscherkunde und Glaziologie 35(1):1–20

Wilhelms F (1996) Leitfähigkeits- und Dichtemessung an Eisbohrkernen. Berichte zur Polarforschung, Bremerhaven

Seismostratigraphic Analysis and Glacial History of the Weddell Sea Region, Antarctica

Xiaoxia Huang and Karsten Gohl

Abstract The Weddell Sea basin is of particular significance for understanding climate processes, including the generation of ocean water masses and their influence on ocean circulation as well as the dynamics of the Antarctic ice sheets. The sedimentary record, preserved below the basin floor, serves as an archive of the pre-glacial to glacial development of these processes, which were accompanied by tectonic processes in its early glacial phase. Three multichannel seismic reflection transects, in total nearly 5,000 km long, are used to interpret horizons and define a seismostratigraphic model for the basin. We expand this initial stratigraphy model to the greater Weddell Sea region through a network of more than 50 additional seismic lines. Information from few boreholes are used to constrain sediment ages in this stratigraphy, supported by magnetic anomalies indicating decreasing oceanic basement ages from southeast to northwest. Using these constraints, we calculate grids to depict the depths, thicknesses and sedimentation rates of pre-glacial (145–34 Ma), transitional (34–15 Ma) and full-glacial (15 Ma to present) units. Sedimentation thicknesses and sedimentation rates were calculated at the 12 selected points in the entire basin to give a brief overview of the deposition history, which will contribute to the understanding of the Antarctic ice sheet development and dynamics from the greenhouse to icehouse world in the Cenozoic.

1 Introduction

The breakup of Gondwana and the subsequent opening of Southern Ocean basins and gateways coincided with changes to global ocean circulation and climatic conditions. Changes in the geometry and geography of landmasses and ocean basins lead to first-order ocean current distribution and marine sedimentation patterns

---

X. Huang (✉) · K. Gohl
Alfred Wegener Institute, Helmholtz-Centre for Polar and Marine Research,
Am Alten Hafen 26, 27568 Bremerhaven, Germany
e-mail: xiaoxia.huang@awi.de

G. Lohmann et al. (eds.), *Towards an Interdisciplinary Approach in Earth System Science*, Springer Earth System Sciences,
DOI 10.1007/978-3-319-13865-7_22

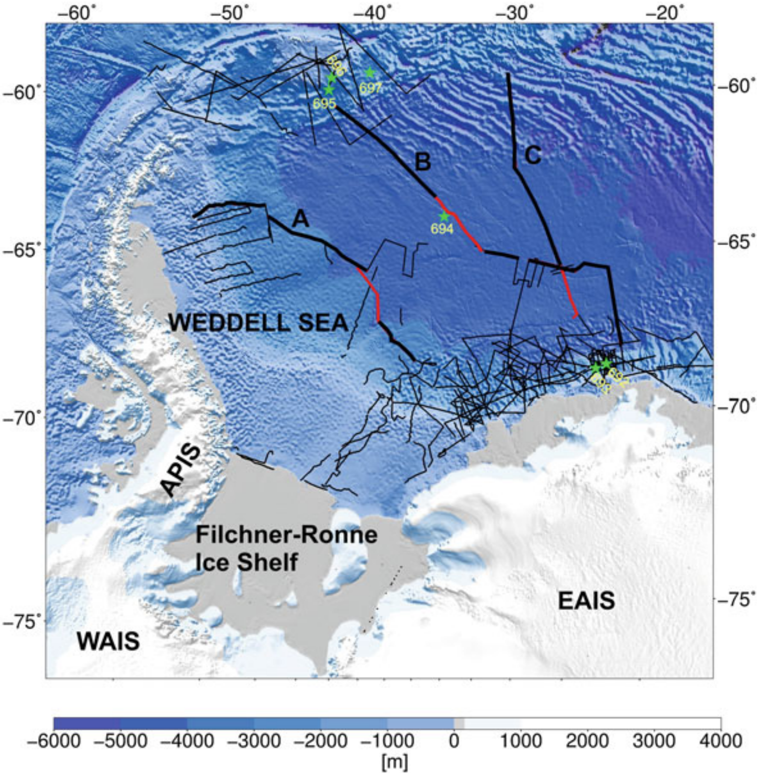

Fig. 1 Bathymetry map of the Weddell Sea region of Antarctica, *red lines* and *black lines* shows existing multichannel seismic profiles. The *green dots* are the ODP leg113 drill sites

(Brown et al. 2006). Changes in the width and depth of oceanic basins and gateways, and changes in seafloor bathymetry influence ocean current transport and overturning circulation. The Weddell Sea has a particular significance to ocean circulation, transport of ice masses and global climate variations due to its giant Weddell Sea gyre. This clockwise circulating ocean gyre system is responsible for the exchange and mixing of Antarctic Deep Water with the global circulation as well as the transport of ice masses from the Filchner-Ronne Ice-Shelves of the Antarctic mainland to the Atlantic Ocean. Understanding the development of the Weddell Sea gyre system is linked to the reconstruction of the development of the paleobathymetry of this large sedimentary basin from pre-glacial to recent times.

The Weddell Sea basin (Fig. 1), experienced approximately 180 million years of tectonic, paleoceanographic and paleoclimate history, spanning from the Mesozoic Gondwana break-up to the present it is bounded to the east by the high-elevation Dronning Maud Land and the East Antarctic Ice Sheet (EAIS), to the west by the mountainous Antarctic Peninsula and its ice sheet (APIS), and to the south by the vast Filchner-Ronne Ice Shelf, which is fed by large ice-streams from both the

EAIS and the West Antarctic Ice Sheet (WAIS) (Fig. 1) (Dalziel 2007; König and Jokat 2010).

Stratigraphy models have been studied from different local scales: in the southeastern Weddell Sea basin (Miller et al. 1990; Rogenhagen et al. 2004), the Antarctic Peninsula (e.g. Smith and Anderson 2010; Rebesco and Camerlenghi 2008), the Jane and Powell Basins in the northwestern Weddell Sea (Bohoyo et al. 2007). Lindeque et al. (2013) analyzed a long transact which crosses the central Weddell Sea. The glacial detail stratigraphic model has been correlated to the southeast Weddell Sea (Huang et al., in revision)

As the best archive of the deep sea, seismic data provide insight into the ice sheet development and paleocirculation of the Weddell Sea from a pre-glacial to a glacial climate. In this paper, we focus on seismic data interpretation based on the existing stratigraphy models and published or unpublished seismic data and expand the new stratigraphic model to the entire Weddell Sea. Stratigraphic horizons were picked and integrated from region to region to achieve a unified acoustic stratigraphy, which would then be merged with seismic velocity models to calculate the depths of key stratigraphic intervals. We deciphered sediment transport, deposition and erosion pattern of this basin from pre-galcial to glacial will contribute to the understanding of the Antarctic ice sheet dynamics and the paleoocean circulation from the greenhouse to icehouse world in the Cenozoic.

2 Data and Methods

Our study is based on multichannel seismic reflection datasets that were collected by Germany, the UK, Norway and Spain between 1984 and 2002. All data are archived in the Antarctic Seismic Data Library System (SDLS) (Wardell et al. 2007). In total, up to 30 seismic lines are incorporated in this study (Fig. 1). The existing seismic stratigraphic models and regional seismic velocity information were applied. P-wave velocities derived from sonobuoy recordings (Hübscher 1994; Hübscher et al. 1996) were used to constrain time-to-depth conversions. For the interpretation and time to depth conversion we used the software packages from LANDMARK.

3 Results

3.1 Seismic Characteristics and Horizon Stratigraphy

In general, we followed the seismostratigraphic models, from Miller et al. (1990) and Rogenhagen et al. (2004) based on the ODP leg113 ODP 693, 694, 696, 697 sites for the age control of the seismic units.

Table 1 Representative examples and short descriptions of seismic facies from Weddell Sea

Sediment units	Tentative age (Ma)	Seismic characteristics	Major events
Full glacial	15 Ma–now ws_u5	Drift, channel and basin fill in, finely laminated, high amplitude reflections, unconformities, parts are chaotic reflections with lower reflectivity due to debris flows	Grounding cycles of EAIS and WAIS on the continental WAIS bring terrigenous sediments to margin Early expansions of APIS onto the continental shelf in the south
Transitional	34–15 Ma? ws_u4	Medium reflectivity, discontinuous and horizontal reflections higher amplitude close to bottom of pre-glacial	Earliest glacial event on the Antarctic Peninsula EAIS and WAIS formation onset of the Antarctic Circumpolar Current Abrut Eocene-Oligocene cooling
Pre-glacial	160–34 Ma?	Lower amplitude sequence with strong discontinuous reflections in parts, horizontal, spaced, transparent background	Drake passage open, ASM-Antarctic Penisula separation complete Antarctic bottom water forms (AABW) Weddell Sea spening

Most of the seismic profiles in the Weddell Sea show three clearly distinguishable sedimentary units (Table 1) above the acoustic basement.

The bottom-most sedimentary unit I is characterized by sub-parallel wavy reflectors, low-amplitude sequences with occasional strong discontinuous reflections and seismically transparent zones (Fig. 2 and 3). Early Cretaceous organic-rich mudstones from this unit were drilled at ODP Site 693 off the southeastern Weddell Sea margin (Barker et al. 1988). The unconformity WS-u4 (Huang and Jokat 2014) is the upper boundary of unit I. Due to its Cretaceous minimum age, we name unit I pre-glacial unit.

Unit II is characterized by medium acoustic response and laminated reflections. Chaotic facies are separated by thin draping layers of medium reflectivity, partly spaced semi-transparent zones (Fig. 2 and 3). The Early Oligocene diatom silty, clayey mud and sandy mudstone from this unit were drilled at the ODP site 693 and the ODP site 696 (Barker et al. 1988). The unit II is overlaid on the unit I and separated from the upper unit by an unconformity mapped as WS-u5. We name unit II as transitional unit according to seismic characteristics and its age indication by the drill cores recovery (Table 1).

Unit III is generally characterized by a regular and thin-bedded pattern of parallel, continuous reflections with high amplitude. Parts of them are chaotic reflections with lower reflectivity in the southern Weddell Sea (Fig. 2, 3 and 4). Abundant drifts and channel-levee systems are present on the southern continental rise in this unit. The sediment drifts show semi-transparent, continuous, sub-parallel or irregular, wavy to discontinuous as well as moderate to low amplitude reflectors (Fig. 2). Within Unit III, glacial turbidities were drilled at ODP site 694 (Barker

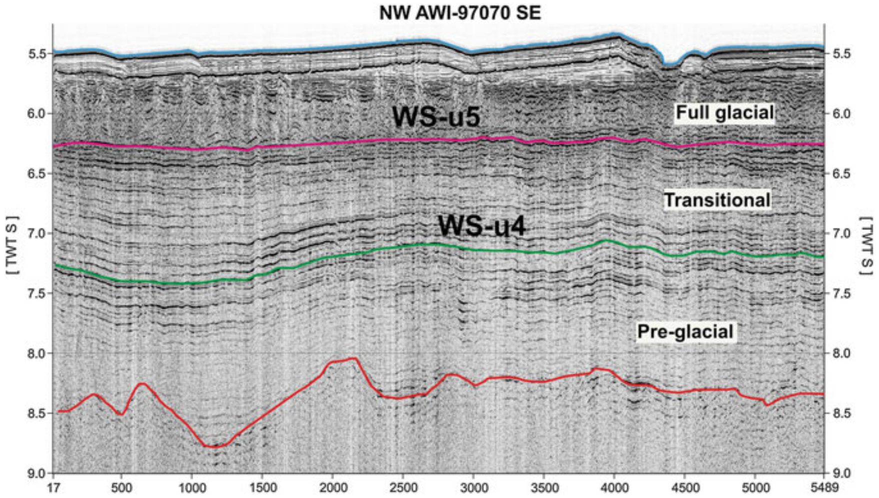

Fig. 2 Multichannel seismic reflection data and interpretation (part of the transect A, AWI-97070, the *red line*) located in the southeast Weddell Sea

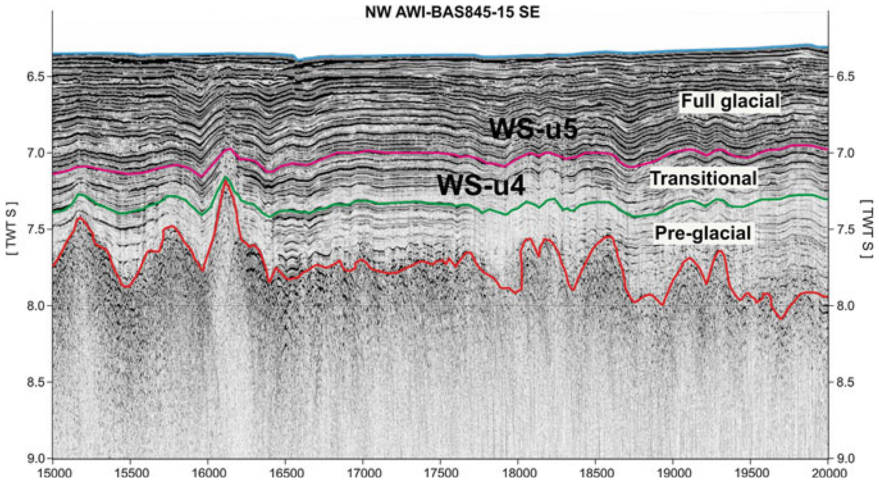

Fig. 3 Multichannel seismic reflection data (part of the transect B, BAS845-15, the *red line*) and interpretation, crossed the central Weddell Sea and linked the southeast Weddell Sea

et al. 1988). At ODP site 693 diatom and mud and clay of the Miocene age were recovered (Barker et al. 1988). Due to this age control and sample proof, we interpret Unit III as a deposit of full-glacial times. Table 1 summarizes the seismic characteristics and major paleooceanographic events of each seismic unit.

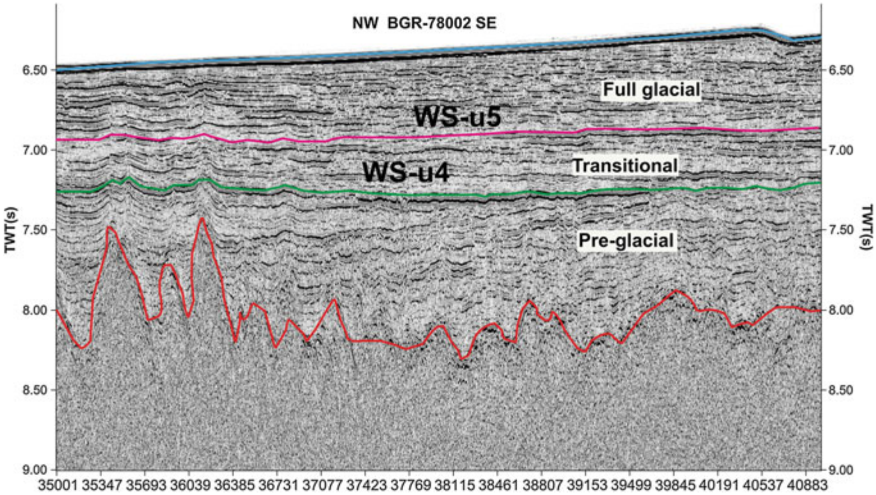

Fig. 4 Multichannel seismic reflection data (part of the transect C, BGR78002, the *red line*) crossing the east and northeast region of the Weddell Sea

3.2 Sedimentation Rates

Twelve points were selected from the three long transects and used to represent the different locations in Weddell Sea basin (Fig. 5). Generally, the sediment thickness shows a trend of decreasing from the continental margin to the abyssal plain of the Weddell Sea. Most sediment was deposited on the continental shelf and slope, with large depocentres in front of the Filchner-Ronne Ice Shelf and along the southern continental rise of the Weddell Sea. The maximum total sediment thickness is up to 8 km (Fig. 5). Sedimentation rates were deduced by combining age range of each unit and sediment thickness (Huang and Jokat 2014). During the pre glacial unit, the sedimentation rates are changing from 1.9–45.5 m/Myr and the maximum sediment thickness is up to 4.5 km. Points 1–4 selected from transect A have relative high values in the southern continental rise, the sedimentation rates are ranging from 21.1–44.5 m/Myr, the sediment thickness is up to 3–4 km. The sedimentation rates from the central and northern Weddell Sea basin are very low, it is changing from 1.9–18.4 m/Myr. The transitional unit yields a higher sedimentation rates than the pre glacial unit. The values are changing from 25.3–78.4 m/Myr with relative thin sediment thickness. Transact A has the highest sedimentation rates in this unit, which are changing from 57.8 to 78.4 m/Myr with a sediment thicknesses of 0.9–1.4 km. During the full glacial unit, the overall sedimentation rates are very high, particularly it is up to 114.3 m/Myr with 1.3 km thick sediment at the transect A (Fig. 5). In the central and northern Weddell Sea basin, the relative high sedimentation rates are observed as well.

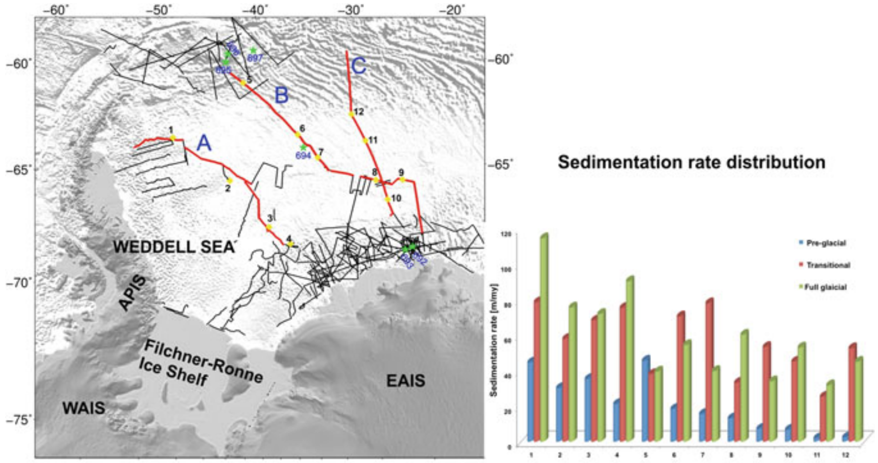

		Sedimentation thickness(m)			Sedimentation rate(m/my)			
Point	Total	Pre-glacial	Transitional	Glacial	Pre-glacial	Transitional	Full glacial	Transacts
1	7080	4454	1255	1371	44.5	78.4	114.3	**Transect A**
Deposition period m.y		28~128	12~28	0~12				
2	4839	3009	925	905	30.1	57.8	75.4	
		28~145	12~28	0~12				
3	5799	3767	954	1078	32.1	68.1	71.8	
		28~145	15~28	0~15				
4	4675	2269	1353	1053	19.4	75.2	90.2	
		28~145	15~28	0~15				
5	944	341	178	425	15.5	25.5	53.2	**Transect B**
		15~37	8~15	0~8				
6	2191	939	492	760	19.1	44.8	63.4	
		23~72	12~23	0~12				
7	2235	1093	467	675	15.6	42.4	56.3	
		23~93	12~23	0~12				
8	2329	1091	396	842	11.6	33.1	60.1	
		26~120	14~26	0~14				
9	1824	694	404	726	6.8	28.9	51.9	
		26~128	14~26	0~14				
10	1993	692	364	937	6.3	30.4	66.9	**Transect C**
		26~135	14~26	0~14				
11	962	196	205	561	1.7	14.6	46.8	
		26~140	12~26	0~12				
12	1462	242	425	795	2.1	30.4	66.3	
		26~140	12~26	0~12				

Selected points's estimated sedimentation rate in Weddell Sea

Fig. 5 Sediment thicknesses and sedimentation rates were calculated at 12 selected points from the three long transects (*yellow dots* and the table). The right chart shows the distribution of the sedimentation rate from three units

4 Discussion and Conclusions

The development of the Weddell Sea basin witnessed the interplay of complex seafloor spreading and tectonic processes with the deposition of large amounts of sediments since the Jurassic. As reported from seismic refraction experiments in front of the Filchner-Ronne Ice Shelf of the southernmost Weddell Sea, 10 km of sediments overlie a basement of stretched continental crust (Hübscher et al. 1996; Kudryavtzev et al. 1987.

Deposition of the pre-glacial unit started with the opening of the Weddell Sea and terminated around early Oligocene (145–34 Ma) from our tentative age model. Due to the fact that this unit experienced a very long deposition history, we expected to find a mass of sediment, particularly at southern margin and continental shelf where the Weddell Sea basin was the earliest spanned. As illustrated in transect A (Fig. 2) (Huang et al. 2014), we observed a large amount of sediments up to 4 km deposited with quite high sedimentation rate (30.1–44.5 m/Myr) on the slope of continental margin in front of Filchner-Ronne Ice Shelf. The pre-glacial sedimentation processes were likely dominated by thermal lithospheric subsidence and variations in terrigenous sediment supply as well as it very long depositional history.

Transitional unit started at the Eocene/Oligocene boundary and lasted until the middle Miocene based on our age model. In comparison with the pre-glacial unit, the transitional unit yields relatively higher sedimentation rates (14.6–78.4 m/Myr) with thinner sediments layers, particularly, in the central and the western Weddell Sea. For instance, point 1 shows a sedimentation rate of 78.4 m/Myr, we suggest it is probably related to several ice sheet retreats and advances. Gravel- and pebble-grade IRDs (Ice Rafting Debris) have been observed in middle to lower Oligocene sediments of ODP Leg 113 Site 693 (Barker et al. 1988). This implies that glaciers were grounded close to the coast or on the inner shelf at that time (Barker and Thomas 2004). We see no obvious evidence to conclude that a major WAIS was grounded on the inner shelf of the Weddell Sea in the Oligocene. The developing and fluctuating Antarctic ice sheets have supplied sediments which interacted with intensified ocean circulation in the Weddell Sea to play a significant role in transporting and distributing sediments, particularly after the opening of Drake Passage/Scotia Sea gateway and intensification of the ACC (Huang et al. 2014).

Sedimentary process in the Weddell Sea is significantly influenced by glacial ice shelf dynamics. We observed relative thick sediment deposited with very high sedimentation rates (Fig. 5), particularly on southern continental margin and western continental rise in the Weddell Sea (points 1–4) during full glacial time. One explanation is that the ice sheets advanced to the shelf edge and trigger enormous gravitational sediment, which was transported from continent to the margin and deep sea (Huang et al. 2014). Multiple evidences supported that the significant ice-sheet expansion happened during the middle Miocene (12 Ma) from previous studies (Miller et al. 1990; Rogenhagen et al. 2004). The pronounced global increase in δ^{18}O ratios from benthic foraminifera indicated that the ice sheet was built up since the middle Miocene (Zachos et al. 2008). A major sea level fall is likely represents the development of polar desert conditions with a permanent ice cap in Antarctica (Kennett and Hodell 1996). The first significant observations of IRDs and turbidite units are reported from the middle Miocene of ODP sites 693, indicating the presence of ice sheets grounding on the shelves and generating a large influx of sediments to the Weddell Sea basin (Barker et al. 1988; Kennett and barker 1990). ODP leg 113 Site 694 also reported glacial turbidity units indicated those grounded ice sheets were present and drained into Weddell Sea basin in Miocene (Barker et al. 1988; Miller et al. 1990; Maldonado et al. 2005, 2007; Leitchenkov et al. 2008, Anderson et al. 2011).

We extended existing local and sub-regional stratigraphic models to the entire Weddell Sea basin. The distribution of the total sediment thickness shows a decreasing trend northward. The maximum sediment thickness of up to 8 km is found on the southern margin. The pre-glacial unit has the thickest sediments owing to its long sedimentation period, but was deposited with a relatively low rate. The tectonic evolution and seafloor spreading history of the Weddell Sea interacted with terrigenous sediment supply processes to control its distribution. The transitional unit accumulated at a relatively high sedimentation rate. Its thickness varies in the range of 0–1.2 km. A relatively strong sediment supply from a growing EAIS grounded to the coast or even inner shelf could be the main contributor to sedimentation on the continental rise. The high sedimentation rate at the full glacial period generated depocenters near the margins of the southern, southeastern and western Weddell Sea. The large amount of sediments, and their deposition at high sedimentation rates in the southern Weddell Sea imply in increase of glacial advances of grounded EAIS, WAIS and APIS to the middle or outer shelf since the middle Miocene.

Acknowledgments The authors would like to thank the masters, crews and seismic teams of the ship expeditions to the Weddell Sea enabling the acquisition of the used data. The British Antarctic Survey (BAS), the German Federal Institute of Geosciences and Resources (BGR) as well as research institutes in Norway and Spain are gratefully acknowledged for their contribution of the used seismic data to the Antarctic Seismic Data Library System (SDLS). X.H. has been receiving a PhD scholarship from the Chinese Scholarship Council. This study has primarily been supported through institutional funds of the Alfred Wegener Institute through Work Package 3.2 of its research program PACES.

References

Anderson JB, Wellner JS (eds) (2011) Tectonic, climatic, and cryospheric evolution of the Antarctic Peninsula. American Geophysical Union, Washington, D.C., 218 p. http://dx.doi.org/10.1029/SP063

Barker PF, Thomas E (2004) Origin, signature and palaeoclimate influence of the Antarctic Circumpolar Current. Earth Sci Rev 55:1–39. doi:10.1016/j.earscirev.2003.10.003

Barker PF, Kennett JP et al (1988) Proceedings of the ocean drilling program, scientific results leg 113. Ocean drilling program: 774. doi:10.2973/odp.proc.ir.113.1988

Bohoyo F, Galindo-Zaldívar J, Jabaloy A, Maldonado A, Rodríguez-Fernández J, Schreider A, Suriñach E (2007) Extensional deformation and development of deep basins associated with the sinistral transcurrent fault zone of the Scotia–Antarctic plate boundary. Geological Society, London, Special Publications, vol 290, pp 203–217. http://dx.doi.org/10.1144/SP290.6

Brown B, Gaina C, Mueller RD (2006) Circum-Antarcitc palaeobathymetry: Illustrated examples from Cenozoic to recent times. Paleogeogr Paleoclimatol Paleoecol 231:158–168. doi:10.1016/j.palaeo.2005.07.033

Dalziel IWD (2007) The Ellsworth mountains: critical and enduringly enigmatic. In: Copper AK, Raymond CF (eds) Antarctica: a keystone in a changing world-online proceedings of the 1-th ISAES. USGS Open-File Report 2007-1047, Short Research Paper 004, 5 p. doi:10.3133/of2007-1047.srp004

Huang X, Gohl K, Joakt W (2014) Variability in Cenozoic sedimentation and paleo-water depths of the Weddell Sea basin related to pre-glacial and glacial conditions of Antarctica. Glob Planet Change. doi:10.1016/j.gloplacha.2014.03.010

Huang, X, Jokat W (2014) Middle Miocene to present sediment transport and deposits in the southeast Weddell Sea, Antarctica, in revision.

Hübscher C (1994) Krustenstrukturen und Verlauf des Kontinentalrandes im Weddell- Meer/ Antarktis. Ber Polarforsch 147:233

Hübscher C, Jokat W, Miller H (1996) Structure and origin of southern Weddell Sea crust: results and implications. In: Storey BC, King EC, Livermore RA (eds) Weddell Sea tectonics and Gondwana break-up. Geological Society, London, Special Publication, vol 108, pp 201–212

Kennett JP, Baker PF (1990) Climatic and oceangraphic developments in the Weddell Sea, Antarctica, since the latest Cretaceous: An ocean-drilling Program. Ocean Drilling Program scientific results, vol 113, pp 865–880

Kennett JP, Hodell DA (1996) Stability or instability of Antarctic ice sheets during warm climates of the Pliocene? GSA Today 5:10–13

König M, Jokat W (2010) Advanced insights into magmatism and volcanism of the Mozambique Ridge and Mozambique Basin in the view of new potential field data. Geophys J Int 180:158–180. doi:10.1111/j.1365-246X.2009.04433.x

Kudryavtzev GA, Smirnova EA, Schumilov VA, Poselov VA (1987) Deep structure of the earth crust in the southern part of the Weddell Sea (by data of the DSS line (in Russian). In: Ivanov VL, Grikurov GE (eds) The geological and geophysical research in Antarctica. Sevmorgeologia, Leningrad, pp 99–108, pp 498–502

Leitchenkov G, Guseva J, Gandyukhin V, Grikurov G, Kristoffersen Y, Sand M, Golynsky A, Aleshkova N (2008) Crustal structure and tectonic provinces of the Riiser-Larsen Sea are (East Antarctica): results of geophysical studies. Mar Geophys Res 29:135–158. http://dx.doi.org/10.1007/s11011-008-9051-z

Lindeque A, Martin Y, Gohl K, Maldonado A (2013) Deep sea pre-glacial to glacial sedimentation in the Weddell Sea and southern Scotia Sea from a cross-basin seismic transect. Mar Geol 336:61–83

Maldonado A, Barnolas A, Bohoyo F, Escutia C, Galindo-Zaldívar J, Hernández-Molina FJ, Jabaloy A, Lobo FJ, Nelson CH, Rodríguez-Fernández J, Somoza L, Vázquez JT, (2005) Miocene to recent contourite drifts development in the northern Weddell Sea (Antarctica). Glob Planet Change 45:99–129. http://dx.doi.org/10.1016/j.gloplacha.2004.09.013

Maldonado A, Bohoyo F, Galindo-Zaldívar J, Hernández-Molina FJ, Lobo FJ, Shreyder AA, Suriñach E (2007) Early opening of Drake passage: regional seismic stratigraphy and paleoceanographic implications, in Antarctica: a keystone in a changing world. In: Cooper AK, Raymond CR et al. (eds) Extended abstract EA57, online proceedings of the 10th international symposium on Antarctic sciences (ISAES) online, USGS Open-File Report. http://pubs.usgs.gov/of/2007/1047/ea/of2007-1047ea057.pdf

Miller H, Henriet JP, Kaul N, Moons A (1990) A fine-scale stratigraphy of the eastern margin of the Weddell Sea. In: Bleil U, Thiede J (eds) Geological history of the Polar Oceans: arctic versus Antarctic. Kluwer Academic Publishers, pp 131–161. doi:10.1007/978-94-009-2029-3_8

Rebesco M, Camerlenghi A (2008) Late pliocene margin development and mega debris flow deposits on the Antarctic continental margins: evidence of the onset of the modern Antarctic Ice Sheet? Paleogeogr Paleoclimatol Paleoecol 260:149–167. doi:10.1016/j.palaeo.2007.08.009

Rogenhagen J, Jokat W, Hinz K, Kristoffersen Y (2004). Improved seismic stratigraphy of the Mesozoic Weddell Sea. Mar Geophys Res 25:265–282. http://dx.doi.org/10.1007/s11001-005-1335-y

Smith RT, Anderson JB (2010) Ice-sheet evolution in James Ross basin, Weddell Sea margin of the Antarctic Peninsula: the seismic stratigraphic record. Geol Soc Am Bull 122(5/6):830–842. http://dx.doi.org/10.1130/B26486.1

Wardell N, Childs JR, Cooper AK (2007) Advances through collaboration: sharing seismic reflection data via the Antarctic seismic data library system for cooperative research (SDLS). In: Cooper AK, Raymond CR (eds) Antarctica: a keystone in a changing world—online proceedings of the 10th ISAES: USGS Open-File Report 2007-1047, Short Research Paper 001, 4 p. http://dx.doi.org/10.3133/of2007-1047.srp001

Zachos CJ, Dickens GR, Zeebe RE (2008) An early Cenozoic perspective on greenhouse warming and carbon-cycle dynamics. Nature 451:279–283. doi:10.1038/nature06588

Part VII
Geoinformatics

Visual Analysis of Relevant Fields in Geoscientific Multifield Data

Anatoliy Antonov and Lars Linsen

Abstract Exploration of multifield geoscientific data sets is a complex task involving the investigation of individual fields and correlations between fields. We present an approach to analyze the importance of fields and their correlations in multifield datasets by treating given or derived fields as multidimensional objects and projecting these objects to a 2D space, and visually investigating the fields using the projected layout. We demonstrate how our approach supports the analysis of atmospheric simulation data in two different settings.

Keywords Visualization · Interactive visual data analysis · Multifield · Dimension projection

1 Introduction

Present technical capabilities enable scientists to produce much more data than can be carefully analyzed. In addition, the visualization techniques that are commonly employed in the geoscientific research do not allow to effectively extract features from more than a few variables: the independent variables are usually visualized side-by-side, and changes in values of a single variable over time are usually depicted with animations. Both approaches do not scale well and impose an excessive cognitive load on the scientist.

We present an approach to analyze relationships between scalar fields, with the goal of finding and choosing fields, both simulated and derived, that add most information to each other. When applied to climate data such an approach allows, among others, for the detection of seasonal changes. For example, temperature

---

A. Antonov (✉) · L. Linsen
Jacobs University Bremen, Bremen, Germany
e-mail: an.antonov@jacobs-university.de

L. Linsen
e-mail: l.linsen@jacobs-university.de

G. Lohmann et al. (eds.), *Towards an Interdisciplinary Approach in Earth System Science*, Springer Earth System Sciences,
DOI 10.1007/978-3-319-13865-7_23

values in January and February are highly correlated, while temperatures in January and July are more distinct.

The main contribution of this paper is the design and application of field-based projection methods to geoscientific multifield datasets.

Our approach is based on two core ideas. First, we derive a number of fields that could potentially be of interest for the exploration of the data. Second, we define a global distance measure between pairs of fields, and generate a difference-based overview of all fields. Here, we interpret fields as high-dimensional data points and project them to a 2D space, where they are visualized in the form of a scatterplot.

We demonstrate how our approach supports the analysis process of a scientist in an interactive visual set-up.

2 Related Work

When exploring a multifield dataset, attention is often given to measuring per-point similarity between fields (Edelsbrunner et al. 2004; Nagaraj and Natarajan 2011; Sauber et al. 2006). Many of these approaches are based on gradients. Gosink et al. (2007) used the normalized dot product between gradients and visualized it over statistically important isosurfaces of a third field. Sauber et al. (2006) introduced the gradient similarity measure (GSIM), which is combined from directional similarity and magnitude similarity. Nagaraj et al. (2011) developed a measure as the norm of the matrix that comprises the gradient vectors, and showed that it is robust to noise in input fields.

Projection methods are commonly used to describe similarities between spatial samples of a multifield, by placing points with similar multivariate attributes close to each other in respective visualizations. There exist various linear (Kandogan 2001) and non-linear (Jänicke et al. 2008; Sammon 1969) projection algorithms.

Our approach, however, depicts global similarities between data fields. Thus, it is closer to Turkay et al. (2011, 2012), who introduced a dual-space analysis of multivariate data using linked visualizations of the item space (where objects are entities represented by their values in different attributes) and dimension space (where objects are attributes represented by their values for the different entities). In their approach, the item space represented results of multivariate analyses. The dimension space was visualized with scatterplots, showing either multidimensional scaling (MDS) projection results with a correlation-based distance measure, or 2D scatterplots of two selected dimension statistics (e.g. mean value vs. standard deviation).

Yuan et al. (2013) introduced a dimension projection matrix, which builds on the concept of scatterplot matrices by assigning a group of dimensions to each row or column and using projections instead of simple 2D plots. It leverages symmetric property of the matrix to create a dual space visualization: the cells in the upper triangle of the matrix contain projections of items in combined set of respective dimensions, and the lower triangle contains projections of dimensions themselves.

Neither Turkay et al. (2011, 2012) nor Yuan et al. (2013) were investigating spatial data stemming from scientific simulations. Thus, our approach is the first to apply dimension visualization for the analysis of multifields. Similar to the dual-space approaches, we apply MDS to dimensions. However, we consider spatial data visualizations to be more appropriate for this scenario than the data item projections of other dual-space approaches.

3 Field Similarity Plot

Our approach focuses on the uniform qualitative comparison of the fields present in a dataset, which requires all fields to be normalized. In the following, we assume that all fields are normalized to the unit interval.

First, a number of commonly studied and newly derived fields are included in the analysis. Specifically, we add gradient magnitudes, Hessian determinants, and fields based on the gradient similarity measure (GSIM) introduced by Sauber et al. (2006). For two gradients g_i and g_j, GSIM is defined as

$$s(g_i, g_j) = (s_d(g_i, g_j) \cdot s_m(g_i, g_j))^r, \tag{1}$$

$$s_d(g_i, g_j) = \left(\frac{g_i^T g_j}{\|g_i\| \cdot \|g_j\|} \right)^2, \tag{2}$$

$$s_m(g_i, g_j) = 4 \frac{\|g_i\| \cdot \|g_j\|}{(\|g_i\| + \|g_j\|)^2}, \tag{3}$$

where s_d is the direction similarity, s_m is the magnitude similarity, and r regulates sensitivity of the measure (set to 1.3 as recommended (Sauber et al. 2006)).

The following GSIM fields are computed: first-order similarity between gradients, second-order similarity between eigenvectors of the principal eigenvalue of the Hessians, and mixed similarity between the first- and the second-order derivatives estimate (i.e. gradients and Hessian eigenvectors, respectively). In the set of derived fields, the gradients and their similarities carry first-order relationships, while other fields might indicate more complex relationships. All derived fields are normalized as well.

Next, for each data field, we interpret the vector of its values at all spatial locations as a multidimensional data point and compute integrated differences between pairs of fields. In the following, we use the global Euclidean distance measure defined on the *-dimensional space, where $* = n_x \times n_y \times n_z$, and n_x, n_y, n_z are respective sizes of the spatial grid in x, y, z dimensions. This distance is computed as

$$d_{ij}^* = \sqrt{\sum_{xyz} [v_{j_{xyz}} - v_{i_{xyz}}]^2}, \tag{4}$$

where $v_{j_{xyz}}$ denotes the value of the jth field at the spatial position xyz. The distance value is 0 for two identical fields, and increases proportional to the differences between the compared fields.

The *-dimensional points are then projected to points in a 2D space while trying to maintain the computed pairwise distances (Eq. 4) as much as possible. We have selected Sammon's mapping (Sammon 1969) as a projection technique. It starts with random point coordinates in the 2D space and then iteratively moves the points to minimize the error given by the equation:

$$E = \frac{1}{\sum_{i<j}\left[d_{ij}^{*}\right]} \sum_{i<j}^{N} \frac{[d_{ij}^{*} - d_{ij}^{2}]^{2}}{d_{ij}^{*}}, \tag{5}$$

where d_{ij}^{2} are the Euclidean distances of projected 2D points in the 2-dimensional space, and d_{ij}^{*} are the distances between original points in the multidimensional space.

Finally, the results of the projection are visualized as a scatterplot. By definition, this scatterplot has no inherent axes (i.e. it is only unique up to rotation), while the distances between the 2D points indicate how similar the respective fields are (Figs. 1, 4 and 5). Colors are used to indicate the types of the fields (original, derivative or similarity fields).

4 Interactive Visual Analysis

The field similarity plot described above helps the scientist to identify informative fields. The plot serves as an interaction widget, where individual fields can be clicked at and investigated using linked views (selected fields are highlighted by increased point size).

The linked views are (1) slice-based volume visualizations for the spatial investigation of field value distributions (Figs. 2a, 3a and 6a) and (2) 1D histograms of the normalized field values for understanding the field value distribution within its range (Figs. 2b, 3b and 6b). In the individual views, we decided to avoid using the typically default rainbow colormap because of its misleading perceptual properties (e.g. it introduces artificial sharp contrasts at the color transitions) (Borland and Taylor 2007; Rogowitz and Treinish 1998; Silva et al. 2007). The selected black body radiance colormap represents data without such issues.

The slice-based visualization renders axis-aligned slices through the volumetric dataset. The position and the orientation of the cutting plane, as well as the orientation and scaling of the 3D view, can be changed interactively. Multiple slice-based visualizations for different data fields are coordinated: all of them use the same view on the volume data as well as the same cutting plane.

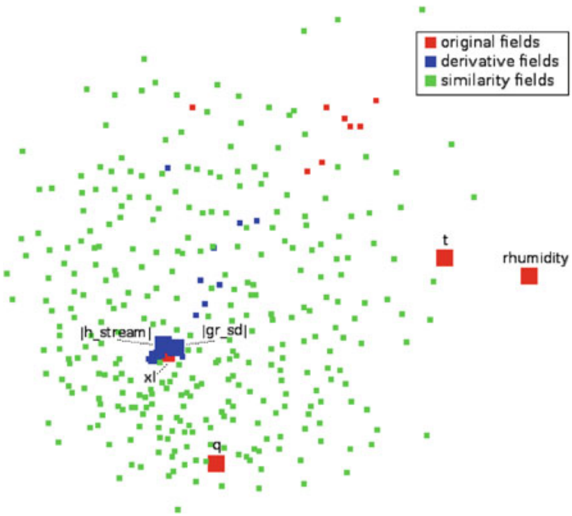

Fig. 1 The field similarity plot for the multifield scenario. There is a tendency towards separation of different types of fields, but large differences exist within the groups of fields of each type. Big points with labels correspond to the fields which have individual views in Figs. 2 and 3. Derivative fields refer to gradient magnitudes and Hessian determinants, similarity fields refer to all the fields computed with GSIM

5 Use Cases

In this section, we demonstrate two possible geoscientific applications, focusing on the atmospheric part of a climate simulation output. The data are a sample run of a climate model setup with a pre-industrial configuration, similar to the pre-industrial control setup described by Zhang et al. (2013), but with different settings of orbital parameters. Details of the employed Community Earth System Models COSMOS (consisting of ECHAM5 for the atmosphere, MPIOM for the ocean, and JSBACH for the vegetation) are outlined, for example, by Stepanek and Lohmann (2012).[1]

The analyzed dataset contains monthly means of ECHAM5 output for 13 volumetric climate variables at the spatial grid resolution of 96 × 48 × 19. The z-axis is given in terms of hybrid sigma-pressure levels.

Our first scenario addresses the multifield constellation with 13 variables at a single time step, while our second scenario is concerned with a single field at all time steps of one year.

---

[1] Data courtesy of Christian Stepanek and Gerrit Lohmann from Alfred-Wegener Institute Helmholtz Centre for Polar and Marine Research in Bremerhaven, Paleoclimate Dynamics research group.

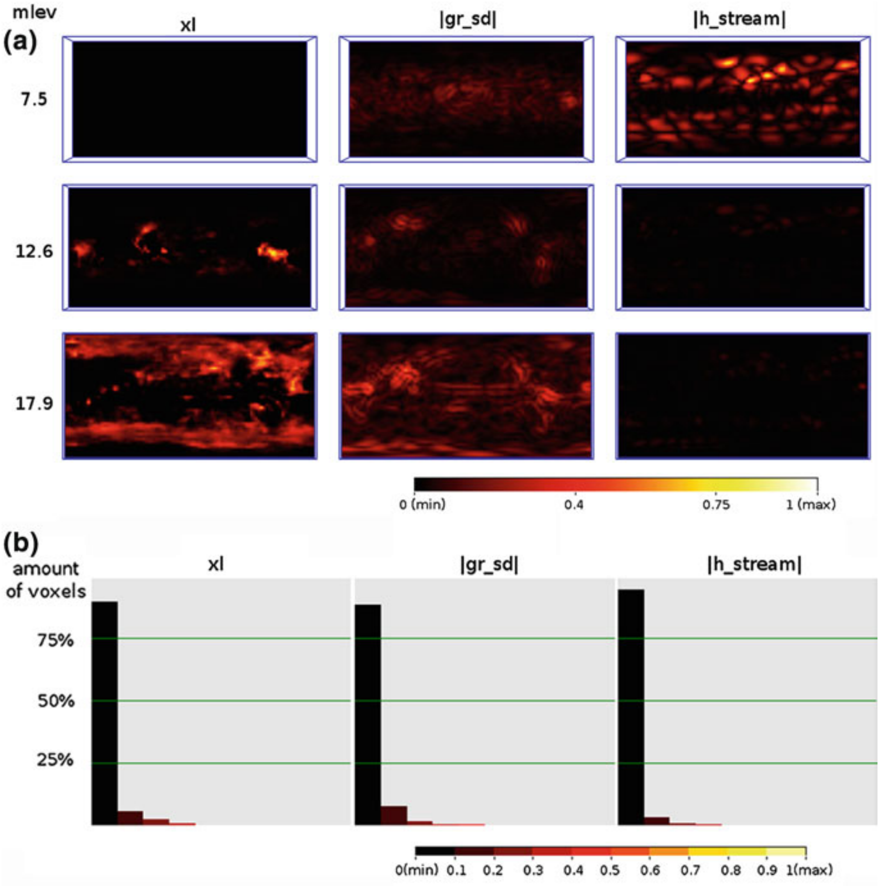

Fig. 2 Individual views for closely located points in Fig. 1: cloud water field *xl*, gradient magnitude of divergence field $|gr\_sd|$ and Hessian determinant of streamfunction field $|h\_stream|$. **a** Slice views, *mlev* is the interpolated layer index of the slice (1—top layer, 19—surface layer). **b** 1D histograms

5.1 Multifield

The 13 fields of ECHAM5 describe temperature (*t*), wind velocity components (*u*, *v*, *omega*), specific and relative humidity (*q* and *rhumidity*), cloud water (*xl*) and cloud ice (*xi*), vorticity (*svo*) and divergence (*sd*), streamfunction (*stream*), velocity potential (*velopot*) and geopotential height (*geopoth*). We consider one time step, namely the monthly means of April of the first year.

In the field similarity plot after adding all the discussed derived fields (Fig. 1) one can observe a wide spread of the original fields. However, we can also see a very dense group of points including all Hessian determinant fields. A few gradient magnitude field points as well as the two original fields of cloud water *xl* and cloud ice *xi* (occluded by *xl* in Fig. 1) are placed very closely to this group. The plot indicates high similarity between the aforementioned fields with respect to Euclidean distance. By looking at the linked views of slice-based volume visualizations and 1D histograms for a few fields from this area (Fig. 2), we see that, while the fields exhibit different patterns, the distribution of the data values are very much in the lower range. Using the Euclidean distance for the projection, the fields are closer to each other than to other fields with values in the upper range.

When observing outliers among the original fields, we can see that each of them has strong unique features (Fig. 3). The overall distribution of the values of the temperature field *t* and the relative humidity field *rhumidity* are more similar than of the values of the specific humidity field *q*. The latter field is more similar to the group described above.

5.2 *Time-Varying Field*

In the second scenario, we investigate the change of the temperature field throughout the first year by treating each month as a separate, independent field.

The projection of only the original fields arranges the points in a loop (Fig. 4) that corresponds to the annual cycle, which documents, again, the feasibility of the overall approach.

The loop has a pendular behavior with the winter months on one side and the summer months on the other. The spring and fall months are close together (there is even a crossing) and form transitional phases. Moreover, we can conclude that changes over months are gradual.

The full projection of original and derived fields (Fig. 5) clearly separates the five types of derived fields as well as the original dataset fields. Thus, we can conclude that each of the chosen types of derived fields conveys distinctly different information from the original data and from each other, i.e. differences within a group are much smaller than between the groups. It can easily be confirmed by looking at the individual views (Fig. 6).

6 Discussion

The presented approach describes a conceptual workflow, where a design choice among many alternatives is made at each step. In this paper, we followed some of the common decisions. In the following, we discuss other possibilities. A thorough

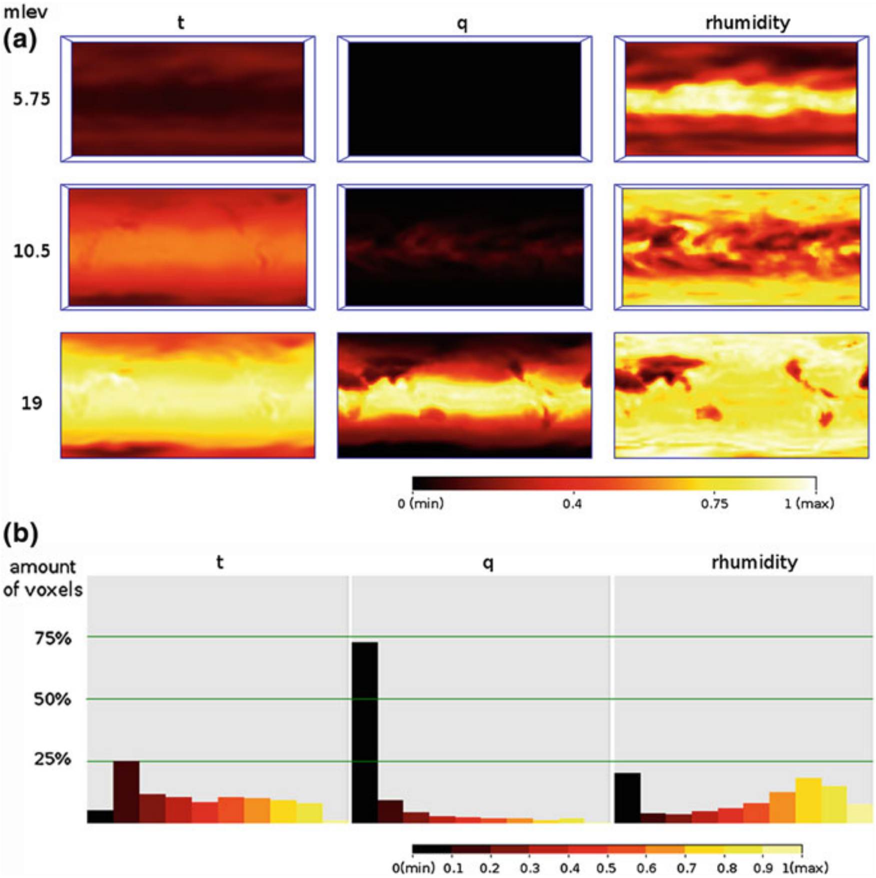

Fig. 3 Individual views for outliers among original fields in Fig. 1: temperature *t*, specific humidity *q*, and relative humidity *rhumidity*. **a** Slice views, *mlev* is the interpolated layer index of the slice (1—top layer, 19—surface layer). **b** 1D histograms

Fig. 4 The field similarity plot for twelve months of the temperature field. Yearly cycle is clearly visible, separating months in three groups: winter, summer, and transitional seasons

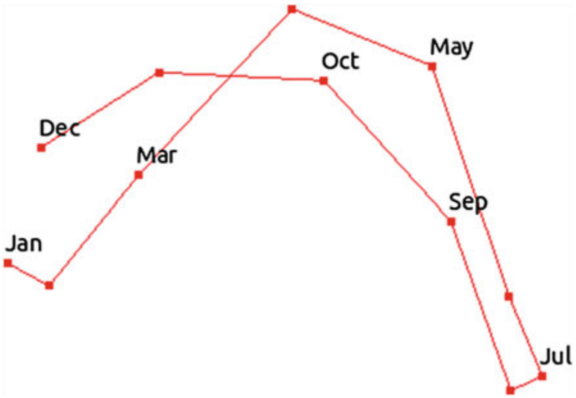

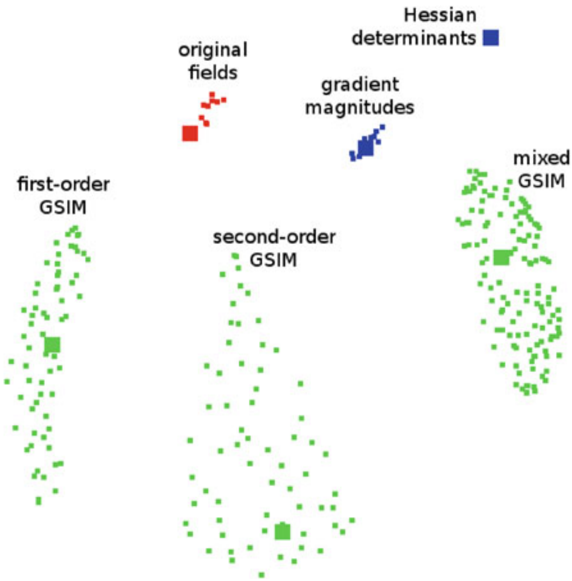

Fig. 5 The field similarity plot in the case of a single time-varying field. Different types of fields are clearly separated. Individual views for the highlighted points are shown in Fig. 6

analysis on which alternatives work best for which application is beyond the scope of this conceptual paper and left for future work.

In this paper, we normalized the range of each field to the [0, 1] interval. In case of noisy data, a distribution-based normalization method can be employed. It puts the mean value of the distribution to 0 and standard deviations to ±1. The latter method is more robust against outliers.

Sammon's mapping is a generally applicable projection method that produces suitable results for many applications. However, our approach is not tied to this particular technique, and other distance-based projection methods (Minghim et al. 2006; Paulovich and Minghim 2006; Paulovich et al. 2008) can be used.

The field similarity plots in Sect. 5 were computed with the Euclidean distance measure. In our experiments, we also employed a correlation-based distance measure. In the multifield case, the correlation measure produced quite different results. Here, the denser groups of original and derivative fields shown in Fig. 1 were widely spread, while the fields chosen for Fig. 3 were placed closer to each other. The reason is that the correlation measure is less sensitive to the scaling of fields. Thus, fields with similar histograms but different spatial patterns are judged to be more different. For the case of a single time-varying field, the results produced by the correlation-based measure were similar to those with the Euclidean distance, only that the groups were overlapping and not so clearly separated.

From the purely information-based point of view, the common recommendation to analyze the general behavior of the data is to take fields that are spread in the projected space and cover it well. However, it is clear that specific targeted questions require inclusion of certain fields that capture the respective information.

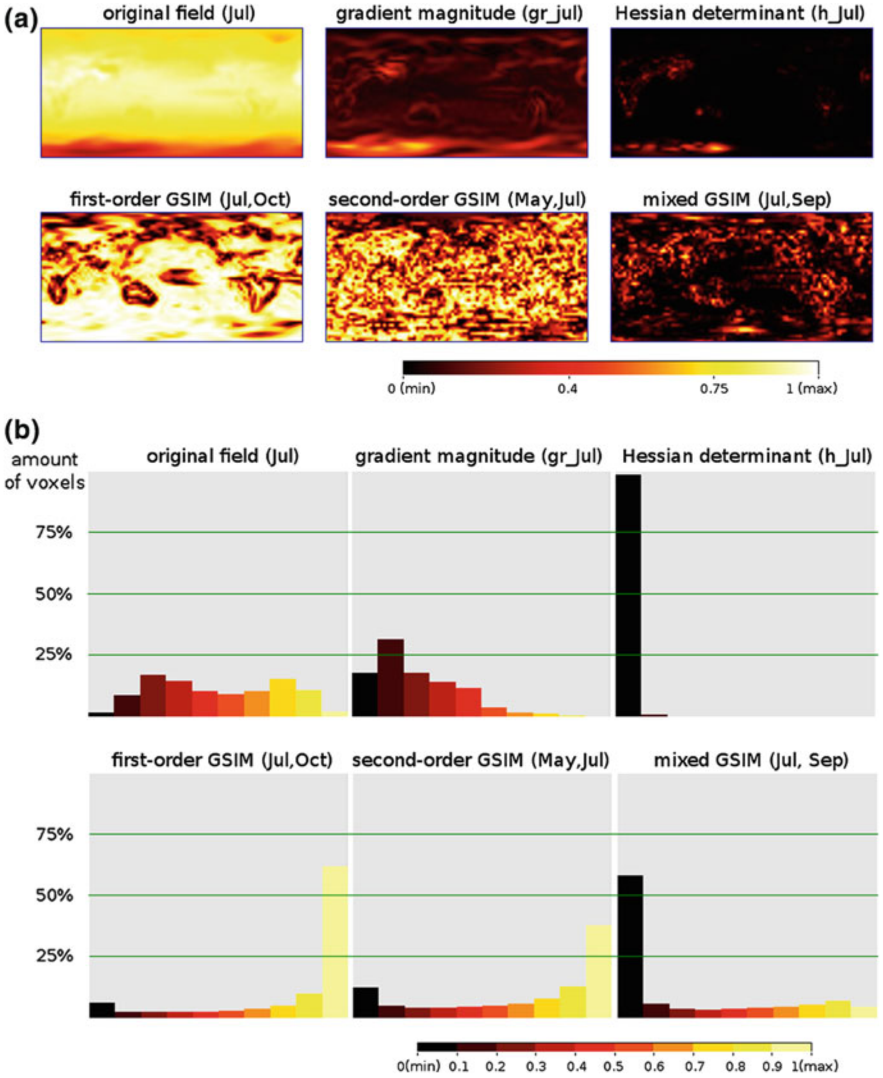

Fig. 6 Individual views for different types of fields, corresponding to the highlighted points in Fig. 5. **a** Slice views at the surface layer. **b** 1D histograms. It is clearly visible that different types of derived fields convey distinctly different information

Depending on the needs of an application, instead of slicing views and 1D histograms, other visualizations can be used for the exploration of the overview, e.g. direct visualization as volume rendering of individual selected fields (Abellán and Tost 2008; Drebin et al. 1988), multimodal volume rendering (Woodring and Shen 2006), plotting correlations or other statistics in scatterplots or parallel coordinates (Inselberg 1985), side-to-side volumetric visualizations, as well as commonly used scatterplot matrices.

7 Conclusion

In this paper, we described a two-step approach to support the analysis process by providing overview of the correlation between scalar fields in the data. At the first step, a number of predefined fields is derived from a given dataset. At the second step, a similarity-based overview of all fields is presented to the user, by employing a multidimensional projection technique.

The described approach allows for the interactive analysis of relationships between multiple fields, including simulated and derived fields. It provides an overview over all fields in the projection view, allows the user to investigate individual fields with coordinated views using slice-based volume visualization and 1D histograms, and provides means to choose fields for further investigation.

Acknowledgements Data courtesy of Christian Stepanek and Gerrit Lohmann from the Alfred Wegener Institute Helmholtz Centre for Polar and Marine Research in Bremerhaven, Paleoclimate Dynamics research group is greatfully acknowledged.

References

Abellán P, Tost D (2008) Multimodal volume rendering with 3d textures. Comput Graph 32(4):412–419

Borland D, Taylor RM (2007) Rainbow color map (still) considered harmful. IEEE Comput Graph Appl 27(2):14–17

Drebin RA, Carpenter L, Hanrahan P (1988) Volume rendering. In: Proceedings of ACM SIGGRAPH ‘88, the 15th annual conference on computer graphics and interactive techniques, pp 65–74

Edelsbrunner H, Harer J, Natarajan V, Pascucci V (2004) Local and global comparison of continuous functions. IEEE Vis 2004:275–280

Gosink LJ, Anderson JC, Bethel EW, Joy KI (2007) Variable interactions in query-driven visualization. IEEE Trans Vis Comput Graph 13(6):1400–1407

Inselberg A (1985) The plane with parallel coordinates. Visual Comput 1(2):69–91

Jänicke H, Böttinger M, Scheuermann G (2008) Brushing of attribute clouds for the visualization of multivariate data. IEEE Trans Vis Comput Graph 14(6):1459–1466

Kandogan E (2001) Visualizing multi-dimensional clusters, trends, and outliers using star coordinates. In: Proceedings of KDD ‘01, the seventh ACM SIGKDD international conference on knowledge discovery and data mining, pp 107–116

Minghim R, Paulovich FV, de Andrade Lopes A (2006) Content-based text mapping using multi-dimensional projections for exploration of document collections. In: Proceedings SPIE, 6060:60600S–60600S–12

Nagaraj S, Natarajan V (2011) Relation-aware isosurface extraction in multifield data. IEEE Trans Vis Comput Graph 17(2):182–191

Nagaraj S, Natarajan V, Nanjundiah RS (2011) A gradient-based comparison measure for visual analysis of multifield data. Comput Graph Forum 30(3):1101–1110

Paulovich FV, Minghim R (2006) Text map explorer: a tool to create and explore document maps. In: IV 2006, Tenth international conference on information visualization, pp 245–251

Paulovich FV, Nonato LG, Minghim R, Levkowitz H (2008) Least square projection: a fast high-precision multidimensional projection technique and its application to document mapping. IEEE Trans Vis Comput Graph 14(3):564–575

Rogowitz B, Treinish LA (1998) Data visualization: the end of the rainbow. IEEE Spectr 35(12):52–59

Sammon JW Jr (1969) A nonlinear mapping for data structure analysis. IEEE Trans Comput C-18 (5):401–409

Sauber N, Theisel H, Seidel H-P (2006) Multifield-graphs: an approach to visualizing correlations in multifield scalar data. IEEE Trans Vis Comput Graph 12(5):917–924

Silva S, Madeira J, Santos BS (2007) There is more to color scales than meets the eye: a review on the use of color in visualization. In: IV '07, 11th international conference on information visualization, pp 943–950

Stepanek C, Lohmann G (2012) Modelling mid-pliocene climate with COSMOS. Geosci Model Dev 5:1221–1243. doi:10.5194/gmd-5-1221-2012

Turkay C, Filzmoser P, Hauser H (2011) Brushing dimensions—a dual visual analysis model for high-dimensional data. IEEE Trans Vis Comput Graph 17(12):2591–2599

Turkay C, Lundervold A, Lundervold AJ, Hauser H (2012) Representative factor generation for the interactive visual analysis of high-dimensional data. IEEE Trans Vis Comput Graph 18(12):2621–2630

Woodring J, Shen H-W (2006) Multi-variate, time varying, and comparative visualization with contextual cues. IEEE Trans Vis Comput Graph 12(5):909–916

Yuan X, Ren D, Wang Z, Guo C (2013) Dimension projection matrix/tree: interactive subspace visual exploration and analysis of high dimensional data. IEEE Trans Vis Comput Graph 19(12):2625–2633

Zhang X, Lohmann G, Knorr G, Xu X (2013) Different ocean states and transient characteristics in last glacial Maximum simulations and implications for deglaciation. Clim Past 9:2319–2333. doi:10.5194/cp-9-2319-2013

A Database Language More Suitable for the Earth System Sciences

Dimitar Misev and Peter Baumann

Abstract Multidimensional array data, including satellite images and weather simulations in the Earth Science, confocal microscopy and CAT scans in the Life Science, as well as telescope and cosmological observations in Space science, is traditionally the type of data seriously contributing to "Big Data". Traditionally, the database community has neglected this, with the effect that ad hoc implementations prevail. With the advent of NewSQL in recent years, however, the database scope has broadened, and array modelling and query support is seriously considered. Hence, we address integration of array queries into SQL by proposing a generic model, ASQL, for modelling and querying multi-dimensional arrays in ISO SQL. The model integrates concepts from the three major array models seen today: rasdaman, SciQL, and SciDB. ASQL has been implemented and is currently being discussed in ISO for extending standard SQL.

1 Introduction

"Big Data" is an extremely popular buzzword in recent years, and for a good reason. Hard, seemingly unsolvable problems are being tackled by employing Big Data tools and techniques on vast amounts of data: natural disaster prediction and management, optimizing the work of various systems—from household appliances, to vehicles, to whole cities and countries, monitoring the real-time spread of diseases and public health, airfare prediction and comparison, etc. Essentially, Big Data strives to turn data into insight, by exploiting the ever-increasing observation resolution and variety.

Data voluminosity and variety is perhaps nowhere more prominent than it is in the field of Earth System Science. Multidimensional array data produced by a wide variety of sensors (Waldrop and Lippel 2008), accompanied by "meta data", is

D. Misev (✉) · P. Baumann
Jacobs University, Bremen, Germany
e-mail: d.misev@jacobs-university.de

G. Lohmann et al. (eds.), *Towards an Interdisciplinary Approach in Earth System Science*, Springer Earth System Sciences,
DOI 10.1007/978-3-319-13865-7_24

combined with a variety of other, non-array types of data in the attempt to answer complex questions about Earth's past, present and future. Harnessing the potential of all this data is still not so trivial for Earth System Scientists. This is largely because the use of databases—a central component of Big Data systems—has been confined to metadata: small, structured, and queryable data describing the actual data, which remained un-queryable. This data is nowadays maintained in ad hoc solutions crafted by data centers, with functionality often constrained to file download.

Hence, database support for massive multi-dimensional arrays is getting into focus. Array models specifically for databases have been published since a while (Cornacchia et al. 2008; Lerner and Shasha 2003; Libkin et al. 1996; Marathe and Salem 2002; van Ballegooij 2004), however, finding general attention by the database community mainly since the appearance of the NewSQL movement. The currently most influential models are (in historical order) rasdaman (Baumann 1994), SciQL (Zhang et al. 2011), and SciDB (Stonebraker et al. 2011). Notably, ISO SQL (1999) already supports arrays, albeit only very rudimentarily. Arrays are confined to 1-D, and without any implicit nor explicit loops there is no practically useful operational support. Nonetheless, the standard offers a suitable hook for injecting array semantics into SQL that would coexist with its set semantics.

In this contribution, we present an overview of the array model ASQL (Sects. 2 and 3, detailed description in Misev and Baumann 2014). Based on the ISO SQL stub, ASQL provides a fully-fledged set of structural and operational array constructs completely integrated and compatible with SQL and orthogonal to its set semantics. While based mainly on the conceptualization of rasdaman, ASQL also honors recent developments in the array databases field, notably SciDB and SciQL. The theoretical underpinnings of ASQL have been implemented and exemplified in practice in ASQLDB, an open-source mediator system based on HSQLDB (T. H. D. Group 2013) and rasdaman[1] (Sect. 4).

2 Data Model

Roughly, array models can be classified according to their relational embedding. ISO SQL (2003), Array Algebra (Baumann 1994, 1999), PostGIS Raster (Obe and Hsu 2011), SciSPARQL (Andrejev and Risch 2012), and other models introduce arrays as a column type which we call "array-as-attribute". This makes arrays a plug-into SQL with the overall set-oriented model unchanged. SciQL and SciDB, on the other hand, follow a model where arrays are emulated by tables. Here, arrays are at the same level as tables, and array cells correspond to tuples. We call this "array-as-table" modeling. With ASQL, we follow the array-as-attribute approach as given by ISO SQL.

---

[1] (www.rasdaman.org, Accessed on 22 Aug, 2013)

SQL has a rich data type support which is already perfectly suitable for scientific applications. Similarly, array dimensions remain integer indexed with a fixed resolution of 1. We remove the restriction of a fixed dimension origin and allow integer coordinates, however. Furthermore, we introduce dimension names which make dimensions position independent in operations like the common array subsetting.

It is worth mentioning that this data model is completely backwards compatible with the existing SQL array model.

3 Query Language

3.1 Array Construction

Constructing new arrays is possible in four different ways.

First, an array can be created by listing all of its elements in row-major order and specifying the array domain.

The second way allows creating an array from a table result of a query, and is detailed in Sect. 3.5.

We introduce a new *array constructor by iteration*, borrowed from Array Algebra. Each element of the result array with the specified domain is constructed from a *value expression* in the `VALUES` clause, which is evaluated in an implicit iteration over the output domain. The dimension names can be referenced in the value expression as iterator variables. For example, constructing a 2 × 2 × 2 integer array by iteration:

```
ARRAY[ x(0:1), y(0:1), z(−1:0) ]
VALUES x + y + z
```

Finally, Sect. 3.6 presents the possibility for creating an array by conversion from a Large Object.

3.2 Array Inspection Operators

Several operations allow to retrieve essential information about array objects:

- $dimension(a) = d$ denotes its dimensionality;
- $cardinality(a) = C$ denotes the number of elements;
- $domain(a) = D$ gives its domain;
- $lo(a, i) = lo(a, n_i) = x_{i,n_i,lo}$ gives the lowest coordinate of a dimension i;
- $hi(a, i) = hi(a, n_i) = x_{i,n_i,hi}$ gives the highest coordinate of a dimension i.

3.3 Array Aggregation

An array aggregation expression returns an aggregated value obtained from iterating over all positions in the spatial domain specified in the `OVER` clause, evaluating an aggregation expression specified in the `USING` clause at each position, and combining the result by applying the aggregation operation in the `AGGREGATE` clause. E.g. assuming array `A[x(1:2), y(1:3)]`, the following expression returns the sum of all values:

```
AGGREGATE +
OVER [ x(1:2), y(1:3) ]
USING A[ x, y ]
```

3.4 Derived Operators

Many useful operators can be defined, based on the general array constructor by iteration and array aggregation constructs alone. These operators are not essential, but having them readily available in the query language greatly simplifies the typical array queries.

Subsetting is an operation that returns an array value consisting of only those elements from its input array `A` whose positions are in the intersection of the subset domain and the domain of `A`.

Extending is an operation that returns an array with the same elements as the input array, plus additional elements with positions filling up the new, extended result domain with `NULL`s.

Shifting returns an array with the same elements as the input array, but with each element shifted by an offset vector.

Scaling is an operation that returns an array with the target domain indicated and values obtained by interpolating the input array element values to the result array domain.

Overlaying is an operator that allows to combine two arrays with matching domains by placing the first array operand “on top” of the second one.

Induced operations return an array with same domain as its input array, where each result cell value is obtained from combining the input cell(s) at the respective position through the operation indicated. Any valid operation defined on the array elements of the input array operands, can be an induced operation.

Finally, from the general aggregation expression, several common array aggregation operations are derived, for adding, averaging, and-ing/or-ing and counting the cells with value 1/`TRUE` of an array.

3.5 Array ↔ Table Conversion

Converting an array into a table is potentially very useful as SQL may provide functionality not present in ASQL, and vice versa. `UNNEST`ing an array simply puts each array element in a separate row of the result table. The `WITH ORDINALITY` flag preserves the order by adding $n = dimension(array)$ integer columns to the result table, that contain the array indexes. `NEST`ing a table into an array works in a similar way, just reversed.

3.6 Array ↔ LOB Conversion

Array data is most often exchanged in a certain format, which allows to bundle further, possibly domain-specific details, besides the array cell values. Therefore ASQL provides flexible and extensible support, to facilitate exporting (via an `encode` operation) and importing (corresponding `decode` operation) of arrays from and into an SQL DBMS.

4 Implementation

The concepts discussed thus far have been largely implemented in an open-source mediator system ASQLDB.[2] ASQLDB extends the HSQLDB relational DBMS (T. H. D. Group 2013) with support for ASQL. Incoming queries are broken down and array sub-queries are constructed as rasql queries (rasdaman GmbH 2013), which are then forwarded to rasdaman (www.rasdaman.org, Accessed on 22 August, 2013) for evaluation. The results are merged with the results of the pure SQL sub-queries and returned to the client. Figure 1 depicts the architecture of ASQLDB.

First performance measurements indicate that our approach of automatic query separation and result merging has only a slight overhead, over a highly specific, manually implemented query integration. Figure 2 shows benchmark results of a mixed query on a 2D map of increasing size (`$s` in the query below increases from 10, 20, 40, …, 500) that determines the number of cell values in the green channel of the map section greater than 150:

```
SELECT count_cells(M.map[x(0:$s), y(0:$s)].green > 150)
FROM Maps as M
```

---

[2] https://github.com/misev/asqldb.

Fig. 1 ASQLDB architecture

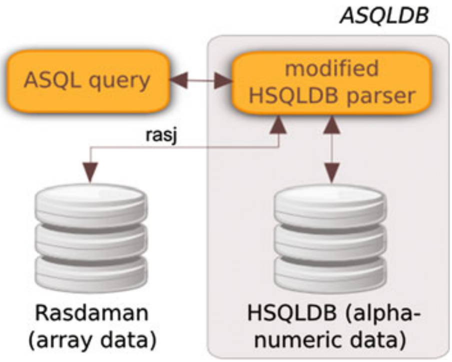

Fig. 2 ASQLDB performance, in comparison to a manually crafted query integration

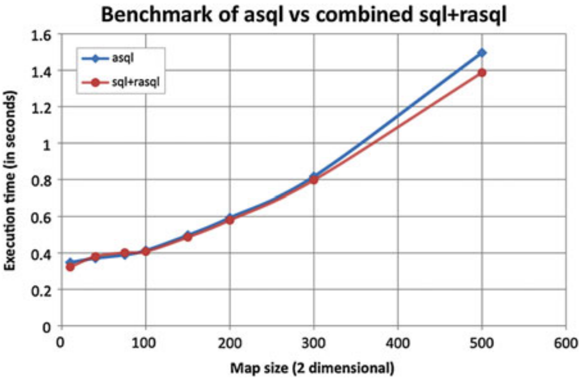

5 Conclusion

In manifold application domains arrays form the core underlying structure of manifold science and engineering data. It is generally accepted today, therefore, that arrays have to become part of the overall data type orchestration in information systems. With ASQL we attempt to integrate arrays into the relational model based on the existing ISO SQL array data type, with the goal of extending applicability of the relational model to a large class of “Big Data” related challenges in science and engineering analytics. An implementation of ASQL has been largely accomplished and is available for testing.

One practical consequence of this integration is that the historical gap between data and metadata can be overcome—quality of service on data catches up with metadata capabilities. Additionally, mixing and combining data and metadata queries has a potential of reducing client/server round-trips and unveils new optimization opportunities.

At the time of this writing, ASQL is being discussed by ISO/IEC JTC1 SC32 WG3 SQL for inclusion in the SQL standard.

Acknowledgments This work is being supported by the European Commission funded project EarthServer.

References

Andrejev A, Risch T (2012) Scientific SPARQL: semantic web queries over scientific data. In: Proceedings of the 2012 IEEE 28th international conference on data engineering workshops, ICDEW '12. IEEE Computer Society, pp 5–10

Baumann P (1994) Management of multidimensional discrete data. VLDB J 3(4):401–444

Baumann P (1999) A database array algebra for spatio-temporal data and beyond. In: Proceedings of the 4th international workshop on next generation information technologies and systems, NGITS '99. Springer, Berlin, pp 76–93

Cornacchia R, Héman S, Zukowski M, Vries AP, Boncz P (2008) Flexible and efficient IR using array databases. VLDB J 17(1):151–168

ISO (1999) Information technology—database language SQL. Standard No. ISO/IEC 9075:1999. International Organization for Standardization (ISO)

ISO (2003) ISO IEC 9075-1:2003: information technology—database languages—SQL—part 1: framework (SQL framework). ISO, Geneva

Lerner A, Shasha D (2003) Aquery: query language for ordered data, optimization techniques, and experiments. In: Proceedings of the 29th international conference on very large data bases, vol 29, VLDB '03. VLDB Endowment, pp 345–356

Libkin L, Machlin R, Wong L (1996) A query language for multidimensional arrays: design, implementation, and optimization techniques. In: Proceedings of the 1996 ACM SIGMOD international conference on management of data, SIGMOD '96. ACM, New York, pp 228–239

Marathe AP, Salem K (2002) Query processing techniques for arrays. VLDB J 11(1):68–91

Misev D, Baumann P (2014) Extending the SQL array concept to support scientific analytics. In: Conference on scientific and statistical database management, SSDBM '14. ACM, Aalborg, 30 June–02 July

Obe R, Hsu L (2011) PostGIS in action. Manning Publications, Manning Pubs Co Series

rasdaman GmbH (2013) *rasdaman query language guide*, 8.5 edition

Stonebraker M, Brown P, Poliakov A, Raman S (2011) The architecture of SciDB. In: Proceedings of the 23rd international conference on scientific and statistical database management, SSDBM '11. Springer, Berlin, pp 1–16

T. H. D. Group (2013) HSQLDB—100 % Java database. http://hsqldb.org/. Accessed on 15 Feb 2014

van Ballegooij AR (2004) RAM: a multidimensional array DBMS. In: Proceedings of the 2004 international conference on current trends in database technology, EDBT '04. Springer, Berlin, pp 154–165

Waldrop M, Lippel P (2008) The sensor revolution. www.nsf.gov/news/special_reports/sensor. Accessed on 22 Aug 2013

Zhang Y, Kersten ML, Ivanova M, Nes N (2011) SciQL, bridging the gap between science and relational DBMS. In: Desai BC, Cruz IF, Bernardino J (eds) IDEAS. ACM, pp 124–133

Towards Collaborative Exploration and Analysis of Big Data from Mars: A Noachis Terra Case Study

Jelmer H.P. Oosthoek, Angelo P. Rossi and Vikram Unnithan

Abstract More and more satellite data are being collected from the planet Mars. The sheer size of this 'Big Data' asks for new access and analysis methods to be developed. We present a novel approach towards collaboratively exploring and analyzing Big Data from Mars. The Noachis Terra region on Mars was selected for a Case Study. Available Context Camera (CTX) and Compact Reconnaissance Imaging Spectrometer for Mars (CRISM) data were processed and analyzed. A web service named 'PlanetServer' is under development, allowing for collaborative exploration and analysis of Mars Big Data. We conclude that the infrastructure is advancing but more work is needed towards integration.

Keywords Mars · Big data · Collaboration · Noachis terra · Case study

1 Introduction

Satellite data from Mars have been gathered since the NASA Mariner 4 satellite flyby mission in 1965, which resulted in 22 pictures (e.g. Rossi and van Gasselt 2010). Since then data size of each successive mission has steadily increased. The most recent orbiting satellite, the NASA Mars Reconnaissance Orbiter (MRO, launched in 2005) (Zurek and Smrekar 2007) has collected more than 50 TB, as of Spring 2014. The size and complexity of the various MRO datasets make it suitable to be defined as "Big Data", a relatively loose term describing data so big and complex that new access and analysis methods need to be developed (Snijders et al. 2012).

Here we present a novel approach towards collaboratively exploring and analyzing Big Data from Mars (Fig. 1), focusing on two instruments on board MRO: Context Camera (CTX) 6 m/pixel visual imagery (Malin et al. 2007) and Compact Reconnaissance Imaging Spectrometer for Mars (CRISM) up to 18 m/pixel

---

J.H.P. Oosthoek (✉) · A.P. Rossi · V. Unnithan
Jacobs University Bremen, Campus Ring 1, 28759 Bremen, Germany
e-mail: j.oosthoek@jacobs-university.de

G. Lohmann et al. (eds.), *Towards an Interdisciplinary Approach in Earth System Science*, Springer Earth System Sciences,
DOI 10.1007/978-3-319-13865-7_25

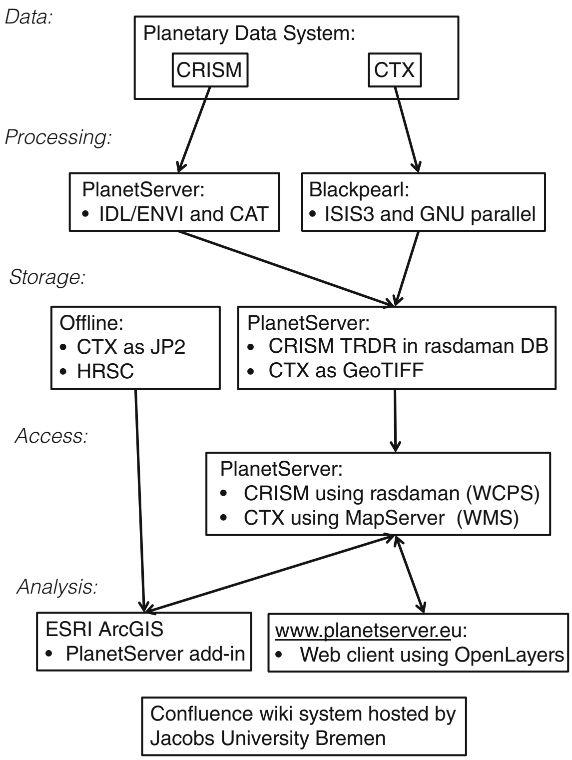

Fig. 1 Diagram outlining the hardware and software used to process, store, access and analyze data

hyperspectral data (Murchie et al. 2007). The Noachis Terra region, Mars, was selected for a Case Study (Fig. 2), focusing on (structural) geological mapping using CTX and a mineralogical investigation using CRISM.

On the hardware side the approach encompasses a HPC (high-throughput computing) cluster for data processing and a server named PlanetServer (Oosthoek et al. 2013; Rossi et al. 2013, 2014), within the FP7 EC project EarthServer. PlanetServer runs the rasdaman Array Database Management System (DBMS) (Baumann 1994, 2009a) and MapServer (Vatsavai et al. 2006) for access to CRISM and CTX, respectively. Rasdaman uses—among other standards—the Open Geospatial Consortium (OGC, www.opengeospatial.org) Web Coverage Processing Service (WCPS) standard (Baumann 2009b) and MapServer uses the Web Map Service (WMS). On the client side we developed an OpenLayers-based web client for quick-view exploration (www.planetserver.eu, Oosthoek et al. 2014). The work on a custom-build ESRI ArcGIS python add-in for advanced scientific data exploration in ESRI ArcGIS 10.1 or newer is in an advanced stage.

Regions of interest are, in addition to the main scientific core area, also covered by PlanetServer-hosted data, based on inputs from scientific collaborators and the planetary (geology) community.

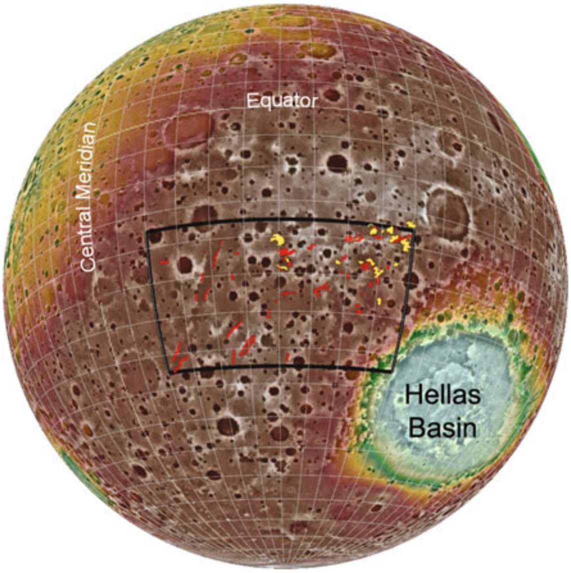

Fig. 2 Globe representation of Mars centered on the case study region of interest in Noachis Terra (*black rectangle*, centered around 30°E, 30°S). The background data is color-coded MOLA data (*white* is high elevation, *light blue* is low elevation). The *red lineaments* are the extensional grabens, mapped by Knapmeyer et al. (2006) as part of a global structural mapping campaign using MOLA data. The *yellow polygons* indicate localities with a basaltic spectral shape (redrawn from Rogers and Nazarian 2013)

2 Data and Methods

MRO CTX and CRISM data are both freely available from the NASA Planetary Data System (PDS) website (pds.nasa.gov). Both datasets need to be further processed before analysis can be performed. CRISM data is normally processed using the CRISM Analysis Tools (CAT) plugin (Seelos et al. 2011) for the Exelis VIS IDL/ENVI software. IDL/ENVI and CAT were installed on PlanetServer (Oosthoek et al. 2013). 1751 (total 674 GB) Targeted Reduced Data Records (TRDR) hyperspectral data and 70 (total 29 GB) Multispectral Reduced Data Records (MRDR) multispectral data were batch processed, encompassing noise removal, atmospheric correction and geo-referencing. The processed TRDR data were added to the rasdaman database on PlanetServer. The MRDR data were further processed into summary products (Pelkey et al. 2007) and added to ArcGIS for offline use.

CTX data is provided as Experiment Data Record (EDR) data, comparable to raw (level 0) Earth Observation (EO) data, which need to be further processed by the Integrated Software for Imagers and Spectrometers v3 (ISIS3) software (Gaddis et al. 1997; Keszthelyi et al. 2013). ISIS3 and GNU parallel (Tange 2011) were installed on the Jacobs University Bremen Computational Laboratory for Analysis, Modeling and Visualization (CLAMV) ‘blackpearl’ HPC cluster enabling

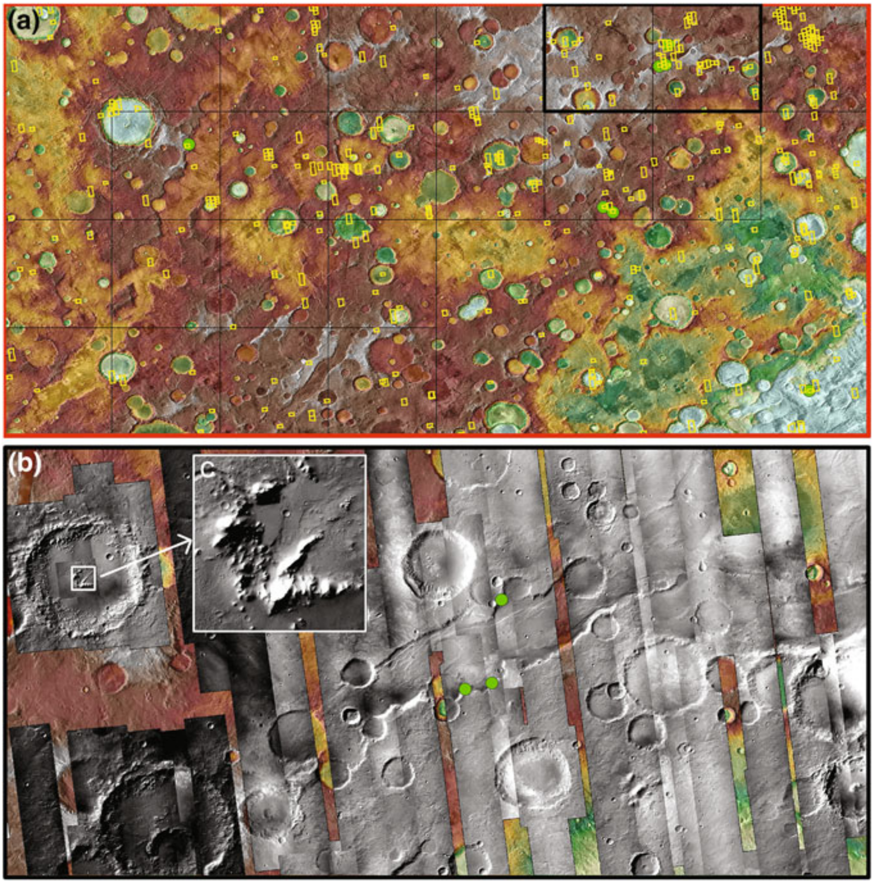

Fig. 3 The case study region of interest in Noachis Terra. The background is semi-transparent THEMIS IR daylight imagery overlaying color-coded MOLA elevation data. The *green dots* are the 6 locations of the Carter et al. (2013b) hydrated mineral detections. **a** The 20 MRDR tiles are shown as *black rectangles*. The *yellow polygons* are the ‘footprints’ of the CRISM TRDR hyperspectral data. The *thick rectangle* shows the extent of (**b**). **b** Two CTX MRDR tile mosaics showing three Carter et al. (2013b) hydrated mineral detections. **c** An example of the CTX data at the full 6 m/pixel scale

calibration, georeferencing and mosaicking of the CTX data using 12 cores in parallel. The CTX were mosaicked into square regions with the same extent as the CRISM MRDR tiles. 20 of these mosaics were created for the Noachis Terra region (Fig. 3). A custom built python script created the ‘blackpearl’ and ISIS3 configuration files for each tile mosaic. The 20 mosaics were made available online as MapServer WMS services on PlanetServer (total 81 GB as GeoTIFF files) and offline as JPEG2000 compressed raster data (total 9 GB).

Next to CTX and CRISM data also Mars Orbiter Laser Altimeter (MOLA, on board the NASA Mars Global Surveyor satellite) GIS-ready gridded (463 m/pixel) topography data (Smith et al. 2001) and Thermal Emission Imaging System (THEMIS, on board the NASA Mars Odyssey orbiter) 100 m/pixel InfraRed (IR) day-time mosaics (Christensen et al. 2004) were used, both provided by the United States Geological Survey (USGS) MeRCaToR Lab (Hare et al. 2012). MOLA data were added to rasdaman and THEMIS data were converted to GeoTIFF in order to be accessed using MapServer. High Resolution Stereo Camera (HRSC, on board the ESA Mars Express orbiter) ortho-rectified (Level 4) visual imagery and stereo-derived DTMs (Neukum et al. 2004; Gwinner et al. 2010) were provided by the Freie Universitaet Berlin.

On the client side a quick-view web client has been developed, based on OpenLayers. The web client provides access to the CRISM and MOLA data using the WCPS protocol and CTX, THEMIS and color-coded MOLA data using the WMS protocol. ESRI ArcGIS 10.2, on the other hand, was used for advanced analysis of the CTX and CRISM data. The CTX could be added to ArcGIS, as a WMS service or as a JP2 raster. ArcGIS, however, does not have a standard capability to analyze hyperspectral data, such as CRISM. Typically a planetary scientist would use spectral analysis software such as IDL/ENVI instead. To enable CRISM analysis directly inside ArcGIS a python add-in toolbox was developed which uses the WCPS protocol to access the CRISM data the same way as the PlanetServer web client does. It also allows for the loading of the various PlanetServer WMS layers directly into ArcGIS.

A wiki system hosted at Jacobs University Bremen was used to collaboratively share the results of the Noachis Terra Case Study among participating researchers.

3 Noachis Terra Case Study

The Noachis Terra region is situated in the heavily cratered southern highlands of Mars. The region is the type location of the Noachian System in the Martian chronostratigraphy (Tanaka et al. 2013; Tanaka 1986), which ended around 3.57–3.74 Ga (Werner and Tanaka 2011). Enigmatic graben systems occur in the region, immediately to the west of the 2,300 km in diameter Hellas impact basin. They have been interpreted by Wichman and Schultz (1989) as distant-concentric "canyon" systems, related to the Hellas impact event (Fig. 2). Rogers and Nazarian (2013) detected olivine signatures in deposits which they interpreted to be effusive volcanic plains, spatially associated with the graben structures (Fig. 2). Carter et al. (2013b) and Ehlmann et al. (2012) observed various types of hydrated minerals, mostly associated with impact craters.

The Case Study involved a 2,000 × 1,000 km^2 area in Noachis Terra, centered around 30°E, 30°S (Figs. 2 and 3). It encompassed (structural) geological mapping using, among others, CTX data and a mineralogical investigation using CRISM data. The relation between the tectonics, volcanism and hydrated minerals was investigated.

The (structural) geological mapping was started regional scale using semi-transparent THEMIS mosaic data on top of color-coded MOLA data in ArcGIS.

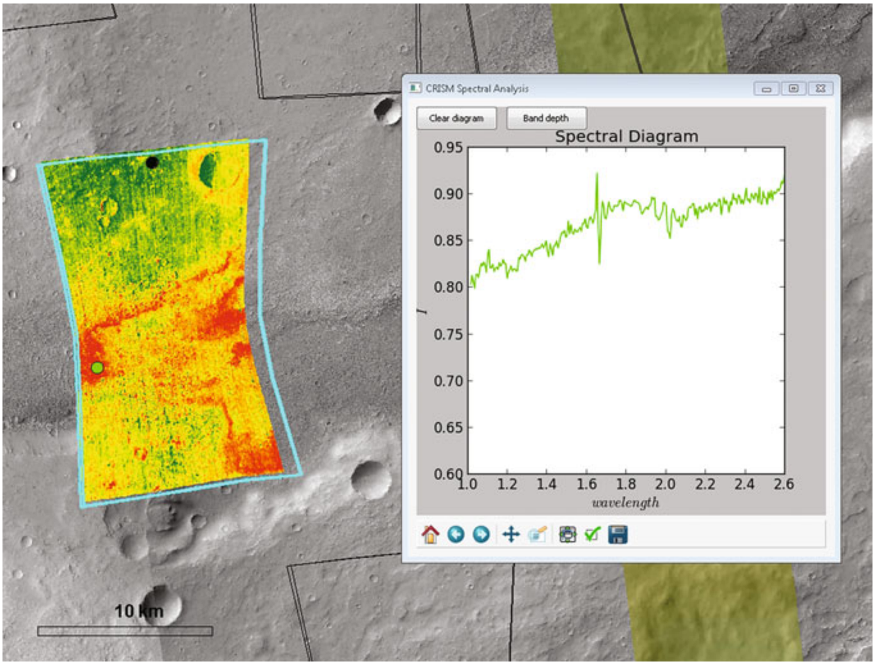

Fig. 4 ArcGIS screenshot showing a color-coded CRISM hyperspectral olivine summary parameter map (*red* is possibly high in olivine, *green* is low) on top of 6 m/pixel CTX data. The *green dot* on the map is the location of the spectrum shown in the ArcGIS PlanetServer add-in CRISM spectral analysis window. By comparing with known mineral spectra the spectrum can subsequently be interpreted

This allowed for regional-scale features to be mapped, such as the graben structures and ‘dark toned’ (in the THEMIS IR day-time) deposits (DTD), previously partially mapped by Rogers and Nazarian (2013). Progressively, higher detail was added by producing multiple CTX mosaic tiles: 20 tiles were created covering graben structures of interest.

The mineralogical investigation started at regional scale by observing the MRDR summary product of the mineral olivine: various mapped DTD proved to be olivine-rich. The CRISM hyperspectral data covering the various DTD were investigated for olivine using the ArcGIS PlanetServer add-in. Locations of possible hydrated minerals detected by Carter et al. (2013b) and Ehlmann et al. (2012) were also further investigated. It was found that 6 of the localities detected by Carter et al. (2013b) were located on top of graben escarpment rims (Fig. 3). During the earlier explorative phase of the investigation, CTX mosaics ‘tiles’ were first produced for the areas covering these localities.

A graben associated with three hydrated mineral detections (Fig. 3b) was chosen for further investigation using CTX and CRISM. The CRISM MRDR olivine summary parameter showed olivine signatures on the graben floor. A custom ArcGIS PlanetServer add-in was subsequently used to investigate the spectra and the visual imagery in a GIS system (Fig. 4). This allowed for an integrated in depth analysis of the possible relation between the hydrated mineral signatures, volcanism and the (structural) geology.

The results of the Case Study will be presented in a separate publication.

4 Discussion

Mars satellite data are typically processed by individual scientists or by the IT facilities of their research institutes and universities. Data are shared among cooperating scientists but are generally not made available online. It is therefore likely that the same data has been processed by different researchers, independent of each other.

In the case of CTX data, mosaics used within publications are usually not made available online. Google, in cooperation with NASA Ames, created a global CTX mosaic within the Google Earth Mars globe (Andersen 2012). Unfortunately this mosaic is currently not accessible outside Google Earth. In our approach, the 'blackpearl' HPC cluster allowed for processing of the CRISM-MRDR-tile-sized CTX mosaics within a couple of hours. The limiting factor was the maximum download speed allowed by the PDS. Once all the CTX data of Noachis Terra had been downloaded the data could be relatively quickly processed, therefore enabling the explorative phase described in the Case Study. Access to the CTX mosaic tiles was provided through WMS, enabling the easy sharing of data within our group, and to potential third parties interested in accessing the data.

In the case of CRISM, processed data are commonly kept offline. IDL/ENVI is used to spectrally analyze the CRISM data and a planetary scientist interested in connecting the geology (using e.g. CTX) with the mineralogy of a certain region on Mars will have to go back and forth between a GIS and IDL/ENVI. This limits CRISM data access to advanced users. The PlanetServer client, on the other hand, allows users to access and analyze CRISM data online, together with available overlapping CTX data. The current client has limited WebGIS capability as online geological mapping cannot be performed. A new client (neo.planetserver.eu, Chiwome et al. 2014), with a more advanced webGIS, is in an early stage of development and not used within the Case Study.

Therefore ArcGIS in combination with the ArcGIS PlanetServer add-in was used, allowing for a direct comparison between the geology and mineralogy of a certain region on Mars in a complete GIS environment. Although IDL/ENVI remains the most advanced software for spectral analysis, the python add-in can be easily extended using the many open source libraries of the python programming language (see for example Laura et al. 2013). On the server-side python could also be used for more computer intensive tasks such as automated mineral detection algorithms (e.g. Carter et al. 2013a).

The CRISM data has been processed on PlanetServer itself during early phases, but later processing is going to be performed on HPC hardware. Although we used the best available processing steps (McGuire et al. 2009) the processing algorithms for CRISM data are still in development, especially noise reduction (e.g. Parente et al. 2014) and atmospheric correction (e.g. Dobrea et al. 2011; Wiseman et al. 2012). PlanetServer will therefore either need to be updated once new corrections have been made available. The feasibility of performing on-the-fly additional corrections, possibly using WCPS, needs to be investigated.

Limited online collaboration among the participating researchers of the Case Study was achieved by using the wiki system. Results could be discussed and ArcGIS screenshots could be uploaded and added as figures. A true collaborative webGIS system for Mars data however does not yet exist. The missing functionality might be similar to that of the Concurrent Online WebGIS (Ottens and van Tilburg 2013), described as 'google docs for maps' and allowing for multiple users to digitize a map in real-time. Timing and technological developments are probably right for such type of collaborative mapping/analysis to emerge and develop in coming years.

5 Conclusions

The use of the Jacobs University HPC facilities allowed for relatively fast processing of image mosaic data. The mosaicking process for the entire $\sim$2,000 tiles of a global CTX mosaic therefore comes into reach, but would still take a considerable amount of time and computing resources. The work could, however, be collectively shared among fellow scientists and institutes (e.g. a form of limited crowdsourcing), where each group or individual would manage one or more CTX tiles. This will possibly be attempted with our close colleagues from cooperating institutes.

Within the Case Study the processed CTX and CRISM data of Noachis Terra have been made available online. A custom-built web client and ArcGIS add-in allow for access to, and analysis of, this data. The data was collaboratively shared among researchers at different locations to investigate the Noachis Terra geology and mineralogy. A wiki system was used to share and discuss results. Collaborative mapping, such as that of the Concurrent Online WebGIS (Ottens and van Tilburg 2013), would possibly allow for future integration. The PlanetServer *Neo* web client is envisioned to evolve into such a system. However for the time being mapping remains best performed using offline GIS software such as ArcGIS. The PlanetServer add-in tool adds online access to processed CRISM data, and is therefore foreseen to mature into an advanced spectral analysis tool.

In summary the Case Study showed that the infrastructure allowing for collaborative exploration and analysis of Mars Big Data is advancing but more work is needed towards integration. This might lead to a collaborative webGIS and wiki system enabling the online collaborative analysis, mapping, documentation and discussion of Mars Big Data in order to unravel the complex geological history of Mars.

Acknowledgments We would like to thank the two reviewers, Monica Pondrelli and Christoph Waldmann for their constructive comments. Achim Geleßus is thanked for granting us access to the CLAMV (Computational Laboratories for Analysis, Modeling and Visualization) HPC cluster at Jacobs University Bremen. We are grateful to the L-SIS group at Jacobs for valuable support throughout the PhD project and the overall work. Jennifer Eidswick, from the Fremdsprachenzentrum Bremen, is thanked for her English language coaching for key parts of the publication. The present work has been carried out within the FP7 EarthServer (EU FP7-INFRA grant no. 283610).

References

Andersen R (2012) Updated Google Mars! The Martian Chronicles, AGU Blogosphere. http://blogs.agu.org/martianchronicles/2012/11/06/updated-google-mars/

Baumann P (1994) On the management of multidimensional discrete data. VLDB J 4(3):401–444 (Special issue on spatial database systems)

Baumann P (2009a) Array databases and raster data management. In: Özsu T, Liu L (eds) Encyclopedia of database systems. Springer, Berlin

Baumann P (2009b) The OGC web coverage processing service (WCPS) standard. GeoInformatica 14:447–479

Carter J, Poulet F, Murchie S, Bibring JP (2013a) Automated processing of planetary hyperspectral datasets for the extraction of weak mineral signatures and applications to CRISM observations of hydrated silicates on Mars. Planet Space Sci 76:53–67

Carter J, Poulet F, Bibring J-P, Mangold N, Murchie S (2013b) Hydrous minerals on Mars as seen by the CRISM and OMEGA imaging spectrometers: updated global view. J Geophys Res Planets 118:831–858

Chiwome V, Kundel D, Oosthoek J, Rossi AP, Unnithan V, Baumann P, Pappalardo M (2014) webclient-neo: Planetserver/Earthserver project end. ZENODO. doi:10.5281/zenodo.11698

Christensen PR, Jakosky BM, Kieffer HH et al (2004) The thermal emission imaging system (THEMIS) for the Mars 2001 Odyssey mission. Space Sci Rev 110(1–2):85–130

Dobrea EZN, Michalski J, Swayze G (2011) Aqueous mineralogy and stratigraphy at and around the proposed Mawrth Vallis MSL Landing Site: new insights into the aqueous history of the region. MARS 6:32–46

Ehlmann BL, Berger G, Mangold N, Michalski JR, Catling DC, Ruff SW, Chassefière E, Niles PB, Chevrier V, Poulet F (2012) Geochemical consequences of widespread clay mineral formation in Mars' ancient crust. Space Sci Rev 174:329–364

Gaddis L, Anderson J, Becker K, Becker T, Cook D, Edwards K, Eliason E, Hare T, Kieffer H, Lee EM, Mathews J, Soderblom L, Sucharski T, Torson J, McEwen A, Robinson M (1997) An overview of the integrated software for imaging spectrometers (ISIS). In: Presented at the 28th lunar and planetary science conference, Lunar and Planetary Institute, Houston (Abstract #1226)

Gwinner K, Scholten F, Preusker F, Elgner S, Roatsch T, Spiegel M, Schmidt R, Oberst J, Jaumann R, Heipke C (2010) Topography of Mars from global mapping by HRSC high-resolution digital terrain models and orthoimages: characteristics and performance. Earth Planet Sci Lett 294:506–519

Hare TM, Skinner JA Jr, Fortezzo CM, Tanaka KL, Navu RA (2012) The astrogeology mapping, remote-sensing, cartography, technology, and research (MRCTR) GIS lab. In: Presented at the 43rd lunar and planetary science conference, Houston, Texas, USA (Abstract #2871)

Keszthelyi L, Becker T, Sides S et al (2013) Support and future vision for the integrated software for imagers and spectrometers (ISIS). In: Presented at the 44th lunar and planetary science conference (Abstract #2546)

Knapmeyer M, Oberst J, Hauber E, Wählisch M, Deuchler C, Wagner R (2006) Working models for spatial distribution and level of Mars' seismicity. J Geophys Res 111

Laura J, Hare TM, Gaddis LR (2013) Using Python, an interactive open-source programming language, for planetary data processing. In: Presented at the 44th lunar and planetary science conference (Abstract #2226)

Malin MC, Bell JF, Cantor BA, Caplinger MA, Calvin WM, Clancy RT, Edgett KS, Edwards L, Haberle RM, James PB, Lee SW, Ravine MA, Thomas PC, Wolff MJ (2007) Context Camera investigation on board the Mars reconnaissance orbiter. J Geophys Res 112

McGuire PC, Bishop JL, Brown AJ, Fraeman AA, Marzo GA, Frank Morgan M, Murchie SL, Mustard JF, Parente M, Pelkey SM, Roush TL, Seelos FP, Smith MD, Wendt L, Wolff MJ (2009) An improvement to the volcano-scan algorithm for atmospheric correction of CRISM and OMEGA spectral data. Planet Space Sci 57:809–815

Murchie S, Arvidson R, Bedini P, Beisser K, Bibring J-P, Bishop J, Boldt J, Cavender P, Choo T, Clancy RT, Darlington EH, Des Marais D, Espiritu R, Fort D, Green R, Guinness E, Hayes J, Hash C, Heffernan K, Hemmler J, Heyler G, Humm D, Hutcheson J, Izenberg N, Lee R, Lees J, Lohr D, Malaret E, Martin T, McGovern JA, McGuire P, Morris R, Mustard J, Pelkey S, Rhodes E, Robinson M, Roush T, Schaefer E, Seagrave G, Seelos F, Silverglate P, Slavney S, Smith M, Shyong W-J, Strohbehn K, Taylor H, Thompson P, Tossman B, Wirzburger M, Wolff M (2007) Compact Reconnaissance imaging spectrometer for Mars (CRISM) on Mars reconnaissance orbiter (MRO). J Geophys Res 112. doi: 10.1029/2006JE002682

Neukum G, Jaumann R (2004) HRSC: the high resolution stereo camera of Mars Express In: Wilson A (ed) Mars express: the scientific payload ESA Publications Division, Noordwijk, The Netherlands

Oosthoek JHP, Flahaut J, Rossi AP, Baumann P, Misev D, Campalani P, Unnithan V (2013) PlanetServer: innovative approaches for the online analysis of hyper spectral satellite data from Mars advances in space research. doi:10.1016/j.asr.2013.07.002

Oosthoek J, Chiwome V, Rossi AP, Unnithan V, Baumann P, Beccati A, Misev D, Campalani P (2014) webclient: Planetserver/Earthserver project end. ZENODO. doi:10.5281/zenodo.11697

Ottens SM van Tilburg T (2013) Concurrent online Webgis: a new way to map together. FOSS4G, Nottingham. http://2013.foss4g.org/conf/programme/presentations/33/

Parente M, Saranathan AM, Wiseman S, Ehlmann BL, Pan L (2014) Denoising CRISM image: a new look. In: Presented at the 45th lunar and planetary science conference (Abstract #2900)

Pelkey SM, Mustard JF, Murchie S, Clancy RT, Wolff M, Smith M, Milliken R, Bibring J-P, Gendrin A, Poulet F, Langevin Y, Gondet B (2007) CRISM multispectral summary products: parameterizing mineral diversity on Mars from reflectance. J Geophys Res 112. doi:10.1029/2006JE002831

Rogers AD, Nazarian AH (2013) Evidence for Noachian flood volcanism in Noachis Terra, Mars, and the possible role of Hellas impact basin tectonics. J Geophy Res Planets 118:1094–1113. doi:10.1002/jgre.20083

Rossi AP, van Gasselt S (2010) Geology of Mars after the first 40 years of exploration. Res Astron Astrophys 10:621. doi:10.1088/1674-4527/10/7/003

Rossi AP, Oosthoek J, Baumann P, Beccati A, Cantini F, Misev D, Orosei R, Flahaut J, Campalani P, Unnithan V (2014). PlanetServer/EarthServer: big data analytics in planetary science. Geophys Res Abstr 16:EGU2014-5149

Rossi AP, Oosthoek J, Baumann P, Hare T (2013) [Getting] Big data from planetary science and exploration and the EarthServer/PlanetServer approach. XLDB Europe Workshop, CERN, Switzerland. http://indico.cern.ch/contributionDisplay.py?sessionId=1&contribId=18&confId=222554

Seelos FP, Murchie SL, Humm DC, Barnouin OS, Morgan F, Taylor HW, Hash C, The CRISM Team (2011) CRISM data processing and analysis products update—calibration, correction, and visualization. In: Presented at the 42nd lunar and planetary science conference (Abstract #1438)

Smith DE, Zuber MT, Frey HV, Garvin JB, Head JW, Muhleman DO, Pettengill GH, Phillips RJ, Solomon SC, Zwally HJ, Banerdt WB, Duxbury TC, Golombek MP, Lemoine FG, Neumann

GA, Rowlands DD, Aharonson O, Ford PG, Ivanov AB, Johnson CL, McGovern PJ, Abshire JB, Afzal RS, Sun X (2001) Mars orbiter laser altimeter: experiment summary after the first year of global mapping of Mars. J Geophys Res 106:23689–23722. doi:10.1029/2000JE001364

Snijders C, Matzat U, Reips U-D (2012) 'Big Data': big gaps of knowledge in the field of Internet. Int J Internet Sci 7:1–5. http://www.ijis.net/ijis7_1/ijis7_1_editorial.pdf

Tanaka KL (1986) The Stratigraphy of Mars. J Geophys Res 91:E139–E158. doi:10.1029/JB091iB13p0E139

Tanaka KL, Robbins SJ, Fortezzo CM, Skinner JA, Hare TM (2013) The digital global geologic map of Mars: Chronostratigraphic ages, topographic and crater morphologic characteristics, and updated resurfacing history. Planet Space Sci. doi:10.1016/j.pss.2013.03.006

Tange O (2011) GNU Parallel—the command-line power tool, login: The USENIX Magazine

Vatsavai RR, Shekhar S, Burk TE, Lime S (2006) Umn-mapserver: a high-performance, interoperable, and open source web mapping and geo-spatial analysis system. In: Geographic information science. Springer, Berlin, pp 400–417

Werner SC, Tanaka KL (2011) Redefinition of the crater-density and absolute-age boundaries for the chronostratigraphic system of Mars. Icarus 215:603–607. doi:10.1016/j.icarus.2011.07.024

Wichman RW, Schultz PH (1989) Sequence and mechanisms of deformation around the Hellas and Isidis impact basins on Mars. J Geophys Res Solid Earth (1978–2012) 94:17333–17357

Wiseman SM, Arvidson RE, Wolff MJ, Morris RV, Seelos FP, Smith MD, Humm D, Murchie SL, Mustard JF (2012) Retrieval of atmospherically corrected CRISM Spectra using radiative transfer modeling. In: Presented at the 43rd lunar and planetary science conference (Abstract #2146)

Zurek RW, Smrekar SE (2007) An overview of the Mars reconnaissance orbiter (MRO) science mission. J Geophys Res 112. doi:10.1029/2006JE002701